

First Measurements of the Polarized Spin Density  
Matrix Elements along with a Partial-Wave  
Analysis for  $\gamma p \rightarrow p\omega$  using CLAS at Jefferson Lab

by

Brian Vernarsky

A dissertation submitted in partial fulfillment of the requirements  
for the degree of

Doctor of Philosophy

in the Department of Physics

Carnegie Mellon University

April 28, 2014



## Abstract

This work presents measurements of the spin density matrix elements for the reaction  $\gamma p \rightarrow p\omega$ . The data were collected using the CLAS detector in Hall B at Jefferson Lab, from two different datasets, g1c and g8b. The results from the g1c dataset cover the energy range  $1720 \text{ MeV} \leq \sqrt{s} \leq 2470 \text{ MeV}$ , and, due to a circularly polarized photon beam, allow access to the  $\rho^3$  spin density matrix elements. The results from the g8b dataset cover the energy range  $1720 \text{ MeV} \leq \sqrt{s} \leq 2210 \text{ MeV}$ , and, due to a linearly polarized photon beam, allow access to the  $\rho^1$  and  $\rho^2$  spin density matrix elements. The results presented here include the first measurements, at any energy, of the  $\rho^{1-3}$  elements. Therefore, our results significantly increase the world's data on  $\omega$  photoproduction spin dependence.

We have also performed a mass-independent partial-wave analysis to determine the dominant resonances involved in  $\omega$  photoproduction. The addition of polarization information is shown to increase our analyzing power over experiments without polarization information. However, it has not allowed us to determine the mass and width of the resonances involved. It may be necessary to modify the models for non-resonant production to be able to determine those.

## Acknowledgments

I would like to thank many people for helping me in my quest for obtaining my Ph.D. I would first like to thank my advisor Curtis Meyer for all of his help in guiding me, allowing me to change paths and experiments, and pushing me to pursue the best results possible. I would also like to thank Brian Quinn, who was also an initial advisor to me, and due to his late working habits and constant need for coffee, also an excellent source of advice and help throughout my time here. Additionally, I would like to thank Reinhard Schumacher and Gregg Franklin for being available whenever I had questions and providing assistance and guidance whenever I asked for it. And I would like to thank Richard Jones, who helped to prove a necessary theory for my work, and for serving on my thesis committee.

I also need to give much thanks to my entire family for their help in keeping me sane throughout my time in graduate school. My parents were a constant source of support, and my brother Chris and sister Renee kept me company, even if just over the phone, for many lonely nights. My niece Victoria brightened my day on so many occasions, with a picture she sent, or by getting to talk to her on the phone, even even better yet, when I got to see her. My extended family was one of the main reasons that I went to school in Pittsburgh and I am so lucky to have been able to spend so much time with my grandparents in the last years of their lives. They were a constant source of support and inspiration and a nice retreat whenever I needed it. And it didn't hurt that they thought that I was much, much smarter than I actually am, and didn't hesitate to say so! My aunt Elaine and uncle Don, and their family, Sue, Daemon, Daniel, Katie, Michelle and Les (I'll exclude all the dogs) have also been a wonderful home away from home, a great way to keep myself grounded and happy and think about things other than physics. I don't know what I would have done without them and without a loving home to go to for every holiday. It was also wonderful being close to my aunt Peggy and her family, and seeing them a few times a year.

I probably never would have made it through my undergrad degrees if it weren't for the luck of ending up with Joseph Dratz as my roommate, with David Forsythe just down the hall. We were able to make it through unbelievable amounts of homework together, and I couldn't have done it without them.

I made many friends at CMU and am indebted to all of them in helping me through my time here. Hef, Buck, Ben, and PS, thanks for wasting so much time with me. Lilli, Mike, Alex, Yves, Booth, Frankie, and Brendan, thanks for spending so much time at the bar with me, I wish Thirsty Thursdays could have lasted forever. Mike Williams deserves special mention because he got me back into grad school after I had left, and has guided my research ever since. This thesis is essentially redoing his thesis work, just for different experiments, and I'm extremely grateful for his help and guidance through the years, even as this work became more and more a distant memory for him. Paul, thanks for being there to talk to the last couple of years. And to the best office mate ever, Katie, thanks for everything, from teaching me to solve the Rubik's cube, to being a great target for pennies, and just being an amazing friend and listening to my insane ideas, thanks. My best memories from CMU are of spending time with you in the office. Sorry I never learned how to hula hoop.

As for my life outside of CMU in Pittsburgh, I have relied on the friendship and support of a few people who have made a world of difference to me. Mike introduced me to Ken many years ago and he's been an amazing friend ever since. Getting an occasional beer and talking is sometimes all the therapy I need. I had only lived in Pittsburgh for a few weeks when I first stopped in to

Pizza Prima after church one Saturday night and met Frank, who ever since has been a constant presence on my Saturday night, provider of great pizza and great conversation. Without him I never would have known how terrible my Italian was as I tried to learn it! As I started branching out and coming to Pizza Prima for lunch during the week I met Lisa, who, after a chance encounter at a Phish concert, has become a great friend and part-time therapist. Without her this past six months I probably wouldn't have eaten anything and almost certainly would have been committed. I also want to thank my piano teacher, Jeffrey Harris, who drove me to attempt perfection in the piano, which in turn helped me strive for perfection in the rest of my work. And Taya, JLab wouldn't have been bearable without your friendship. It was always great to talk to you, and play tennis, and play the piano for you. It was nice having someone who actually wanted to listen to me play!

Thanks to all of you, I couldn't have done it without you!



# Contents

<b>1</b>	<b>Introduction</b>	<b>1</b>
1.1	Quantum Chromodynamics . . . . .	1
1.1.1	Spectroscopy . . . . .	2
1.2	The Missing Baryon Problem . . . . .	4
1.3	The $\omega$ Meson . . . . .	4
1.3.1	Physical Observables . . . . .	7
1.4	Previous $\gamma p \rightarrow p\omega$ Measurements . . . . .	7
1.5	Summary . . . . .	8
<b>2</b>	<b>Jefferson Lab</b>	<b>9</b>
2.1	Continuous Electron Beam Accelerator Facility (CEBAF) . . . . .	9
2.2	Photon Tagger . . . . .	11
2.3	CEBAF Large Acceptance Spectrometer Detector . . . . .	12
2.3.1	Target . . . . .	12
2.3.2	Start Counter . . . . .	12
2.3.3	Superconducting Toroidal Magnet . . . . .	14
2.3.4	Drift Chambers . . . . .	14
2.3.5	Time-of-flight Scintillators . . . . .	16
2.4	Beamline Devices . . . . .	17
2.5	Trigger and Data Acquisition . . . . .	18
2.6	Summary . . . . .	18
<b>3</b>	<b>Data Selection</b>	<b>19</b>
3.1	Excluded Runs . . . . .	20
3.1.1	g1c . . . . .	20
3.1.2	g8b . . . . .	21
3.2	Energy and Momentum Corrections . . . . .	21
3.2.1	Energy Loss Corrections . . . . .	21
3.2.2	Tagger Corrections . . . . .	22
3.2.3	Momentum Corrections . . . . .	24
3.2.4	Final Corrections . . . . .	25
3.3	Kinematic Fit of $\gamma p \rightarrow p\pi^+\pi^-(\pi^0)$ . . . . .	26
3.4	Particle Identification . . . . .	26
3.5	Detector Performance Cuts . . . . .	27
3.5.1	Fiducial Cuts . . . . .	27
3.5.2	TOF Paddle Cuts . . . . .	27
3.6	The Cut on $\cos\theta_{CM}^{\pi^0}$ . . . . .	27
3.7	Signal-Background Separation . . . . .	30
3.7.1	Near Threshold Bins . . . . .	31

3.8	Polarization . . . . .	32
3.8.1	Circular Polarization in g1c . . . . .	32
3.8.2	Linear Polarization in g8b . . . . .	32
3.9	Monte Carlo . . . . .	34
3.9.1	GSIM . . . . .	35
3.9.2	Polarization Values . . . . .	35
3.10	Summary . . . . .	35
<b>4</b>	<b>Partial-Wave Analysis Formulas</b>	<b>37</b>
4.1	Notation . . . . .	37
4.2	Extended Maximum Likelihood Method . . . . .	38
4.2.1	Normalization . . . . .	39
4.2.2	Log Likelihood . . . . .	40
4.3	Spin Density Matrices . . . . .	41
4.3.1	Photon Spin Density Matrix . . . . .	42
4.3.2	Target Spin Density Matrix . . . . .	42
4.3.3	Vector Meson Spin Density Matrix . . . . .	42
4.3.4	Symmetries in the Spin Density Matrix of Vector Mesons . . . . .	45
4.3.5	Schilling's Method . . . . .	45
4.3.6	Measurable Elements . . . . .	46
4.3.7	Relationship to Vector and Tensor Polarizations . . . . .	47
4.3.8	Summary . . . . .	47
4.4	Likelihood Equations . . . . .	48
4.4.1	Unpolarized Photons . . . . .	48
4.4.2	Polarized Photons . . . . .	49
4.4.3	Polarized Target . . . . .	49
4.4.4	Polarized Photons and Polarized Target . . . . .	49
4.5	The Angles $\alpha$ and $\beta$ . . . . .	49
4.6	Coupling Multiple Datasets . . . . .	50
4.7	Summary . . . . .	51
<b>5</b>	<b>Spin Density Matrix Elements</b>	<b>53</b>
5.1	The Mother of All Fits . . . . .	53
5.1.1	Partial Wave Amplitudes . . . . .	53
5.1.2	Maximum Likelihood Fit . . . . .	54
5.1.3	Differential Cross Sections . . . . .	55
5.2	Spin Density Matrix Elements . . . . .	55
5.2.1	Errors . . . . .	55
5.2.2	$\rho^0$ Elements in g1c and g8b . . . . .	59
5.2.3	$\rho^1$ Elements in g8b . . . . .	68
5.2.4	$\rho^2$ Elements in g8b . . . . .	76
5.2.5	$\rho^3$ Elements in g1c . . . . .	80
5.3	Schilling's Method . . . . .	82
5.4	Summary . . . . .	89
<b>6</b>	<b>Partial-Wave Analysis</b>	<b>91</b>
6.1	Theoretical Models for Non-Resonant Photoproduction . . . . .	92
6.1.1	The Oh, Titov and Lee Model . . . . .	92
6.2	The s-channel Scans . . . . .	93
6.2.1	One s-channel Wave and OTL t-channel . . . . .	93
6.2.2	Two s-channel Waves and OTL t-channel . . . . .	93

6.2.3	Three s-channel Waves and OTL t-channel . . . . .	95
6.3	Examining the Parameters . . . . .	98
6.3.1	Decay Parameters . . . . .	98
6.3.2	Multipole Parameters . . . . .	102
6.4	Comparison to SDMEs . . . . .	104
6.4.1	The $\frac{3}{2}^-, \frac{5}{2}^-$ Plus t-channel Fits . . . . .	104
6.4.2	The $\frac{3}{2}^-, \frac{5}{2}^+$ Plus t-channel Fits . . . . .	105
6.4.3	The $\frac{5}{2}^+, \frac{7}{2}^-$ Plus t-channel Fits . . . . .	105
6.4.4	Summary . . . . .	112
6.5	Combined Fits . . . . .	112
6.5.1	s-wave Scans . . . . .	112
6.5.2	Examining the Parameters . . . . .	112
6.5.3	Summary . . . . .	117
6.6	Summary . . . . .	117
7	<b>Summary</b>	<b>119</b>
7.1	Recap of Analysis Procedure . . . . .	119
7.2	Conclusions and Future Work . . . . .	120
A	<b>Issues with the Time-of-Flight Detectors in g8b</b>	<b>127</b>
A.1	The Adair Angles . . . . .	131
A.2	The Time-of-Flight Detectors . . . . .	132
A.3	The Effects on Monte Carlo . . . . .	132
A.4	After Recooking . . . . .	135
A.5	Summary . . . . .	137
B	<b>Special Comparisons of the SDMEs</b>	<b>139</b>



# Chapter 1

## Introduction

Since at least the 5<sup>th</sup> century BC, when the atomic theory was first proposed by Leucippus and Democritus, scientists have been interested in determining the fundamental particles of the universe. In the centuries since Leucippus and Democritus, scientists have discovered atoms, realized they were not fundamental particles, but are in fact made of protons, neutrons, and electrons, and then further determined that the nucleons (protons and neutrons) were themselves made of smaller particles as well.

A major goal of medium energy physics is then to understand what is happening inside of a nucleon. We have some knowledge of how nucleons interact with each other and with other particles, such as electrons, and we know what the constituent particles of the nucleons are; but our understanding of nucleons is considerably less complete than our understanding of atoms and molecules. In order to discover what we do not yet know about nucleons, it is instructive to first consider what we do know about nucleons. In order to make it easier to comprehend that, we will present our knowledge of nucleons in comparison to our knowledge of atoms.

### 1.1 Quantum Chromodynamics

Atoms can be considered particles that are made up of smaller, constituent particles. These constituent particles are known as protons and neutrons, which constitute the nucleus, and electrons. The nucleus and the electrons are bound to each other by the electromagnetic force, which is mediated by a massless spin-1 (vector) boson known as the photon. The theory that describes the electromagnetic interaction is known as Quantum Electrodynamics (QED). Different combinations of these three types of particles behave differently and have different characteristics. The photon is able to interact with charged particles, however it does not carry a charge itself and thus two photons cannot couple directly to each other. An atom generally interacts with a photon by absorbing or emitting a photon.

Nucleons are members of a group of particles known as baryons, which we think of as particles characterized by three constituent particles known as quarks. Quarks are (currently thought to be) fundamental particles, that is, they are not themselves composed of constituent particles. There are six *flavors* of quarks with ridiculous names. The quarks are held together by the strong force, which is mediated by a massless vector boson known as the gluon. The theory that describes the strong interaction is known as Quantum Chromodynamics (QCD). The term *chromodynamics* comes from the fact that the *charge* term for QCD is known as a color charge and comes in three types, often denoted red, green, and blue. Quarks carry electromagnetic charge as well as a color charge. One significant difference between QCD and QED is that the gluon also carries color charge, while the photon does not carry electromagnetic charge. Unlike in QED, where the photon cannot, to lowest order, interact with other photons, in QCD the gluon can interact with other gluons. Thus, quarks

can not only emit or absorb a gluon, but gluons can also emit or absorb another gluon, and two gluons can interact directly with each other. Because of those last two possibilities, it is not possible to calculate a complete, analytic, solution to QCD and new techniques are required to approximate a solution.

### 1.1.1 Spectroscopy

One of the easiest ways atoms have been studied to obtain information about the electromagnetic force was to create interactions between photons and atoms. One way to study this consisted of shining light through a gas and observing what came out on the other side (practically, this was accomplished by studying the spectra of starlight which passed through clouds of gas in space). What was found when experiments like this were conducted was that if light containing many different wavelengths (starlight) was shone through the gas, the resulting spectrum of light after passing through the gas would no longer contain the full spectrum that was passed into it, certain wavelengths were missing. This discrete set of missing wavelengths, coupled with other results, led to the idea that the energy levels of an atom are discrete and thus quantum mechanics was born.

If we tried a completely analogous approach to studying the strong force, we would need to shine a beam of gluons at nucleons in an attempt to excite them and then observe the absorption spectrum coming out the other side. We take as a given that, due to the nature of quantum mechanics, the energy spectrum for the excited states of nucleons will be discrete and there will be a limited number of excited states. There are several difficulties in this approach, the main being that a beam of gluons is not possible. We can, however, approach the problem by recalling that quarks and gluons can interact not only via the strong force, but also via the electromagnetic force, which allows them to interact with photons. Since the goal is simply to excite the nucleons, it does not matter where the energy is coming from. In fact, a beam of any type of particles could be used, but only a few are practical. There is still a difficulty associated with this method. While atoms can be excited by photons with relatively low energies, nucleons can only be excited by much higher energies, and this requires a particle accelerator.

There are still many details that need to be worked out in order to determine the spectrum of excited nucleons. First of all, because of the method we are using, and the energy of the photons involved, it is not possible to simply measure an absorption spectrum, or look for an emission spectrum. Excited nucleons do not simply re-emit a photon of the same energy as the one that excited them, as atoms usually do. Instead, they often decay by releasing at least one other particle, and that particle may subsequently decay into other particles before being detected. The excited nucleons (also referred to as  $N^*$ 's or resonances) decay into combinations of baryons and mesons. While baryons are characterized by three constituent three quarks held together by the strong force, mesons are characterized by a quark and an anti-quark, also held together by the strong force. The  $\omega$  meson is such a particle, and will be the subject of this work.

Another problem is the fact that resonances are very short-lived, on the order of  $10^{-23}$  s. Heisenberg's uncertainty principle tells us that we can only determine the energy of a state to be within a range,  $\Delta E$ , given by

$$\Delta E \sim \frac{\hbar}{\tau}, \quad (1.1)$$

where  $\tau$  is the mean lifetime of the particle. As a result of this, there will always be some uncertainty in the exact excitation energy of the particular  $N^*$  state. Fortunately, the width of these lines is still narrow enough that it is often possible to separate out one state from another.

One final issue is that photons are not the only particles that can be used to excite a nucleon; for instance, beams of pions, kaons, electrons or other particles can be used for exciting the nucleon. Many early experiments to measure nucleon excitation used a pion beam. Due to different properties of pions and photons, some of the excited nucleon states may be more likely to form if they are excited with pions instead of photons, and vice versa. It is also possible to use either unpolarized or polarized

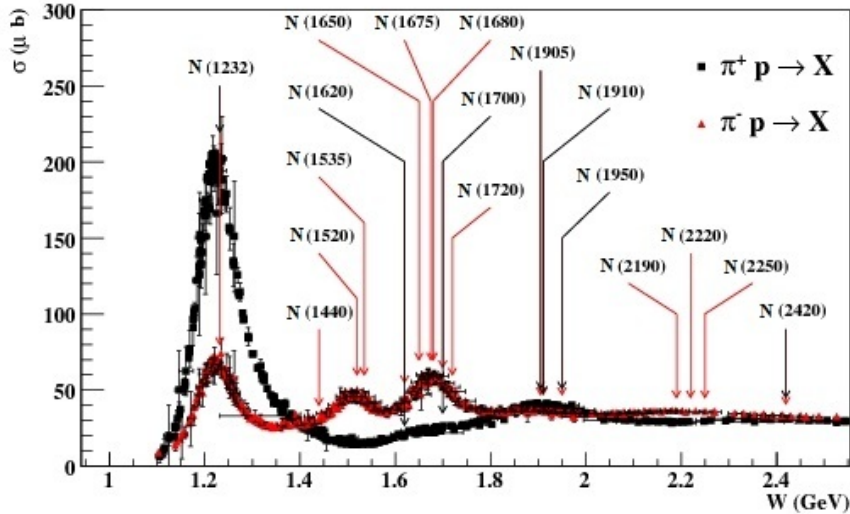


Figure 1.1: Nucleon resonances with a \*\*\* rating from the PDG [3]. The notation is  $N(M)$ , where  $N$  indicates that it is an excited nucleon with spin- $\frac{1}{2}$  and  $M$  is the mass in  $(\text{MeV}/c^2)$ . There are also five \*\*\* states which are not shown here [1].

beams. Polarized-beam experiments will provide more information and be more sensitive to certain properties of the resonances. Thus, to get the best measure of the spectrum of excited nucleon states, it is necessary to perform experiments with as many types of beam as are possible.

Figure 1.1 shows the cross section, as a function of center-of-mass energy, for two different types of beams interacting with a proton. The black points show the cross section for a beam of positively charged pions,  $\pi^+$ , and the red points represent the results from a beam of negatively charged pions,  $\pi^-$ . It is clear from the figure that there are several peaks present in the data, and these peaks are indicative of the presence of a resonance. From this figure, it is possible to see many of the properties of resonances mentioned above. Notice that some of the peaks are very broad, see the peak around 1.9 GeV, while others are much narrower, see the peak near 1.2 GeV. Also note that the cross sections from the two different pion beams are different, indicating that some resonances couple more strongly to  $p\pi^+$ , see the peak near 1.9 GeV, while others couple more strongly to  $p\pi^-$ , see the peaks near 1.52 GeV and 1.675 GeV.

In a similar way to how resonances couple differently to initial states involving photons or pions, each resonance has a different likelihood of decaying into certain particles. Thus, if one limits attention to only resonances that decay into one particular meson or baryon, many resonances may be missed. That being said, each meson or baryon has its own properties and features that make studying each independently a logical step. In the present analysis, the  $\omega$  meson resulting from the decay of a resonance will be studied. The hope is that this study will allow us to determine which resonance(s) is responsible for the production of  $\omega$  mesons in a given energy range. It is unlikely that it will be possible to fully determine this because multiple resonances are likely to decay to produce an  $\omega$ . However, it might be possible to determine several states that contribute to  $\omega$  production in a given energy range. The method used here for searching for which resonances are important for production of a given particle is known as partial-wave analysis and will be explained in Chapter 6.

## 1.2 The Missing Baryon Problem

In baryon spectroscopy, as well as atomic spectroscopy and many other fields, there are two separate yet equally important groups, those who run experiments and physically measure results, and those who make theories based on those results. Ideally, once enough data have been collected, a theory can be formed which will not only explain what has been measured but will be able to predict results that have not yet been measured. In the case of baryon spectroscopy these theories should be able to predict  $N^*$  states that have not been measured yet, and then experiments should be able to confirm or disprove their existence.

The particle physics community has an international collaboration which collects and catalogs all of the current results from particle physics experiments; they are known as the Particle Data Group. This group publishes a book, containing all of this collected data, known generally as the PDG [3]. When listing excited nucleon states they have a star system to determine how certain they are that a state is known to exist based on current measurements. The best rating is a four star (\*\*\*\*) rating, which denotes that *existence is certain, and properties are at least fairly well explored* [3]. Currently there are ten  $N^*$  states with a \*\*\*\* rating, other than the proton and neutron, along with an additional five states with a \*\*\* rating, indicating existence is likely, but not all properties have been confirmed.

Recently, the list of resonances has undergone a transformation, as several new states have been added to the list of experimentally observed states, other states have been removed, and several others have gained or lost stars, indicating more or less reliability in their existence. The list of currently accepted states can be seen in Table 1.1, which highlights the differences between the 2010 and 2012 versions of the PDG. Also indicated on the table are the type of final states that the resonance has been seen in, graded using the same star system. Many of the changes to the list came as a result of adding in recent studies of the  $K\Lambda$  and  $K\Sigma$  channels. One of the reasons that those studies are important is that they added new polarization observables, which were able to refine the partial-wave analysis. Note that the  $N\omega$  final state is only seen for four of the states, and each at only the one- or two-star level. This is because precise measurements of the polarization observables for the  $\omega$  have not yet been performed. This study will provide the first measurements of several new polarization observables for the  $\omega$  meson.

Even with all of these states observed, theorists expect many more states than just these. Table 1.2 shows all of the states predicted to exist based on a certain model, the Constituent Quark Model by Capstick and Roberts [5], as well as which states have been observed in experiments accepted by the PDG. This model is based on simple harmonic oscillations and includes relativistic effects, but is not carried out in a completely covariant framework. There are approximately twice as many states theorized to exist as have been discovered; this discrepancy is known as the *missing baryon problem*. It is possible that the states simply do not exist and the theory is wrong. But it is also possible that the states do exist and simply have not yet been seen in experiments, perhaps because they do not couple to pions and photons. The hope is that by examining a decay particle like the  $\omega$  thoroughly, over a wide range of energies, angles, and experimental setups (varying photon and target polarizations for instance), we will be able to determine the properties of the resonances which are important in its production. If this can be determined, then it is possible to determine if these resonances have already been observed or if they are newly measured; and, if they are newly measured, are they similar to what is predicted by theory. Several of the new states seen in Table 1.1 match up well with formerly missing states.

## 1.3 The $\omega$ Meson

The  $\omega$  meson is a spin-1 meson. Spin-1 mesons with odd parity are also referred to as vector mesons. The  $\omega$  has an observed rest mass of  $782.59 \pm 0.11$  MeV/ $c^2$ . It is a neutral particle, meaning that its electromagnetic charge is 0. It has isospin=0, which means that the  $p\omega$  final state can only couple

$N^*$	$J^P$	2010	2012	$N\eta$	$N\sigma$	$N\omega$	$\Lambda K$	$\Sigma K$	$N\rho$	$\Delta\pi$
$p$	$1/2^+$	***	***							
$n$	$1/2^+$	***	***							
$N(1440)$	$1/2^+$	***	***		***			*		***
$N(1520)$	$3/2^-$	***	***	***				***		***
$N(1535)$	$1/2^-$	***	***	***				**		*
$N(1650)$	$1/2^-$	***	***	***		***	**	**		***
$N(1675)$	$5/2^-$	***	***	*		*		*		***
$N(1680)$	$5/2^+$	***	***	*	*			***		***
$N(1685)$		*								
$N(1700)$	$3/2^-$	***	***	*		*	*	*		***
$N(1710)$	$1/2^+$	***	***	***		**	***	**	*	**
$N(1720)$	$3/2^+$	***	***	***		**	**	**	*	*
$N(1860)$	$5/2^+$		**					*		*
$N(1875)$	$3/2^-$		***			**	***	**		***
$N(1880)$	$1/2^+$		**		**	*				
$N(1895)$	$1/2^-$		**	**		**	*			
$N(1900)$	$3/2^+$	**	***	**		**	***	**	*	**
$N(1990)$	$7/2^+$	**	**				*			
$N(2000)$	$5/2^+$	**	**	**		**	*		**	
$N(2080)$										
$N(2090)$										
$N(2040)$	$3/2^+$		*							
$N(2060)$	$5/2^-$		**	*				**		
$N(2100)$	$1/2^+$	*	*					**		
$N(2150)$	$3/2^-$		**			**			**	
$N(2190)$	$7/2^-$	***	***			*	**		*	
$N(2200)$										
$N(2220)$	$9/2^+$	***	***							
$N(2250)$	$9/2^-$	***	***							
$N(2600)$	$11/2^-$	***	***							
$N(2700)$	$13/2^+$	**	**							

Table 1.1: Baryon Summary Table for  $N^*$  resonances including recent changes from PDG 2010 [2] to PDG 2012 [3]. The entries in red highlight significant changes between the 2010 and 2012 editions of the PDG. This chart was first compiled in [4].

$J^P$	$M_{CQM}$	$M_{PDG}$	Rating	$J^P$	$M_{CQM}$	$M_{PDG}$	Rating
$1/2^-$	1460	1535	****	$1/2^+$	1540	1440	****
$1/2^-$	1535	1650	****	$1/2^+$	1770	1710	***
$1/2^-$	1945	1895	**	$1/2^+$	1880	1880	**
$1/2^-$	2030			$1/2^+$	1975		
$1/2^-$	2070			$1/2^+$	2065	2100	*
$1/2^-$	2145			$1/2^+$	2210		
$1/2^-$	2195						
$3/2^-$	1495	1520	****	$3/2^+$	1795	1720	****
$3/2^-$	1625	1700	***	$3/2^+$	1870	1900	***
$3/2^-$	1960	1875	***	$3/2^+$	1910		
$3/2^-$	2055			$3/2^+$	1950		
$3/2^-$	2095	2120	**	$3/2^+$	2030	2040	*
$3/2^-$	2165						
$3/2^-$	2180						
$5/2^-$	1630	1675	****	$5/2^+$	1770	1680	****
$5/2^-$	2080	2060	**	$5/2^+$		1860	**
$5/2^-$	2095			$5/2^+$	1980	2000	**
$5/2^-$	2180			$5/2^+$	1995	2000	**
$5/2^-$	2235						
$5/2^-$	2260						
$5/2^-$	2295						
$5/2^-$	2305						
$7/2^-$	2090	2190	****	$7/2^+$	2000	1990	**
$7/2^-$	2205			$7/2^+$	2390		
$7/2^-$	2255			$7/2^+$	2410		
$7/2^-$	2305			$7/2^+$	2455		
$7/2^-$	2355						
$9/2^-$	2215	2250	****	$9/2^+$	2345	2220	****
$11/2^-$	2600	2600	***				
$11/2^-$	2670						
$11/2^-$	2700						
$11/2^-$	2770						
$13/2^-$	2715	2700	**				

Table 1.2: Constituent Quark Model predictions for the  $N^*$  spectrum from Capstick and Roberts [5]. This model is based on simple harmonic oscillations and includes relativistic effects, but is not carried out in a completely covariant framework. If a state with properties similar to a predicted state have been seen in experiments it will have a mass in the  $M_{PDG}$  column along with a rating for that observation. All masses,  $M_{CQM}$  and  $M_{PDG}$ , are in units of  $\text{MeV}/c^2$ . The ratio of predicted to observed states is  $\sim 2 : 1$ .

to states with  $I=1/2$ , i.e.  $N^*$  states, and not other states, like the  $\Delta^*$  states with  $I=3/2$ . It has a mean width of 8.49 MeV, which corresponds to a lifetime of  $7.75 \times 10^{-23}$ s. This short lifetimes means that we cannot detect it on its own before it decays, and instead must look for the particles into which it decays. It decays into a  $\pi^+$ ,  $\pi^-$ , and  $\pi^0$  89.1% of the time, and thus the main way that we hope to detect it is by detecting these particles.

### 1.3.1 Physical Observables

The  $\omega$  meson has two main physical observables that we can measure in a photoproduction experiment. The first is its cross section, which is basically the likelihood of scattering. The second is the polarization, which is characterized by a spin density matrix. The spin density matrix will be discussed in depth in Chapter 4; it is a 3x3 matrix with complex elements that vary with angle and energy. These nine complex values are related to each other, and some are required to be real, which reduces the total number of independent values in the matrix to five real values. Thus, there are basically six values that can be measured for this reaction.

However, it is overly simplistic to say that there are only six values to measure. In reality these six numbers can be measured in a variety of situations and should be different. For instance, the cross section can be very different depending on the angle under study. Photoproduced  $\omega$  mesons are forward-peaked, meaning that it is much more likely for it to be found moving forward, in the direction of the incident photon, than other directions. Also, depending on the energy of the incident photon, it may be more or less likely to be forward-peaked. Thus we will break our  $\omega$  datasets up based on its direction relative to the photon direction in the center-of-mass frame,  $\cos \theta_{CM}^\omega$ , and the photon energy, or, more precisely, the center-of-mass energy,  $\sqrt{s}$ . We will choose the width of each of these sets of bins based on the amount of data we have.

Also, as will be explained in Chapter 4, the spin density matrix is really a sum of 64 3x3 matrices. Depending on whether or not the polarization of the photon, target proton, and recoil proton can be determined in a particular experiment, most of those 64 matrices are not included in the measured spin density matrix for that experiment, but when more than one of them can be measured, then we will have more observables. It is this addition of more polarization observables that will be used to refine the partial-wave analysis and assist in searching for the resonances important in  $\omega$  photoproduction.

## 1.4 Previous $\gamma p \rightarrow p\omega$ Measurements

The basis for the current analysis is very heavily influenced by a previous analysis of the properties of  $\omega$  photoproduction at the same facility and using (mostly) the same equipment as the present study. That run period is known as g11a and it was analyzed by Mike Williams for his thesis [1]. The g11a run period used a beam of unpolarized photons incident on an unpolarized target, while the run periods used for this study utilized beams of polarized photons incident on an unpolarized target. Because the polarized data contains more information than unpolarized data, the fitting code has been changed slightly, as will be explained in Chapter 4. Otherwise, the data for both studies was analyzed in the same way and fit using the same basic framework. Thus, the g11a analysis will provide a constant check on our results.

In [1] Williams compared his results for the differential cross section and spin density matrix to previous experiments from SAPHIR [7, 9], CLAS [8], SLAC [10], and Daresbury [11, 12]. He also compared the results of his partial-wave analysis to those of Zhao [13], Oh, Titov and Lee [14], Titov and Lee [15], and Penner and Mosel [16, 17], all of whom were mainly using 1998 SAPHIR data [7] and 2003 SAPHIR data [9]. Because Williams' results are much more precise ( $\sim 250$  times more precise [1]), cover a much wider range in angles and energy, and have been performed with the same equipment and analysis techniques we choose to compare our results only to these. In Chapters 5

and 6, it will become clear that the results of this analysis are close enough to Williams' results that any comparison between his results and previous experiments will be equally valid for this analysis.

The Williams results include  $\sim 2000$   $(\sqrt{s}, \cos \theta_{CM}^\omega)$  points over the energy range  $1720 \leq \sqrt{s} \leq 2850$  MeV, and all but the most forwards and backwards angles in  $\cos \theta_{CM}^\omega$ . The current analysis contains data from two different run periods with different energy ranges, however both are completely contained within the g11a energy range, and the angles measured are the same between the run periods as well. Thus, at every energy and angle we will be able to compare our results with those from g11a. However, we will be able to measure more observables than were possible in g11a, all of them for the first time, and thus we cannot compare these new results to previous measurements. We will determine the reliability of the new measurements based on how good agreement is between g11a and each run period for the observables that can be measured in both of them.

The Williams partial-wave analysis indicated the presence of several  $N^*$  states, the  $^{***}N(1680)$ , with  $J^P = \frac{5}{2}^+$ , the  $^{***}N(1700)$ , with  $J^P = \frac{3}{2}^-$ , and the  $^{***}N(2190)$ , with  $J^P = \frac{7}{2}^-$ . We will attempt to see if the addition of polarization information, and thus extra spin density matrix elements, will help to confirm these, or other, states.

## 1.5 Summary

The g11a analysis by Williams provided the first high precision measurements for the polarization observables for  $\gamma p \rightarrow p\omega$ . This analysis will be able to make comparisons to those measurements as well as add in new measurements. The additional information coming from those new measurements will be able to further constrain the partial-wave analysis method and help to determine which resonances are present in the production of the  $\omega$  meson. Ideally, if we can determine which resonances are present in  $\omega$  production, we could help to determine whether some of the *missing* states are present.

Before extracting the observables and running a partial-wave analysis, we will first cover how and where the data for this study were collected, in Chapter 2, and how the data were prepared for fitting, in Chapter 3, before discussing the fitting formulas and the basics of spin density matrices in Chapter 4. In Chapter 5, the polarization observables will be presented, and in Chapter 6, the results of the partial-wave analysis will be discussed.

# Chapter 2

## Jefferson Lab

The data used in this analysis come from datasets collected at the Thomas Jefferson National Accelerator Facility (TJNAF), commonly known as Jefferson Lab or JLab, which is located in Newport News, VA. JLab consists of four experimental halls designated as Halls A, B, C and D. The different halls allow different types of physics experiments to be conducted at the same time, and allow existing devices to stay in place without having to move them for different types of studies. The accelerator at JLab is known as the Continuous Electron Beam Accelerator Facility (CEBAF). JLab is also home to a free-electron laser. A picture of the JLab campus is shown in Figure 2.1.

This analysis uses data from two run periods known as g1c and g8b, as well as the results of a previous analysis of a run period known as g11a, which were collected in Hall B using the CEBAF Large Acceptance Spectrometer (CLAS). Both run periods used a liquid hydrogen target and photons tagged to determine which photon energy is associated with each event. CLAS is intended to detect multi-particle final states and has a large acceptance to detect all of the particles in that final state.

### 2.1 Continuous Electron Beam Accelerator Facility (CEBAF)

The halls are delivered a continuous beam of electrons by CEBAF. The electron beam is produced at the injector with pulsed lasers on a GaAs photocathode. These pulses are timed to give bunches to each hall every 2 ns. 2 1/4 superconducting RF cryomodules accelerate the electrons extracted from the photocathode up to 45 MeV [20] before an optical chopper separates the bunches, and they are sent into the linear accelerators (Linacs). For large-acceptance coincidence experiments, like the ones analyzed here, a low current is necessary, and the continuous supply of electrons allows high statistics to be gathered quickly, even under these circumstances. A picture displaying the main components of the accelerator is shown in Figure 2.2.

The accelerator at JLab is set up like a racetrack, with two long Linacs connected by nine recirculating arcs. The acceleration occurs along the two Linacs where 168 superconducting Niobium cavities are set up with standing RF waves in phase with the electron bunches, see Figure 2.3, providing a continuous positive electric force. The Niobium cavities are kept at their superconducting temperature of 2 K by liquid Helium. The use of superconducting material allows a 100% duty factor. Each pass through the length of a Linac provides up to 600 MeV of acceleration (only 400 MeV at the time of the g1c run period) and bunches can go through the Linacs from 1-5 times, by using the recirculating arcs, giving a maximum final energy of  $\sim 4$  GeV for g1c and  $\sim 6$  GeV for g8b and g11a. Each hall can select how many passes through the Linacs it desires and the bunches are extracted after the requested number of passes using RF separator cavities.



Figure 2.1: An aerial view of Jefferson Lab, showing the mile long racetrack accelerator. The two linear accelerators can be seen in the background, while in the foreground to the right there are three humps in the ground, which show where the experimental halls A, B, and C are located [18].

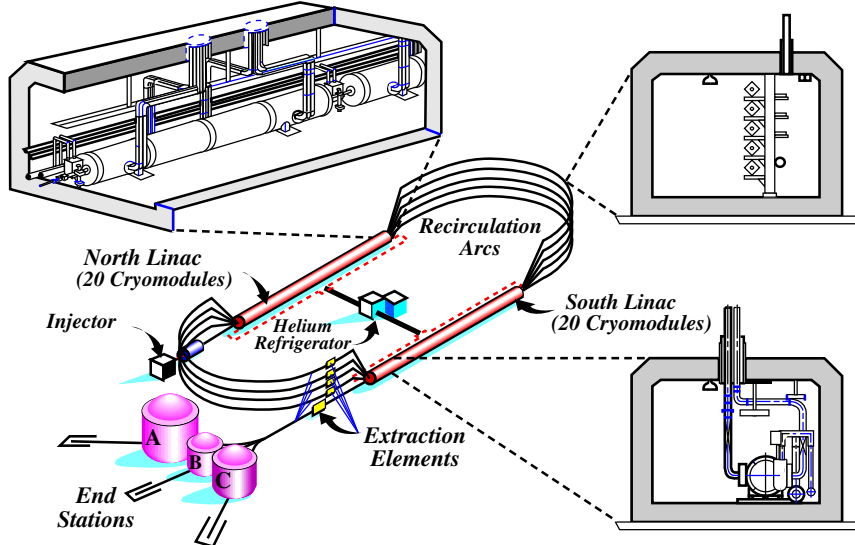


Figure 2.2: Diagram of the CEBAF facility, showing the racetrack accelerator. The electron beam begins at the injector, near the North Linac, and then is accelerated by the two Linacs up to a maximum energy of 4 GeV (at the time of g1c) or 6 GeV (at the time of g8b) before being directed to one of the experimental halls [19].

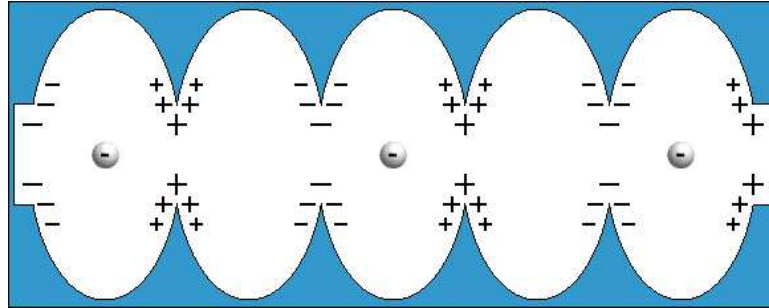


Figure 2.3: Superconducting cavities with standing RF waves, which provide an acceleration gradient for the electrons, such that they always experience a positive force throughout the cavity [21].

## 2.2 Photon Tagger

Since the g1c and g8b run periods required photons and not electrons, it was necessary to convert the electrons into photons. This was carried out using bremsstrahlung radiation in conjunction with a tagging system, which can be seen in Figure 2.4. For the g1c run period, a gold radiator with a thickness of  $1 \times 10^{-4}$  radiation lengths was used for data production, while a thinner, gold foil was used for *normalization* runs [23]. The g8b run period used linearly polarized photons, which required a thin diamond to generate the photons; some runs, however, were taken with a standard gold radiator, these runs are known as *amorphous* runs. The linearly polarized photons are generated via coherent bremsstrahlung production, which results in a characteristic energy distribution for the photons, defined by a *coherent peak*, which is the upper edge of this energy range. The energy difference from the coherent peak, in part, determines the polarization of the photon. A more detailed discussion of the linearly polarized photons may be found in Section 3.8.2.

Once the photons have been generated, by either means, a 1.75 T dipole magnet separates the recoiling electrons, and any electrons that have not interacted with the gold, from the photons, which pass into the target cryostat. The recoiling electrons are pulled to two hodoscope planes, which contain overlapping arrays of scintillators.

The first plane of scintillators, known as the E-plane, consists of 384 paddles used to determine the momentum of the electrons. The paddles are set up in an overlapping fashion, allowing for a total of 767 logical paddles. Each of these paddles is 20 cm long, 4 mm thick and between 6 and 18 mm wide. Since the trajectory of a charged particle through a magnetic field is determined by its momentum, it is possible to determine the momentum of the electron based on which paddle it strikes. The momentum of the recoil electron can then be used to determine the energy of the photon associated with it. The resolution of the detectors is 0.1% of the electron beam energy. The second plane, known as the T-plane, is used to collect timing information. This plane is located 20 cm below the E-plane and consists of 61 2-cm thick paddles. This thickness allows for timing resolution of 110 ps. The tagging system is able to tag photons with between 20 and 95% of the beam energy.

After being produced, the photons pass through a series of collimators to trim the profile of the beam. Between the collimators, there are sweeping magnets which remove any remaining charged particles from the beam before the beam goes to the target.

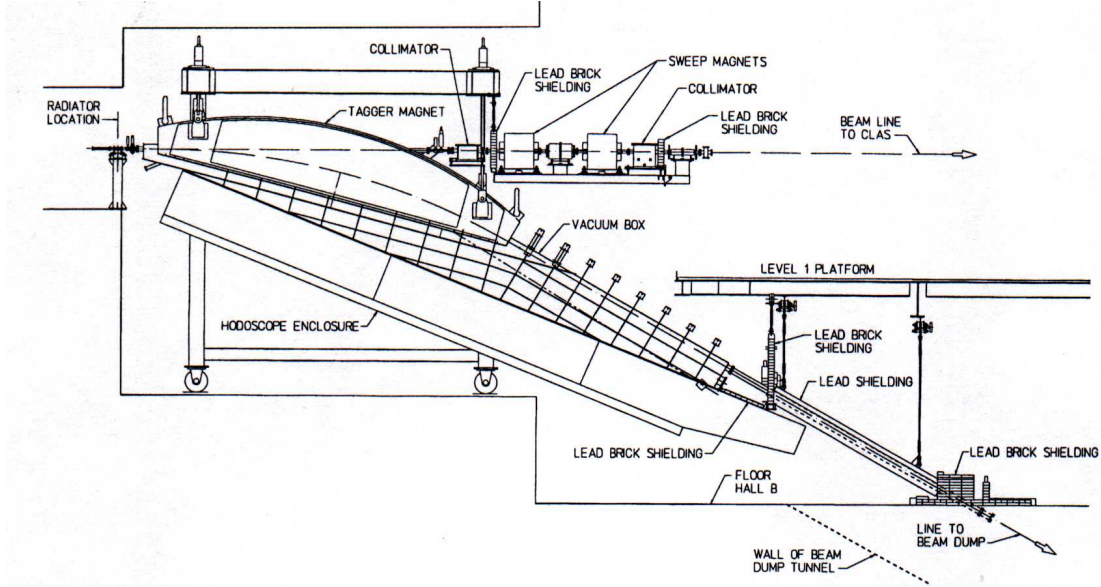


Figure 2.4: The Hall B photon tagger. The electrons strike the radiator at the far left and then proceed to the right, where they are bent by the tagger magnet into the spectrometer. Photons proceed through the collimator where the sweep magnets remove any charged particles from the beam, which then proceeds towards the target. [22]

## 2.3 CEBAF Large Acceptance Spectrometer Detector

The CLAS detector is used to detect charged particles produced from the photons interacting with the target. CLAS is comprised of several subsystems, which include a start counter, drift chambers and a wall of time-of-flight (TOF) scintillators. A schematic for CLAS can be found in Figure 2.5. Charged particles pass through the start counter and then are bent by a magnetic field set up by a large superconducting torus while they pass through the drift chambers before finally passing through the time-of-flight scintillators. The magnetic field around the drift chambers allows for determining the momentum of the particles, while the difference between the times recorded for the start counter and TOF detectors aids in particle identification. CLAS is split up into 6 segments of  $60^\circ$  in  $\phi$ , known as sectors.

### 2.3.1 Target

The g1c and g8b run periods used different targets. Both targets were Kapton cylinders made by Steve Christo of Jefferson Lab and filled with liquid hydrogen. Each had their pressure and temperature recorded approximately once an hour to determine the density. The g1c target was 17.85 cm long and is shown in Figure 2.6(a), while the g8b target was 40 cm long and can be seen in Figure 2.6(b). The g1c target was located at the center of CLAS while the g8b target was centered 20 cm upstream. The g8b target was the same target used in the g11a run period.

### 2.3.2 Start Counter

As its name suggests, the start counter is the first detector to be triggered by a charged particle and sets the start time for the event. It is used in the Level 1 trigger to determine whether or not

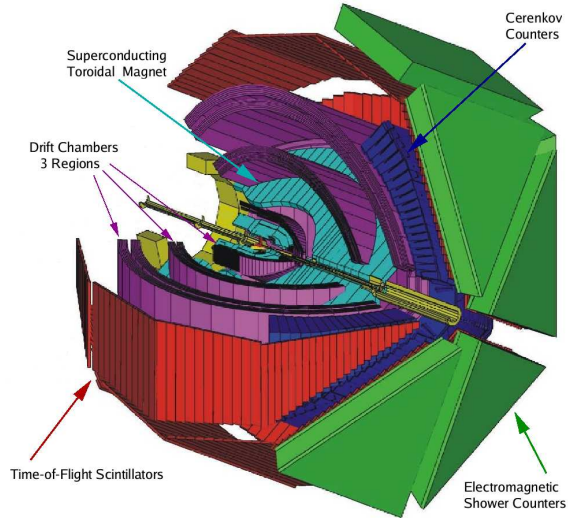


Figure 2.5: A schematic drawing of CLAS showing the location of the toroidal magnet, as well as the drift chambers and time-of-flight scintillators. The entire detector is around 8m in diameter and is located in Hall B at Jefferson Lab. [18].

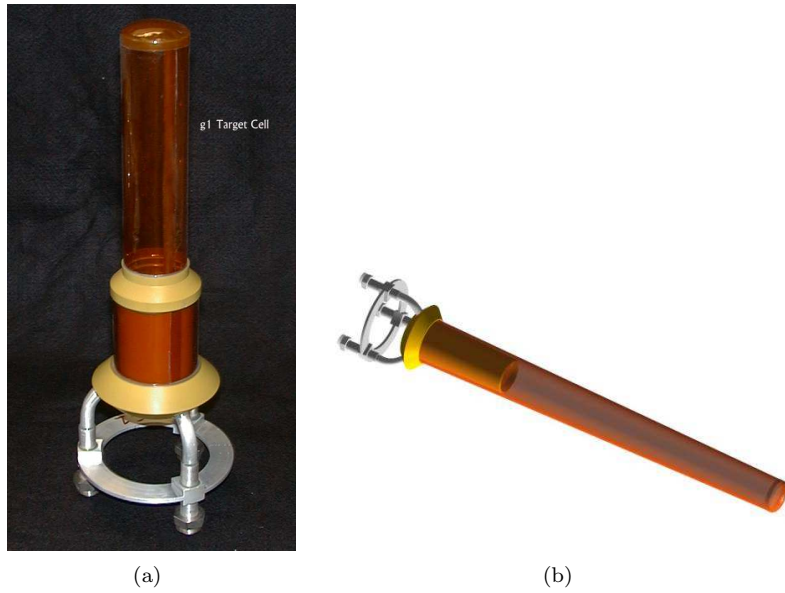


Figure 2.6: Target cells for the (a) g1c run period [23], and (b) g8b and g11a run periods [25].

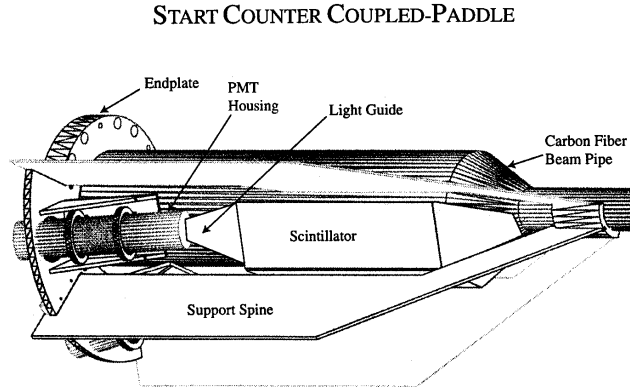


Figure 2.7: Start Counter in use for the g1c run period. [26]

to record an event. However, other than being required for detecting an event, it is not used in our analysis.

The start counter for g1c consists of three pairs of scintillator coupled-paddle detectors surrounding the target. The coupled paddles allowed for greater acceptance in the forward direction by linking two paddles together so they could share a set of PMTs, which reduced the total number of PMTs that would otherwise obscure the area downstream of the target. A diagram of the start counter can be seen in Figure 2.7.

In the years between the g1c and g8b run periods, a new start counter was installed in CLAS. The start counter for g8b consists of 6 sets of 4 scintillator paddles. The timing resolution is  $\sim 400$  ps. A diagram of the start counter can be seen in Figure 2.8. g8b and g11a used the same start counter.

### 2.3.3 Superconducting Toroidal Magnet

The superconducting toroidal magnet, seen in Figure 2.9, is used to bend the trajectories of charged particles as they pass through the drift chambers, giving them curved paths. As with the tagger system, the momentum of the particles can be determined from the curvature of their trajectory as they pass through the drift chambers, given the knowledge of the surrounding magnetic field. The magnets are cooled to the superconducting temperature of 4.4 K by liquid helium [28]. The field is generated by six kidney-shaped superconducting coils, set apart in the azimuth by  $60^\circ$ . The current running through the coils determines the magnetic field, and the maximum current for the torus is 3861 A, which yields a field of 3.5 T. The g1c and g8b run periods used about half of that current, only  $\sim 1930$  A. This does not provide the best momentum resolution possible, but it improves the acceptance for negative particles. The magnet bends forward-going, positively-charged particles away from the axis and negatively charged particles towards the axis. Thus, a high current and field causes many negatively charged particles to go undetected as they are too close to the beamline to be detected.

### 2.3.4 Drift Chambers

The trajectory of the charged particles is determined by a series of three drift chambers. This trajectory, along with detailed knowledge of the magnetic field maps, is able to determine the

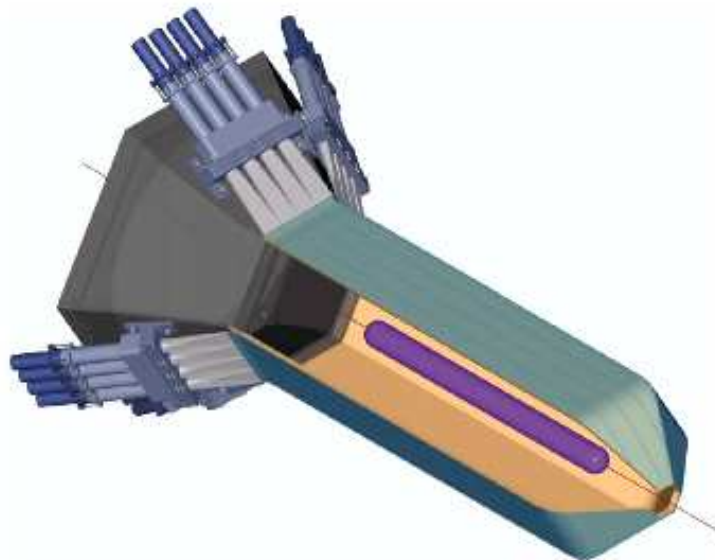


Figure 2.8: Start Counter in use for the g8b and g11a run periods [27].



Figure 2.9: The CLAS magnet separated from the rest of the detector before installation [18].

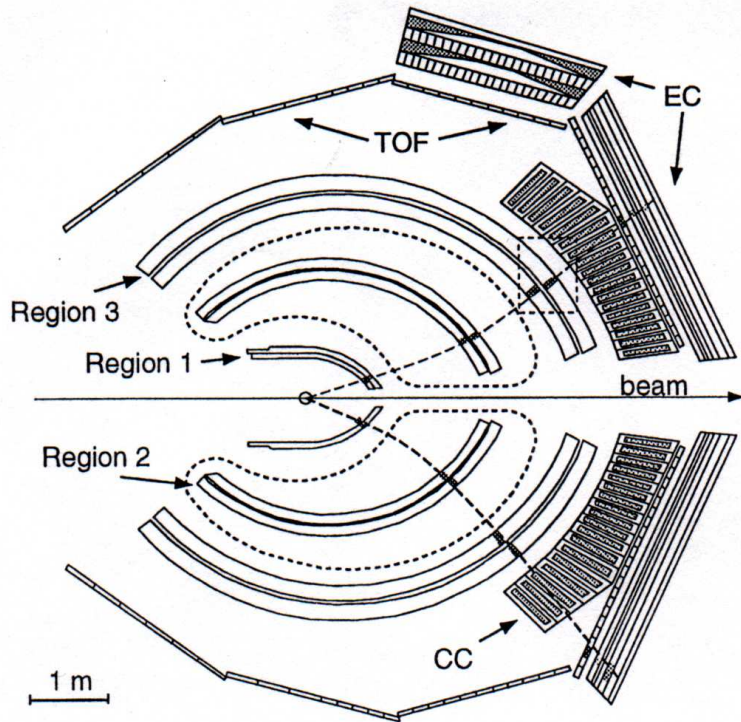


Figure 2.10: Diagram of CLAS showing the location of all of the major detectors. The dashed lines around the region 2 drift chambers outline the kidney shaped toroidal magnet coils [29].

momentum of these particles. Figure 2.10 shows the location of the drift chambers in CLAS, along with the extent of the toroidal magnet. Each region of drift chambers is separated into six sectors. The region 1 drift chambers are located inside of the torus magnet at an area of low magnetic field. The region 2 drift chambers are mounted on the torus coils and therefore are located at the area of maximum magnetic field. The region 3 drift chambers are located outside of the torus coils at an area of weak field. Each region consists of two *superlayers*, one that is oriented along the magnetic field and one that is oriented at a  $6^\circ$  angle to them. The superlayers consist of 6 layers of hexagonal drift cells, with each layer offset from the other layers by half a cell width. Each cell has a  $20\mu\text{m}$ -radius sense wire at the center made of gold-plated tungsten, and is kept at a positive potential. Around the sense wire are six  $140\mu\text{m}$  field wires made of gold-plated aluminum alloy and kept at a negative potential. The gas in the drift chambers is mix of 90% Argon and 10%  $\text{CO}_2$ .

### 2.3.5 Time-of-flight Scintillators

The wall of time-of-flight scintillators is located outside the region 3 drift chambers about 4 m from the target. Combining the time from the TOF detectors with the time from the start counter allows for rough particle identification, although we use a different method. The TOF detector is separated into six sectors as well, each consisting of four panels with 57 2-inch thick bars of varying lengths and widths distributed among the panels, as is shown in Figure 2.11. The thickness of the bars is to allow for 100% detection of the charged particles. The TOF detectors have a timing resolution of 80-160 ps, depending on the length of the bars, with the longest bars having the worst resolution.

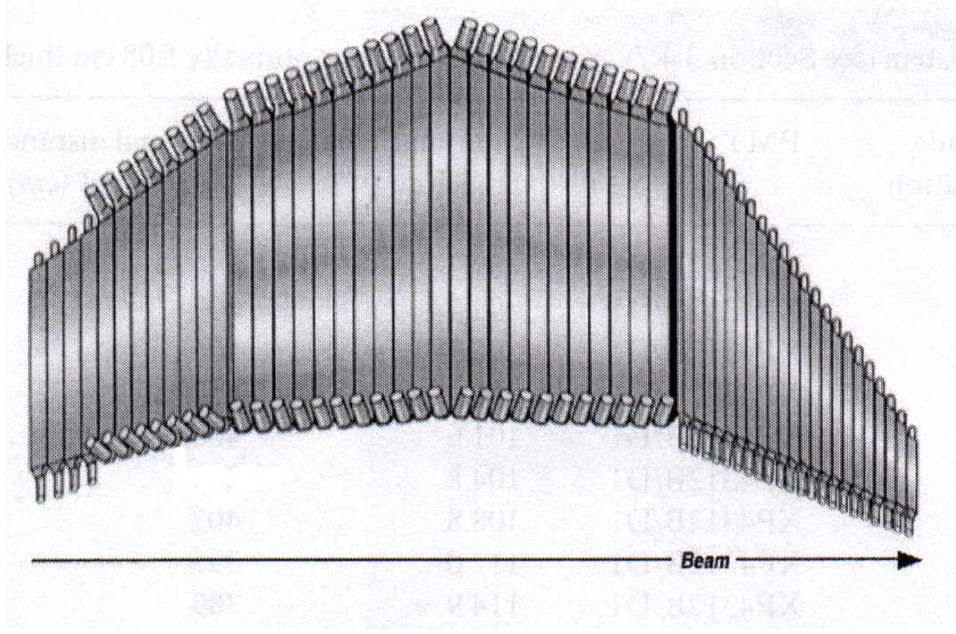


Figure 2.11: Diagram of the time-of-flight detector from one sector of CLAS. There are 57 bars separated into four panels [30].

## 2.4 Beamline Devices

There are several devices located along the beam, either upstream or downstream, to provide information on the beam. Upstream of the target, there are harps and current measuring devices, while downstream there is a pair spectrometer (PS) and a pair counter (PC), which are used for determining the photon flux; the total absorption shower counter (TASC) is also located downstream, which is used in determining a tagging ratio for the T-Counters in the tagger system, used for *gflux* [31]. The TASC uses four lead-glass blocks, each with a phototube, to detect 100% of the photons that pass through it. This device can be used to get an absolute measurement of the photon flux for currents below 100 pA [22]. This device was not used for the g8b dataset however, and so no *gflux* information was recorded for g8b. Low current *normalization* runs were taken occasionally during g1c to calibrate the flux measurements.

The g1c run period used a circularly polarized photon beam. To determine the degree of polarization for the photons it is necessary to know the polarization of the electron beam. A Møller polarimeter located just downstream of the target was used to measure the electron polarization. The polarimeter consisted of a permendur (a cobalt-iron alloy) target, two quadrupole magnets, and scintillators with photomultiplier tubes.

The polarimeter target was polarized by a Helmholtz coil generating a 100 gauss magnetic field. Electrons incident on the electrons in the target produced  $e^- + e^- \rightarrow e^- + e^-$  events at a rate measured by the device. The two quadrupole magnets then collected the electrons which were detected by the scintillators. The asymmetry,  $A$ , can then determine the beam polarization,  $\zeta_{beam}$ , using

$$A = \frac{N_+ - N_-}{N_+ + N_-} = A_z \zeta_{beam} \zeta_T^z, \quad (2.1)$$

where  $N_\pm$  are the yields for each helicity,  $A_z = 0.7826 \pm 0.0079$  is the analyzing power of an ideal 100% polarized target, and  $\zeta_T^z$  is the polarization of the target [32].

Using the Møller polarimeter disrupts the experiment because the radiator must be taken out of the beam to allow electrons to pass through to the device, and thus no actual events can be recorded during this time. Only three measurements of the beam polarization were made during the runs used for this analysis. The measurements were performed by Arne Freyberger of Jefferson Lab and the average polarization was measured to be  $\zeta_{beam} = 0.654 \pm 0.013$  for the 2.445 GeV dataset and  $\zeta_{beam} = 0.641 \pm 0.012$  for the 2.897 GeV dataset.

## 2.5 Trigger and Data Acquisition

A trigger is employed for each run period to determine when to write events to magnetic tape. A set of trigger criteria was chosen for each run period to ensure that only events of a certain type are recorded. Both g1c and g8b used a one-track trigger which means that an event is recorded as long as there is a coincidence of a signal in the start counter and a TOF paddle in the same sector. Once an event passed this trigger, the event was written out using the data acquisition system (DAQ) for offline analysis. The DAQ was capable of writing out events at a rate of  $\sim 2.5$  kHz during the g1c run and  $\sim 5$  kHz during the g8b run period.

## 2.6 Summary

In order to perform our analysis of  $\gamma p \rightarrow p\omega$  events, we first need to run an experiment and measure these events. This requires an impressive facility like Jefferson Lab with the means of producing the electrons and photons to start the reaction and detecting the final particles. This is accomplished using the injector to put electrons into the linear accelerator, through which they pass several times before interacting with a radiator to produce photons. The electrons are then bent out of the way using the tagger magnet and measured using the tagging detector. The tagged photons proceed through the collimator and interact with the target, in some cases producing our desired output of  $p\omega$ . These two particles then travel out towards the detector, the  $\omega$  decays into  $\pi^+\pi^-\pi^0$  and the three charged particles trigger the start counter and then pass through the drift chambers and the magnetic field produced by the superconducting toroidal magnet before finally being detected in the time-of-flight scintillators, indicating an end to the event. As each detector measures data for each event, it is recorded by the data acquisition system. After the run has ended, we must take that data and convert it into useful physics observables. That process will be detailed in the following chapter.

# Chapter 3

## Data Selection

The data used in the following analysis are taken from two separate run periods conducted by the CLAS collaboration. The first is denoted *g1c* and was collected in October and November of 1999. In the g1c dataset there were approximately 4.5 billion triggers of data collected. It was collected in three sets of data with different beam energies, though only two of the sets are used in this analysis. Table 3.1 shows the runs we use in each setting as well as the number of  $\omega$  signal events collected in each setting. For this period, circularly polarized photons were incident on an unpolarized liquid hydrogen target.

The second run period is denoted *g8b* and was collected from June 28, 2005 to August 31, 2005. The g8b dataset includes 10.5 billion triggers of data. This period had a linearly polarized photon beam and an unpolarized target. As will be shown in Section 3.8.2, linearly polarized photons are produced via coherent bremsstrahlung reactions, by electrons incident on a diamond. The angle with which the electrons strike the crystal results in a characteristic energy distribution for the outgoing photons, which is defined by a *coherent edge*. For the data in g8b, there were five separate coherent edge settings. These were chosen in 200 MeV increments starting at 1.3 GeV and going up to 2.1 GeV.

The photon beam can be linearly polarized in any direction perpendicular to the beam direction by adjusting the azimuthal angle of the relevant crystal axes in the diamond. For this run period, two directions were chosen to reduce systematic errors. These directions were chosen to be parallel to the floor in the x direction in lab coordinates (this will be denoted as *para* or *horiz*) and perpendicular to the floor in the y direction in lab coordinates (this will be denoted as *perp* or *verti*). Most of the data were collected in either the para or perp state, but for some runs the direction was automatically rotated between these two states periodically during the run (these runs are referred to as *auto-flip* or just *auto*). The auto-flip data were later separated into para and perp events which were analyzed separately.

Data were collected in all five coherent edge settings in both the para and perp alignment, with roughly equal statistics. Table 3.2 shows the runs used in each setting as well as the number of  $\omega$  signal events collected in each of the ten settings. Note that we have separated the auto-flip runs into their constituent components as noted above.

After the data were collected for each run period, the information from the detectors had to be converted into a form in which we could perform our analyses. During this process, all of the detectors and their subsystems were calibrated and the particle paths were determined as well as their momenta and other kinematics for each event. This process is known as *cooking*. The g1c data were cooked by Luminita Todor, a post-doctoral researcher at Carnegie Mellon at the time, and the g8b data were cooked by Franz Klein, of Catholic University. After those calibrations, the datasets were still not completely ready to be analyzed until a few more corrections have been applied. We will determine those corrections in this chapter.

Run Setting	Runs	Signal Events	$\sqrt{s}$ Range (MeV)
2.445 GeV	21763-21983	370,430	1720-2290
2.897 GeV	21427-21615	282,172	1720-2470
Total g1c		652,602	1720-2470

Table 3.1: *g1c* run list

Run Setting	Runs	Signal Events	$\sqrt{s}$ Range (MeV)
PARA 1.3	48224-48236, 48255-48262, 48278-48286, 48309-48320	432,378	1720-1840
PARA 1.5	48418-48426, 48445-48455, 48462-48465, 48493-48509	459,665	1810-1940
PARA 1.7	48544-48574	244,010	1910-2030
PARA 2.1	48357-48365, 48388-48408	158,935	2090-2210
PERP 1.3	48240-48251, 48268-48277, 48291-48298, 48321-48330	432,485	1720-1840
PERP 1.5	48431-48444, 48466-48488	353,520	1810-1930
PERP 1.7	48580-48610, 48620-48630	328,803	1910-2030
PERP 2.1	48332-48351, 48366-48377	155,514	2100-2200
AUTO 1.9	48088-48091, 48093-48096, 48098-48100, 48102-48105 48107-48110, 48114-48120, 48126-48132, 48137 48139-48146, 48148-48150, 48152-48154, 48156-48159 48163-48176, 48178-48182, 48185-48187, 48189-48192 48194-48196, 48199-48200	133,295 PARA 206,092 PERP	2010-2120 PARA 2010-2120 PERP
Total g8b		2,904,697	1720-2210

Table 3.2: *g8b* run list

The present analysis is focused on events of the type  $\gamma p \rightarrow p\omega$ . However, the  $\omega$  decays before it can be detected, so we must look for its decay products. To maximize the statistics of our data, we have chosen to look for events where the  $\omega$  decays to  $\pi^+\pi^-\pi^0$ , which has an 89.1% branching fraction. Since the CLAS detector has poor efficiency and resolution for neutral particles, like the  $\pi^0$ , we must look for events that are detected as  $\gamma p \rightarrow p\pi^+\pi^-$ , and then try to reconstruct the missing  $\pi^0$  using kinematic fits [33], which enforce the conservation of energy and momentum in the results. We skim the data looking only for events that have at least two positive tracks and one negative track detected ( $++-$ ). Further constraints on which events will be used for analysis are outlined in the following sections.

### 3.1 Excluded Runs

Data were collected for each of these run periods in chunks of 10-20 million events, on average. These chunks are called runs and are labeled sequentially. The separation of the data into runs allows us to change the state of the detectors and easily determine the settings for the events in question. Sometimes a run needs to be removed from the dataset for various reasons. The runs used and excluded from each of the two run periods analyzed here are listed below, along with reasons for exclusion.

#### 3.1.1 g1c

The g1c dataset consists of the runs from 20926 to 21983. There were three different electron beam energies used during the run period. Runs 20926-21359 used an electron beam energy of 3.115 GeV,

Run	Description
20929-21359	3.115 GeV Electron Beam Energy
21905-21908	Drift Chamber Voltage
21941	DAQ crash
21966	Pretrig1 crash

Table 3.3: *g1c* runs excluded from our analysis.

runs 21427-21645 used a beam energy of 2.897 GeV, and runs 21763-21983 used a beam energy of 2.445 GeV. This run period was the first at JLab to use circularly polarized photons, and for the first set of runs, at 3.115 GeV, there was a problem in measuring the polarization properly [23]. Since we wish to study events created with a polarized beam, all runs from the 3.115 GeV dataset have been excluded from this analysis.

The second set of runs, at 2.897 GeV, had issues measuring the flux for certain runs, and therefore the total flux cannot be determined from measurements. However, since the overall flux is not necessary for measuring the spin density matrix elements, it is possible to use this dataset with only an approximation of the flux. In section 5.1.3 a method for determining the approximate flux will be discussed.

In the 2.445 GeV dataset, six full runs were excluded: 21905-21908, 21941 and 21966 for various reasons. Parts of several other runs were also excluded due to corruption of a data file after cooking. The set of runs used for *g1c* can be found in Table 3.1. The excluded runs and files are summarized on Table 3.3.

### 3.1.2 g8b

The g8b dataset consists of the runs from 47827 to 48657. All of the events used an electron beam energy of 4.559 GeV. As mentioned above, the data were taken in five different coherent edge settings, and with the photons polarized in both the parallel and perpendicular mode, or in a mode that automatically flipped between those two modes. There were also runs that were taken with a standard gold radiator in place of the diamond radiator, and thus the events coming from these runs are unpolarized; these runs are referred to as *amorphous*. The amorphous runs have not been included in our analysis, although they were used for diagnostic purposes, such as calculating the tagger and momentum corrections. The runs that are included in each setting are shown in Table 3.2. Several of the runs have been excluded for various reasons; they are summarized on Table 3.4. The auto-flip runs at 1.3 GeV and 1.5 GeV have not been analyzed because of issues with finding their polarization values. Also, the auto-flip runs at 1.7 GeV have not been analyzed because of difficulties encountered while trying to cook the files and since they would only increase statistics in a range already covered, not add to our range.

## 3.2 Energy and Momentum Corrections

### 3.2.1 Energy Loss Corrections

The particles that we detect, and whose momenta we are able to reconstruct, have traveled from the target to the detectors, a distance of roughly 4 m, through various materials both in the target and the detector, as well as other equipment in the lab. As charged particles pass through this material they lose some of their energy due to ionization and atomic excitations [3]. The initial reconstruction of the momentum for the particle does not take this energy loss into account. Thus, a package called *ELoss* was developed by Eugene Pasyuk to account for this energy loss in the CLAS

Run	Description
48208-48218	Auto 1.3 No polarization info
47924-47944	Auto 1.5 No polarization info
47946	AMOTAC
47953-47954	Not found on silo
48201	DTAC (0 current)
48325	Not found on silo
48331	Not found on silo
48334	Not found on silo
48334	Changing torus current
48378	DTESTL2 (changed L2, and then torus)
48410-48411	Normalization run
48521	Testing new settings
48523-48527	Testing new settings
48539-48543	Bad T-counters 41-44
48606	Bad T-counters 41-44
48613	Testing new settings
48616-48619	Testing new settings, current 1
48625	Small Run Perp 1.7
48645-48657	End of run tests

Table 3.4:  $g8b$  runs excluded from our analysis.

detectors [34]. This correction is applied to all charged particles in a given event before any further analysis is performed.

### 3.2.2 Tagger Corrections

In 2003, it was discovered that the photon tagger's focal plane was sagging, causing alignment issues which resulted in the photon's energy being calculated incorrectly from the measured tagger data [35, 36, 37]. The method which we have used to correct for this sag was developed by Mike Williams [1], which we will summarize below. The corrections are generally on the order of 10 MeV.

We start by selecting events which have a detected proton,  $\pi^+$ , and  $\pi^-$ , with no other particles detected. We then apply the energy loss corrections to the events. Then, we perform a kinematic fit which ignores the tagger's measurement of the photon energy and fits to the hypothesis of  $(\gamma)p \rightarrow p\pi^+\pi^-$ . The fit yields a calculated photon energy and a confidence level. Only events with a confidence level of more than 10% are used to determine the correction. For events that pass this confidence level cut the difference between the kinematically fit photon energy and the measured photon energy is determined,

$$\Delta E_\gamma = E_\gamma^{kinfit} - E_\gamma^{measured}. \quad (3.1)$$

These differences are then binned by the tagger E-counter that measured the electron energy, and for each bin a Gaussian mean is determined. This number will be added to the photon energy depending on which E-counter the measurement came from.

**g1c** Even though the g1c dataset was taken before the tagger-sag problem was first identified in 2003, the problem was already present, and therefore we correct for it. The process was straightforward for this dataset, and the results can be seen in Figure 3.1.

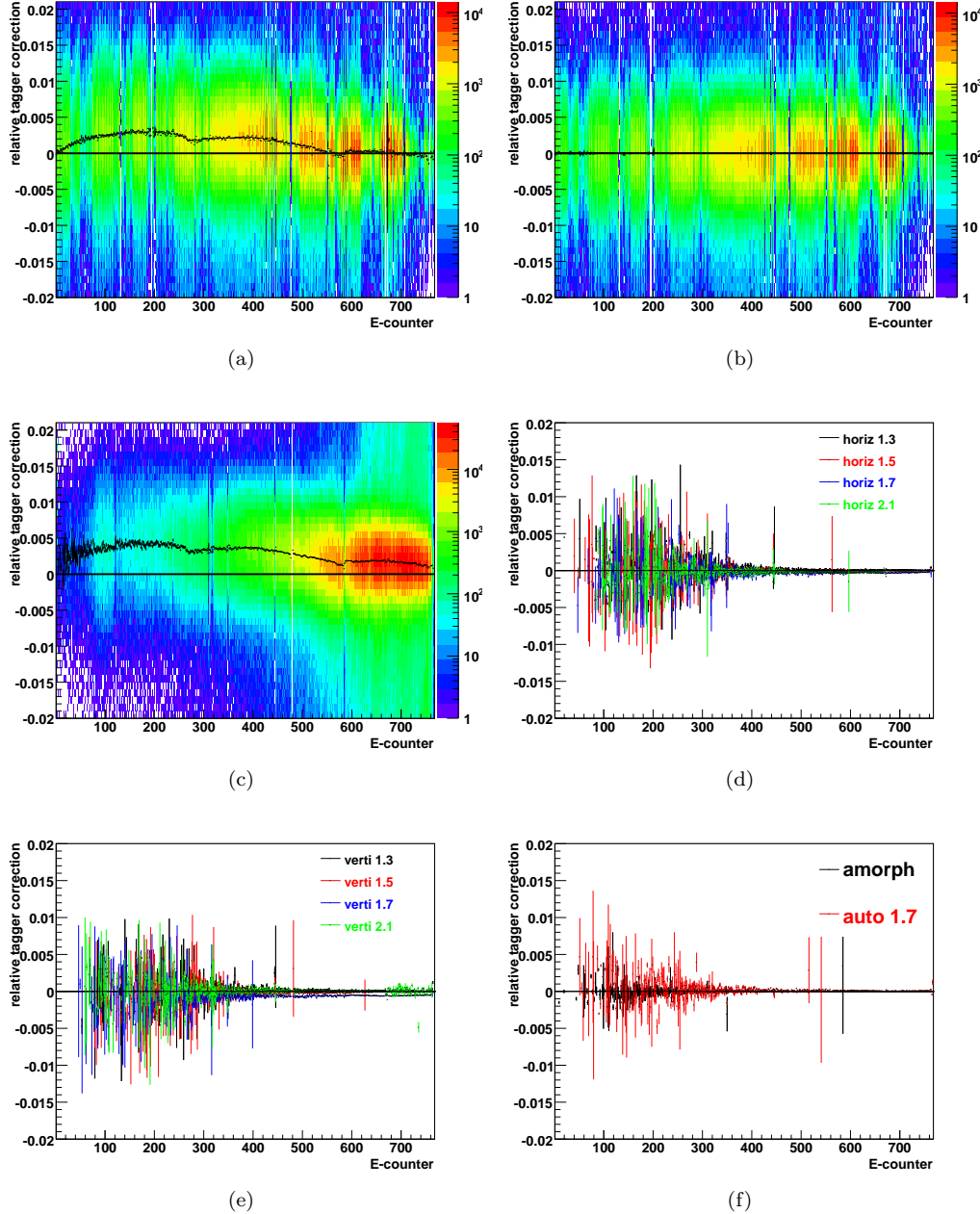


Figure 3.1: Tagger Corrections: (a)  $\Delta E_\gamma/E_{beam}$  vs E-counter for  $(\gamma)p \rightarrow p\pi^+\pi^-$  events in g1c with the Gaussian mean for each E-counter shown in black. Notice the humped structure of the Gaussian means, indicating that the data have not been properly calibrated. (b) g1c events after the corrections from (a) are applied. Notice that the humped structure is removed and the Gaussian mean for each E-counter is at 0. (c)  $\Delta E_\gamma/E_{beam}$  vs E-counter for g8b, calculated from the amorphous dataset to be applied to all of the data. (d) The four horizontal datasets from g8b after corrections have been applied. (e) The four vertical datasets from g8b after corrections have been applied. (f) The amorphous and auto-flip datasets from g8b after corrections have been applied. The error bars are quite large for E-counters below 400 in g8b because the statistics are low, which is why the amorphous dataset was used to calculate the corrections.

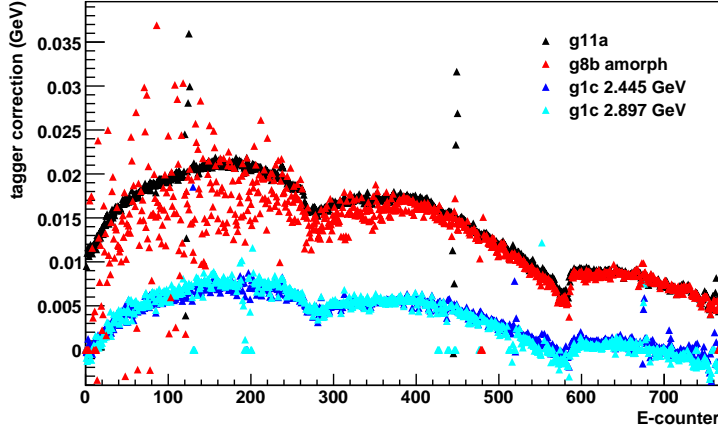


Figure 3.2:  $\Delta E_\gamma$  (GeV) vs E-counter for  $(\gamma)p \rightarrow p\pi^+\pi^-$  events in g11a (black), g8b (red), the 2.445 GeV dataset of g1c (blue), and the 2.897 GeV dataset of g1c (cyan). These are absolute corrections, not relative corrections as in Figure 3.1. The g11a and g8b datasets have very similar corrections, and the two g1c datasets are similar to each other, but there is a distinct difference between the corrections for g11a and g8b vs the corrections for g1c.

**g8b** For g8b, the ten different datasets created a problem because some of the datasets did not have enough statistics to allow determination of the corrections. Having so many different corrections was not desirable. However, we were able to obtain corrections from the amorphous dataset, which suitably corrected all of the datasets. Each of the datasets was examined on its own to see if the corrections worked, and the results of those corrections are shown in Figure 3.1. It is clear that the corrections do a very good job on all of the datasets. Note the large error bars for E-counters below 400, these are due to low statistics. This lack of statistics is why the amorphous dataset was used.

**Comparing the Tagger Corrections** From the corrections shown in Figures 3.1 (a) and (c) it is apparent that the corrections are not the same for the g1c and g8b datasets. Figure 3.2 shows the corrections for g8b and the two g1c datasets on a single plot, along with the corrections for g11a used as a point of reference. It is clear that g8b corrections are nearly the same as the g11a corrections, but that the g1c corrections are both quite different from the g11a corrections. This difference could arise because of uncertainties in the end-point energy for the electron beam, or because of some change in hardware between the g1c runs in 1999 and the g11a and g8b runs in 2004-2005. This difference is the reason why each run period should generate its own set of tagger corrections.

### 3.2.3 Momentum Corrections

The measured momenta for the detected particles also require small corrections, due to various differences between the toroidal field map and the drift chamber survey information. These corrections are generally less than 20 MeV for the measured momentum, and on the order of hundredths of a radian for angles. The method we use to determine these corrections was also developed by Mike Williams [1], however we differ slightly in carrying out the procedure he detailed.

Once again, we choose events with a final state of  $p\pi^+\pi^-$ , with no other detected particles. Then, we apply the energy loss and tagger corrections. Next, we run three separate kinematic fits, each ignoring one of final state particles and fitting to the hypothesis  $\gamma p \rightarrow (p)\pi^+\pi^-$ ,  $\gamma p \rightarrow p(\pi^+)\pi^-$  and

$\gamma p \rightarrow p\pi^+(\pi^-)$ . We cut any event which has a confidence level for any of the three fits of less than 10%.

The kinematic fit has given an estimate for the value of each of the three tracking parameters ( $p, \lambda, \phi$ ), which correspond to the magnitude of momentum, polar angle, and azimuthal angle respectively, for each of the three particles. Following the method of (3.1), we define

$$\Delta p_x = p_x^{kinfit} - p_x^{measured} \quad (3.2a)$$

$$\Delta \lambda_x = \lambda_x^{kinfit} - \lambda_x^{measured} \quad (3.2b)$$

$$\Delta \phi_x = \phi_x^{kinfit} - \phi_x^{measured}, \quad (3.2c)$$

where x is the excluded particle.

Each of the variables defined in (3.2) is a function of the particle's magnitude of momentum, p, the lab coordinates  $\theta_{lab}$  and  $\phi_{lab}$ , the CLAS sector it is detected in, and the particle's charge. In order to account for all of these dependencies, we have binned the data in each of these variables. Each sector is separated into twelve  $5^\circ$  bins in the azimuthal angle  $\phi_{lab}$ . There are fifteen bins for the polar angle  $\theta_{lab}$ , but they are not equally spaced. There are nine  $5^\circ$  bins for  $\theta_{lab} \in [5^\circ, 50^\circ]$ , four  $10^\circ$  for  $\theta_{lab} \in [50^\circ, 90^\circ]$  and two  $25^\circ$  bins for  $\theta_{lab} \in [90^\circ, 140^\circ]$ . This leads to a total of 180 bins in each of the six CLAS sectors or 1080 bins overall for each particle.

In each of these (sector,  $\theta_{lab}$ ,  $\phi_{lab}$ ) bins we create a histogram of  $\Delta X_x$  vs  $p_x$ , where X refers to p,  $\lambda$  or  $\phi$ , and x refers to either the proton,  $\pi^+$  or  $\pi^-$ . Since our tracking is done in terms of  $\frac{q}{p}$ , we bin the magnitude of momentum p in 20, equally-sized  $\frac{1}{p}$  bins. Then, in each of these bins the Gaussian mean of  $\Delta X_x$  is calculated. Finally, a  $3^{rd}$  order or lower polynomial is fit to the means obtained in the bin. This function will be used to determine the final correction.

There are two ways in which our method differs from that outlined by Mike Williams. The first is that we treat the proton and the  $\pi^+$  separately instead of combining them together as positive particles. The second is that we iterated the process, correcting one of the nine variable in each iteration. Subsequent iterations include all previous corrections. This approach was chosen after suitable corrections could not be obtained even after many iterations while changing all variables at once. The order in which we iterate the corrections does not have an effect on the final result.

**g8b** Once again g8b needs separate mention because of the ten different datasets. In the same way as the tagger corrections were obtained, we used the amorphous dataset to find corrections and then applied them to each of the datasets independently. Due to the fine binning, most of the bins did not have enough statistics to allow full determination of the success of corrections, but in the bins with sufficient statistics the corrections were very successful. For bins without sufficient statistics, we used a broader binning method to check the results, which also looked good.

### 3.2.4 Final Corrections

As mentioned above, this was an iterative process. Starting from no corrections, other than ELoss, first a tagger correction was obtained, and then each of the nine momentum variables was corrected. Once that first iteration was complete, the tagger corrections were again calculated, and any further corrections were added to the previous iteration's correction. Then, the momentum corrections were again calculated and combined with the previous iteration. This process was repeated until all of the variables converged at a satisfactory level. This level was determined both by trying to keep  $\Delta X_x \leq 0.01$ , where X refers to the variable and x refers to the particle in (3.2), in as many bins as possible, and also by noting when further iterations either had no effect, or made things worse for the other variables.

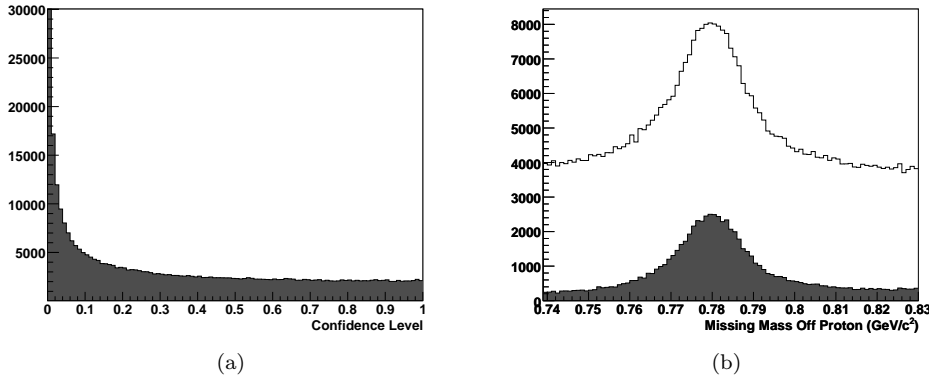


Figure 3.3: (a) Confidence levels from the kinematic fit of  $\gamma p \rightarrow p\pi^+\pi^-(\pi^0)$ , for all events in runs 21763-21791 from g1c. (b) Missing mass off the proton for all events in runs 21763-21791 in g1c, the shaded area are those events that pass a 10% confidence level cut. The background has clearly been greatly reduced.

### 3.3 Kinematic Fit of $\gamma p \rightarrow p\pi^+\pi^-(\pi^0)$

We have elected to use the covariance matrix that was built for the g11a dataset [1], as testing revealed no need to make any changes. Now we can move on to selecting the events which we will use for the analysis. We begin by selecting events that have two positive tracks and one negative track detected. We then assume the negative track is the  $\pi^-$  and choose one of the positive tracks as the proton and the other one as the  $\pi^+$ . Then, we apply the energy loss, tagger, and momentum corrections to each particle in the event. At this point, we remove any events which have a proton with magnitude of momentum less than 350 MeV. This cut is based on the work of Matt Bellis, who showed that low momentum protons are not possible to accurately model in CLAS. We then require the total missing mass to be between 0 and 450 MeV, and that the total missing mass off the proton be within 150 MeV of the  $\omega$  mass of 782 MeV. Notice that these are very wide cuts, and, at this point, no other cuts are placed on the data. Later, we will place a tighter cut on the mass off the proton, within 25 MeV, but for now, we want a very loose cut for our signal-background separation method, which will be detailed in Section 3.7.

Each event is kinematically fit to the hypothesis  $\gamma p \rightarrow p\pi^+\pi^-(\pi^0)$ . This fit will yield a confidence level, and we discard events with a confidence level less than 10%. We now try the same event with the positive particles switched, so that both combinations of the positive particles are tested. Only one version of each event could pass the confidence level cut, as misidentifying the positively charged particles will lead to a lower confidence level.

The confidence levels for events in the 2.445 GeV dataset of g1c are shown in Figure 3.3(a). The effect of the 10% CL cut, which is what we will use as our final cut, on the signal can be seen, in Figure 3.3(b) for g1c, by looking at the missing mass off the proton. The unshaded histogram is all events before the CL cut, and the shaded histogram is after the cut. This cut greatly reduces our background, while cutting away little of our signal, just slightly more than 10%.

### 3.4 Particle Identification

The next cut that we place on the data is a particle identification cut. This cut takes the events that pass the previous confidence level cut, and tries to determine if the positive tracks are correctly

associated with a proton and  $\pi^+$ . This cut depends on the quantity

$$\Delta tof = tof_{measured} - tof_{calculated}, \quad (3.3)$$

where  $tof_{measured}$  is the measured time of flight, the difference between the time at which the particle struck the CLAS TOF scintillator and the time the photon was projected to have been at the interaction vertex, based on which R.F. bucket the event is associated with, and

$$tof_{calculated} = \frac{L}{v} = \frac{L}{cp/E} = \frac{L}{c} \frac{\sqrt{p^2 + m^2}}{p} = \frac{L}{c} \sqrt{1 + \left(\frac{m}{p}\right)^2}, \quad (3.4)$$

where L is the distance from the TOF scintillator to the interaction vertex, v is the velocity of the particle, c is the speed of light, and m and p are the mass and momentum of the particle.

Figure 3.4 shows  $\Delta tof_{\pi^+}$  vs  $\Delta tof_p$  for both datasets. The region near the origin shows correctly identified events. The regions near  $(\pm 2, \pm 2)$ ,  $(\pm 4, \pm 4)$ , etc, come from events that have particles associated with a wrong RF bucket. These events need to be removed and will not remove any of our signal. Our cut takes the shape of a cross that removes the bad events away from the axes. This cut has been shown, by the method of Feldman and Cousins [38], to remove on the order of 1.3% of the signal [1].

## 3.5 Detector Performance Cuts

The next set of cuts is required due to issues with the detectors that cannot be modeled in the Monte Carlo. The cut placed on low momentum protons, already mentioned, is an example of this kind of cut.

### 3.5.1 Fiducial Cuts

Matt Bellis studied the regions of the detectors that could not be modeled in the Monte Carlo, and developed cuts based on the results [1]. Regions very close to the torus coils show changes in the acceptance that are too rapid to be modeled, and so events with a particle too close to the torus coils are removed. This is most severe in the forward direction, i.e. closer to the coils. The same cuts that were used for g11a were used again here for both g1c and g8b. Figure 3.5 shows the results of this cut for both g1c and g8b

### 3.5.2 TOF Paddle Cuts

In each CLAS run period, there have been some problems with certain TOF paddles, however the exact paddles are highly variable from run period to run period, as paddles are fixed and new ones fail. Thus, the list of paddles that must be removed from g1c and g8b are quite different. The removed paddles are listed by sector in Table 3.5 for g1c. There are no time-of-flight paddles removed from the g8b analysis, however, for a detailed discussion of the time-of-flight paddles in g8b please see Appendix A.

## 3.6 The Cut on $\cos \theta_{CM}^{\pi^0}$

Continuing to follow the example of Mike Williams in his g11a analysis, we remove events with kinematically fit values of  $\cos \theta_{CM}^{\pi^0} > 0.99$  in order to limit contamination from  $\gamma p \rightarrow p\pi^+\pi^-$  events [1]. Figure 3.6 shows the distribution of  $\cos \theta_{CM}^{\pi^0}$  in g1c and g8b. From this it is clear that we could have made the cut even tighter, perhaps at 0.995, but to stay consistent with g11a, we have chosen to keep the cut at 0.99.

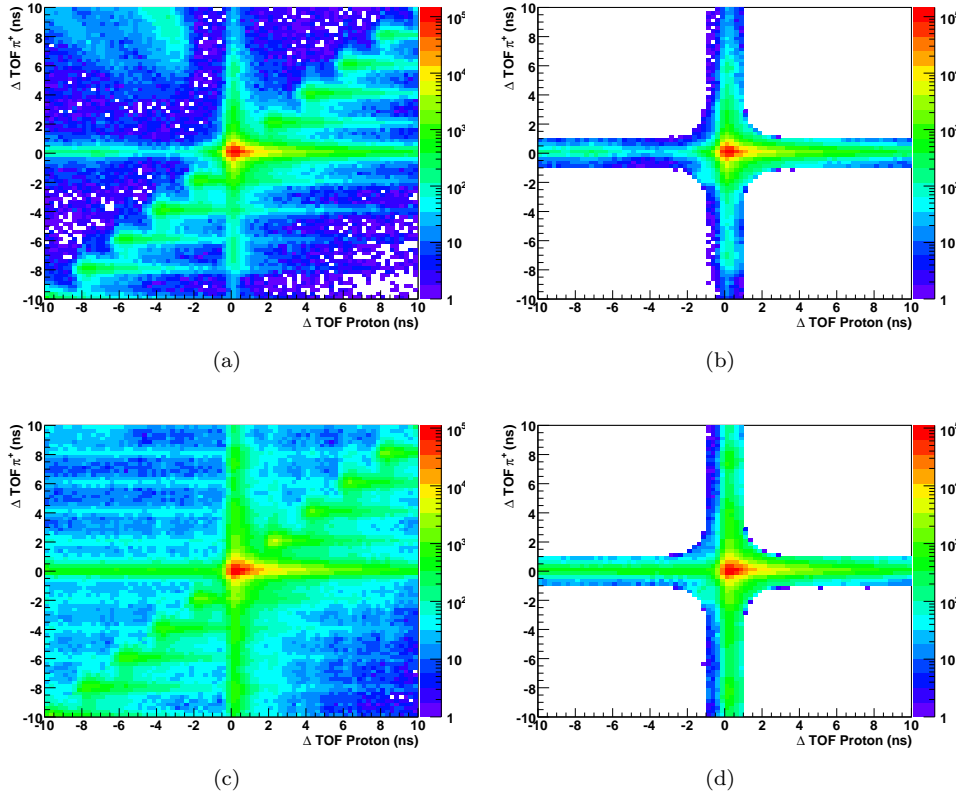


Figure 3.4:  $\Delta \text{TOF } \pi^+ \text{ (ns)}$  vs  $\Delta \text{TOF proton (ns)}$ . (a) All events in runs 21763-21983 in g1c passing a 10% CL cut. (b) All events for the same runs that also pass our timing cut. (c) All events in the PARA 1.5 dataset of g8b passing a 10% CL cut. (d) All events for the same runs that also pass our timing cut.

Sector	Removed Paddles
1	44,29
3	45
4	21,23
6	32

Table 3.5: Time-of-flight paddles removed from the *g1c* analysis.

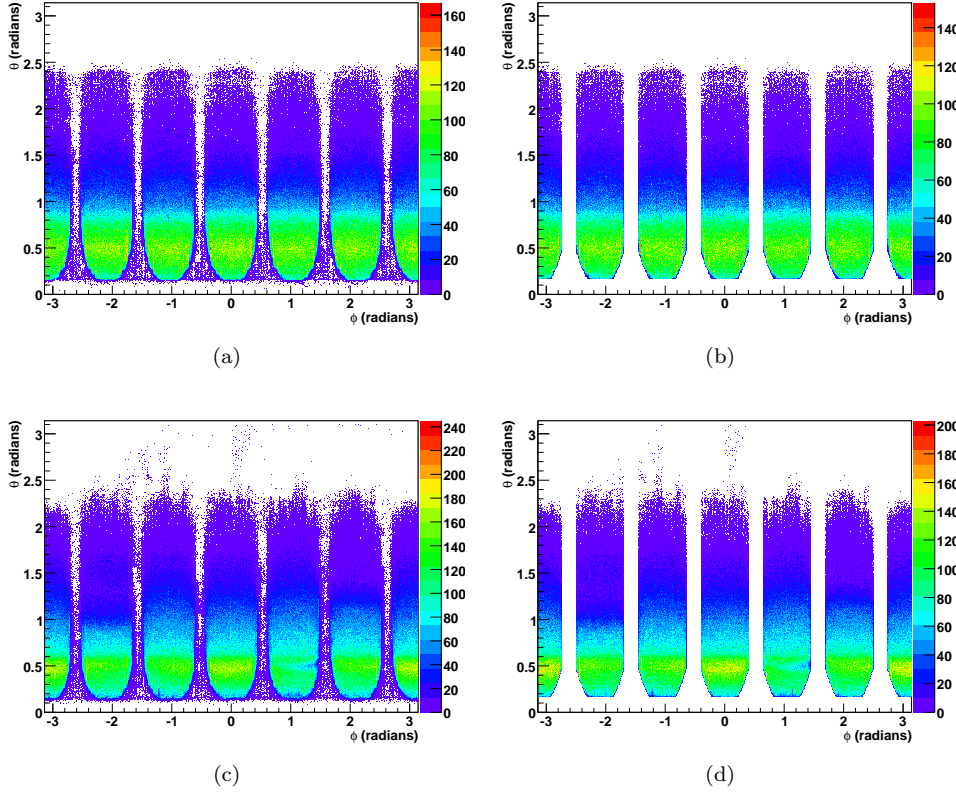


Figure 3.5:  $\theta_{lab}$  (radians) vs  $\phi_{lab}$  (radians). (a) All events in runs 21763-21983 in g1c passing the 10% CL cut and the PID cut. (b) All events for the same runs that also pass the fiducial cuts. (c) All events in the PARA 1.5 dataset of g8b passing a 10% CL cut and the PID cut. (d) All events for the same runs, that also pass our timing cut.

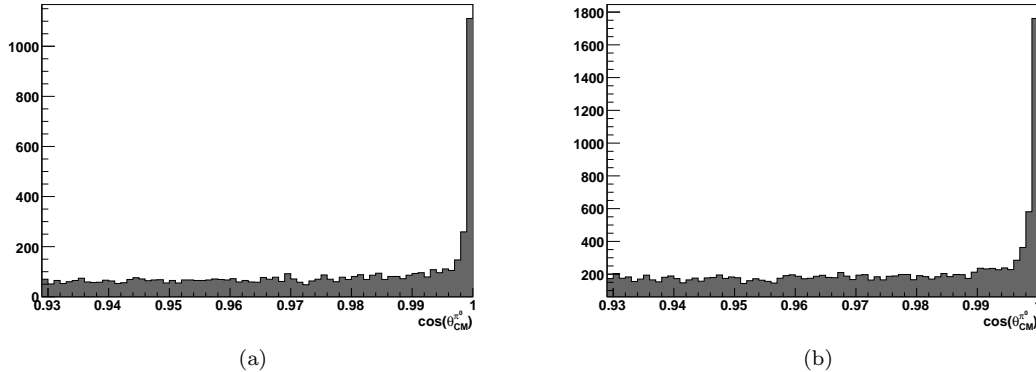


Figure 3.6:  $\cos \theta_{CM}^{\pi^0}$  for (a) all events in runs 21763-21983 in g1c, passing the 10% CL cut, the PID cut, the fiducial cut and the TOF paddle knock out; (b) all events in the PARA 1.5 dataset of g8b passing the 10% CL cut, the PID cut, the fiducial cut and the TOF paddle knock out. The large number of events at very forward angles come from  $\gamma p \rightarrow p\pi^+\pi^-$  events.

### 3.7 Signal-Background Separation

Lastly, we need to determine which events are signal events and which are background. To do this, we follow the method developed by Williams in [1] to obtain a signal weight for every event, known as the Q-value. In this method, we define a metric to determine the *distance* between events. The metric we define here will be based on four kinematic variables for each  $\sqrt{s}$  bin, the  $\omega$  production angle,  $\cos \theta_{CM}^\omega$ , the decay helicity angles,  $\cos \theta_{HEL}$  and  $\phi_{HEL}$ , and the quantity

$$\lambda \propto |\vec{p}_{\pi^+} \times \vec{p}_{\pi^-}|^2 \quad (3.5)$$

where the pion momenta are here measured in the rest frame of the  $\omega$ . We then define the distance metric in the space created by these variables as

$$d_{ij}^2 = \sum_{k=1}^4 \left[ \frac{\xi_k^i - \xi_k^j}{r_k} \right]^2, \quad (3.6)$$

where  $\xi_k^i$  is the value of one of the four kinematic variables for the  $i^{th}$  event, and  $r_k$  is the range of that variable, where  $\vec{r} = (2, 2, 2\pi, 1)$ , although other choices could be made for the weighting [39]. We will also use the variable  $m$ , which is the invariant mass of the  $3\pi$  system for each event, in our calculations.

Next, for each event, with  $\vec{\xi}_0$  and  $m_0$ , in a given  $\sqrt{s}$  bin, we calculate the distance to every other event in that bin and choose the  $N_c$  closest events to it (we use  $N_c = 100$ ). These events should form a very small region around  $\vec{\xi}_0$  in our space.

Now we define a signal and a background function that we can use to describe the data. The signal function we will take to be a Voigtian scaled by an unknown function,  $F_s(\xi)$ , which contains the dependence on the kinematics for the signal function, such that

$$S(m, \vec{\xi}) = F_s(\vec{\xi})V(m, \mu, \sigma, \Gamma) \quad (3.7)$$

where

$$V(m, \mu, \sigma, \Gamma) = \frac{1}{\sqrt{2\pi}\sigma} \text{Re}[w(\frac{1}{2\sqrt{\sigma}}(m - \mu) + i\frac{\Gamma}{2\sigma\sqrt{2}})], \quad (3.8)$$

and  $\sigma$  is the Gaussian width of the Voigtian,  $\Gamma$  is the width of the non-relativistic Breit-Wigner function with a mean of  $\mu$ , and  $w(z)$  is the complex error function. The background is simply referred to as  $B(m, \vec{\xi})$  since we don't know its form. If we did know the form of the background, we would not need this method.

Now, since our  $N_c$  events are in a small region around  $\vec{\xi}_0$ , we can approximate our signal and background functions as

$$S(m_i, \vec{\xi}_i) = F_s(\vec{\xi}_0)V(m_i, \mu, \sigma, \Gamma) \approx A * V(m_i, \mu, \sigma, \Gamma), \quad (3.9)$$

$$B(m_i, \vec{\xi}_i) = F_s(\vec{\xi}_0)V(m_i, \mu, \sigma, \Gamma) \approx am_i + b, \quad (3.10)$$

where  $A$ ,  $a$ , and  $b$  are fit parameters. The choice of a linear background function can be justified because we are considering a small slice of phase space.

Now we fit the  $N_c$  closest events to a function that combines the signal and background functions to obtain  $A$ ,  $a$  and  $b$ . From this, we can calculate the expected number of signal events,  $s_i$ , and background events,  $b_i$ , at  $m_0$  to obtain our Q-value

$$Q_i = \frac{s_i}{s_i + b_i}. \quad (3.11)$$

This number will be used in subsequent chapters to weight each event based on its likelihood of being a signal event.

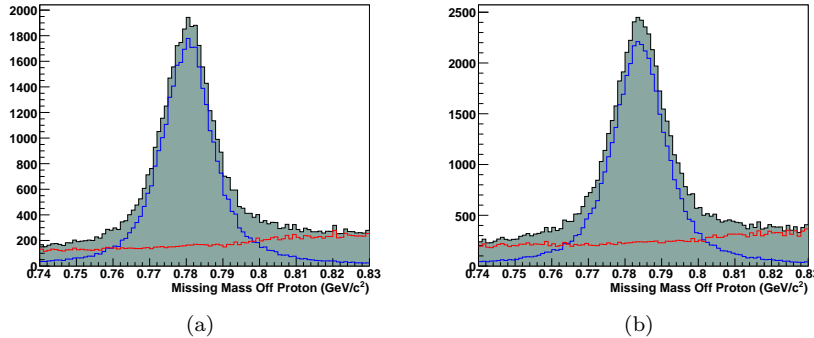


Figure 3.7: Signal-Background in the  $\sqrt{s} = 1855$  MeV bin. The shaded region is all events passing our cuts (wider mass cut), the blue line is the sum of the Q-values for all events in the bin (signal), the red line in the sum of 1-Q for all events (background). (a) g1c events. (b) g8b events.

Figure 3.7 shows the missing mass of the proton for the 1855 MeV bin in both the g1c and g8b datasets. A blue line represents the signal, or sum of the Q-values, in the bin, and a red line represents the background, or sum of 1-Q. It seems clear that this method is correctly weighting the signal and background in this bin.

### 3.7.1 Near Threshold Bins

For  $\sqrt{s}$  bins that are near the  $\omega$  threshold, the CLAS detector does not have acceptance for events that are on the high side of the  $\omega$  mass peak. With only events on one side of the peak, it is not possible to extract the shape of the background. To deal with the bins below  $\sqrt{s} = 1.77$  GeV, we developed a new method.

The method used is a slightly modified version of the one utilized by Mike Williams [1]. For each event in a sub-threshold bin, we find the Q-value of the closest event in each of the bins in the range  $1770 \leq \sqrt{s} \leq 1900$  MeV, using the distance function in (3.6) with the same four kinematic variables, but also adding in the  $\omega$  mass as a kinematic variable, with  $r_{m\omega} \equiv 25.5$  MeV, three times the width of the  $\omega$ . The final Q-value for the event was then the weighted average of each of the values of Q just obtained, where the weights were equal to  $1/d^2$ , in order to weight the *closer* events more than the *far* events. In the case of 10-MeV-wide bins, we use 13 bins in the range  $1770 \leq \sqrt{s} \leq 1900$  MeV.

In the case of g8b, only the horizontal and vertical datasets with a coherent edge of 1.3 GeV contained these near-threshold bins. Since those datasets only went up to  $\sqrt{s} = 1840$  MeV, there were only 7 bins to use for our method, since we used 10-MeV-wide bins.

Figure 3.8 shows the modified background subtraction for the  $\sqrt{s}=1735$  MeV bin from g1c and the 1755 MeV bin from g8b. Note in the 1735 MeV bin that there is significant background on the low side of the  $\omega$  mass peak and almost none above the peak. It appears there is still some background getting through on the low end, however this is much improved from using the standard method for this bin. The difficulty in finding good Q-values in this bin, in both g1c and g8b, will affect the quality of the fits that we are able to obtain in these bins. The 1755 MeV bin shows much less background on the low side of the mass peak and a little bit more of both signal and background above the mass peak. We are able to do a better job of separating the signal and background in these bins.

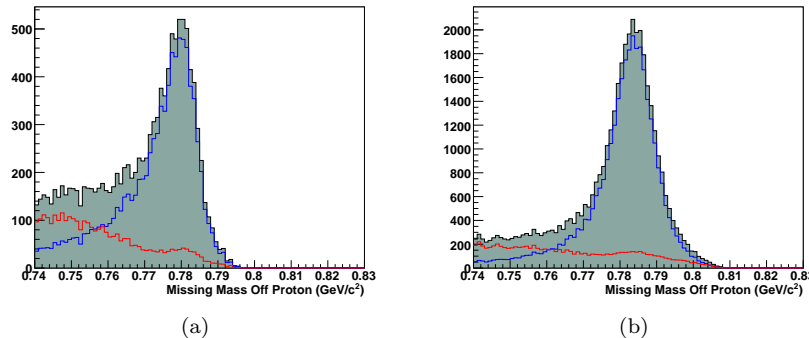


Figure 3.8: Signal-Background in near-threshold bins. The notation is the same as in Figure 3.7.  
 (a) g1c events for  $\sqrt{s} = 1735$ . (b) g8b events for  $\sqrt{s} = 1755$ .

### 3.8 Polarization

Both of the run periods under study here utilize polarized photon beams. The g1c dataset had a circularly polarized photon beam, and the g8b dataset used a linearly polarized photon beam. In order to use this extra information in our fits, we need to be able to determine the degree of polarization and, for g1c, the helicity of the photon.

### 3.8.1 Circular Polarization in g1c

A circularly polarized electron beam with an energy of 2.445 GeV or 2.897 GeV was delivered to the hall, then passed through a gold radiator to produce polarized photons. The polarization of the photon for a given event can then be calculated using the Maximon and Olson relation [40],

$$\zeta_c = \frac{k(\epsilon_{beam} + \frac{1}{3}\epsilon_{recoil})\zeta_{beam}}{\epsilon_{beam}^2 + \epsilon_{recoil}^2 - \frac{2}{3}\epsilon_{beam}\epsilon_{recoil}}, \quad (3.12)$$

where  $\epsilon_{beam}$  is the energy of the electron beam,  $\epsilon_{recoil}$  is the energy of the recoiling electron,  $k$  is the energy of the outgoing photon, and  $\zeta_{beam}$  is the polarization of the electron beam.  $\epsilon_{beam}$  and  $\zeta_{beam}$  are constants, and clearly  $\epsilon_{beam} = \epsilon_{recoil} + k$ , thus the polarization of the photon is equal to that of the electron beam when the energy is completely transferred to the photon and falls off as the photon energy decreases.

Determination of the polarization of the electron beam was discussed in Section 2.4. The helicity of each event was determined from the helicity of the incident electron, which was recorded for each event. In the following chapters, we will want to use one number that contains both the helicity and polarization of the photon so we introduce the variable

$$\eta_c \equiv h * \zeta_c. \quad (3.13)$$

Figure 3.9 shows  $\eta_C$  from events in g1c which have passed all of our cuts.

### 3.8.2 Linear Polarization in g8b

For the g8b run period, the linearly polarized photons were produced via coherent bremsstrahlung reactions, using a 50  $\mu\text{m}$ -thick diamond radiator. This process produces photons in a tighter energy range, generally around 200 MeV wide, than is produced from a standard radiator. The upper edge

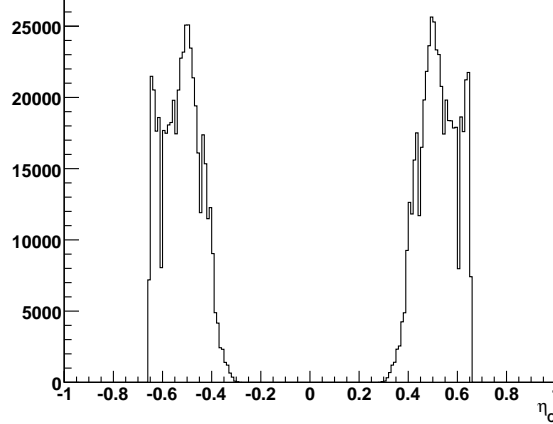


Figure 3.9:  $\eta_c$  measured from all events in runs 21763-21983 in g1c which have passed all listed cuts.

of this energy range is known as the coherent edge, and photons are not generated with energies beyond the coherent edge. The majority of the photons are produced by the electron's interaction with the (022) plane of the diamond radiator; by adjusting the azimuthal angle, in lab coordinates, of this plane, we can set the polarization direction of the photons, and we can set the coherent edge energy by adjusting the angle between the electron beam direction and the diamond [41].

The polarization,  $\zeta$ , of the photons is related to measurable variables by the following equation [41],

$$\zeta(x, G, \theta) = -\phi_{tot}(x, G, \theta) \left[ 1 - \frac{1}{\xi_{tot}(x, G, \theta)} \right], \quad (3.14)$$

where we define the following variables:

$$x = \frac{E_\gamma}{E_e}, \quad (3.15a)$$

$$\theta = \frac{m_e a}{4\sqrt{2}\pi g E_e \left[ \frac{1}{x_g^d} - 1 \right]}, \quad (3.15b)$$

$$\xi_{tot}(x, G, \theta) = \frac{I_{incoherent}(x) + I_{coherent}(x)}{\frac{m_e a}{4\sqrt{2}\pi} I_{amorphous}(x)}, \quad (3.15c)$$

where  $G$  is the maximum lattice vector (0GG),  $E_\gamma$  is the photon energy,  $E_e$  is the electron energy,  $m_e$  is the mass of the electron,  $a$  is the diamond lattice constant,  $x_g^d$  are the discontinuities for the vector  $g$  (0gg),  $\phi_{tot}$  is the upper limit on the polarization, and the  $I_x$  are the intensities coming from coherent or incoherent scattering off the diamond or scattering off of the amorphous radiator. Under ideal circumstances, (3.14) could be used to calculate the polarization of the photons. However, the diamond radiator was not completely stable in its location during the runs, and even very small movements can affect the position of the discontinuities,  $x_g^d$ , which affects the angle,  $\theta$ , between the beam and the (022) plane of the diamond, and thus the polarization. In order to account for this, it is necessary to smear the enhancement spectrum,  $\xi_{tot}$ , assuming a Gaussian form around  $\theta$  with the width  $\sigma$ . Using these now smeared functions, it is possible to calculate the polarization.

For g8b, the polarization is determined by consulting tables, compiled by Ken Livingston of the University of Glasgow, that require only the instantaneous coherent edge position at the time of

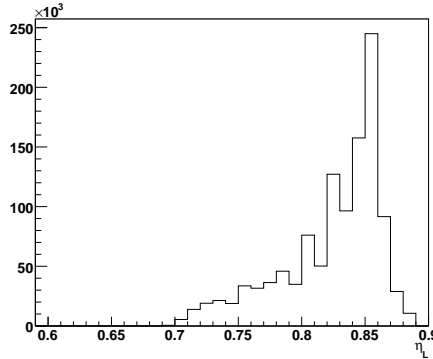


Figure 3.10:  $\eta_L$  measured from all events in the PARA 1.5 dataset of g8b which have passed all listed cuts.

the event and the energy of the photon. Subsequent corrections to these values were calculated by Michael Dugger and Barry Ritchie of Arizona State University [42], which are also applied.

In addition to setting the values of the polarization, we also remove events at this point that are above the instantaneous coherent edge, or more than 200 MeV below the coherent edge. There should not be events above the coherent edge, and any events that have an energy above the edge will not have the polarization properly defined. Events with a photon energy more than 200 MeV below the instantaneous coherent edge position also show inconsistencies in their polarization values and thus are removed [42]. In order to be consistent with the notation from g1c, we define  $\eta_L \equiv \zeta$ . Figure 3.10 shows  $\eta_L$  for events from the para 1.5 dataset of g8b.

### 3.9 Monte Carlo

Now that we have the data in a form acceptable for our fits, we must account for the inefficiencies in the detectors used to measure the data. The detectors have a limited ability to gather data, whether due to the extent that they span, the acceptance, or problems with the detector hardware. The likelihood that a given particle will be detected by the hardware, processed properly, and admitted into the dataset is known as the efficiency. In order to perform our fits, we will need to have a model of our detectors' acceptance and efficiency, and then we can use simulated (or Monte Carlo) data to normalize our results.

The model for the acceptance of each detector comes from detailed measurements made throughout the experiment. These measurements determine, for instance, if certain wires in a detector are inactive, or malfunctioning. During the cooking process, all of this information is fed into a database so that results from malfunctioning detectors are not accepted into the data stream.

Monte Carlo data for  $\gamma p \rightarrow p\omega \rightarrow p\pi^+\pi^-\pi^0$  was generated for both the g1c and g8b datasets using the beam energies appropriate for each dataset. For g1c, there were two separate Monte Carlo datasets created because there were two separate beam energies. All of the g8b measurements were generated with a single beam energy, although the photon energy depended on the coherent edge setting. However, only one Monte Carlo dataset was generated for g8b. The number of events generated was chosen so as to get roughly 100,000 events in each  $\sqrt{s}$  bin. In all kinematic variables, other than photon energy, the events were thrown according to  $p\omega$  and  $\omega \rightarrow \pi^+\pi^-\pi^0$  phase space, which included the Breit-Wigner width of the  $\omega$ .

### 3.9.1 GSIM

After we generated the Monte Carlo data, it was processed using the CLAS GSIM package [43], which is a GEANT-based simulation of the CLAS detectors. The generated Monte Carlo data contains only the four-vectors for each particle in the reaction; GSIM takes these four-vectors and propagates them through the CLAS detectors, generating a set of detector signals for each track in the simulated event. It also will simulate any particle decays, scattering, energy loss, and any other interactions the particle may have as it passes through the detectors. These results are then processed by another CLAS package, known as GPP, which smears simulated measurements to match the detector resolutions according to what was measured during the actual experiment. It is at this point that signals from parts of the detectors that were inactive or malfunctioning during the actual experiment are removed from the simulation data.

Once the simulated data passes through these two packages, it is in the same form as the raw experimental data, and is cooked with the same software that was used to cook the corresponding experimental data. At this point, the Monte Carlo data undergoes the exact same cuts as were detailed for the experimental data in this chapter. There are several checks in place to assure that the Monte Carlo data is accurately mimicking the experimental data. If the detector acceptances are not properly modeled, the results from our analysis will be affected. To see a more detailed discussion of this, see Appendix A, which details a problem with the acceptance for the time-of-flight scintillators that could not be properly modeled in the Monte Carlo, but which was later corrected.

### 3.9.2 Polarization Values

The Monte Carlo data does not have any polarization information included when it is generated. As a result, we need to add in that information after generation. For the circularly polarized data, this is accomplished by calculating the polarization using the Maximon and Olson equation (3.12), which depends only on values present in the Monte Carlo data. The helicity for each event is randomly decided.

For the linearly polarized data, however, the polarization cannot be determined for each event. This is because the polarization depends on the instantaneous coherent edge, and other factors, that are not present in the Monte Carlo data. Instead of assigning each event a unique polarization, it is necessary to give each event in a given  $\sqrt{s}$  bin the average polarization of all of the experimental events in that bin. This approximation will be valid so long as all of the events in a given bin lie within a fairly tight range. The range of polarizations in two  $\sqrt{s}$  bins from the para 1.5 GeV dataset in g8b can be seen in Figure 3.11. Notice that, for most events, the average polarization is less than 0.05 away from the average.

## 3.10 Summary

We have now outlined how the data has gone from the values measured in the CLAS detectors to the final form that will be used to generate our amplitudes. The criteria used to select which events will be used in our fits has also been discussed. As mentioned earlier, in order to perform the signal-background separation, a wide mass cut was placed around the  $\omega$  mass. Now that we have the Q-values for each event, we place a much tighter, 25 MeV, cut around the  $\omega$  mass. The total signal for each  $\sqrt{s}$  bin for both datasets can be seen in Figure 3.12. The total signal from the g1c dataset is 652,603; the total signal from the g8b dataset is 2,904,701.

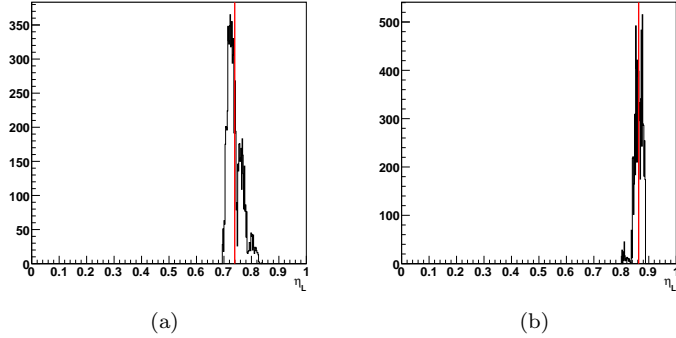


Figure 3.11:  $\eta_L$  for all events in the (a) 1825 MeV and (b) 1925 MeV bins from the PARA 1.5 GeV dataset in g8b. The red line indicates the average of all of the  $\eta_L$  measurements in that bin, which will be used as the polarization for all Monte Carlo events in that bin.

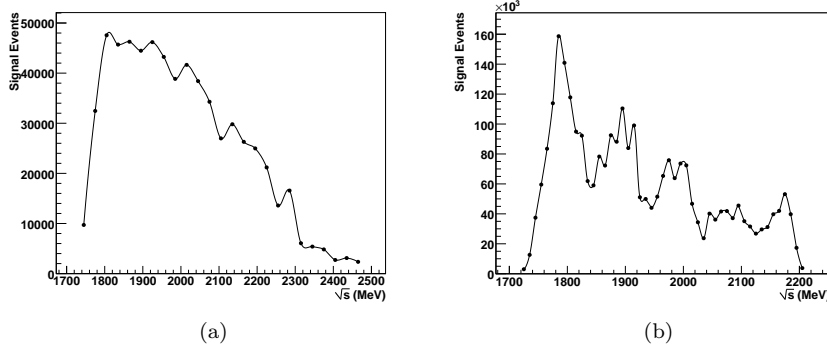


Figure 3.12: Signal Events vs  $\sqrt{s}$  (MeV): (a) Signal Events from g1c after all cuts detailed in this chapter have been applied. The total number of signal events is 652,603. (b) Signal events from g8b after all cuts detailed in this chapter have been applied. The total number of signal events is 2,904,701.

# Chapter 4

## Partial-Wave Analysis Formulas

In this chapter, we will follow the method set forth by Mike Williams in his thesis [1] to develop the formulas necessary for our partial-wave fits, and we will extend them to deal with both photon and target polarization. Though we will not be analyzing any experiments with a polarized target, the method used to incorporate photon polarization is easily generalized to the case of target polarization so we have included it here as well. The formulas in this chapter are derived assuming all the data in a given fit falls within a narrow  $\sqrt{s}$  bin. Our data have been binned in either 10 MeV- or 30 MeV-wide bins in  $\sqrt{s}$ .

### 4.1 Notation

In this chapter, the four-momenta of the four particles involved in the reaction will be denoted as  $k$ ,  $p_i$ ,  $p_f$  and  $q$  for the photon, initial proton, final proton and  $\omega$  respectively. We choose to work in the  $\gamma$ -p CM frame, see Figure 4.1, choosing the photon direction,  $\hat{k}$ , as the z-axis, and the y-axis normal to the production plane; this is known as the Adair frame [47]. The x-axis is perpendicular to both the z- and y-axes. We define the directions to be

$$\hat{X} = \frac{(\vec{k} \times \vec{q}) \times \vec{k}}{|\vec{k} \times \vec{q}|} = \frac{1}{\sqrt{q_x^2 + q_y^2}}(q_x, q_y, 0) \quad (4.1a)$$

$$\hat{Y} = \frac{\vec{k} \times \vec{q}}{|\vec{k} \times \vec{q}|} = \frac{1}{\sqrt{q_x^2 + q_y^2}}(-q_y, q_x, 0) \quad (4.1b)$$

$$\hat{Z} = \frac{\vec{k}}{|\vec{k}|} = (0, 0, 1), \quad (4.1c)$$

as can be seen in Figure 4.1

For a given particle x, all spin projections are along the beam direction of the incident photon and are denoted by  $m_x$ , and the mass is denoted by  $w_x$ . The Mandelstam variables are given in terms of the four-momenta of the particles as

$$s = (p_i + k)^2 = (p_f + q)^2, \quad (4.2a)$$

$$t = (q - k)^2 = (p_i - p_f)^2, \quad (4.2b)$$

$$u = (p_i - q)^2 = (p_f - k)^2. \quad (4.2c)$$

Let us consider a set of  $n$  events, the  $i^{th}$  event of which has kinematics denoted by  $X_i$ , and the set of all kinematics is denoted simply as  $X$ . In a fit, the set of the fit parameters is denoted as  $\vec{x}$ . The partial-wave amplitudes used here are generated following the method described in [1]. They

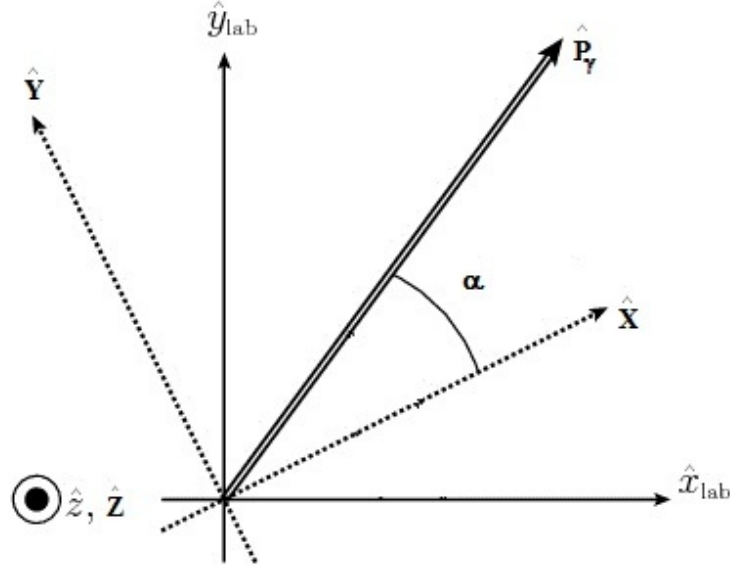


Figure 4.1: Axes in the Adair frame. The  $\hat{Z}$  direction corresponds to the photon direction.

may be written in several ways throughout this chapter. Amplitudes written with three indices have include the decay of the  $\omega \rightarrow \pi^+ \pi^- \pi^0$ , and are written as

$$\mathcal{A}_{m_\gamma, m_i, m_f} = \sum_a \alpha_a(\vec{x}, X) \mathcal{A}_{m_\gamma, m_i, m_f}^a(X), \quad (4.3)$$

where  $\alpha_a(\vec{x}, X)$  is a complex function of the fit parameters, and the sum over  $a$  indicates a sum over all such amplitudes with the same set of spin projections,  $m_\gamma$ ,  $m_i$ , and  $m_f$ . Amplitudes written with four indices are calculated without the  $\omega$  decaying and thus the fourth index is for the spin of the  $\omega$ , which is -1, 0 or 1,

$$\mathcal{A}_{m_\gamma, m_i, m_f, m_\omega} = \sum_a \alpha_a(\vec{x}, X) \mathcal{A}_{m_\gamma, m_i, m_f, m_\omega}^a(X). \quad (4.4)$$

Note that  $\alpha_a(\vec{x}, X)$  does not depend on the particle spin states. This means that we can fit using amplitudes of the type  $\mathcal{A}_{m_\gamma, m_i, m_f}$ , and use the parameters from that fit with amplitudes of the type  $\mathcal{A}_{m_\gamma, m_i, m_f, m_\omega}$  to calculate observables, such as the spin density matrix elements. If the amplitudes are missing an index it should be assumed that it has been summed over.

## 4.2 Extended Maximum Likelihood Method

To perform our fits, we make use of the extended maximum likelihood method, which is a fit to both the shape and the number of events in a given data distribution. This method allows us to do *event-based* fits in each  $\sqrt{s}$  bin [1, 44].

We begin with the likelihood function

$$\mathcal{L} = \left( \frac{\bar{n}^n}{n!} e^{-\bar{n}} \right) \prod_i^n \mathcal{P}(\vec{x}, X_i), \quad (4.5)$$

where the factor in the parentheses is the Poisson distribution for the probability of  $n$  total events given  $\bar{n}$  expected events, and  $\mathcal{P}(\vec{x}, X_i)$  is the probability distribution function. The probability distribution function for an event with an acceptance, defined by  $\eta(X_i)$ , phase space element  $\phi(X_i)$ , a Lorentz invariant transition amplitude  $\mathcal{M}$ , which depends on the amplitudes weighted by the fit parameters and will be defined in Section 4.4, and normalization  $\mathcal{N}(\vec{x})$ , can be written as

$$\mathcal{P}(\vec{x}, X_i) = \frac{|\mathcal{M}(\vec{x}, X_i)|^2 \eta(X_i) \phi(X_i)}{\mathcal{N}(\vec{x})}. \quad (4.6)$$

The normalization is chosen such that

$$\int \mathcal{P}(\vec{x}, X) dX = 1. \quad (4.7)$$

The goal then is to maximize  $\mathcal{L}$  to find the best set of fit parameters.

### 4.2.1 Normalization

In order to properly normalize the likelihood function, it is necessary to be able to calculate the number of expected events,  $\bar{n}$ , in each  $\sqrt{s}$  bin. To that end, we introduce the cross section, which is defined to be the transition rate per unit of incident flux per target particle [45]. In terms of observable quantities, we can write it as

$$\sigma = \frac{N}{\mathcal{F} \rho_{target} \ell_{target} N_A / A_{target}}, \quad (4.8)$$

where  $N$  is the total number of scattering events,  $\mathcal{F}$  is the integrated incident photon flux,  $\rho_{target}$ ,  $\ell_{target}$  and  $A_{target}$  are the density, length and atomic weight of the target, and  $N_A$  is Avogadro's number.

We can also write the cross section in terms of the Lorentz invariant transition amplitude,  $\mathcal{M}$ , in the following form [3]

$$\sigma = \frac{1}{4} \frac{(2\pi)^4}{2(s - w_p^2)} \int |\mathcal{M}(\vec{x}, X)|^2 d\Phi(X), \quad (4.9)$$

where the factor of one quarter in front comes from averaging over the spin states of the initial particles, the photon and the target proton. Setting (4.8) and (4.9) equal to each other and solving for  $N$  we get the total number of scattering events to be

$$N = \left( \frac{\mathcal{F} \rho_{target} \ell_{target} N_A}{A_{target}} \right) \frac{(2\pi)^4}{8(s - w_p^2)} \int |\mathcal{M}(\vec{x}, X)|^2 d\Phi(X), \quad (4.10)$$

which can be converted into the number of expected (detected) events by including the acceptance of the detector into the integral

$$\bar{n} = \left( \frac{\mathcal{F} \rho_{target} \ell_{target} N_A}{A_{target}} \right) \frac{(2\pi)^4}{8(s - w_p^2)} \int |\mathcal{M}(\vec{x}, X)|^2 \eta(X) d\Phi(X). \quad (4.11)$$

The integral in (4.11) must be calculated numerically as our detectors, and the topology of the event, have too complicated of an acceptance to be described by a simple function. So we take Monte Carlo events and run them through our detector simulation software, GEANT and GSIM, to model the effect of the acceptance. Then, we must replace the integral by a discrete sum over all the Monte Carlo events that were generated, called the *raw* Monte Carlo events, normalizing by the total number of raw Monte Carlo events. This yields

$$\int |\mathcal{M}(\vec{x}, X)|^2 \eta(X) d\Phi(X) \approx \frac{\int d\Phi(X)}{N_{raw}} \sum_i^{N_{raw}} |\mathcal{M}(\vec{x}, X_i)|^2 \eta(X_i). \quad (4.12)$$

The simulation software either accepts an event or rejects it, thus  $\eta(X_i)$  is either a 1 or a 0, so we can take our Monte Carlo dataset and separate the accepted events from the rejected ones and change our sum to a sum over only the accepted Monte Carlo, removing the acceptance, which yields

$$\int |\mathcal{M}(\vec{x}, X)|^2 \eta(X) d\Phi(X) \approx \frac{\int d\Phi(X)}{N_{raw}} \sum_i^{N_{acc}} |\mathcal{M}(\vec{x}, X_i)|^2. \quad (4.13)$$

In (4.13) we still have the integral over phase space to calculate:

$$\begin{aligned} \int d\Phi(X) &= \int \delta^4(p_i + k - p_f - q) \frac{d^3 \vec{p}_f}{(2\pi)^3 2E_f} \frac{d^3 \vec{q}}{(2\pi)^3 2E_\omega} \\ &= \frac{1}{4(2\pi)^6} \int \delta(\sqrt{s} - E_f - E_\omega) \frac{|\vec{p}_f|^2 d\Omega}{E_f E_\omega} \\ &= \frac{1}{4(2\pi)^6} \int \frac{|\vec{p}_f| d\Omega}{\sqrt{s}} \\ &= \frac{[(s - (w_p + w_\omega)^2)(s - (w_p - w_\omega)^2)]^{1/2}}{8(2\pi)^5 s}, \end{aligned} \quad (4.14)$$

Now, we can rewrite (4.11), substituting (4.13) and (4.14) to obtain

$$\bar{n} \approx \frac{\mathcal{S}(s)}{N_{raw}} \sum_i^{N_{acc}} |\mathcal{M}(\vec{x}, X_i)|^2, \quad (4.15)$$

where

$$\mathcal{S}(s) = \frac{\mathcal{F} \rho_{target} \ell_{target} N_A}{A_{target}} \frac{[(s - (w_p + w_\omega)^2)(s - (w_p - w_\omega)^2)]^{1/2}}{64\pi s(s - w_p^2)}. \quad (4.16)$$

We can now determine  $\mathcal{N}(\vec{x})$  in (4.6), using the normalization in (4.7) and (4.11) we can write

$$\mathcal{N}(\vec{x}) = \mathcal{C}(s) \bar{n}, \quad (4.17)$$

where

$$\mathcal{C}(s) = \frac{8(s - w_p^2)}{(2\pi)^4} \frac{A_{target}}{\mathcal{F} \rho_{target} \ell_{target} N_A}. \quad (4.18)$$

We can define the total cross section,  $\sigma$ , by inserting (4.12) and (4.14) into (4.9), leaving out the detector acceptance, yielding

$$\sigma = \frac{[(s - (w_p + w_\omega)^2)(s - (w_p - w_\omega)^2)]^{1/2}}{64\pi s(s - w_p^2)} \frac{1}{N_{raw}} \sum_i^{N_{raw}} |\mathcal{M}(\vec{x}, X_i)|^2. \quad (4.19)$$

## 4.2.2 Log Likelihood

Since minimization functions rather than maximization functions exist, it is desirable to derive our equations such that they can be minimized rather than maximized. Given that the natural logarithm is a monotonically increasing function, we choose to minimize the negative of the natural logarithm of the likelihood function, which will turn our product of probabilities into a sum over the logs of the probabilities. The fit parameters which minimize  $-\ln \mathcal{L}$  will maximize  $\mathcal{L}$ . Taking the natural logarithm of (4.5), we get

$$-\ln \mathcal{L} = -n \ln \bar{n} + \ln n! + \bar{n} - \sum_i^n \ln \mathcal{P}(\vec{x}, X_i). \quad (4.20)$$

Plugging in (4.6) for  $\mathcal{P}(\vec{x}, X_i)$  we obtain

$$-\ln \mathcal{L} = -n \ln \bar{n} + \ln n! + \bar{n} - \sum_i^n \ln [|\mathcal{M}(\vec{x}, X_i)|^2 \eta(X_i) \phi(X_i)] + n \ln \mathcal{N}(\vec{x}). \quad (4.21)$$

Utilizing (4.17), we can further simplify to

$$-\ln \mathcal{L} = -\sum_i^n \ln [|\mathcal{M}(\vec{x}, X_i)|^2 \eta(X_i) \phi(X_i)] + \bar{n} + \ln n! + n \ln \mathcal{C}(s). \quad (4.22)$$

Given that we are only trying to minimize  $-\ln \mathcal{L}$ , without caring about the actual value of the function at the minimum, we can ignore all terms which do not depend on  $\vec{x}$ , treating them simply as constants, so that

$$-\ln \mathcal{L} = -\sum_i^n \ln |\mathcal{M}(\vec{x}, X_i)|^2 + \bar{n} + const. \quad (4.23)$$

To obtain the final form of the log likelihood function, we substitute (4.15) for  $\bar{n}$ , and add in the Q-values from our background-subtraction method to weight the experimental data, which yields

$$-\ln \mathcal{L} = -\sum_i^n Q_i \ln |\mathcal{M}(\vec{x}, X_i)|^2 + \frac{\mathcal{S}(s)}{N_{raw}} \sum_i^{N_{acc}} |\mathcal{M}(\vec{x}, X_i)|^2 + const, \quad (4.24)$$

where the first sum is over the data events, and the second sum is over the accepted Monte Carlo events. This is the final form, but recall that we still have not calculated the Lorentz invariant transition amplitude,  $\mathcal{M}$  yet.

### 4.3 Spin Density Matrices

In order to calculate the Lorentz invariant transition amplitude,  $\mathcal{M}$ , for events generated with a polarized photon beam and polarized target, it will be necessary to calculate the photon and target spin density matrices first.

We shall briefly look at density matrices in general, before constructing the specific ones required here. Density matrices can be used to represent particles that exist in a statistical ensemble of states. If the density matrix for a particle is known, then all quantum mechanical observables can be calculated. For a particle with  $n$  states, in a given basis, each having wave function  $|\psi_i\rangle$ , the density matrix can be constructed as [46]

$$\rho = \sum_{i,i'}^n a_{ii'} |\psi_{i'}\rangle \langle \psi_i|. \quad (4.25)$$

Diagonal elements of the matrix,  $a_{ii}$ , represent the probability that the particle is in state  $|\psi_i\rangle$ . Density matrices are Hermitian and have a trace of 1. As a result of this, for particles which can exist in only two distinct states, it is always possible to write a density matrix as a linear combination of the identity matrix and the Pauli matrices [47].

For our purposes, the *spin* density matrix is constructed in the spin space. Spin  $\frac{1}{2}$  particles, as well as photons, have only two spin states, and thus can be written as a linear combination of the identity matrix and the Pauli matrices, where a vector,  $\vec{P}$ , related to the polarization vector, will provide the weights for the Pauli matrices. The general case for a particle with only two states then can be written as

$$\rho_x = \frac{1}{2} \mathcal{I} + \frac{1}{2} \vec{P} \cdot \vec{\sigma}. \quad (4.26)$$

One quick result of this is that unpolarized particles will have the identity matrix as their spin density matrix.

### 4.3.1 Photon Spin Density Matrix

Photons have two spin states, denoted as  $|m_\gamma = + \rangle$  and  $|m_\gamma = - \rangle$ , which are states of pure + circular polarization and pure - polarization, respectively. The wave function for linearly polarized photons is a linear combination of the two circular polarization spin states. Linearly polarized photons have a polarization vector that is defined, in the  $\hat{X}$ ,  $\hat{Y}$ ,  $\hat{Z}$  basis, as

$$\vec{\epsilon} = (\cos \alpha, \sin \alpha, 0), \quad (4.27)$$

where  $\alpha$  is the angle between  $\vec{\epsilon}$  and the  $\hat{X}$  axis in the production plane [47]. The vector  $\vec{P}$  in (4.26) for polarized photons in the center of mass is the Stoke's vector,

$$\vec{P}_{CM}^\gamma = (-\eta_L^\gamma \cos(2\alpha), -\eta_L^\gamma \sin(2\alpha), \eta_C^\gamma), \quad (4.28)$$

where  $\eta_{L/C}$  are as defined in Section 3.8;  $\eta_L$  is the degree of linear polarization, such that  $0 \leq \eta_L^\gamma \leq 1$ ; and  $\eta_C$  is the degree of circular polarization multiplied by the helicity of the photon, such that  $-1 \leq \eta_C^\gamma \leq 1$ . Following (4.26) the photon density matrix is written

$$\rho_\gamma = \frac{1}{2} \left[ \begin{pmatrix} 1 & 0 \\ 0 & 1 \end{pmatrix} - \eta_L^\gamma \cos 2\alpha \begin{pmatrix} 0 & 1 \\ 1 & 0 \end{pmatrix} - \eta_L^\gamma \sin 2\alpha \begin{pmatrix} 0 & -i \\ i & 0 \end{pmatrix} + \eta_C^\gamma \begin{pmatrix} 1 & 0 \\ 0 & -1 \end{pmatrix} \right] \quad (4.29)$$

or more compactly,

$$\rho_\gamma = \frac{1}{2} \begin{pmatrix} (1 + \eta_C^\gamma) & -\eta_L^\gamma e^{-2i\alpha} \\ -\eta_L^\gamma e^{2i\alpha} & (1 - \eta_C^\gamma) \end{pmatrix}. \quad (4.30)$$

### 4.3.2 Target Spin Density Matrix

Though we will not be analyzing an experiment with a polarized target here, it is worthwhile to follow through with this method to extend it to experiments with a polarized target. Run periods at CLAS such as *FROST* and *HD-ICE* with polarized targets may find them useful.

In a similar way, the target spin density matrix can be written, taking into account the two possible spin states, and the options of having either transversely or longitudinally polarized nucleons. The vector  $\vec{P}$  in (4.26) for a polarized target in the center of mass is

$$\vec{P}_{CM}^T = (-\eta_T^T \cos(2\beta), -\eta_T^T \sin(2\beta), \eta_L^T), \quad (4.31)$$

where  $\eta_T^T$  is the degree of transverse polarization and,  $0 \leq \eta_T^T \leq 1$ ; and  $\eta_L^T$  is the degree of longitudinal polarization multiplied by the helicity of the target nucleon, such that  $-1 \leq \eta_L^T \leq 1$ ; and  $\beta$  is the angle between the polarization vector of the target nucleon and the  $\hat{X}$  axis in the production plane of the vector meson. This leads to the following spin density matrix for the target,

$$\rho_i = \frac{1}{2} \left[ \begin{pmatrix} 1 & 0 \\ 0 & 1 \end{pmatrix} - \eta_T^T \cos 2\beta \begin{pmatrix} 0 & 1 \\ 1 & 0 \end{pmatrix} - \eta_T^T \sin 2\beta \begin{pmatrix} 0 & -i \\ i & 0 \end{pmatrix} + \eta_L^T \begin{pmatrix} 1 & 0 \\ 0 & -1 \end{pmatrix} \right] \quad (4.32)$$

or more compactly,

$$\rho_i = \frac{1}{2} \begin{pmatrix} (1 + \eta_L^T) & -\eta_T^T e^{-2i\beta} \\ -\eta_T^T e^{2i\beta} & (1 - \eta_L^T) \end{pmatrix} \quad (4.33)$$

### 4.3.3 Vector Meson Spin Density Matrix

The spin density matrix for the vector meson (the  $\omega$  meson in the present case) is related to the density matrices for the photon and target by a matrix of the production amplitudes,  $J$ . The relationship, assuming an unpolarized recoil nucleon, is [47]

$$\rho_V = J (\rho_\gamma \otimes \rho_i) J^\dagger. \quad (4.34)$$

The direct product between (4.29) and (4.32) leads to 16 4x4 matrices of complex numbers (the number to the top right of each matrix is simply a label to keep track of all 16 matrices)

$$\begin{aligned}
 (\rho_\gamma \otimes \rho_i) = & \left( \begin{array}{cccc} 1 & 0 & 0 & 0 \\ 0 & 1 & 0 & 0 \\ 0 & 0 & 1 & 0 \\ 0 & 0 & 0 & 1 \end{array} \right)^0 \\
 -\eta_L^\gamma \cos 2\alpha & \left( \begin{array}{cccc} 0 & 0 & 1 & 0 \\ 0 & 0 & 0 & 1 \\ 1 & 0 & 0 & 0 \\ 0 & 1 & 0 & 0 \end{array} \right)^1 - \eta_L^\gamma \sin 2\alpha \left( \begin{array}{cccc} 0 & 0 & -i & 0 \\ 0 & 0 & 0 & -i \\ i & 0 & 0 & 0 \\ 0 & i & 0 & 0 \end{array} \right)^2 + \eta_C^\gamma \left( \begin{array}{cccc} 1 & 0 & 0 & 0 \\ 0 & 1 & 0 & 0 \\ 0 & 0 & -1 & 0 \\ 0 & 0 & 0 & -1 \end{array} \right)^3 \\
 -\eta_T^T \cos 2\beta & \left( \begin{array}{cccc} 0 & 1 & 0 & 0 \\ 1 & 0 & 0 & 0 \\ 0 & 0 & 0 & 1 \\ 0 & 0 & 1 & 0 \end{array} \right)^4 - \eta_T^T \sin 2\beta \left( \begin{array}{cccc} 0 & -i & 0 & 0 \\ i & 0 & 0 & 0 \\ 0 & 0 & 0 & -i \\ 0 & 0 & i & 0 \end{array} \right)^5 + \eta_L^T \left( \begin{array}{cccc} 1 & 0 & 0 & 0 \\ 0 & -1 & 0 & 0 \\ 0 & 0 & 1 & 0 \\ 0 & 0 & 0 & -1 \end{array} \right)^6 \\
 +\eta_L^\gamma \eta_T^T \cos 2\alpha \cos 2\beta & \left( \begin{array}{cccc} 0 & 0 & 0 & 1 \\ 0 & 0 & 1 & 0 \\ 0 & 1 & 0 & 0 \\ 1 & 0 & 0 & 0 \end{array} \right)^7 + \eta_L^\gamma \eta_T^T \cos 2\alpha \sin 2\beta \left( \begin{array}{cccc} 0 & 0 & 0 & -i \\ 0 & 0 & i & 0 \\ 0 & -i & 0 & 0 \\ i & 0 & 0 & 0 \end{array} \right)^8 \\
 -\eta_L^\gamma \eta_L^T \cos 2\alpha & \left( \begin{array}{cccc} 0 & 0 & 1 & 0 \\ 0 & 0 & 0 & -1 \\ 1 & 0 & 0 & 0 \\ 0 & -1 & 0 & 0 \end{array} \right)^9 + \eta_L^\gamma \eta_T^T \sin 2\alpha \cos 2\beta \left( \begin{array}{cccc} 0 & 0 & 0 & -i \\ 0 & 0 & -i & 0 \\ 0 & i & 0 & 0 \\ i & 0 & 0 & 0 \end{array} \right)^{10} \\
 +\eta_L^\gamma \eta_T^T \sin 2\alpha \sin 2\beta & \left( \begin{array}{cccc} 0 & 0 & 0 & -1 \\ 0 & 0 & 1 & 0 \\ 0 & 1 & 0 & 0 \\ -1 & 0 & 0 & 0 \end{array} \right)^{11} - \eta_L^\gamma \eta_L^T \sin 2\alpha \left( \begin{array}{cccc} 0 & 0 & -i & 0 \\ 0 & 0 & 0 & i \\ i & 0 & 0 & 0 \\ 0 & -i & 0 & 0 \end{array} \right)^{12} \\
 -\eta_C^\gamma \eta_T^T \cos 2\beta & \left( \begin{array}{cccc} 0 & 1 & 0 & 0 \\ 1 & 0 & 0 & 0 \\ 0 & 0 & 0 & -1 \\ 0 & 0 & -1 & 0 \end{array} \right)^{13} - \eta_C^\gamma \eta_T^T \sin 2\beta \left( \begin{array}{cccc} 0 & -i & 0 & 0 \\ i & 0 & 0 & 0 \\ 0 & 0 & 0 & i \\ 0 & 0 & -i & 0 \end{array} \right)^{14} \\
 +\eta_C^\gamma \eta_L^T & \left( \begin{array}{cccc} 1 & 0 & 0 & 0 \\ 0 & -1 & 0 & 0 \\ 0 & 0 & -1 & 0 \\ 0 & 0 & 0 & 1 \end{array} \right)^{15}. \tag{4.35}
 \end{aligned}$$

We shall refer to the matrices from (4.35) as  $\rho_V^a$  where  $a$  can range from 0-15. These can be combined together into a single matrix as:

$$(\rho_\gamma \otimes \rho_i) = \begin{pmatrix} (1 + \eta_C^\gamma)(1 + \eta_L^T) & -(1 + \eta_C^\gamma)\eta_T^T e^{-2i\beta} & -(1 + \eta_L^T)\eta_L^\gamma e^{-2i\alpha} & \eta_L^\gamma \eta_T^T e^{-2i(\alpha+\beta)} \\ -(1 + \eta_C^\gamma)\eta_T^T e^{2i\beta} & (1 + \eta_C^\gamma)(1 - \eta_L^T) & \eta_L^\gamma \eta_T^T e^{-2i(\alpha-\beta)} & -(1 - \eta_L^T)\eta_L^\gamma e^{-2i\alpha} \\ -(1 + \eta_L^T)\eta_L^\gamma e^{2i\alpha} & \eta_L^\gamma \eta_T^T e^{2i(\alpha-\beta)} & (1 - \eta_C^\gamma)(1 + \eta_L^T) & -(1 - \eta_C^\gamma)\eta_T^T e^{-2i\beta} \\ \eta_L^\gamma \eta_T^T e^{2i(\alpha+\beta)} & -(1 - \eta_L^T)\eta_L^\gamma e^{-2i\alpha} & -(1 - \eta_C^\gamma)\eta_T^T e^{2i\beta} & (1 - \eta_C^\gamma)(1 - \eta_L^T) \end{pmatrix} \tag{4.36}$$

The  $J$  in (4.34) is a matrix of the 24 production amplitudes. Since the recoil proton's spin is not measured, it is summed over, reducing the number of production amplitudes to 12, which will

be labeled as  $\mathcal{A}_{m_\gamma, m_i, m_V}$ . The J matrix then is

$$J = \begin{pmatrix} A_{+++} & A_{++-} & A_{+-+} & A_{-+-} \\ A_{++0} & A_{+-0} & A_{-+0} & A_{--0} \\ A_{+-+} & A_{+-0} & A_{-+-} & A_{---} \end{pmatrix} \quad (4.37)$$

The vector meson's spin density matrix then can be calculated using either (4.35) or (4.36), but it is more useful to see it as the sum of the 16 matrices. Those 16 matrices then read:

$$\rho_{m_V m_{V'}}^0 = \frac{1}{2N} \sum_{m_\gamma m_i m_f} \mathcal{A}_{m_\gamma, m_i, m_f, m_V} * \mathcal{A}_{m_\gamma, m_i, m_f, m_{V'}}^\dagger \quad (4.38a)$$

$$\rho_{m_V m_{V'}}^1 = \frac{1}{2N} \sum_{m_\gamma m_i m_f} \mathcal{A}_{m_\gamma, m_i, m_f, m_V} * \mathcal{A}_{-m_\gamma, m_i, m_f, m_{V'}}^\dagger \quad (4.38b)$$

$$\rho_{m_V m_{V'}}^2 = \frac{1}{2N} \sum_{m_\gamma m_i m_f} i * (-m_\gamma) \mathcal{A}_{m_\gamma, m_i, m_f, m_V} * \mathcal{A}_{-m_\gamma, m_i, m_f, m_{V'}}^\dagger \quad (4.38c)$$

$$\rho_{m_V m_{V'}}^3 = \frac{1}{2N} \sum_{m_\gamma m_i m_f} m_\gamma \mathcal{A}_{m_\gamma, m_i, m_f, m_V} * \mathcal{A}_{m_\gamma, m_i, m_f, m_{V'}}^\dagger \quad (4.38d)$$

$$\rho_{m_V m_{V'}}^4 = \frac{1}{2N} \sum_{m_\gamma m_i m_f} \mathcal{A}_{m_\gamma, m_i, m_f, m_V} * \mathcal{A}_{m_\gamma, -m_i, m_f, m_{V'}}^\dagger \quad (4.38e)$$

$$\rho_{m_V m_{V'}}^5 = \frac{1}{2N} \sum_{m_\gamma m_i m_f} i * (-m_i) \mathcal{A}_{m_\gamma, m_i, m_f, m_V} * \mathcal{A}_{m_\gamma, -m_i, m_f, m_{V'}}^\dagger \quad (4.38f)$$

$$\rho_{m_V m_{V'}}^6 = \frac{1}{2N} \sum_{m_\gamma m_i m_f} m_i \mathcal{A}_{m_\gamma, m_i, m_f, m_V} * \mathcal{A}_{m_\gamma, m_i, m_f, m_{V'}}^\dagger \quad (4.38g)$$

$$\rho_{m_V m_{V'}}^7 = \frac{1}{2N} \sum_{m_\gamma m_i m_f} \mathcal{A}_{m_\gamma, m_i, m_f, m_V} * \mathcal{A}_{-m_\gamma, -m_i, m_f, m_{V'}}^\dagger \quad (4.38h)$$

$$\rho_{m_V m_{V'}}^8 = \frac{1}{2N} \sum_{m_\gamma m_i m_f} i * (-m_i) \mathcal{A}_{m_\gamma, m_i, m_f, m_V} * \mathcal{A}_{-m_\gamma, -m_i, m_f, m_{V'}}^\dagger \quad (4.38i)$$

$$\rho_{m_V m_{V'}}^9 = \frac{1}{2N} \sum_{m_\gamma m_i m_f} m_i \mathcal{A}_{m_\gamma, m_i, m_f, m_V} * \mathcal{A}_{-m_\gamma, m_i, m_f, m_{V'}}^\dagger \quad (4.38j)$$

$$\rho_{m_V m_{V'}}^{10} = \frac{1}{2N} \sum_{m_\gamma m_i m_f} i * (-m_\gamma) \mathcal{A}_{m_\gamma, m_i, m_f, m_V} * \mathcal{A}_{-m_\gamma, -m_i, m_f, m_{V'}}^\dagger \quad (4.38k)$$

$$\rho_{m_V m_{V'}}^{11} = \frac{1}{2N} \sum_{m_\gamma m_i m_f} (-m_\gamma * m_i) \mathcal{A}_{m_\gamma, m_i, m_f, m_V} * \mathcal{A}_{-m_\gamma, -m_i, m_f, m_{V'}}^\dagger \quad (4.38l)$$

$$\rho_{m_V m_{V'}}^{12} = \frac{1}{2N} \sum_{m_\gamma m_i m_f} (-m_\gamma * m_i) \mathcal{A}_{m_\gamma, m_i, m_f, m_V} * \mathcal{A}_{-m_\gamma, m_i, m_f, m_{V'}}^\dagger \quad (4.38m)$$

$$\rho_{m_V m_{V'}}^{13} = \frac{1}{2N} \sum_{m_\gamma m_i m_f} m_\gamma \mathcal{A}_{m_\gamma, m_i, m_f, m_V} * \mathcal{A}_{m_\gamma, -m_i, m_f, m_{V'}}^\dagger \quad (4.38n)$$

$$\rho_{m_V m_{V'}}^{14} = \frac{1}{2N} \sum_{m_\gamma m_i m_f} (-m_\gamma * m_i) \mathcal{A}_{m_\gamma, m_i, m_f, m_V} * \mathcal{A}_{m_\gamma, -m_i, m_f, m_{V'}}^\dagger \quad (4.38o)$$

$$\rho_{m_V m_{V'}}^{15} = \frac{1}{2N} \sum_{m_\gamma m_i m_f} m_\gamma * m_i \mathcal{A}_{m_\gamma, m_i, m_f, m_V} * \mathcal{A}_{m_\gamma, m_i, m_f, m_{V'}}^\dagger. \quad (4.38p)$$

The total spin density matrix for the vector meson is then found by adding together the  $\rho_V^a$ , weighted

by the same factors multiplying the  $\rho_V^a$  in (4.35). If we define a new vector

$$\begin{aligned}\vec{P}_{16} = & (-\eta_L^\gamma \cos 2\alpha, -\eta_L^\gamma \sin 2\alpha, \eta_C^\gamma, -\eta_T^T \cos 2\beta, -\eta_T^T \sin 2\beta, \eta_L^T, \\ & \eta_L^\gamma \eta_T^T \cos 2\alpha \cos 2\beta, \eta_L^\gamma \eta_T^T \cos 2\alpha \sin 2\beta, -\eta_L^\gamma \eta_L^T \cos 2\alpha, \\ & \eta_L^\gamma \eta_T^T \sin 2\alpha \cos 2\beta, \eta_L^\gamma \eta_T^T \sin 2\alpha \sin 2\beta, -\eta_L^\gamma \eta_L^T \sin 2\alpha, \\ & -\eta_C^\gamma \eta_T^T \cos 2\beta, -\eta_C^\gamma \eta_T^T \sin 2\beta, \eta_C^\gamma \eta_L^T)\end{aligned}\quad (4.39)$$

then we can further define a more compact way to write this as

$$\rho_V = \rho^0 + \sum_{a=1}^{15} \vec{P}_{16}^a \rho^a. \quad (4.40)$$

Note, that in experiments with an unpolarized target, such as g1c and g8b, only elements in the first four of these matrices can be measured.

#### 4.3.4 Symmetries in the Spin Density Matrix of Vector Mesons

The Hermitian nature of the density matrices implies some symmetries for the vector meson's spin density matrix. Being Hermitian itself,  $\rho_{V'V} = \rho_{VV'}^\dagger$ . There is also a relationship between the amplitudes such that [47]

$$\mathcal{A}_{-m_\gamma, -m_i, -m_f, -m_V} = (-1)^{m_V - m_\gamma - m_f + m_i} \mathcal{A}_{m_\gamma, m_i, m_f, m_V}, \quad (4.41)$$

which leads to several more properties. To refer to individual spin density matrix elements (SDMEs), we will adopt the notation  $\rho_{m_V m_{V'}}^i$ , where i indicates which spin density matrix the element belongs to, and the subscript indicates the indices for the element. Thus,  $\rho_{00}^0$  is the 00 element from the  $\rho^0$  matrix. For  $a = 0, 1, 5, 8, 10, 13, 14$  and  $15$ ,

$$\rho_{00}^a \neq 0 \quad (4.42a)$$

$$\rho_{0-1}^a = -\rho_{10}^{a\dagger} \quad (4.42b)$$

$$Im\{\rho_{1-1}^a\} = 0 \quad (4.42c)$$

$$\rho_{11}^a = \rho_{-1-1}^a. \quad (4.42d)$$

For  $a = 2, 3, 4, 6, 7, 9, 11$  and  $12$ ,

$$\rho_{00}^a = 0 \quad (4.43a)$$

$$\rho_{0-1}^a = \rho_{10}^{a\dagger} \quad (4.43b)$$

$$Re\{\rho_{1-1}^a\} = 0 \quad (4.43c)$$

$$\rho_{11}^a = -\rho_{-1-1}^a. \quad (4.43d)$$

#### 4.3.5 Schilling's Method

It is possible to constrain the SDMEs from the decay distribution of the vector meson. This method was discussed by Schilling in [47]. In this method, the decay angular distribution,  $W(\cos \theta, \phi)$ , is related to the spin density matrix of the vector meson by a matrix of the decay amplitudes

$$W(\cos \theta, \phi) = M \rho_V M^\dagger = D_{m_V 0}^{1\dagger}(\phi, \theta, -\phi) \rho_V D_{m_V 0}^1(\phi, \theta, -\phi). \quad (4.44)$$

Here, the  $D_{ii'}^1$  are the Wigner rotation functions, which can be used to replace the decay amplitudes because all of the decay particles are spin 0. This leads to the full function for  $W$

$$\begin{aligned} W(\cos \theta, \phi) = & \frac{3}{4\pi} \left( \frac{1}{2} (\rho_{11} + \rho_{-1-1}) \sin^2 \theta + \rho_{00} \cos^2 \theta \right. \\ & + \frac{1}{\sqrt{2}} (-Re(\rho_{10}) + Re(\rho_{-10})) \sin 2\theta \cos \phi + \frac{1}{\sqrt{2}} (Im(\rho_{10}) - Im(\rho_{0-1})) \sin(2\theta) \sin(\phi) \\ & \left. - Re(\rho_{1-1}) \sin^2 \theta \cos 2\phi + Im(\rho_{1-1}) \sin^2 \theta \sin 2\phi \right). \end{aligned} \quad (4.45)$$

This full expression can of course be split up into 16 separate equations by replacing the full vector meson spin density matrix in (4.47) with the  $\rho_V^a$ , such that

$$W(\cos \theta, \phi) = W^0(\cos \theta, \phi) + \sum_{a=1}^{16} \vec{P}_{16}^a W^a(\cos \theta, \phi), \quad (4.46)$$

where

$$W^a(\cos \theta, \phi) = M \rho_V^a M^\dagger = D_{m_V 0}^{1\dagger}(\phi, \theta, -\phi) \rho_V^a D_{m_V 0}^1(\phi, \theta, -\phi). \quad (4.47)$$

We can write the first four, exploiting the symmetries in (4.42) and (4.43), as

$$\begin{aligned} W^0(\cos \theta, \phi) = & \frac{3}{4\pi} \left( \frac{1}{2} (1 - \rho_{00}^0) \sin^2 \theta + \rho_{00}^0 \cos^2 \theta \right. \\ & \left. - \sqrt{2} Re(\rho_{10}^0) \sin 2\theta \cos \phi - \rho_{1-1}^0 \sin^2 \theta \cos 2\phi \right) \end{aligned} \quad (4.48a)$$

$$\begin{aligned} W^1(\cos \theta, \phi) = & \frac{3}{4\pi} \left( \rho_{11}^1 \sin^2 \theta + \rho_{00}^1 \cos^2 \theta \right. \\ & \left. - \sqrt{2} Re(\rho_{10}^1) \sin 2\theta \cos \phi - \rho_{1-1}^1 \sin^2 \theta \cos 2\phi \right) \end{aligned} \quad (4.48b)$$

$$W^2(\cos \theta, \phi) = \frac{3}{4\pi} (\sqrt{2} Im(\rho_{10}^2) \sin 2\theta \sin \phi + Im(\rho_{1-1}^2) \sin^2 \theta \sin 2\phi) \quad (4.48c)$$

$$W^3(\cos \theta, \phi) = \frac{3}{4\pi} (\sqrt{2} Im(\rho_{10}^3) \sin 2\theta \sin \phi + Im(\rho_{1-1}^3) \sin^2 \theta \sin 2\phi). \quad (4.48d)$$

Since these equations get their form from the symmetries among the  $\rho^a$  matrices, the remaining  $W^a$  follow the pattern above, where they match  $W^1$  for  $a = 5, 8, 10, 13, 14$  and  $15$ , and they match  $W^2$  for  $a = 4, 6, 7, 9, 11$  and  $12$ . Looking at these equations, it is apparent that the consequence of the symmetry properties in (4.42) and (4.43) is that some of the SDMEs cannot be measured, for instance the  $Im(\rho_{10}^0)$  element.

Given the equations in (4.48), it is possible to extract some information about the SDMEs using only the decay distribution of the data. To do so, first construct the full equation for  $W(\cos \theta, \phi)$  following (4.46). This will serve as the fitting function with the SDMEs as the fitting parameters and the data providing the raw values for  $\cos(\theta)$  and  $\phi$  in the Adair frame for each event, along with the polarization values. This method does not rely on the amplitudes, though it does use the Q-values to weight the signal and background. This method for extracting the SDMEs is thus independent of the previous method and will provide a good check on the results we obtain from that method.

### 4.3.6 Measurable Elements

We can write out the first four spin density matrices in terms of their elements as

$$\rho^0 = \begin{pmatrix} \frac{1}{2}(1 - \rho_{00}^0) & Re(\rho_{10}^0) + iIm(\rho_{10}^0) & Re(\rho_{1-1}^0) \\ . & \rho_{00}^0 & -Re(\rho_{10}^0) + iIm(\rho_{10}^0) \\ . & . & \frac{1}{2}(1 - \rho_{00}^0) \end{pmatrix} \quad (4.49a)$$

$$\rho^1 = \begin{pmatrix} \underline{\rho_{11}} & \underline{Re(\rho_{10}^1) + iIm(\rho_{10}^1)} & \underline{Re(\rho_{1-1}^1)} \\ \cdot & \underline{\rho_{00}^1} & \underline{-Re(\rho_{10}^1) + iIm(\rho_{10}^1)} \\ \cdot & \cdot & \underline{\rho_{11}^1} \end{pmatrix} \quad (4.49b)$$

$$\rho^2 = \begin{pmatrix} \underline{\rho_{11}^2} & \underline{Re(\rho_{10}^2) + iIm(\rho_{10}^2)} & \underline{iIm(\rho_{1-1}^2)} \\ \cdot & 0 & \underline{Re(\rho_{10}^2) - iIm(\rho_{10}^2)} \\ \cdot & \cdot & \underline{-\rho_{11}^2} \end{pmatrix} \quad (4.49c)$$

$$\rho^3 = \begin{pmatrix} \underline{\rho_{11}^3} & \underline{Re(\rho_{10}^3) + iIm(\rho_{10}^3)} & \underline{iIm(\rho_{1-1}^3)} \\ \cdot & 0 & \underline{Re(\rho_{10}^3) - iIm(\rho_{10}^3)} \\ \cdot & \cdot & \underline{-\rho_{11}^3} \end{pmatrix} \quad (4.49d)$$

where the underlined entries can be measured, and the others cannot. The bottom half of the matrices are the Hermitian conjugates of the upper half. The remaining  $\rho^a$  matrices follow the same pattern as with the W equations and other symmetries, that is they look like  $\rho^1$  for  $a = 5, 8, 10, 13, 14$  and  $15$ , and they look like  $\rho^2$  for  $a = 4, 6, 7, 9, 11$  and  $12$ . Note that the  $\rho_{11}^0$  element is a function of the  $\rho_{00}^0$  because we require that  $Tr\rho^0 = 1$ .

#### 4.3.7 Relationship to Vector and Tensor Polarizations

The overall spin density matrix elements give information about the likelihood of finding the vector meson in a given state, along the diagonal, but it can also be linked to the vector and tensor polarizations of the vector meson. Biplab Dey, in his thesis [48], derived the spin density matrix for a vector meson in terms of the vector,  $\vec{P}$ , and tensor,  $T_{2\mu}$ , polarizations, which we have shown below, after imposing the Hermicity requirements which force  $T_{2-1} = -T_{21}$ ,  $T_{2-2} = T_{22}$ , and each of those  $T_{2\mu}$  values to be real,

$$\rho = \frac{1}{3} \begin{pmatrix} 1 - \frac{3}{2}P_z + \sqrt{\frac{1}{2}}T_{20} & \frac{3}{2\sqrt{2}}(P_x - iP_y) + \sqrt{\frac{3}{2}}T_{21} & \sqrt{3}T_{22} \\ \frac{3}{2\sqrt{2}}(P_x + iP_y) + \sqrt{\frac{3}{2}}T_{21} & 1 - \sqrt{2}T_{20} & \frac{3}{2\sqrt{2}}(P_x - iP_y) - \sqrt{\frac{3}{2}}T_{21} \\ \sqrt{3}T_{22} & \frac{3}{2\sqrt{2}}(P_x + iP_y) - \sqrt{\frac{3}{2}}T_{21} & 1 + \frac{3}{2}P_z + \sqrt{\frac{1}{2}}T_{20} \end{pmatrix}. \quad (4.50)$$

Comparing this to the matrices in (4.49), it is clear that some values can only be measured with polarization of either the target or photon. For instance, in an experiment with unpolarized beam and unpolarized target the vector polarization cannot be measured [48], as symmetry requirements force  $P_x = P_z = 0$  and the  $P_y$  term can only be measured by the  $Im(\rho_{10})$  term, which cannot be measured in such an experiment. Adding polarization to the experiment allows us to gain some knowledge of these values.

#### 4.3.8 Summary

This section has given an overview of the spin density matrices of the photon, target and final vector meson for the case of photoproduction off of a nucleon. There is also a spin density matrix associated with the recoiling nucleon, however we are aware of no such experiment that is capable of measuring this for vector mesons and so have chosen to omit it. However, from the method that we have set here, it is very easy to produce all of the additions to the vector meson's spin density matrix. There would be an additional 48 matrices, three from the polarized recoil nucleon with no other polarized particles, nine each from pairing with one additional polarized particle, and 27 from having all three particles polarized. The form of each of these matrices is easy to guess from the form of (4.38), and their prefactors will follow the form of  $P_{16}$  given in (4.40).

The full form of the spin density matrix is good for reference, but, for the run periods under analysis here, only elements of the first four will be measured. Full knowledge of the vector meson's

spin density matrix would require an experiment that could measure all three particle polarizations at the same time and such an experiment is not likely to be run any time soon. Even with full knowledge of the measurable portions of the density matrix, there would still be elements which could not be fully known, at least not solely with photoproduction experiments.

The spin density matrices are also necessary to determine the likelihood equations as will be seen in the next section.

## 4.4 Likelihood Equations

The Lorentz invariant transition amplitude,  $\mathcal{M}$ , is related to the cross section by (4.9). However, we can also determine the cross section from the density matrices [6],

$$\sigma = \sigma_0 \frac{\text{Tr}[\rho_{final}]}{\text{Tr}[\rho_{initial}]}, \quad (4.51)$$

where  $\rho_{initial/final}$  are the direct products of the density matrices of all the initial/final state particles, and  $\sigma_0$  is a constant of proportionality. This means  $\rho_{initial}$  is just  $\rho_\gamma \otimes \rho_i$  which we have already calculated in (4.35) and

$$\rho_{final} = J \rho_{initial} J^\dagger, \quad (4.52)$$

though here note that we can simplify the  $J$  matrix by summing over the  $m_f$  and  $m_\omega$  indices that are not measured, and we get

$$J = \begin{pmatrix} A_{++} & A_{+-} & A_{-+} & A_{--} \end{pmatrix}. \quad (4.53)$$

If we now set (4.9) and (4.51) equal to each other we find that

$$\sigma_0 \frac{\text{Tr}[J(\rho_\gamma \otimes \rho_i)J^\dagger]}{\text{Tr}[(\rho_\gamma \otimes \rho_i)]} = \frac{1}{4} \frac{(2\pi)^4}{2(s - w_p^2)} \int |\mathcal{M}(\vec{x}, X)|^2 d\Phi(X). \quad (4.54)$$

Following the same path as we did for the Monte Carlo, we can turn the integral into a sum over the events in the data, yielding

$$\sigma_0 \text{Tr}[J(\rho_\gamma \otimes \rho_i)J^\dagger] = \frac{[(s - (w_p + w_\omega)^2)(s - (w_p - w_\omega)^2)]^{1/2}}{64\pi s(s - w_p^2)} \sum_{data} |\mathcal{M}(\vec{x}, X)|^2, \quad (4.55)$$

where we have applied the fact that  $\text{Tr}[\rho_{initial}] = 1$ . From this equation, it seems clear that everything except the  $|\mathcal{M}|^2$  is a constant and thus can be labeled as  $\sigma_0$ , and so we get the equation for  $\mathcal{M}$  to be

$$\sum_{data} |\mathcal{M}(\vec{x}, X)|^2 = \text{Tr}[J(\rho_\gamma \otimes \rho_i)J^\dagger]. \quad (4.56)$$

It is now only necessary to substitute (4.29) and (4.32) into (4.56). For simplicity we have separated these into four general cases presented below.

### 4.4.1 Unpolarized Photons

If neither the beam nor the target is polarized (4.56) can be written as

$$|\mathcal{M}|^2 = \frac{1}{4} \sum_{m_\gamma m_i, m_f} |A_{m_\gamma m_i, m_f}|^2. \quad (4.57)$$

#### 4.4.2 Polarized Photons

If we now consider the case with a polarized beam and unpolarized target, (4.56) can be written as

$$|\mathcal{M}|^2 = \frac{1}{4} \sum_{m_i, m_f} ( (1 + \eta_C^\gamma) |A_{+, m_i, m_f}|^2 + (1 - \eta_C^\gamma) |A_{-, m_i, m_f}|^2 - \eta_L^\gamma (e^{-2i\alpha} A_{+, m_i, m_f} A_{-, m_i, m_f}^\dagger + e^{2i\alpha} A_{-, m_i, m_f} A_{+, m_i, m_f}^\dagger)). \quad (4.58)$$

It is clear from this equation that when  $\eta_C^\gamma = \eta_L^\gamma = 0$  we have the unpolarized case. The term multiplying the  $\eta_L^\gamma$  has two terms which are the Hermitian conjugates of each other that are being added, so we have a purely real result.

#### 4.4.3 Polarized Target

If we now consider the case with an unpolarized beam and a polarized target, (4.56) can then be written as

$$|\mathcal{M}|^2 = \frac{1}{4} \sum_{m_\gamma, m_f} ( (1 + \eta_L^T) |A_{m_\gamma, +, m_f}|^2 + (1 - \eta_L^T) |A_{m_\gamma, -, m_f}|^2 - \eta_T^T (e^{-2i\beta} A_{m_\gamma, +, m_f} A_{m_\gamma, -, m_f}^\dagger + e^{2i\beta} A_{m_\gamma, -, m_f} A_{m_\gamma, +, m_f}^\dagger)). \quad (4.59)$$

#### 4.4.4 Polarized Photons and Polarized Target

Lastly, when we consider the case of both the photon beam and the target being polarized, (4.56) can then be written as

$$\begin{aligned} |\mathcal{M}|^2 = \frac{1}{4} \sum_{m_f} ( & (1 + \eta_C^\gamma)(1 + \eta_L^T) |A_{+, +, m_f}|^2 + (1 + \eta_C^\gamma)(1 - \eta_L^T) |A_{+, -, m_f}|^2 + \\ & (1 - \eta_C^\gamma)(1 + \eta_L^T) |A_{-, +, m_f}|^2 + (1 - \eta_C^\gamma)(1 - \eta_L^T) |A_{-, -, m_f}|^2 \\ & - \eta_L^\gamma(1 + \eta_L^T)(e^{-2i\alpha} A_{+, +, m_f} A_{-, +, m_f}^\dagger + e^{2i\alpha} A_{-, +, m_f} A_{+, +, m_f}^\dagger) \\ & - \eta_L^\gamma(1 - \eta_L^T)(e^{-2i\alpha} A_{+, -, m_f} A_{-, -, m_f}^\dagger + e^{2i\alpha} A_{-, -, m_f} A_{+, -, m_f}^\dagger) \\ & - (1 + \eta_C^\gamma)\eta_T^T (e^{-2i\beta} A_{+, +, m_f} A_{+, -, m_f}^\dagger + e^{2i\beta} A_{+, -, m_f} A_{+, +, m_f}^\dagger) \\ & - (1 - \eta_C^\gamma)\eta_T^T (e^{-2i\beta} A_{-, +, m_f} A_{-, -, m_f}^\dagger + e^{2i\beta} A_{-, -, m_f} A_{-, +, m_f}^\dagger) \\ & + \eta_L^\gamma \eta_T^T (e^{-2i(\alpha+\beta)} A_{+, +, m_f} A_{-, -, m_f}^\dagger + e^{2i(\alpha+\beta)} A_{-, -, m_f} A_{+, +, m_f}^\dagger) \\ & + e^{-2i(\alpha-\beta)} A_{+, -, m_f} A_{-, +, m_f}^\dagger + e^{2i(\alpha-\beta)} A_{-, +, m_f} A_{+, -, m_f}^\dagger \\ & + e^{-2i(\beta-\alpha)} A_{-, +, m_f} A_{+, -, m_f}^\dagger + e^{2i(\beta-\alpha)} A_{+, -, m_f} A_{-, +, m_f}^\dagger). \end{aligned} \quad (4.60)$$

This equation is the most general form of the likelihood function, with no recoil polarization, and all the other cases can be taken as special cases of it.

### 4.5 The Angles $\alpha$ and $\beta$

In the preceding sections, we have used the angles  $\alpha$  and  $\beta$  with only a brief description of their form. Here, we will calculate them precisely. Both  $\alpha$  and  $\beta$  describe the angle between a polarization vector and the vector meson production plane. Let us first recall our center of mass frame and polarization plane. Recall that (4.1) defines the center-of-mass coordinates and these coordinates are simply a rotation of the lab coordinates about the z axis, see Figure 4.1.

The angle  $\alpha$  then is just the angle between the photon polarization vector,  $\hat{P}$ , and the the  $\hat{X}$  axis in the production plane. Thus, we can define  $\alpha$  as:

$$\hat{P} \cdot \hat{X} = \cos \alpha \quad (4.61)$$

or

$$\hat{P} \times \hat{X} = \sin \alpha \hat{z} \quad (4.62)$$

or, more usefully,

$$\alpha = \arctan \frac{\hat{P} \times \hat{X}}{\hat{P} \cdot \hat{X}}. \quad (4.63)$$

In the experiments run using CLAS, the photon polarization is chosen to be along either the x or y lab axes. Thus, we can write out the two common cases. For horizontal polarization we get

$$\hat{P} \cdot \hat{X} = \frac{q_x}{\sqrt{q_x^2 + q_y^2}} \quad (4.64a)$$

$$\hat{P} \times \hat{X} = \frac{q_y}{\sqrt{q_x^2 + q_y^2}} \hat{z} \quad (4.64b)$$

$$\alpha = \arctan \frac{q_y}{q_x}, \quad (4.64c)$$

and for vertical polarization we get

$$\hat{P} \cdot \hat{X} = \frac{q_y}{\sqrt{q_x^2 + q_y^2}} \quad (4.65a)$$

$$\hat{P} \times \hat{X} = \frac{-q_x}{\sqrt{q_x^2 + q_y^2}} \hat{z} \quad (4.65b)$$

$$\alpha = \arctan \frac{-q_x}{q_y}. \quad (4.65c)$$

If the target is polarized, the transverse polarization requires calculating the angle  $\beta$ . For transverse polarization, the same formulas for  $\alpha$  work here as well.

For polarization that is not along one of the axes, one can simply find the angle between the  $\hat{x}_{lab}$ -axis and the polarization vector, and then the angle between the  $\hat{x}_{lab}$ -axis and the  $\hat{X}$ -axis and then find the difference between the two of them, as can be seen in Figure 4.1.

## 4.6 Coupling Multiple Datasets

Both of the datasets under analysis are composed of multiple smaller datasets. Since these small datasets require their own corrections and cuts and background subtraction, we need to be able to combine the datasets together in the fitting process.

In order to combine the datasets, it is simply necessary to minimize the sum of our  $-ln\mathcal{L}$ ,

$$-ln\mathcal{L} = \sum_d^{N_d} -ln\mathcal{L}_d, \quad (4.66)$$

where  $N_d$  is the number of datasets summed over. Thus, we find a single set of parameters that minimizes the collective dataset. This can be expanded to include datasets with different types of polarization as well. This requires that all of the datasets be properly normalized according to the same set of criteria. In Section 5.1.3 we discuss how we adjust the flux for the g8b datasets and the g1c 2.897 GeV dataset that did not have proper flux measurements.

## 4.7 Summary

We have now derived the extended maximum likelihood function that will be used to perform all of the fits that we will perform in subsequent chapters. This method had been well known before for the case of unpolarized photon and target experiments, but has been expanded here to deal with polarized photon beams and polarized targets. This analysis will only make use of the polarized photon equations, but the others are useful to see how the formalism generalizes, and will be useful for future run periods from CLAS, such as the FROST (g9a and g9b) and HD-ICE (g14) run periods. Additionally, the spin density matrix for the vector meson has been derived and expanded beyond what was seen in [47] and elsewhere.



# Chapter 5

# Spin Density Matrix Elements

In this chapter, we will present the spin density matrix elements (SDMEs) that have been measured in the g1c and g8b datasets, including the first-ever measurements of elements of the  $\rho^1$ ,  $\rho^2$ , and  $\rho^3$  matrices. Before presenting these results, we will demonstrate the quality of the fits by comparing certain observables with previous measurements. We will compare the cross sections, as well as the three  $\rho^0$  SDMEs, with the results from another run period using CLAS at JLab, g11a, that had an unpolarized target and unpolarized photon beam. The g11a run period covered the  $\sqrt{s}$  range from threshold for the  $\omega$  at 1720 MeV up to 2840 MeV, more than the range of either the g1c or g8b run periods, allowing for comparisons at all energies. The  $\rho^0$  elements can be obtained from all experiments of this kind, regardless of the beam and target polarization. They can therefore act as an excellent means of comparison, and as a check of systematic errors between run periods.

## 5.1 The Mother of All Fits

The results in this chapter all come from a fit known as the *Mother of All Fits*, which consists of all s-channel waves with  $J \leq 11/2$ . The purpose of using so many waves is to provide a complete enough basis to allow the fit to fully describe the data. The results of this fit should NOT be taken as physics, only a very accurate description of the data.

The g8b dataset contains  $2.9 \times 10^6$  signal events in the energy range  $1720 \text{ MeV} \leq \sqrt{s} \leq 2210 \text{ MeV}$ , which is sufficient statistics to be binned in 10-MeV-wide bins. The g1c dataset contains  $6.5 \times 10^5$  signal events in the energy range  $1720 \text{ MeV} \leq \sqrt{s} \leq 2470 \text{ MeV}$ . For the purpose of extracting the spin density matrix elements, this is insufficient to be binned in 10-MeV-wide bins, so it is binned in 30-MeV-wide bins. Both widths are sufficiently narrow to ensure that the physics does not change significantly over the width of the bin.

### 5.1.1 Partial Wave Amplitudes

The partial wave amplitudes that are used in this analysis are calculated following the formalism set up in Mike Williams thesis [1], which covers both resonant and non-resonant amplitudes. This analysis has not changed anything with respect to the generation of the amplitudes.

The amplitudes generated in [1] include both the production and decay of a  $J^P$  state. Each amplitude for a given  $J^P$  state can be characterized by six variables: the production multipole (MP); the orbital angular momentum of the  $p\omega$  system (L); the spin of the  $p\omega$  system (S); and the spin projections along the beam direction of the incident photon, target proton, and recoil proton ( $m_\gamma$ ,  $m_i$  and  $m_f$  respectively). Thus, we can write the amplitudes as  $A_{MP,L,S,m_\gamma,m_i,m_f}$ . The amplitudes include the decay of the  $\omega \rightarrow \pi^+ \pi^- \pi^0$ .

Each  $\sqrt{s}$  bin will be fit independently. To perform our fits, we need to provide enough freedom to fully describe the data and thus we write the amplitudes in each  $\sqrt{s}$  bin as

$$A_{\gamma p \rightarrow J^P \rightarrow p\omega \rightarrow p\pi^+\pi^-\pi^0} = f_{MP}(\theta_{JP}) r_{J^P L S} e^{i\phi_{JP}} \omega_\mu(p_{\pi^+}, p_{\pi^-}, p_{\pi^0}) A_{MP, L, S, m_\gamma, m_i, m_f}^\mu, \quad (5.1)$$

where the parameters for the fit are  $r_{J^P L S}$ , corresponding to the decay of the  $J^P$  state into a  $p\omega$  state with quantum numbers L and S,  $\theta_{JP}$ , the multipole production angle, and  $\phi_{JP}$ , the phase. Each of these parameters is free to vary with no limits and are real-valued.  $\theta_{JP}$  and  $\phi_{JP}$  are angles, so the lack of bounds does not affect them. We also define the function

$$f_{MP}(\theta_{JP}) = \left\{ \begin{array}{ll} \cos \theta_{JP}, & \text{for electric multipoles} \\ \sin \theta_{JP}, & \text{for magnetic multipoles} \end{array} \right\}, \quad (5.2)$$

which automatically normalizes the contribution from each multipole. The  $\omega_\mu(p_{\pi^+}, p_{\pi^-}, p_{\pi^0})$  term handles the direct decay of the  $\omega \rightarrow \pi^+\pi^-\pi^0$ .

### 5.1.2 Maximum Likelihood Fit

For the mother fits, we will use the maximum likelihood function method, which was detailed in Chapter 4. In that method, we attempt to minimize the negative log likelihood

$$-\ln \mathcal{L} = - \sum_i^n Q_i \ln |\mathcal{M}(\vec{x}, X_i)|^2 + \frac{\mathcal{S}(s)}{N_{raw}} \sum_i^{N_{acc}} |\mathcal{M}(\vec{x}, X_i)|^2 + const. \quad (5.3)$$

Since the datasets to be analyzed here, g1c and g8b, had polarized photons and unpolarized targets, we will use the Lorentz invariant transition amplitude

$$|\mathcal{M}|^2 = \frac{1}{4} \sum_{m_i, m_f} ( (1 + \eta_C^\gamma) |A_{+, m_i, m_f}|^2 + (1 - \eta_C^\gamma) |A_{-, m_i, m_f}|^2 - \eta_L^\gamma (e^{-2i\alpha} A_{+, m_i, m_f} A_{-, m_i, m_f}^\dagger + e^{2i\alpha} A_{-, m_i, m_f} A_{+, m_i, m_f}^\dagger)), \quad (5.4)$$

which was originally written in (4.58). The amplitudes above are indexed only by the three spin projections and are given by (4.4).

Recall, from Section 3.9, that, for the circularly polarized g1c data, the polarization is calculated using (3.12), depending only on the electron beam energy, the photon energy and the polarization of the beam. Thus, the polarization of the Monte Carlo can be calculated for each event; the helicity is randomly assigned. For the linearly polarized g8b data, the polarization is calculated using (3.14), which cannot be calculated for the Monte Carlo events, and so each Monte Carlo event in a given  $\sqrt{s}$  bin is assigned the average polarization of all of the data events in that bin.

Each  $\sqrt{s}$  bin contains between one and four datasets, depending on the energy range covered by each dataset. The log likelihoods are added together for each of the datasets as described in Section 4.6. Each  $\sqrt{s}$  bin is then fit separately at least five different times. Each of these iterations starts the fit with random values for each parameter, and then proceeds to minimize the value of the log likelihood. The reason for these iterations is to make sure that the overall minimum is found, and not a false minimum. Ideally, if there is one true minimum, then all five random starting points would lead to this one minimum. However, there may be local minima that will cause a fit to stop before reaching the true minimum. By using several different, and random, starting points we hope to be able to find the overall minimum. Thus, after performing all iterations of the fit we choose the parameters from the iteration with the best likelihood to extract our measurements.

### 5.1.3 Differential Cross Sections

There are several quality checks in place to ensure that the results of the fit are correct and reliable. One benefit of analyzing data from CLAS is that there are many other run periods that have been run using the same equipment under similar conditions. For our purposes, the g11a run period from 2004 is the best comparison. This run period was run with an unpolarized photon beam on an unpolarized target and was analyzed for the  $\omega$  by Mike Williams [1], using the same techniques and software as the present analysis. It contained  $\sim 10.1$  million signal events covering the energy range  $1720 \text{ MeV} \leq \sqrt{s} \leq 2840 \text{ MeV}$ , which completely covers the energy range of both g1c and g8b, allowing for comparison at all energies. In the next section, we will show comparisons for the  $\rho^0$  spin density matrix elements between the g11a dataset and each of the datasets under analysis here. In this section, we will show the comparison between those datasets for the differential cross sections.

The g8b run has been taken without *gFlux* measurements, which means that we were unable to measure exact flux values in each  $\sqrt{s}$  bin. Additionally, the 2.897 GeV data from the g1c dataset did not take reliable flux measurements. For the purposes of obtaining the spin density matrix elements, the absolute flux is not required, but for the cross sections it is necessary. Since we did not have measurements, we were required to come up with a different way of calculating the fluxes for these datasets. The following method was used to determine the flux. We start by setting an arbitrary value for the flux in each bin. Then, we perform our fits and calculate the cross sections from these fits. We can then compare the values of the cross section at a certain number of values of  $\cos\theta_{CM}^\omega$  to the values reported from g11a. We then scale the flux by the ratio of the g11a values to the g8b or g1c values, averaged over that bin. Using these adjusted flux values we then redo the fits and recalculate the cross sections. This method does not affect the shape of the cross sections, only the overall scale. Each g8b dataset and the single g1c dataset were treated separately and the cross sections are calculated for each dataset separately, even though the mother fit may contain several datasets in a single  $\sqrt{s}$  bin.

Figure 5.1 shows the comparison between g11a and the 1.5 GeV PARA dataset from g8b. The agreement is excellent everywhere. The other g8b datasets show similarly good agreement. The results for the g1c 2.897 GeV dataset can be seen in Figure 5.2 and show similarly good agreement, with the exception of the first bin. The agreement over the entire range in all datasets is a good indication that our fits are reliable, however we also want to check that the results from the  $\rho^0$  spin density matrix match what we see in g11a as well. The results of that check can be seen in the next section.

## 5.2 Spin Density Matrix Elements

The method of calculating the SDMEs can be seen in Section 4.3.3. The results for g1c and g8b can be seen on the following pages. For the  $\rho^0$  elements, we can compare the results to those from g11a; for the other elements, these are the first measurements produced, so the points of comparison will be the values calculated from the same data using the Schilling Method, explained in Section 4.3.5, and shown in Section 5.3.

### 5.2.1 Errors

The errors on the SDMEs cannot be calculated in a standard way, as the amplitudes and parameters that they are calculated from do not have standard errors. Previously [1, 48, 49], the errors have been calculated on a point-by-point basis by computing the standard deviation of a given point in  $\cos\theta_{CM}^\omega$  in the current  $\sqrt{s}$  bin and the energy bins on either side of it. However, a statistically-more-correct method has been used here to estimate the errors on these points, the so-called Bootstrap Method [50].

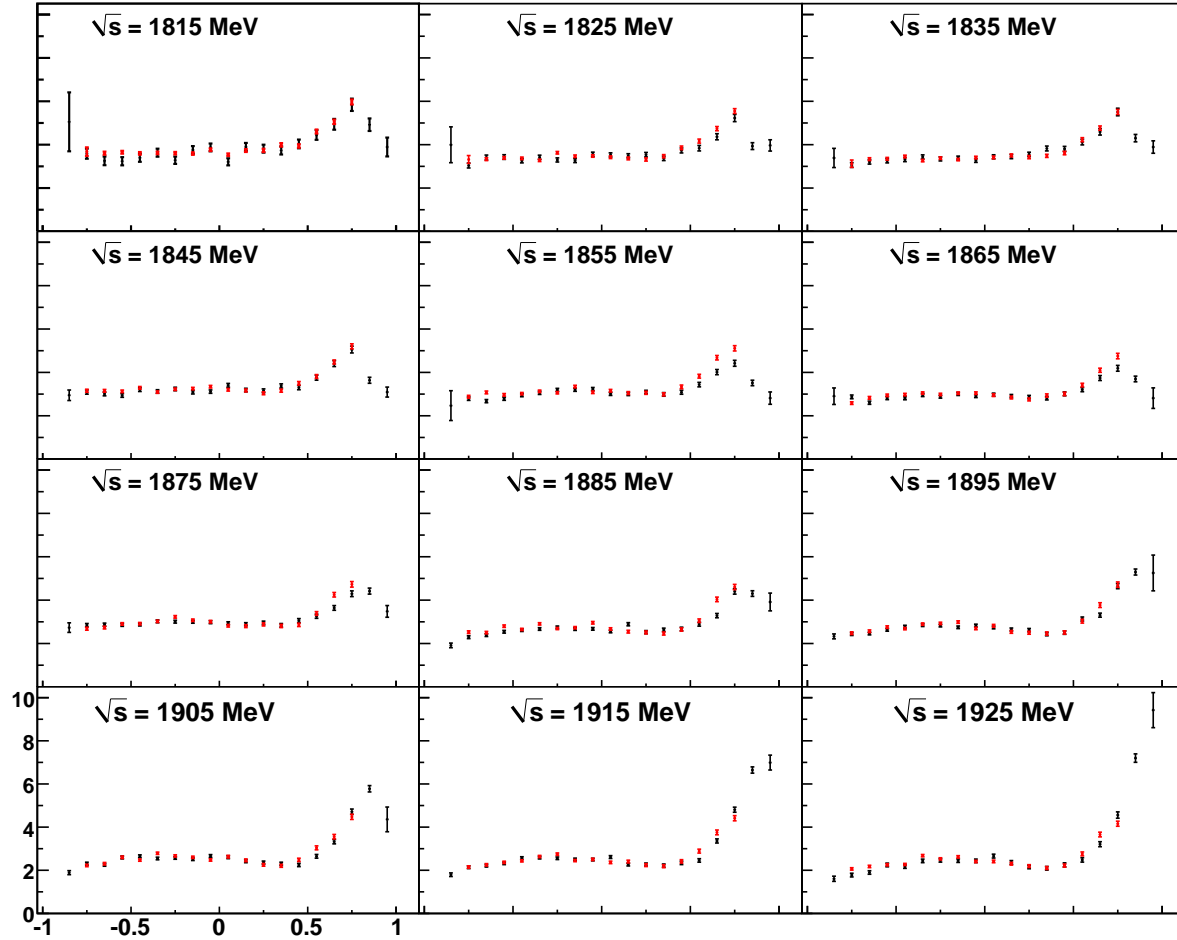


Figure 5.1:  $\frac{d\sigma}{dcos(\theta_{CM}^\omega)} (\mu b)$  vs  $\cos \theta_{CM}^\omega$  in bins of  $\sqrt{s}$ . The results from the PARA 1.5 GeV dataset from g8b (black) are shown in comparison to the g11a (red) values. The g8b run period did not record flux values and so an approximate flux was calculated using a normalization factor to minimize the difference with the g11a data. Agreement is excellent in all bins.

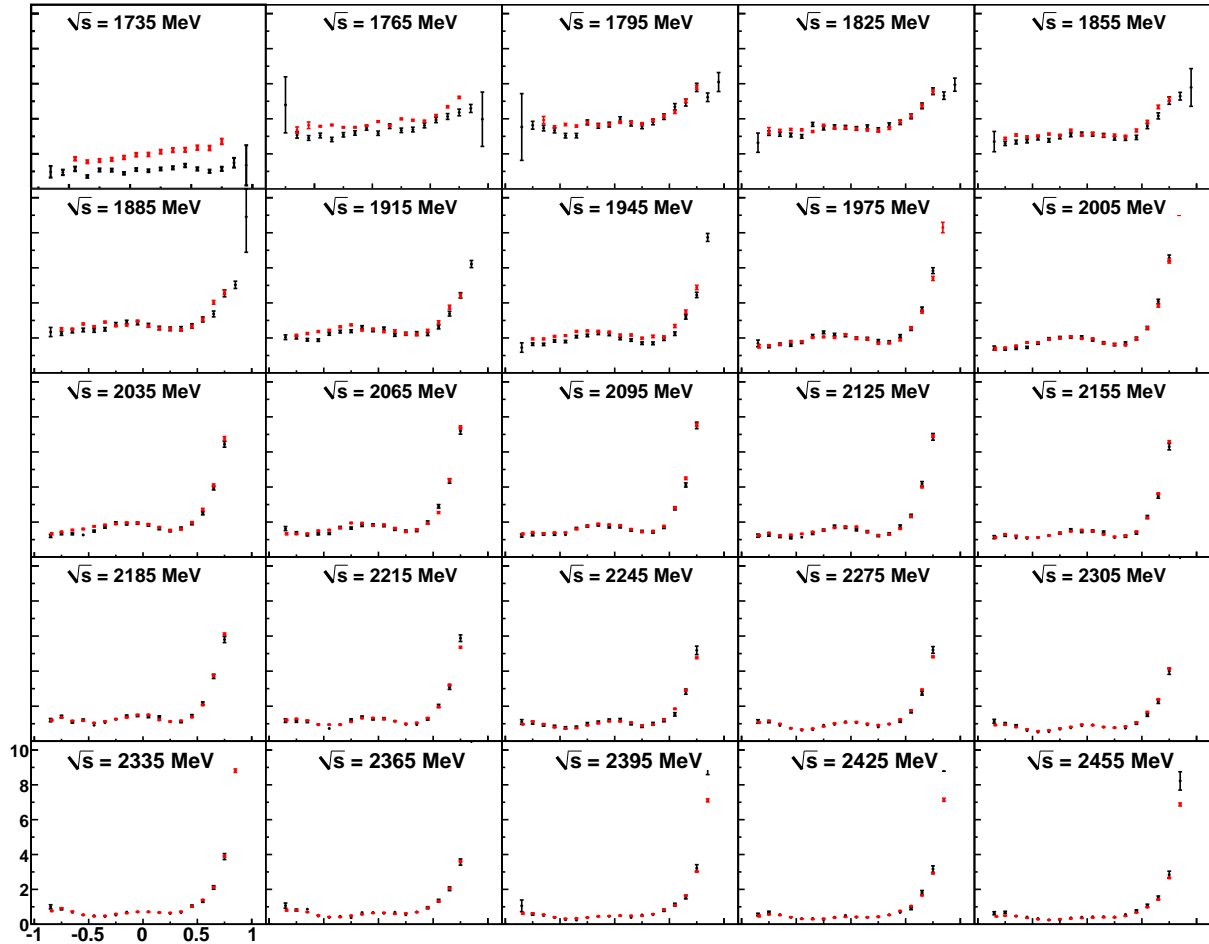


Figure 5.2:  $\frac{d\sigma}{d \cos(\theta_{CM}^\omega)} (\mu b)$  vs  $\cos \theta_{CM}^\omega$  in bins of  $\sqrt{s}$ . The results from the 2.445 GeV dataset from g1c (black) are shown in comparison to the g11a (red) values. Other than the first energy bin, agreement is excellent.

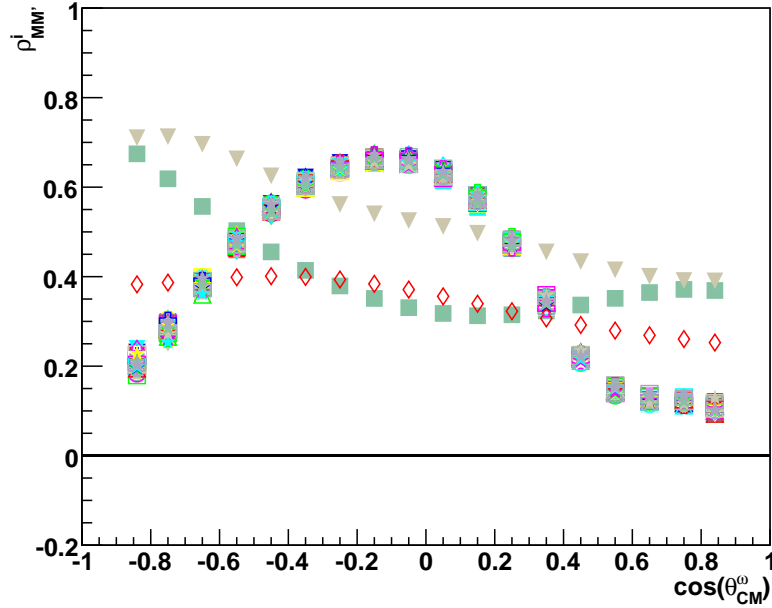


Figure 5.3:  $\rho_{00}^0$  element vs  $\cos \theta_{CM}^\omega$  for all 100 bootstrap iterations. Almost all of the fits lie on top of each other. Three *bad* fits can be seen; they are removed before calculating the errors.

The Bootstrap Method consists of performing our fits in each bin  $N_{boot}$  times, using a *sampled with replacement* version of our data. We describe that method as follows. Consider a  $\sqrt{s}$  bin consisting of  $N$  events. From those  $N$  events, we construct a bootstrap copy by randomly selecting  $N$  events from our dataset, allowing some events to be chosen more than one time and some events to be omitted. In practice, this is accomplished by using a random number generator that picks a number between 0 and  $N-1$ , a total of  $N$  times. This bootstrap copy will then be fit in the same way as the normal dataset. We then construct  $N_{boot}$  bootstrap copies, and run fits on each of them. We can calculate the SDMEs for each of these bootstrap fits according to (4.38). Then, for each  $\cos \theta_{CM}^\omega$  point, the error is estimated to be the standard deviation of the bootstrap values for that point.

We have chosen  $N_{boot} = 100$ . For each bootstrap copy, at least two iterations were run to minimize the chance that a fit would fail to converge. Since each bin requires 100 fits, it is very computationally expensive, and so only two iterations could be run. Thus, it is still possible that a fit could fail to converge in both iterations. In that case, that bootstrap copy is thrown out, and not used for calculating the error bars. It is generally not possible to tell if a fit has failed from the values of the parameters, or the final log likelihood value. However, it is readily apparent when looking at the spin density matrix elements, particularly the  $\rho_{00}^0$  element. Figure 5.3 shows the  $\rho_{00}^0$  element for all 100 bootstrap copies for a single  $\sqrt{s}$  bin. Each copy is given its own combination of shape and color to differentiate them. The vast majority of the results lie directly on top of each other and are indistinguishable. However, there are three, clearly visible, *bad* fits that would be removed before calculating the error bars for each SDME in this bin. As a result of this, most bins have between 95 and 100 bootstrap copies used in calculating the error bars; this is more than sufficient to calculate the error bars consistently.

### 5.2.2 $\rho^0$ Elements in g1c and g8b

The  $\rho^0$  elements are calculated using the amplitude-based expression

$$\rho_{m_V m_{V'}}^0 = \frac{1}{2N} \sum_{m_\gamma m_i m_f} \mathcal{A}_{m_\gamma, m_i, m_f, m_V} * \mathcal{A}_{m_\gamma, m_i, m_f, m_{V'}}, \quad (5.5)$$

note that we are using amplitudes that do not include the decay of the  $\omega \rightarrow \pi^+ \pi^- \pi^0$ . These unpolarized elements can be obtained from any  $\omega$  photoproduction experiment. There are three elements that can be measured:  $\rho_{00}^0$ ;  $\text{Re}(\rho_{10}^0)$ ; and  $\rho_{1-1}^0$ . On the following pages we present the  $\rho^0$  elements from g1c and then g8b, together with the measurements from g11a. We will present a brief discussion of the agreement between the two datasets after each set of plots.

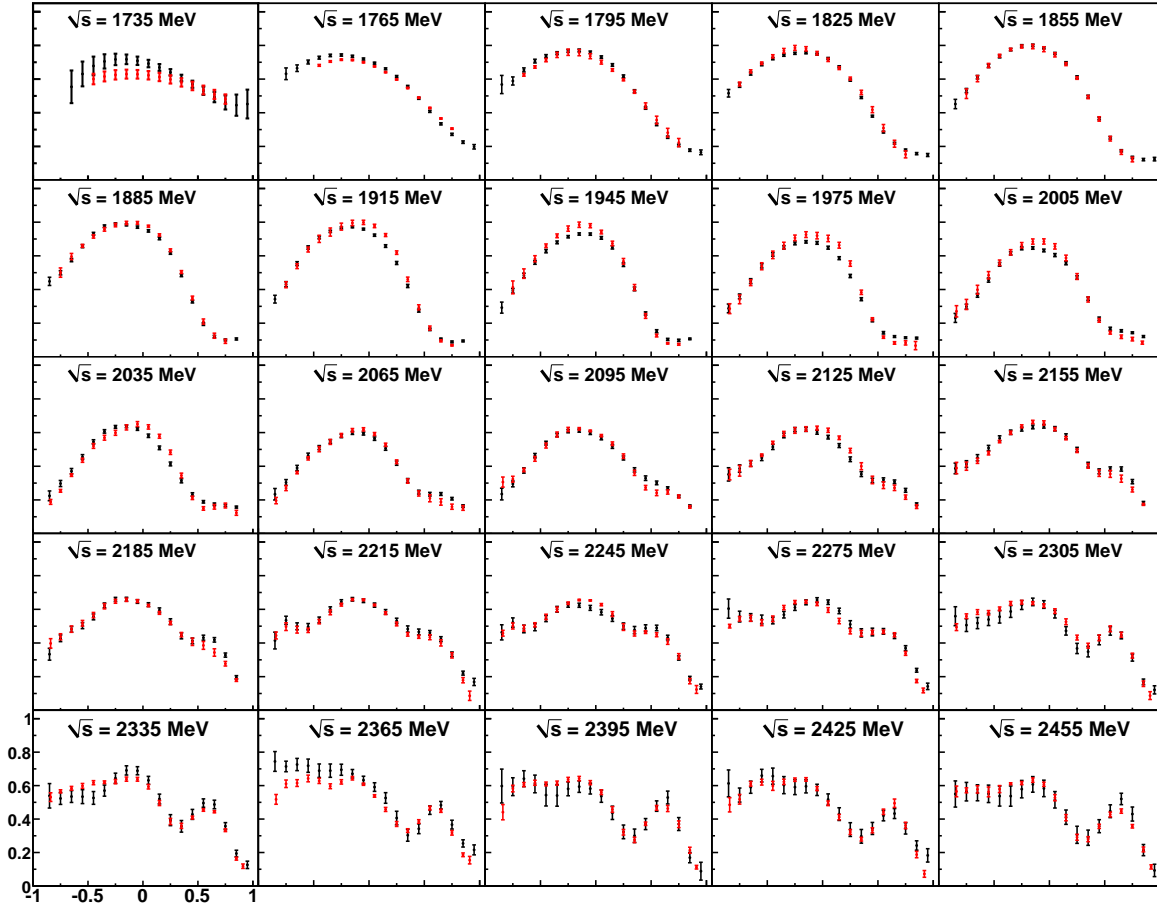


Figure 5.4:  $\rho_{00}^0$  element vs  $\cos \theta_{CM}^\omega$  in bins of  $\sqrt{s}$ . The results from g1c (black) are shown in comparison to the g11a (red) values. The errors for g1c are as calculated in Section 5.2.1.

The  $\rho_{00}^0$  element is the largest element and also has the smallest fractional error bars. As such, it is particularly well-suited to determining the agreement between the two datasets and estimating systematic errors. Agreement overall is excellent. In many cases, the two sets of points are indistinguishable from each other, for instance the 1855 MeV bin. In some bins, particularly from 1915-2035 MeV, there is a small difference between the datasets, particularly near  $\cos \theta_{CM}^\omega = 0$ .

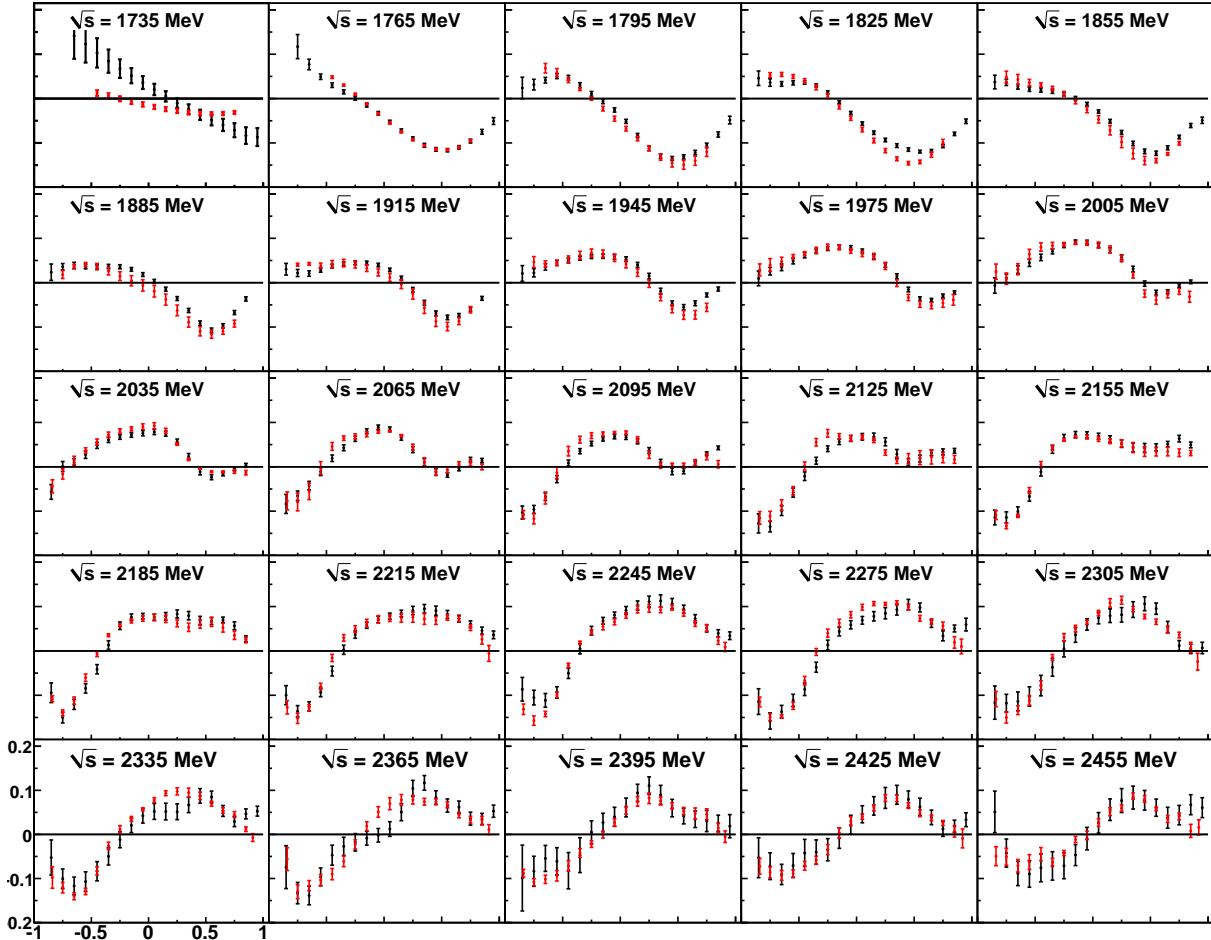


Figure 5.5:  $\text{Re}(\rho_{10}^0)$  element vs  $\cos \theta_{CM}^\omega$  in bins of  $\sqrt{s}$ . The results from g1c (black) are shown in comparison to the g11a (red) values. The errors for g1c are as calculated in Section 5.2.1.

The  $\rho_{10}^0$  element contains both real and imaginary parts, however it is only possible to measure the real part in these experiments, it is shown in Figure 5.5. These values are smaller than the  $\rho_{00}^0$  elements, and the error bars tend to be larger as well. This element also shows more structure, with multiple changes of direction as it evolves in  $\cos \theta_{CM}^\omega$ . Again, the overall agreement is excellent. Almost all differences between the datasets are within the error bars. There are a few bins, the 1825 MeV and 2365 MeV bins for example, where there is a significant difference between the two datasets, again it is mainly near  $\cos \theta_{CM}^\omega = 0$ . The 1735 MeV bin shows particularly poor agreement. The near-threshold bins have low statistics and the background subtraction is the most difficult, which could explain the poor fit.

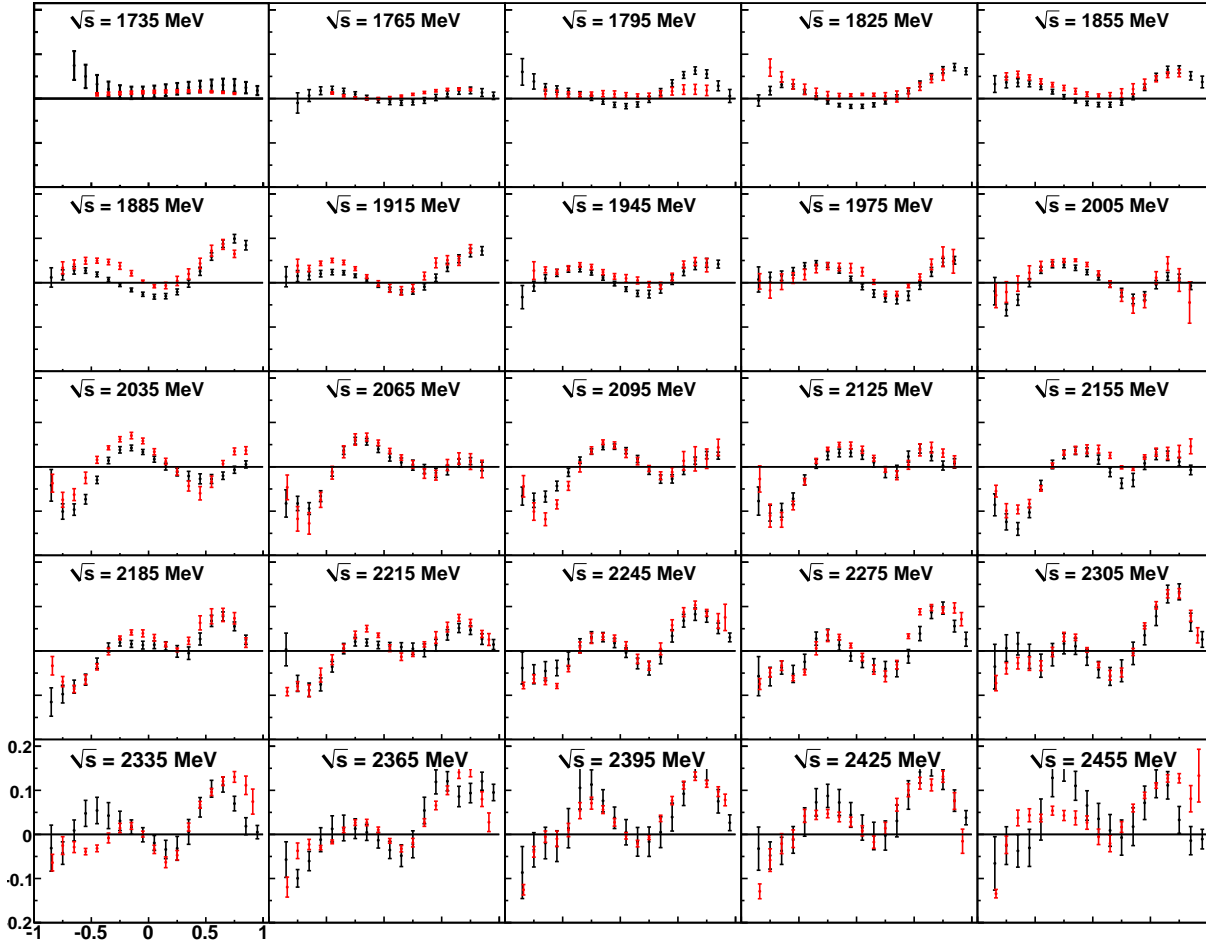


Figure 5.6:  $\rho_{1-1}^0$  element vs  $\cos \theta_{CM}^\omega$  in bins of  $\sqrt{s}$ . The results from g1c (black) are shown in comparison to the g11a (red) values. The errors for g1c are as calculated in Section 5.2.1.

The  $\rho_{1-1}^0$  element is purely real. The imaginary component must be 0 due to symmetries mentioned in Section 4.3.4. It is also a small element that shows multiple changes of direction, as seen in Figure 5.6. This element has the worst agreement between the two datasets among the three  $\rho^0$  elements, however it is still quite good. The shape in each bin is the same between datasets. In a few bins, 1885 MeV and 2035 MeV, the g1c result is systematically lower than the g11 result across the entire range. The 2335 MeV and 2455 MeV bins also show significant discrepancies. Despite these differences, the agreement everywhere else is very good.

### Summary

Having looked at all three  $\rho^0$  elements, the agreement between the g1c dataset and g11a is excellent, apart from a few anomalies. This agreement is important because the  $\rho^0$  elements should match, regardless of the polarization of the photon beam. This indicates that the fits are reliable, and that the newly measured  $\rho^3$  elements are similarly robust.

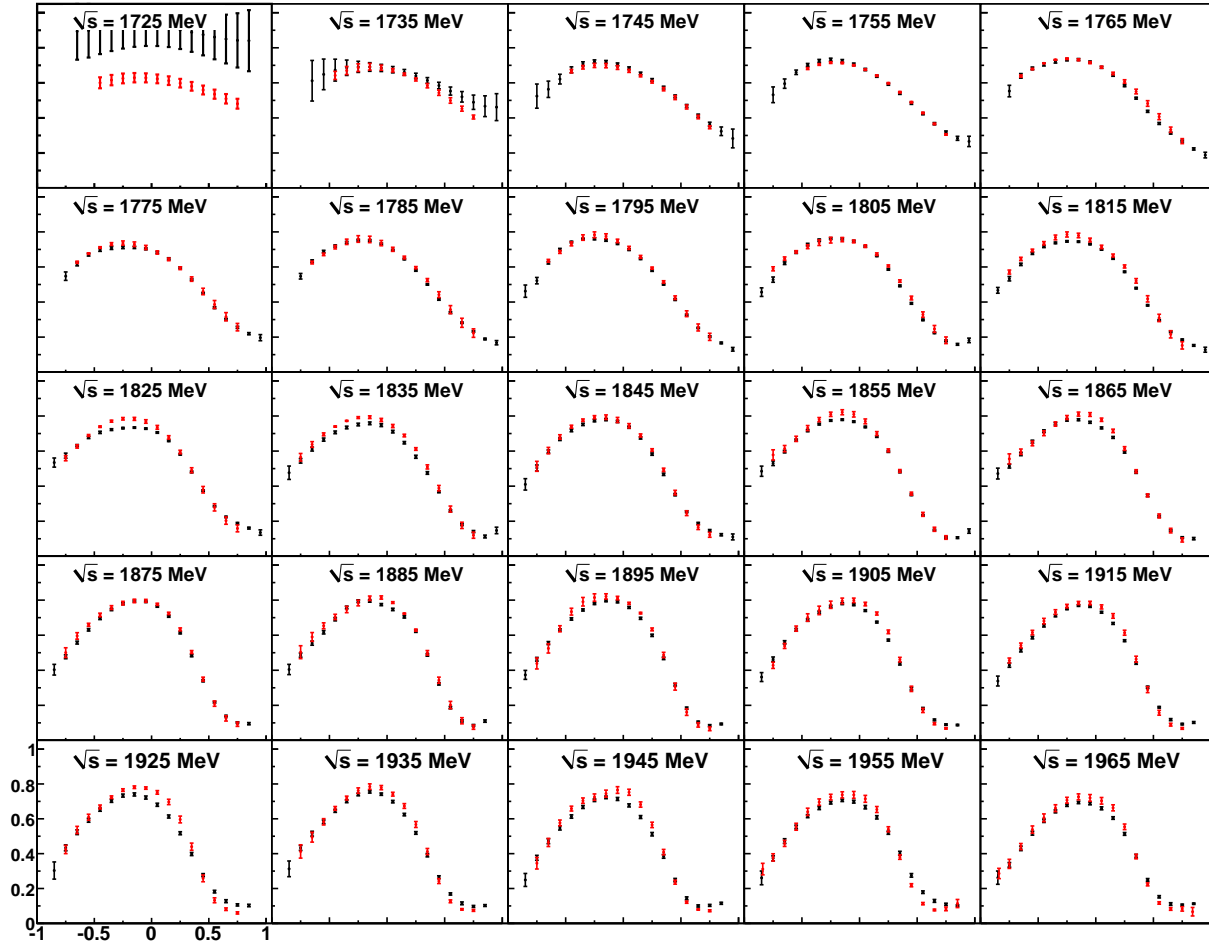


Figure 5.7:  $\rho_{00}^0$  element vs  $\cos \theta_{CM}^\omega$  in bins of  $\sqrt{s}$ , up to 1965 MeV. The results from g8b (black) are shown in comparison to the g11a (red) values. The errors for g8b are as calculated in Section 5.2.1. Agreement is generally excellent, with the exception of the first bin at 1725 MeV, where poor statistics lead to a poor fit result.

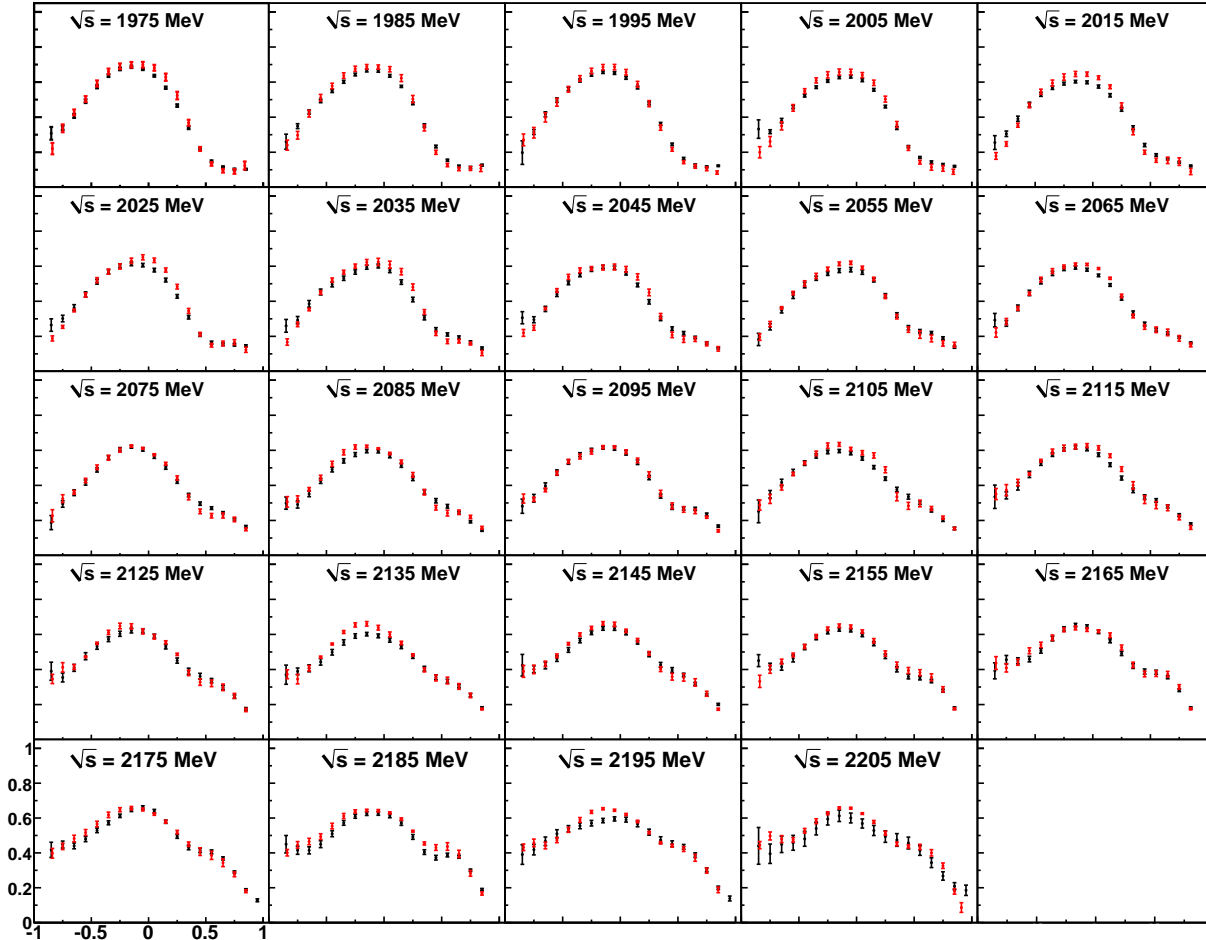


Figure 5.8:  $\rho_{00}^0$  element vs  $\cos \theta_{CM}^\omega$  in bins of  $\sqrt{s}$ , beyond 1965 MeV. The results from g8b (black) are shown in comparison to the g11a (red) values. The errors for g8b are as calculated in Section 5.2.1.

The  $\rho_{00}^0$  element for g8b, in Figures 5.7 and 5.8, shows very good agreement with the g11a results as well. With the exception of the first bin at 1725 MeV, the shape and scale of the data are in good agreement. The poor fit in the first bin is likely due to statistics and the difficulty of separating the signal and background. The large error bars attest to the fact that the fit is poor in this bin. There is a very slight systematic offset between the datasets near  $\cos \theta_{CM}^\omega = 0$  in some bins however, see the 1825 MeV bin for a particularly egregious example. It is unclear what has caused this offset. The  $\rho_{00}^0$  element is particularly sensitive to issues relating to acceptance, which could be causing the problem. The problem with the time-of-flight paddles, detailed in Appendix A, caused a much more pronounced version of this discrepancy. It cannot simply be ascribed to a systematic error, as in some bins, see the 1785 MeV and 1875 MeV bins, the agreement is near perfect. Figure B.1, in Appendix B, shows g1c, g8b and g11a on the same plot. Comparing the results for g1c and g8b, the agreement is much better towards these central angles, note in particular the 1825 MeV bin, so perhaps the g11a result is too high, and these new values should be taken as the standard.

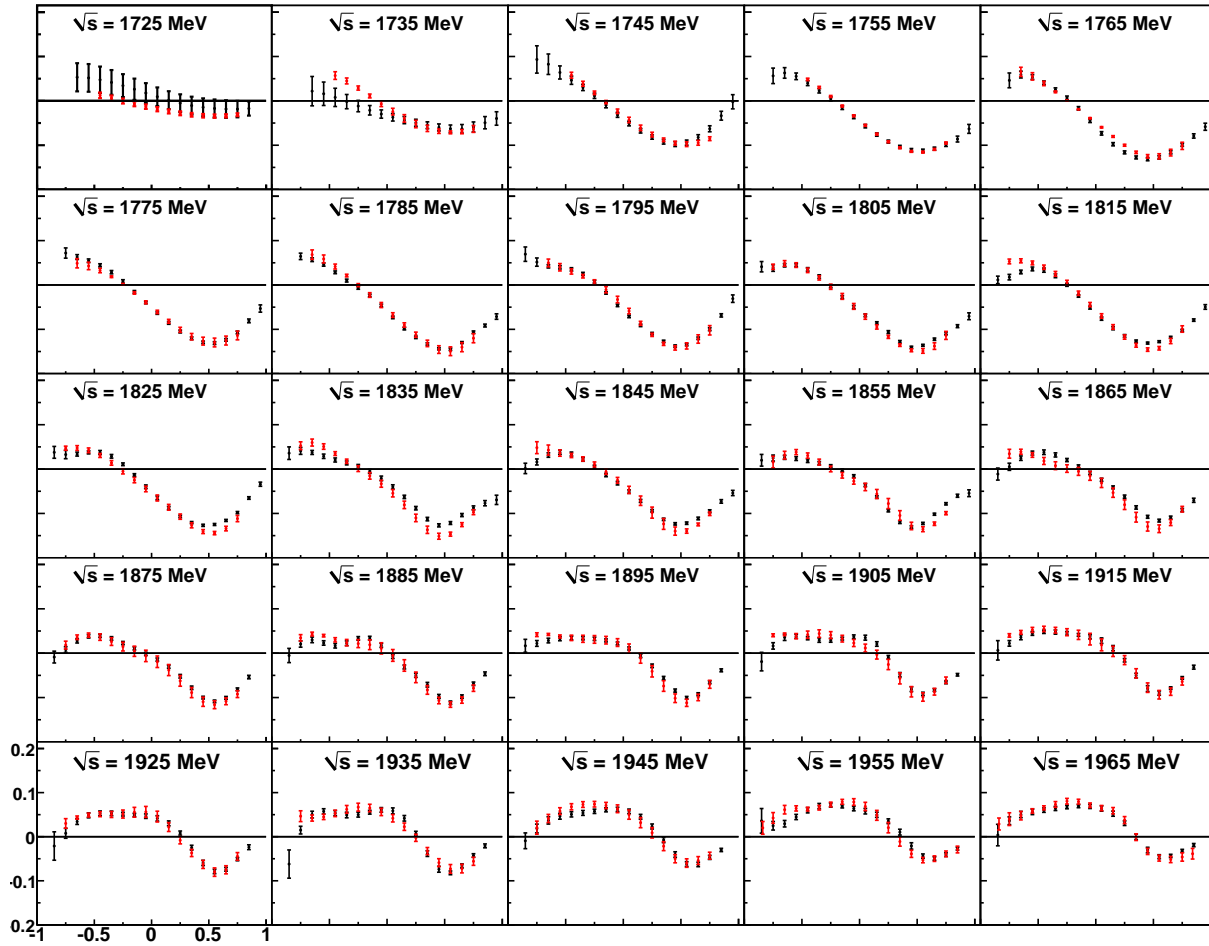


Figure 5.9:  $\text{Re}(\rho_{10}^0)$  element vs  $\cos \theta_{CM}^\omega$  in bins of  $\sqrt{s}$ , up to 1965 MeV. The results from g8b (black) are shown in comparison to the g11a (red) values. The errors for g8b are as calculated in Section 5.2.1.

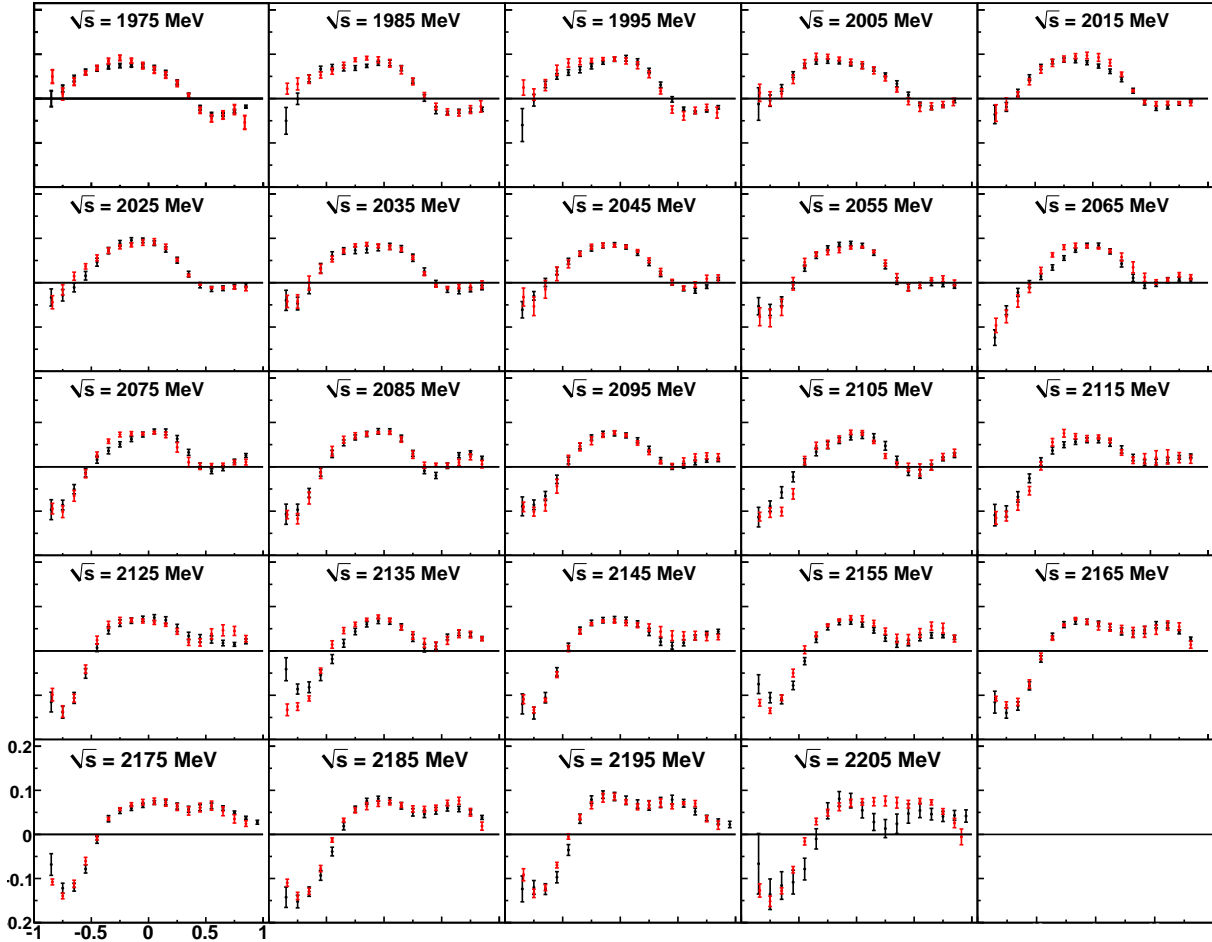


Figure 5.10:  $\text{Re}(\rho_{10}^0)$  element vs  $\cos \theta_{CM}^\omega$  in bins of  $\sqrt{s}$ , beyond 1965 MeV. The results from g8b (black) are shown in comparison to the g11a (red) values. The errors for g8b are as calculated in Section 5.2.1.

The  $\text{Re}(\rho_{10}^0)$  element for g8b, in Figures 5.9 and 5.10, shows near-perfect agreement over the entire range in both  $\cos \theta_{CM}^\omega$  and  $\sqrt{s}$ . There is no systematic offset anywhere and each bin has excellent agreement.

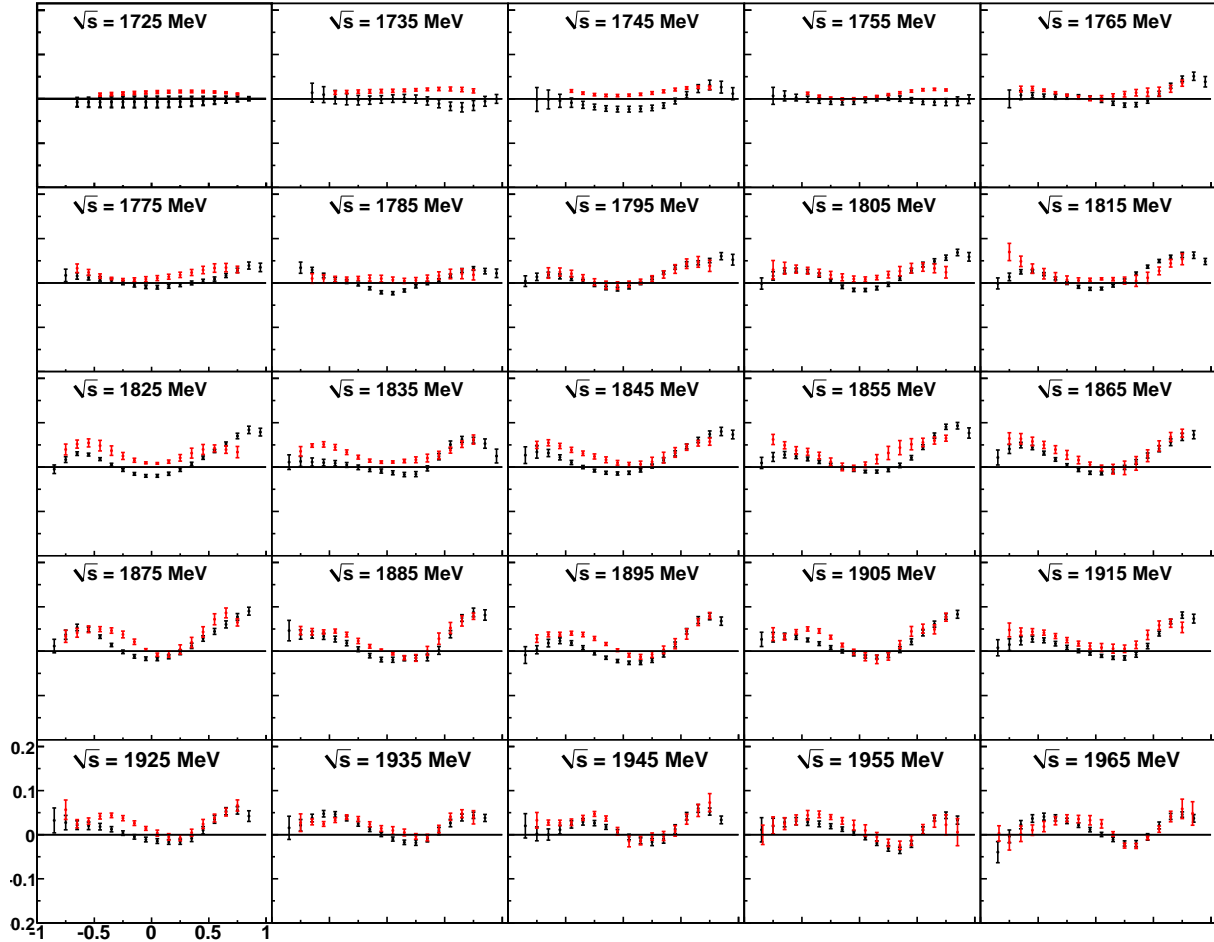


Figure 5.11:  $\rho_{1-1}^0$  element vs  $\cos \theta_{CM}^\omega$  in bins of  $\sqrt{s}$ , up to 1965 MeV. The results from g8b (black) are shown in comparison to the g11a (red) values. The errors for g8b are as calculated in Section 5.2.1.

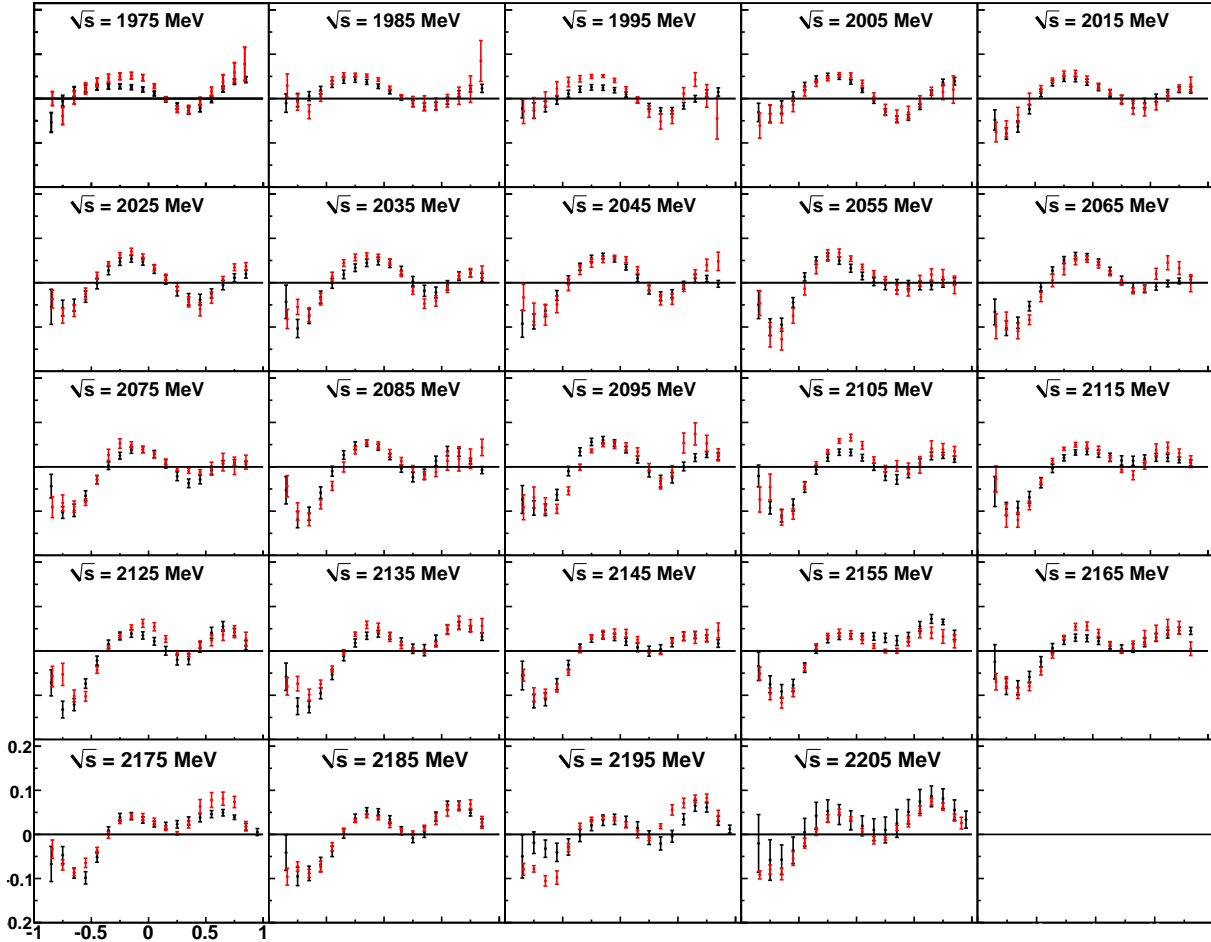


Figure 5.12:  $\rho_{1-1}^0$  element vs  $\cos \theta_{CM}^\omega$  in bins of  $\sqrt{s}$ , beyond 1965 MeV. The results from g8b (black) are shown in comparison to the g11a (red) values. The errors for g8b are as calculated in Section 5.2.1.

Similar to the results in g1c, the  $\rho_{1-1}^0$  element in g8b, seen in Figures 5.11 and 5.12, has the worst agreement between the two datasets. In some bins, the 1825 MeV bin is a good example, the g8b result is well below that of g11a. However, again note that similar behavior was seen in g1c. Figure B.2 in Appendix B shows this element in g1c, g8b and g11a on the same plot. The agreement between g8b and g1c in that bin is excellent, as it is across the entire range. Once we get above 1935 MeV, there are few discrepancies and no major offsets between g8b and g11a.

### Summary

As with g1c, we have seen very impressive agreement between the g8b dataset and the g11a dataset. This again indicates that the fits are robust and reliable. The ability to reproduce the unpolarized results so reliably from our new polarized fitting equations indicates that the new equations are correct and we can be confident in the results for the newly measured SDMEs.

### 5.2.3 $\rho^1$ Elements in g8b

The  $\rho^1$  elements are calculated using

$$\rho_{m_V m_{V'}}^1 = \frac{1}{2N} \sum_{m_\gamma m_i m_f} \mathcal{A}_{m_\gamma, m_i, m_f, m_V} * \mathcal{A}_{m_\gamma, m_i, m_f, m_{V'}}^\dagger. \quad (5.6)$$

Note that the sign of  $m_\gamma$  changes in the two amplitudes above. This is why linear polarization is required to measure these elements. There are four measurable elements:  $\rho_{00}^1$ ;  $\text{Re}(\rho_{10}^1)$ ;  $\rho_{1-1}^1$ ; and  $\rho_{11}^1$ . We will present each on the following pages, along with a brief discussion of the results. We will note, in particular, the extrema, or changes in direction, which persist over several energy bins. These extrema contribute strongly to the shape and will be important when determining agreement with our partial wave analysis fits in the next chapter. Particular interest is given to extrema at  $\cos \theta_{CM}^\omega$  values not seen in the  $\rho^0$  elements.

Since the  $\rho^1$  elements have never been measured before, there is nothing to compare them to. However, in some cases, they can be compared or contrasted to elements from one of the other matrices.

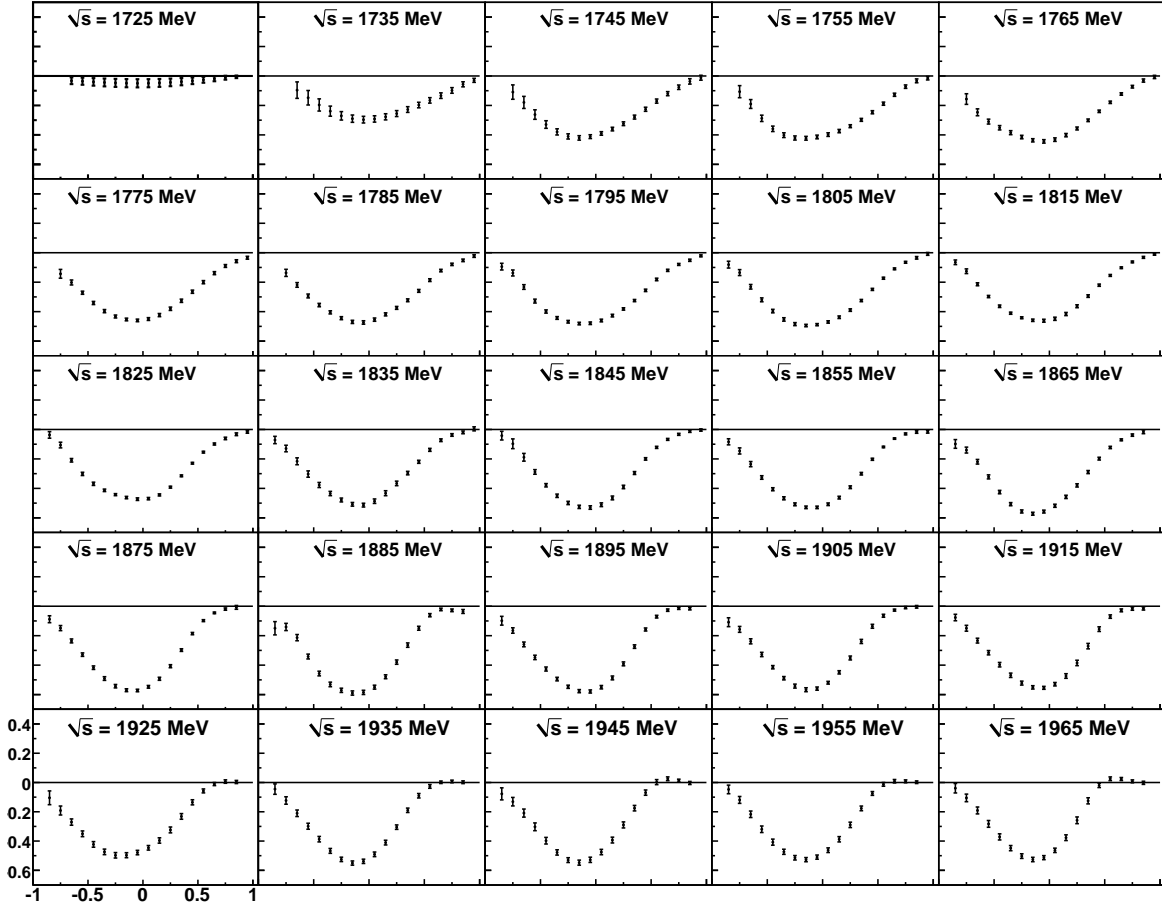


Figure 5.13:  $\rho_{00}^1$  element vs  $\cos \theta_{CM}^\omega$  in bins of  $\sqrt{s}$ , up to 1965 MeV, for g8b. The errors are as calculated in Section 5.2.1. Note the striking difference between the first two  $\sqrt{s}$  bins; this is most likely due to statistics, as we see similar differences between these bins in the  $\rho^0$  elements as well.

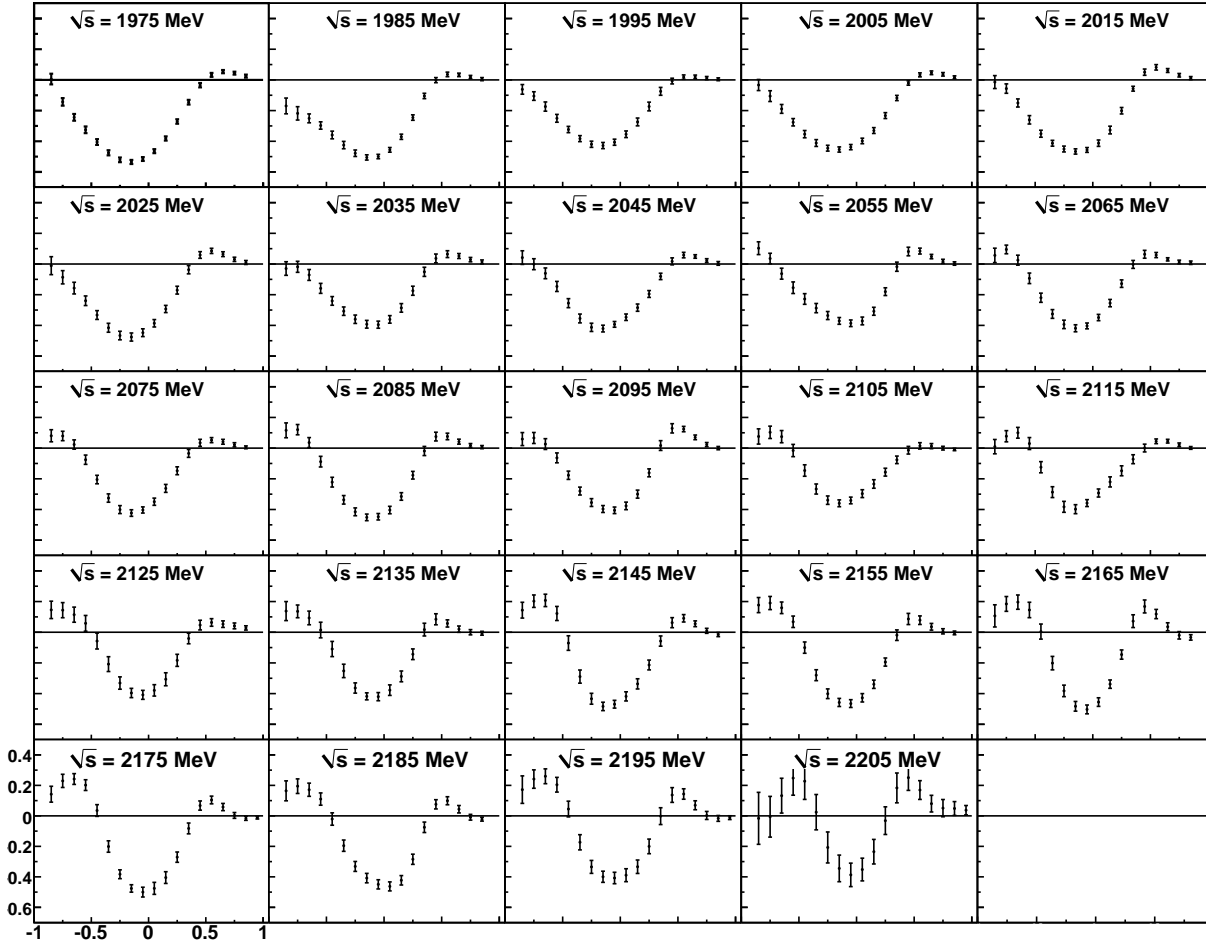


Figure 5.14:  $\rho_{00}^1$  element vs  $\cos \theta_{CM}^\omega$  in bins of  $\sqrt{s}$ , beyond 1965 MeV, for g8b. The errors are as calculated in Section 5.2.1.

The  $\rho_{00}^1$  element is similar to the  $\rho_{00}^0$  element, in that it is the largest element in its matrix. Although, in this case, it is predominantly negative. Across the entire range in  $\sqrt{s}$ , the  $\rho_{00}^1$  element mirrors the  $\rho_{00}^0$  element as a function of  $\cos \theta_{CM}^\omega$ , see Figure B.3 in Appendix B for a direct comparison. When  $\rho_{00}^0$  rises,  $\rho_{00}^1$  falls, and vice versa. Their scale is somewhat different however, and  $\rho_{00}^1$  is mostly negative but at higher energies becomes positive at forward and backward angles, while  $\rho_{00}^0$  is strictly positive. At higher energies, the change in direction is more pronounced in  $\rho_{00}^1$  than in  $\rho_{00}^0$ , however its absolute value never exceeds the value of  $\rho_{00}^0$ . There is a prominent minimum near  $\cos \theta_{CM}^\omega = 0$  in all bins. A forward maximum, near  $\cos \theta_{CM}^\omega = 0.5$  is noticeable from 1885-2205 MeV. A maximum is also present in the backwards angles near  $\cos \theta_{CM}^\omega = -0.7$ , starting from 2065 MeV and lasting to the highest energies.

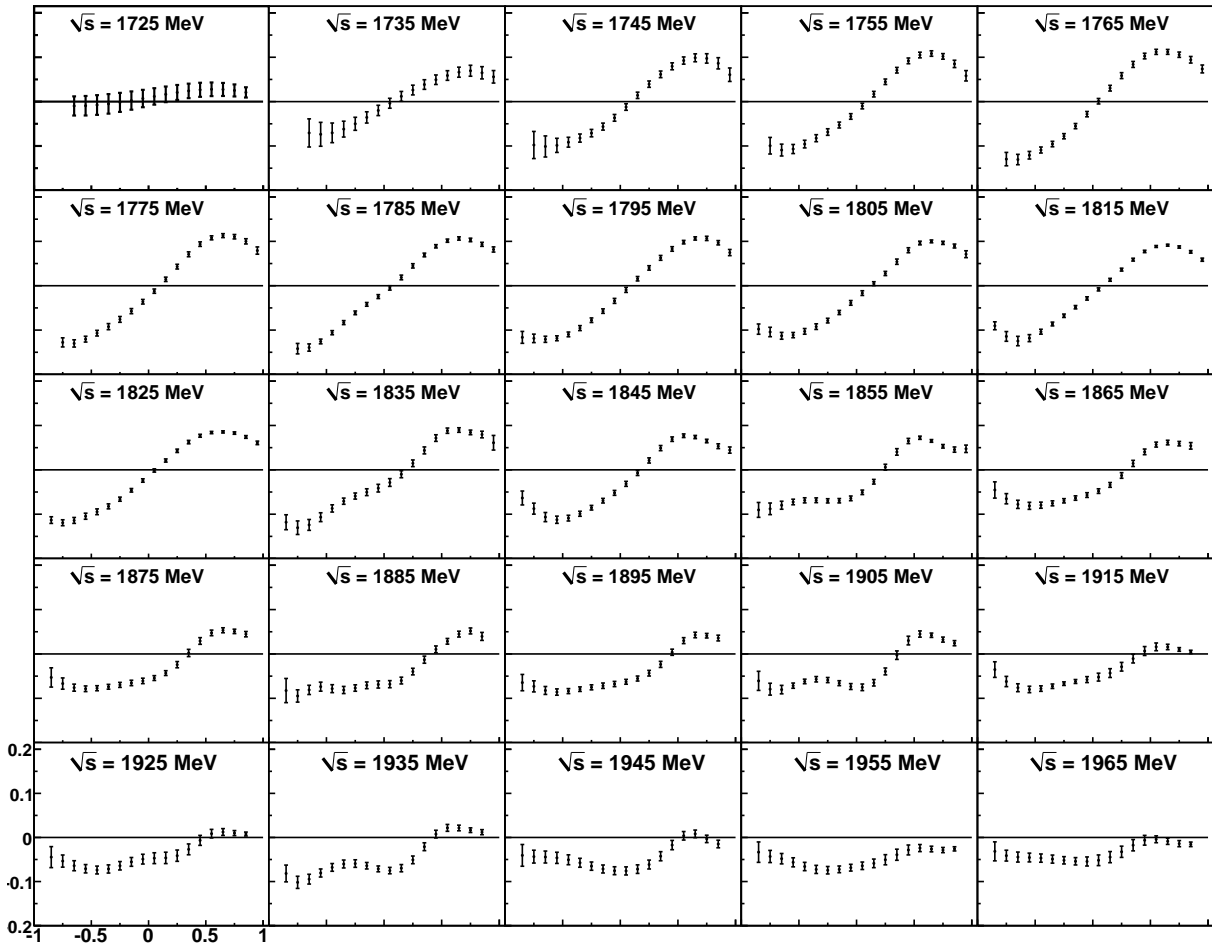


Figure 5.15:  $\text{Re}(\rho_{10}^1)$  element vs  $\cos \theta_{CM}$  in bins of  $\sqrt{s}$ , up to 1965 MeV, for g8b. The errors are as calculated in Section 5.2.1. Notice again the striking difference between the first two  $\sqrt{s}$  bins.

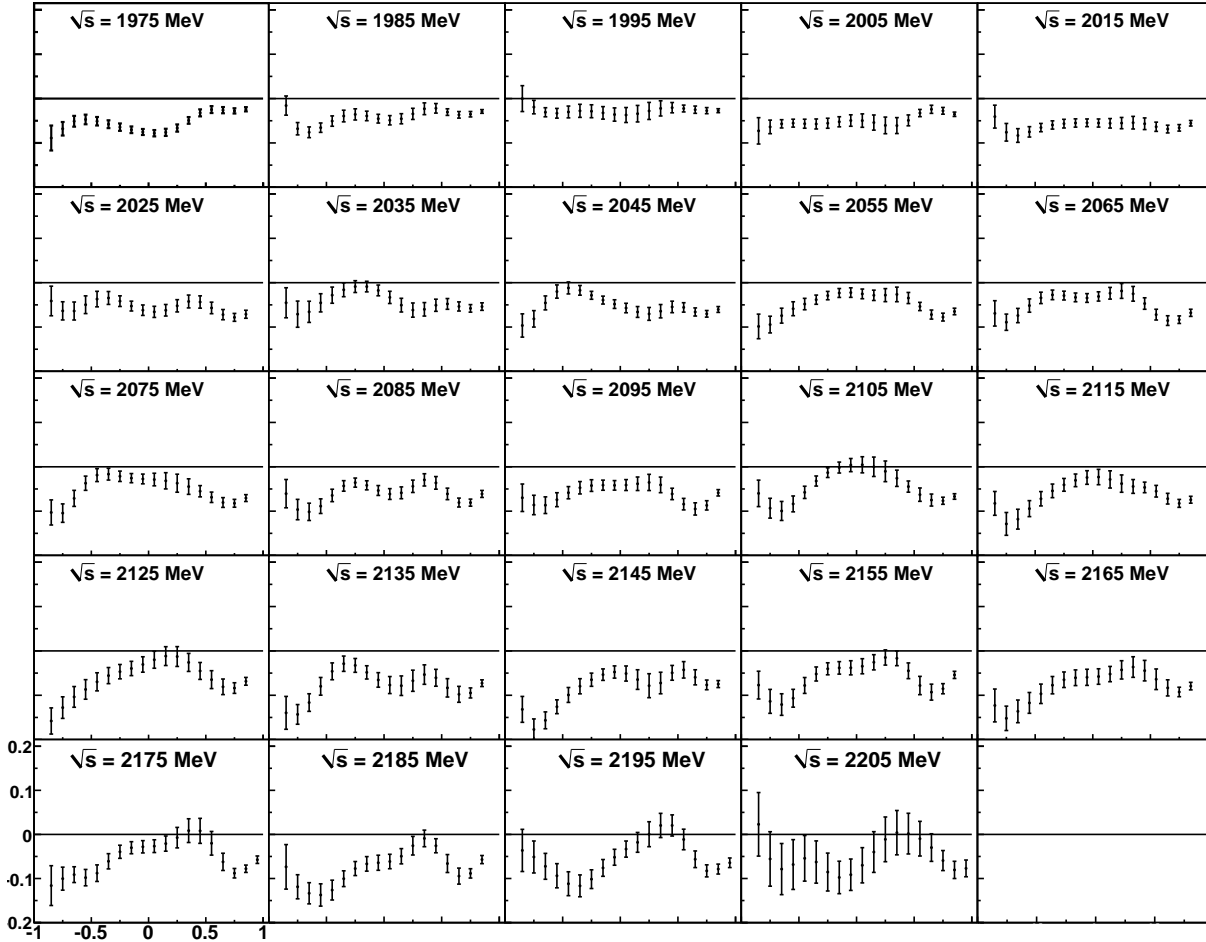


Figure 5.16:  $\text{Re}(\rho_{10}^1)$  element vs  $\cos \theta_{CM}^\omega$  in bins of  $\sqrt{s}$ , beyond 1965 MeV, for g8b. The errors are as calculated in Section 5.2.1.

Like the  $\rho_{10}^0$  element, this element has both real and imaginary components. We can only measure the real part with this experiment, which is shown in Figures 5.15 and 5.16. At low energies, below 1970 MeV, the  $\text{Re}(\rho_{10}^1)$  element is very strongly correlated with the  $\text{Re}(\rho_{10}^0)$ , see Figure B.4 in Appendix B, one rising when the other falls, and vice versa. However, as we will see later, it is even more closely related to the  $\text{Im}(\rho_{10}^2)$  element at these energies. Above 1970 MeV, the symmetry breaks down and the two elements evolve independently. Below 1845 MeV, it is negative at backwards angles and positive at forward angles, however the crossing point moves forward as the energy goes up until, by 1955 MeV, it is entirely negative. In some bins, for instance the 2005 MeV bin, it is almost completely flat. At higher energies, some shape starts to develop, however it is not consistent from bin to bin. At the highest energies measured, there is an indication that it may be positive at some forward angles. There is a prominent maximum at  $\cos \theta_{CM}^\omega = 0.5$  visible from threshold up to 1965 MeV. Other extrema are more transient.

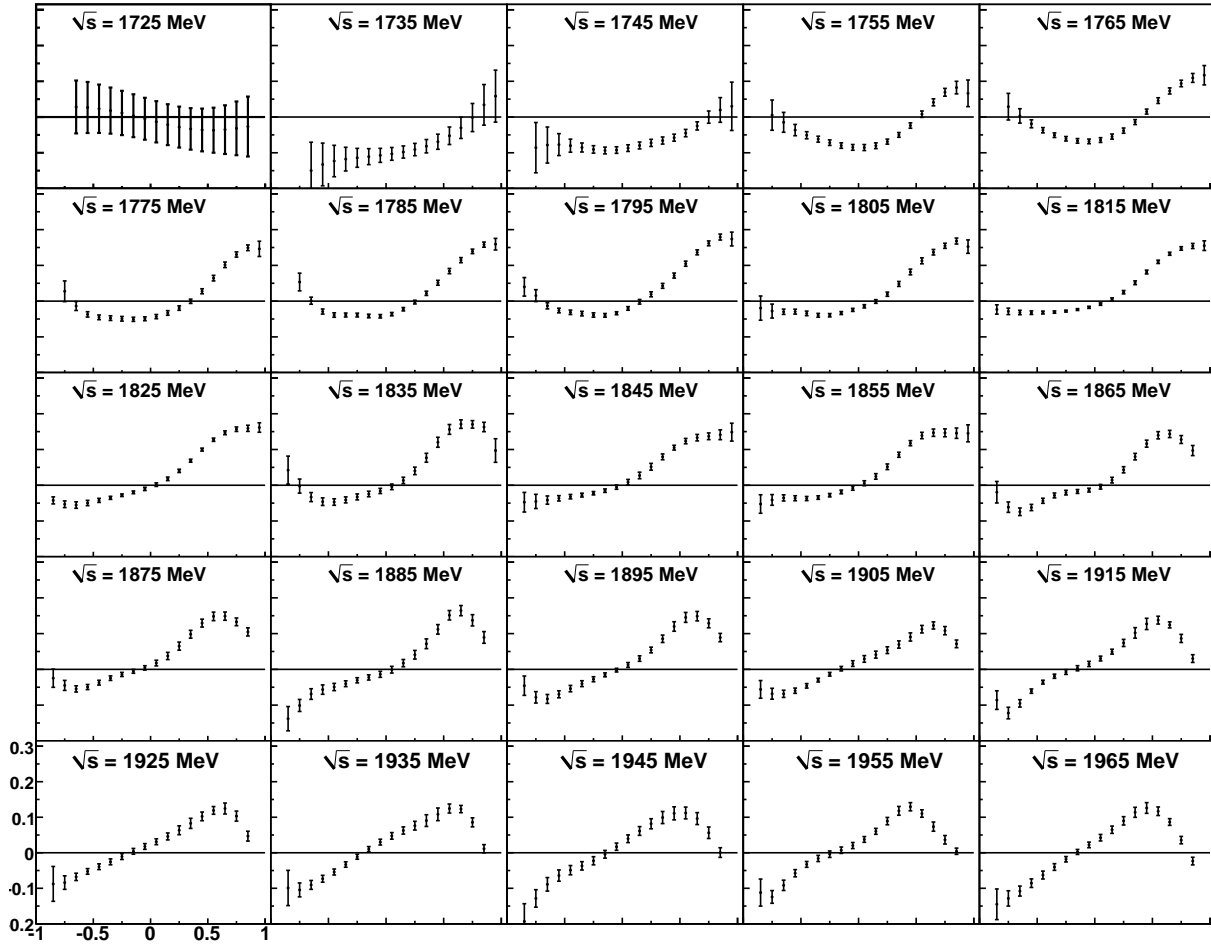


Figure 5.17:  $\rho_{1-1}^1$  element vs  $\cos \theta_{CM}$  in bins of  $\sqrt{s}$ , up to 1965 MeV, for g8b. The errors are as calculated in Section 5.2.1.

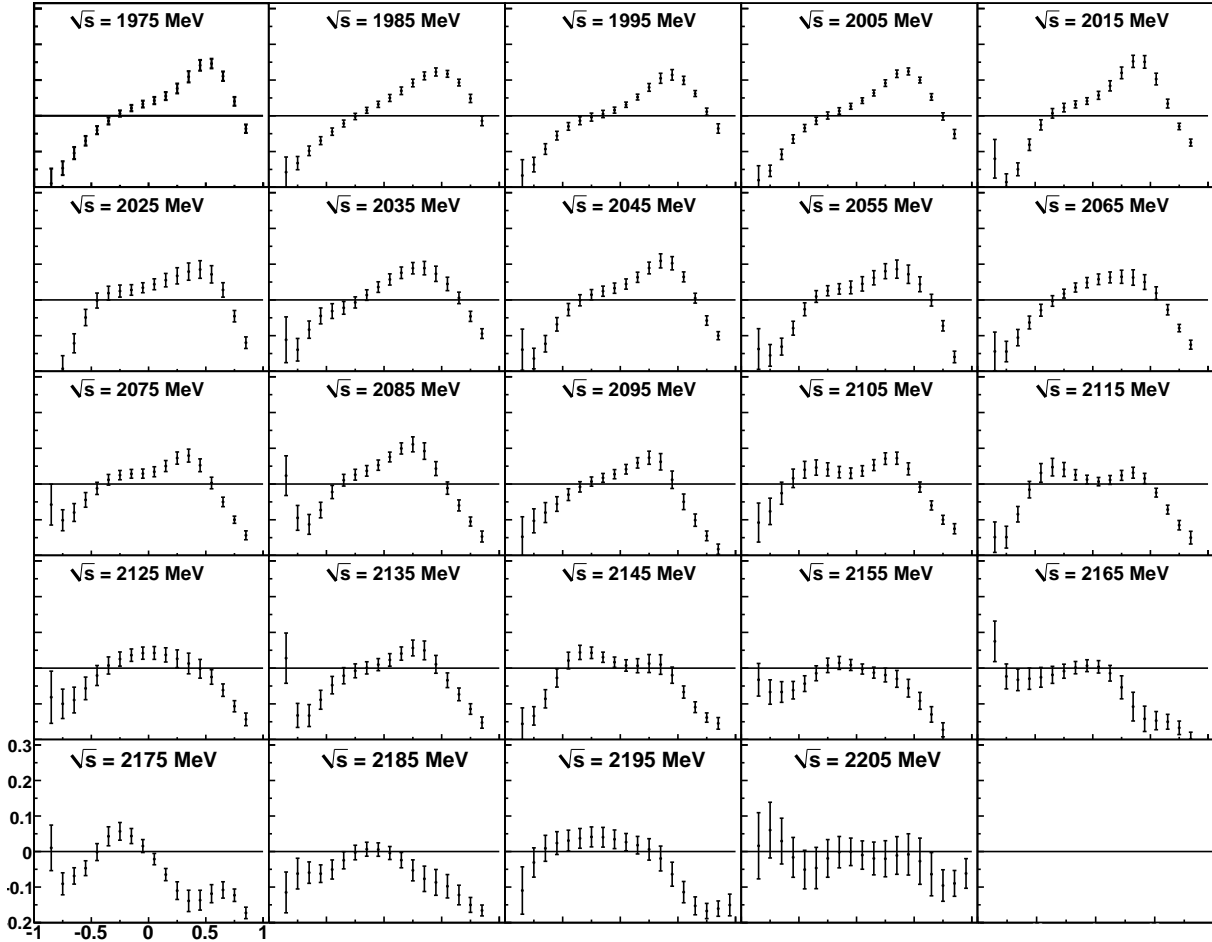


Figure 5.18:  $\rho_{1-1}^1$  element vs  $\cos \theta_{CM}^\omega$  in bins of  $\sqrt{s}$ , beyond 1965 MeV, for g8b. The errors are as calculated in Section 5.2.1.

The  $\rho_{1-1}^1$  element, shown in Figures 5.17 and 5.17, is purely real, like the  $\rho_{1-1}^0$  element. However, unlike the other two  $\rho^1$  elements seen so far, this element is not strongly correlated with its  $\rho^0$  counterpart at low energies, see Figure B.5 in Appendix B. Its shape does not change significantly from 1755–1835 MeV. Above that energy, we start to see the most backwards values get more and more negative, and see a maximum form at forward angles that persists until at least 2115 MeV. The maximum is consistently near  $\cos \theta_{CM}^\omega = 0.45$ . This turning point can also be seen in the  $\rho_{1-1}^0$  element. Above 1965 MeV, the most forward angles become negative, and, as we go to higher energies, more of the forward angles values are negative, until, by 2155 MeV, all values beyond  $\cos \theta_{CM}^\omega = 0$  are negative. Above 2035 MeV, the backwards angles of the  $\rho_{1-1}^0$  and  $\rho_{1-1}^1$  elements are roughly equal, but they differ at forward angles while still sharing the extrema at  $\cos \theta_{CM}^\omega = 0.45$ . At the highest energies, there is little consistency between the values from bin to bin and the error bars get quite large.

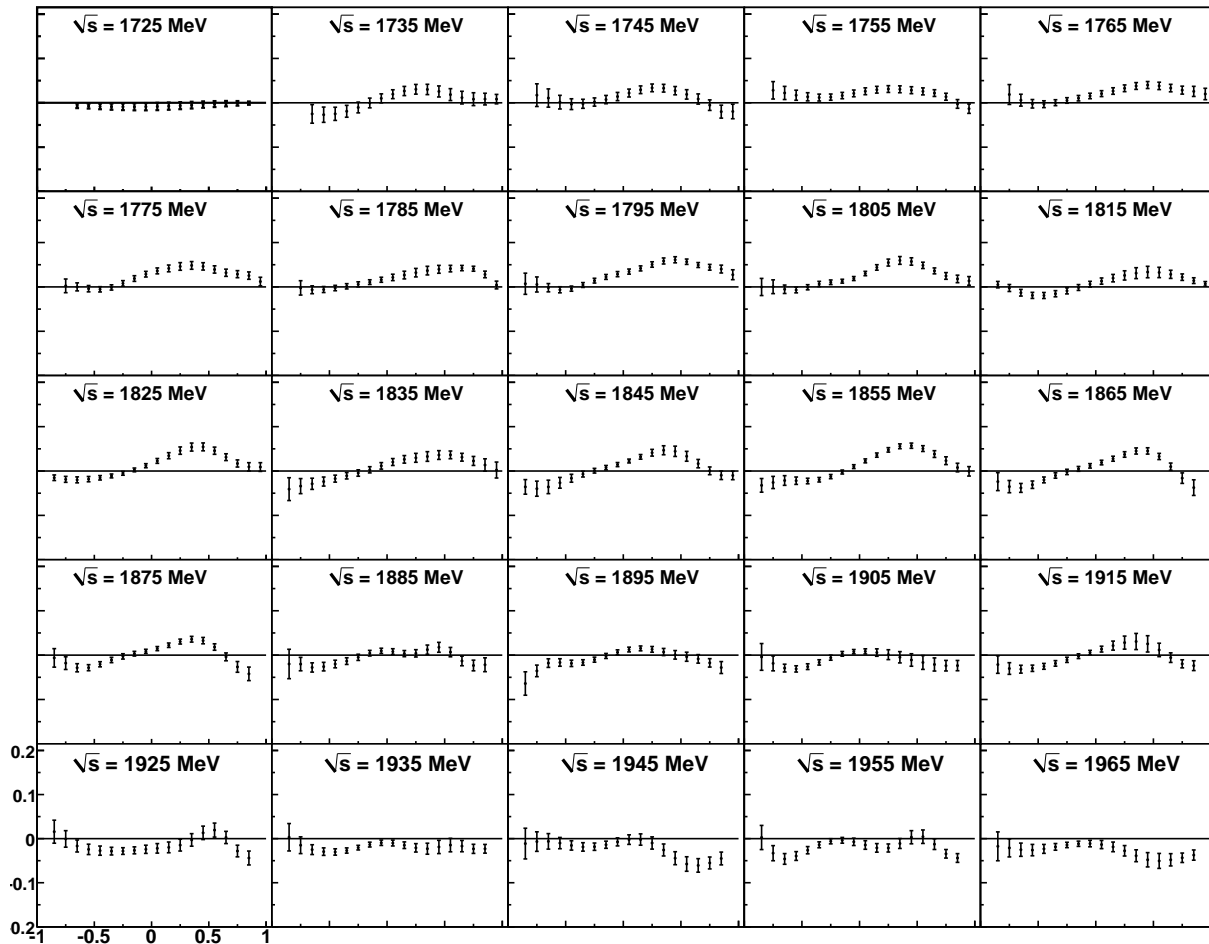


Figure 5.19:  $\rho_{11}^1$  element vs  $\cos \theta_{CM}^\omega$  in bins of  $\sqrt{s}$ , up to 1965 MeV, for g8b. The errors are as calculated in Section 5.2.1.

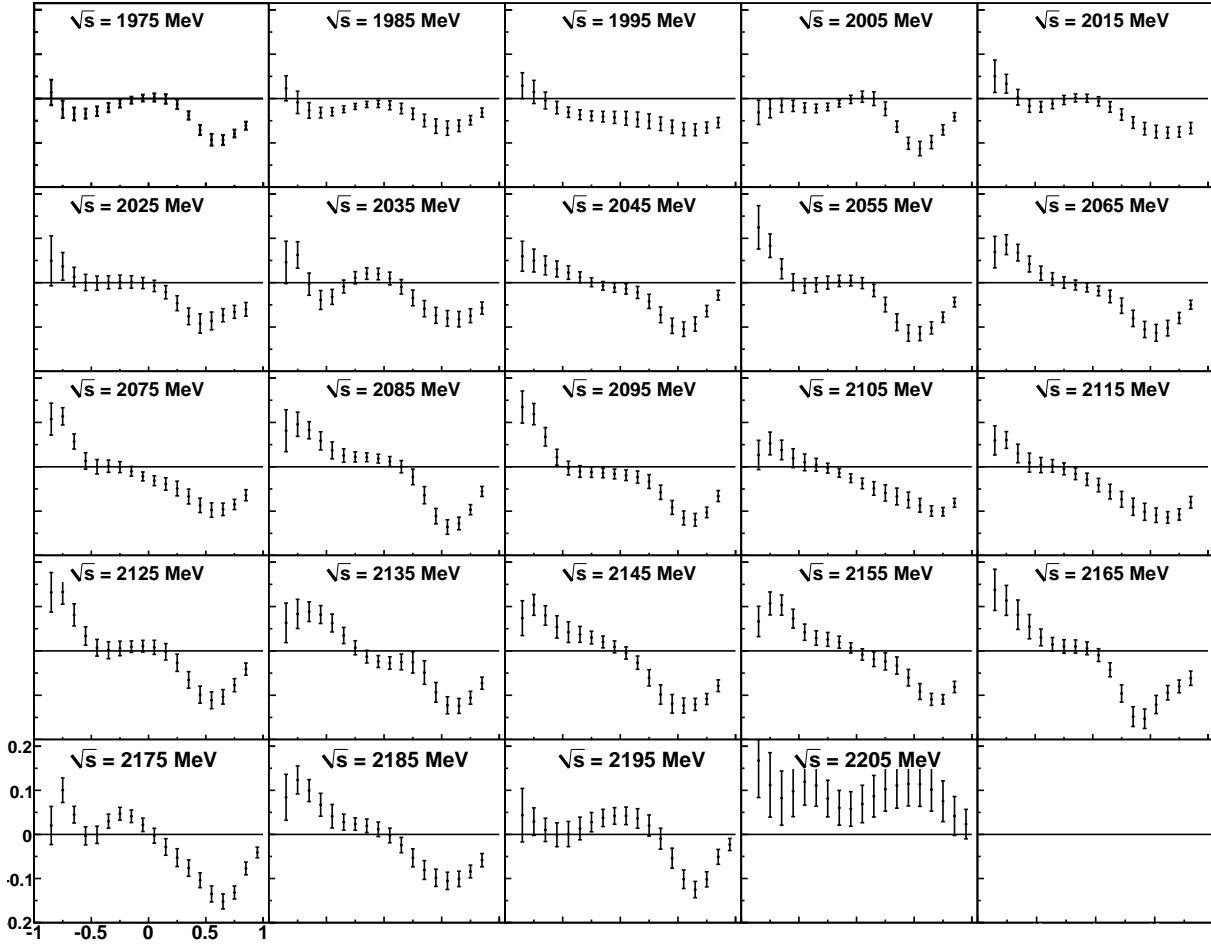


Figure 5.20:  $\rho_{11}^1$  element vs  $\cos \theta_{CM}^\omega$  in bins of  $\sqrt{s}$ , beyond 1965 MeV, for g8b. The errors are as calculated in Section 5.2.1.

The  $\rho_{11}^1$  element, shown in Figures 5.19 and 5.19, is unique for experiments without a polarized target because it is the only 11 element that can be independently measured. Due to the trace conditions on the  $\rho^0$  matrix, the  $\rho_{11}^0$  is a function of the  $\rho_{00}^0$  element, and (4.48) shows that the  $\rho_{11}^{2,3}$  elements cannot be measured. There does not appear to be any relationship between the  $\rho_{11}^1$  element and the  $\rho_{11}^0$  element. It is a relatively small element, and it is purely real since it is on the diagonal. It looks like it may be zero at threshold. Shortly after threshold, it starts off as entirely positive, but as the energy increases the backwards angles become negative and there is a minimum near  $\cos \theta_{CM}^\omega = 0.4$ , similar to what we see at high energies in the  $\rho_{1-1}^1$  elements. This fades away as the energy increases. By 1935 MeV, it is entirely negative and very flat. It starts to regain shape by 1975 MeV, and is positive at backwards angles by 2015 MeV. A minimum appears at  $\cos \theta_{CM}^\omega = 0.55$  by 2005 MeV that persists until the highest energies. There is also an extremum of some kind visible at  $\cos \theta_{CM}^\omega = -0.55$  throughout almost the entire energy range.

### 5.2.4 $\rho^2$ Elements in g8b

The  $\rho^2$  elements are calculated using

$$\rho_{m_V m_{V'}}^2 = \frac{1}{2N} \sum_{m_\gamma m_i m_f} i * (-m_\gamma) \mathcal{A}_{m_\gamma, m_i, m_f, m_V} * \mathcal{A}_{-m_\gamma, m_i, m_f, m_{V'}}^\dagger. \quad (5.7)$$

Note that the sign of  $m_\gamma$  changes in the two amplitudes above, as with the  $\rho^1$  elements. The two calculations are the same except for the  $-im_\gamma$  multiplying each term. There are two elements that can be measured in this experiment, as well as the  $\rho_{00}^2$  element which is identically 0, due to the symmetry properties of the amplitudes, see (4.43). The two elements that can be measured are  $\text{Im}(\rho_{10}^2)$  and  $\text{Im}(\rho_{1-1}^2)$ . We present each on the following pages, along with a brief discussion of the results.

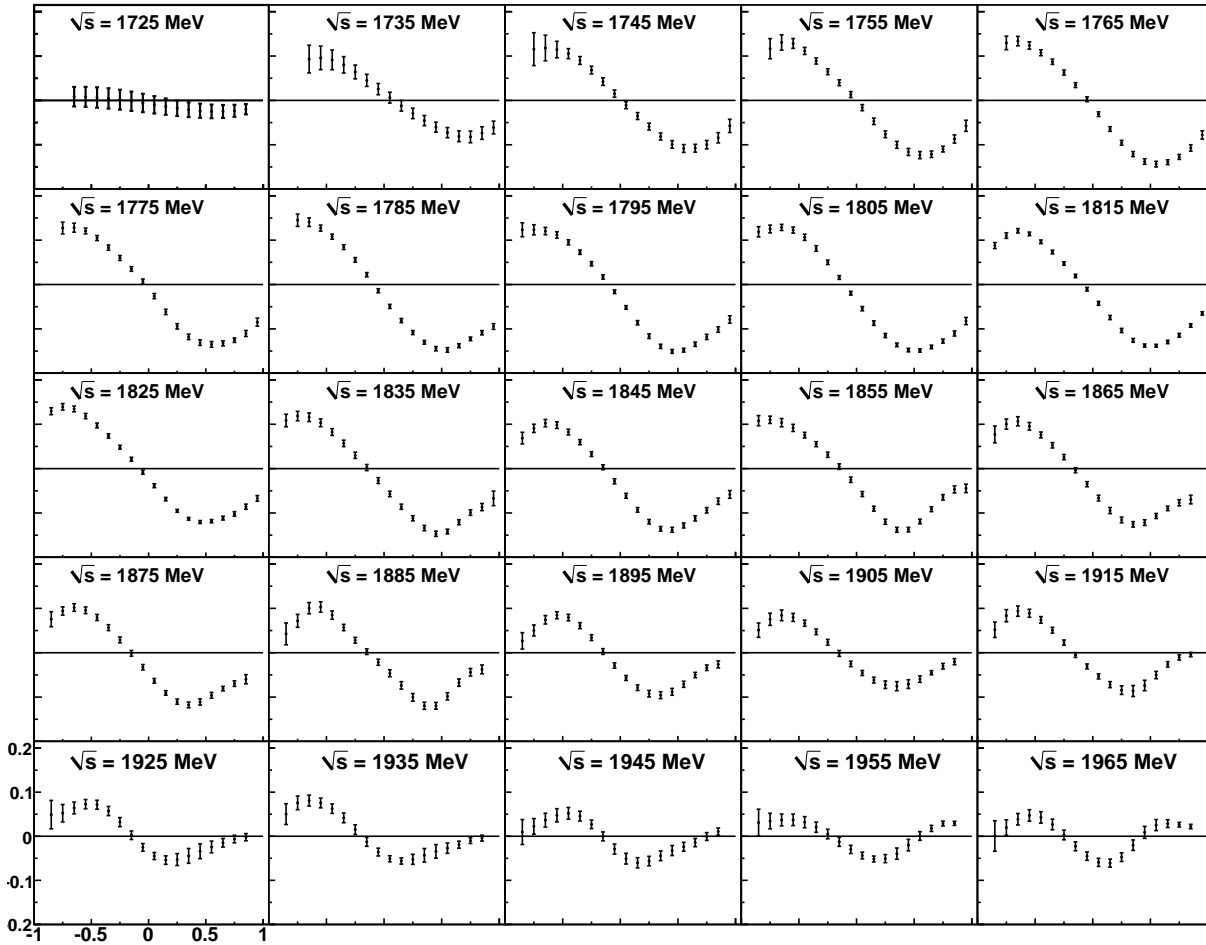


Figure 5.21:  $\text{Im}(\rho_{10}^2)$  element vs  $\cos \theta_{CM}^\omega$  in bins of  $\sqrt{s}$ , up to 1965 MeV, for g8b. The errors are as calculated in Section 5.2.1.

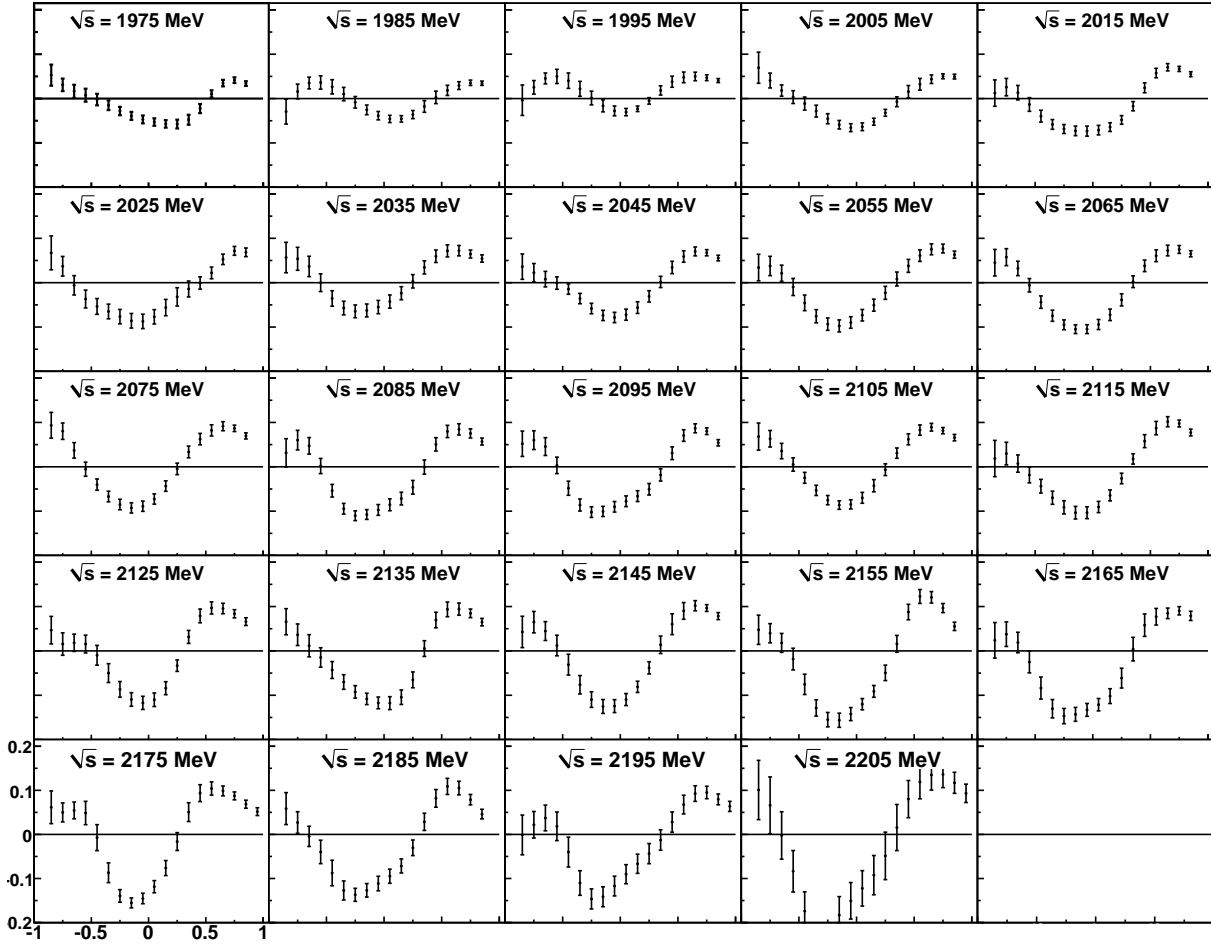


Figure 5.22:  $\text{Im}(\rho_{10}^2)$  element vs  $\cos \theta_{CM}^\omega$  in bins of  $\sqrt{s}$ , beyond 1965 MeV, for g8b. The errors are as calculated in Section 5.2.1.

The  $\rho_{10}^2$  element has both a real and an imaginary part, but only the imaginary part can be measured in this experiment, and is presented in Figures 5.21 and 5.22. This element is very closely correlated with the real part of the  $\rho_{10}^1$  element, see Figure B.6 in Appendix B. At angles forward of  $\cos \theta_{CM}^\omega = 0.45$ , they are a near exact mirror image of each other over the entire energy range. For all other angles, this symmetry is broken in many places. From threshold up to 1845 MeV, they mirror each others' changes, one rising while the other falls, and vice versa. Above that energy, the symmetry breaks except at the most forward angles, and the two elements evolve independently. There is a maximum at  $\cos \theta_{CM}^\omega = -0.55$  in the 1845 MeV bin, that persists until 2015 MeV, although it moves around a little bit over that range. There is also a minimum visible at  $\cos \theta_{CM}^\omega = 0.55$  in the 1845 MeV bin that moves towards the central angles as the energy rises and persists over the rest of the energy range, getting much more pronounced at high energies. Lastly, a maximum becomes visible at very forward angles at 1965 MeV that persists for the rest of the energy range.

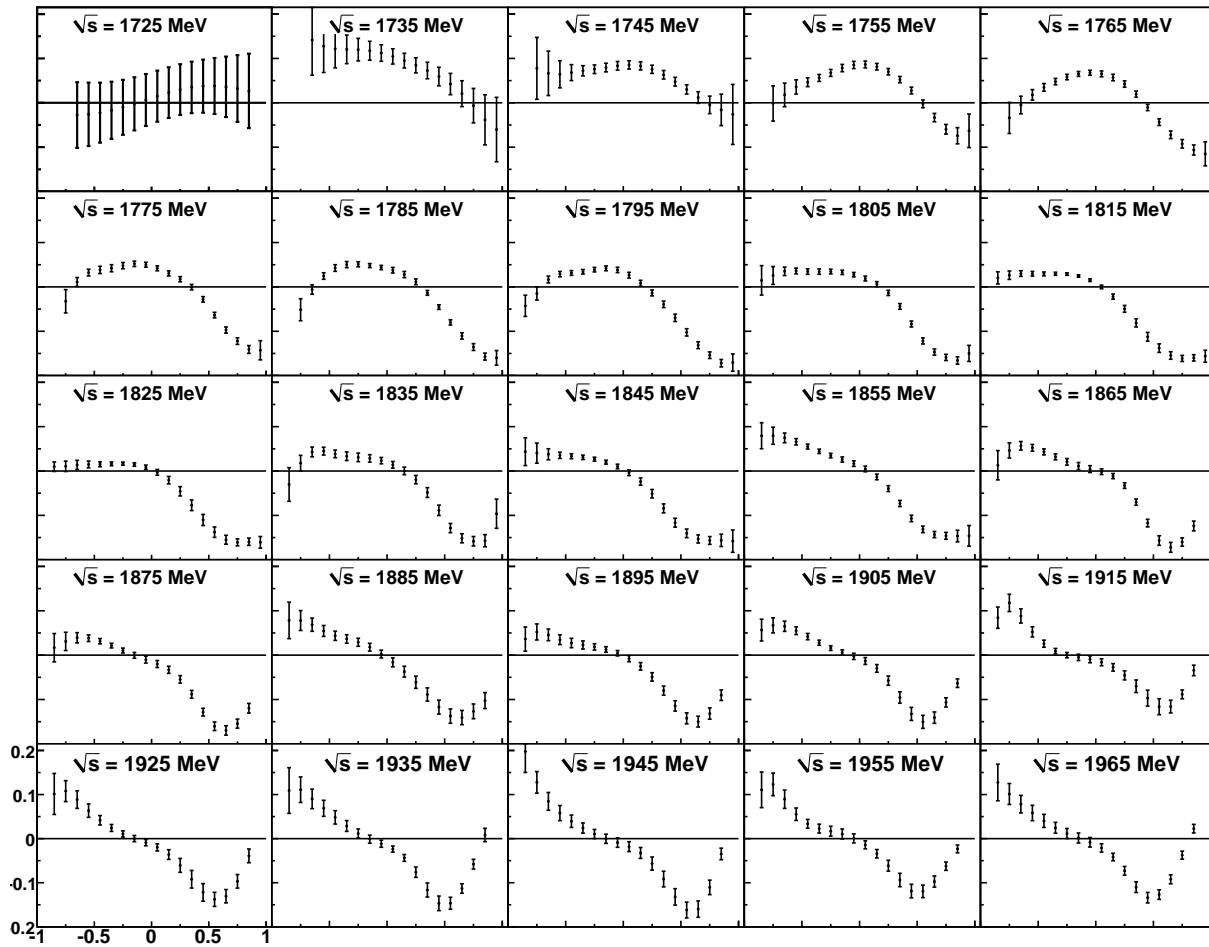


Figure 5.23:  $\text{Im}(\rho_{1-1}^2)$  element vs  $\cos \theta_{CM}^\omega$  in bins of  $\sqrt{s}$ , up to 1965 MeV, for g8b. The errors are as calculated in Section 5.2.1.

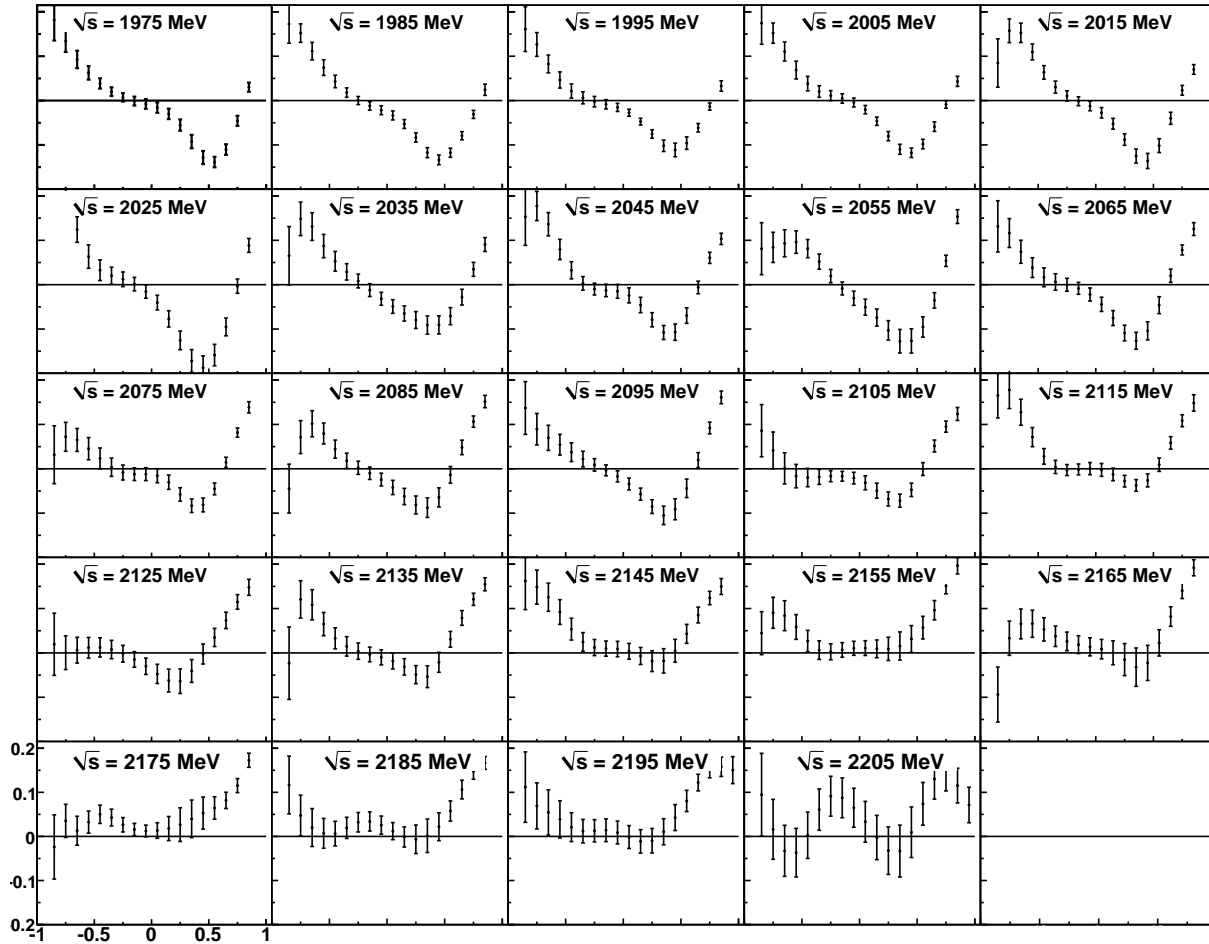


Figure 5.24:  $\text{Im}(\rho_{1-1}^2)$  element vs  $\cos \theta_{CM}^\omega$  in bins of  $\sqrt{s}$ , beyond 1965 MeV, for g8b. The errors are as calculated in Section 5.2.1.

The  $\rho_{1-1}^2$  element, presented in Figures 5.23 and 5.24, is purely imaginary. It is almost the exact mirror of the  $\rho_{1-1}^1$  element over the entire energy range, see Figure B.7 in Appendix B. This is very interesting because, based on the formulas for these elements, one would not expect this to be the case. Looking more closely at the values it is clear that it is not true that  $\text{Im}(\rho_{1-1}^2) = -\rho_{1-1}^1$ , but they do have remarkably close values, and their shapes are the same over a wide range of energies. It is unclear if this symmetry is important or if it would persist at higher energies than measured by g8b, as slight differences between the two do start to appear above 2010 MeV. However, the uncertainties also increase at higher energies, so it is difficult to draw conclusions.

### 5.2.5 $\rho^3$ Elements in g1c

The  $\rho^3$  elements are calculated using

$$\rho_{m_V m_{V'}}^3 = \frac{1}{2N} \sum_{m_\gamma m_i m_f} m_\gamma \mathcal{A}_{m_\gamma, m_i, m_f, m_V} * \mathcal{A}_{m_\gamma, m_i, m_f, m_{V'}}^\dagger. \quad (5.8)$$

Note that this is the same equation as for the  $\rho^0$  elements except for the addition of the  $m_\gamma$  before each term. There are again only two elements that can be measured in this experiment, the  $\text{Im}(\rho_{10}^3)$  and  $\text{Im}(\rho_{1-1}^3)$  elements, but the  $\rho_{00}^3$  term can again be determined to be 0, see (4.43).

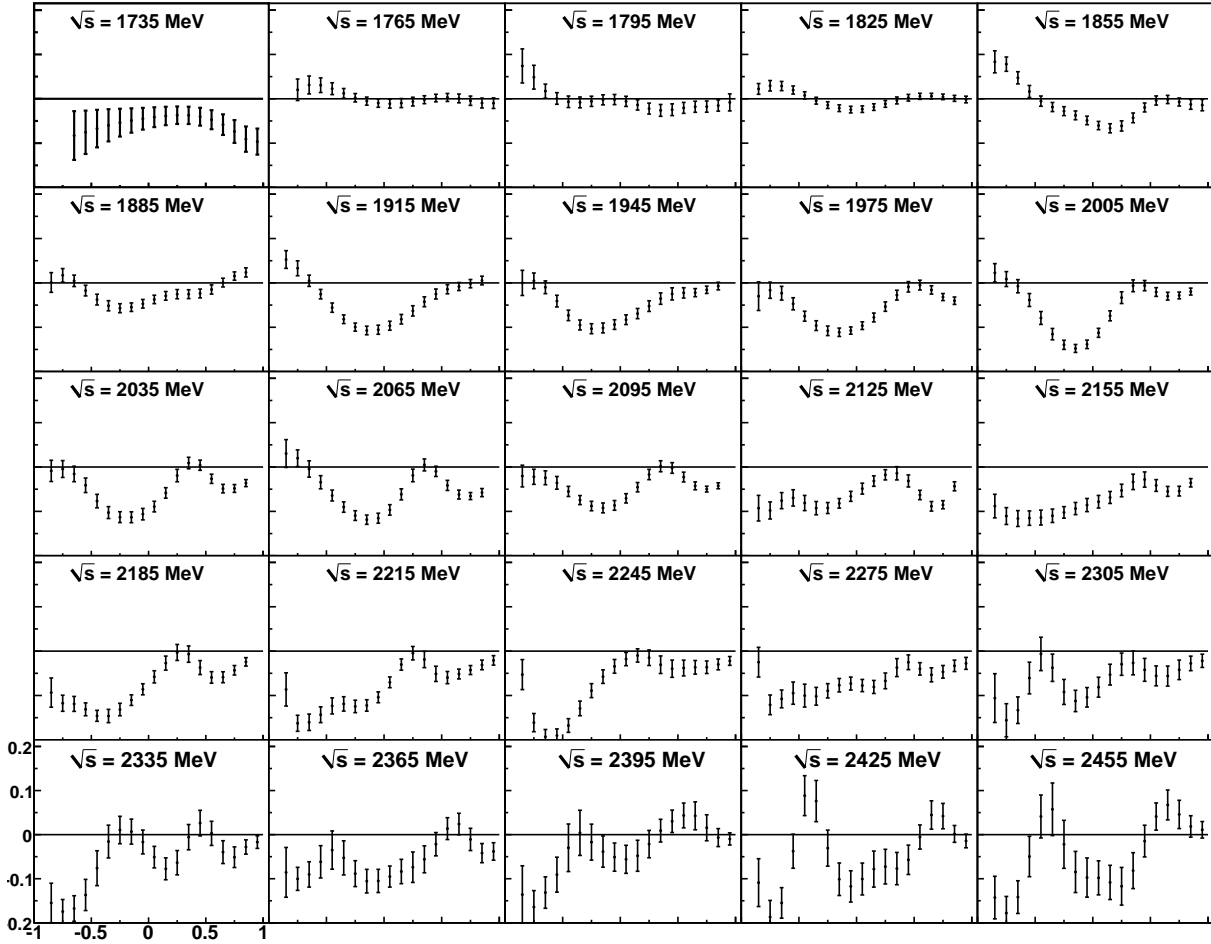


Figure 5.25:  $\text{Im}(\rho_{10}^3)$  element vs  $\cos \theta_{CM}^\omega$  in bins of  $\sqrt{s}$  for g1c. The errors are as calculated in Section 5.2.1.

The  $\rho_{10}^3$  element contains both a real and imaginary part, but only the imaginary part can be measured in this experiment. That is shown in Figure 5.25. There is less bin-to-bin stability in this element than in other elements, though recall that the bins are 30-MeV wide here, as opposed to 10-MeV-wide bins in g8b. It is possible to detect two extrema that persist through most of the energy range. The first is a minimum near  $\cos \theta_{CM}^\omega = -0.15$ , starting from 1885 MeV and lasting up to 2185 MeV. The second is a maximum that starts at  $\cos \theta_{CM}^\omega = 0.5$  in the lowest energy bins

and persists to the highest energies, though the position of the maximum varies slightly over the range. While there is some evidence of symmetry between this element and the  $\text{Re}(\rho_{10}^0)$  element, see Figure B.8, it is not as strong as was seen in the other elements.

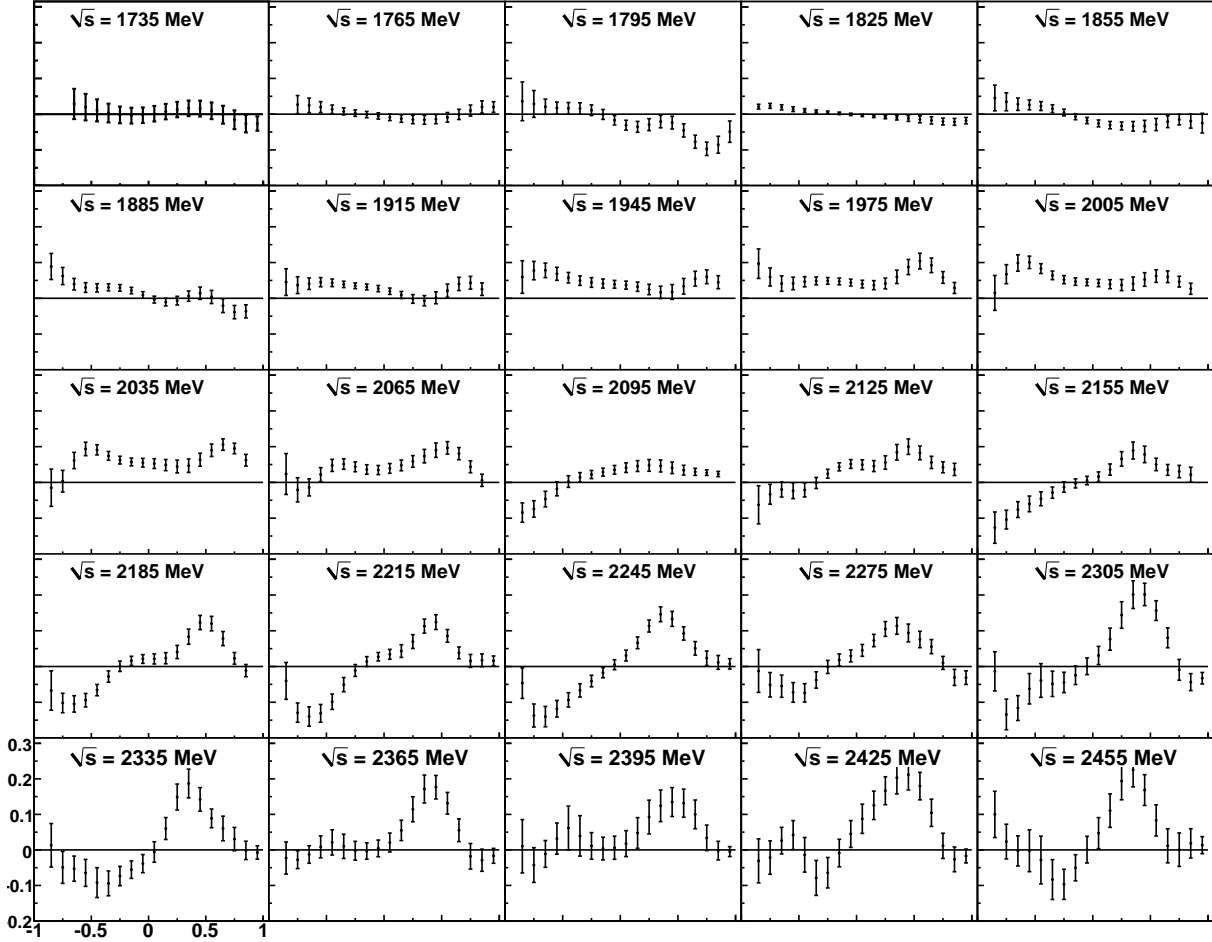


Figure 5.26:  $\text{Im}(\rho_{1-1}^3)$  element vs  $\cos \theta_{CM}^\omega$  in bins of  $\sqrt{s}$  for g1c. The errors are as calculated in Section 5.2.1.

The  $\rho_{1-1}^3$  element, shown in Figure 5.26, is purely imaginary. It is slightly more stable from bin to bin than the  $\text{Im}(\rho_{10}^3)$  element. At low energies, it is fairly flat. Starting at about 1885 MeV, a maximum starts to appear at  $\cos \theta_{CM}^\omega = 0.5$  that is visible for the rest of the energy range. The backwards angles start to go negative around 2095 MeV and there is a hint of a minimum in the far backwards angles, however it is not consistently visible. As with the  $\text{Im}(\rho_{10}^3)$  element, there is little correlation between this element and its corresponding element in the  $\rho^0$  matrix, see Figure B.9 in Appendix B.

### 5.3 Schilling's Method

In Section 4.3.5, the Schilling Method for calculating the spin density matrix elements from the decay distribution is discussed. Here, the results of that method are compared to the results from our mother-fit method presented in the last section. Only comparisons to the newly measured, polarized spin density matrix elements are presented. Note that the error bars from the Schilling method are the errors calculated by MINUIT, not using the bootstrap method. The results are presented as functions of  $\sqrt{s}$  in bins of  $\cos \theta_{CM}^\omega$ , in contrast to the last section. Presenting the data in this way will show how some of the features evolve as a function of  $\sqrt{s}$ . For all elements, excellent agreement is seen between the two methods. The advantage of using the mother-fit method over the Schilling method can be seen in the bin-to-bin stability and smaller error bars. We will follow each set of plots with a brief discussion of the features visible as functions of the energy as these *may be* indicative of resonance structures.

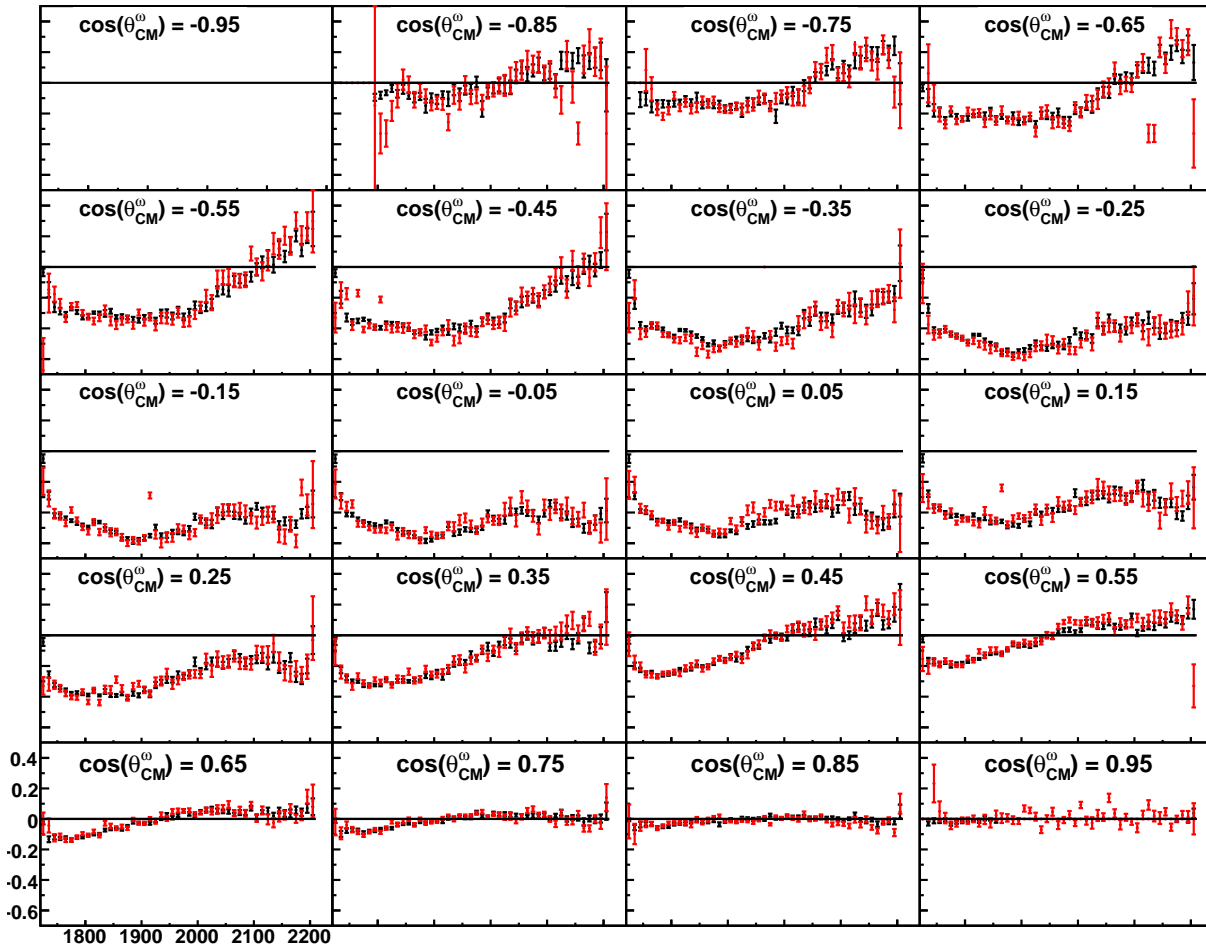


Figure 5.27:  $\rho_{00}^1$  element vs  $\sqrt{s}$  in bins of  $\cos \theta_{CM}^\omega$  for g8b. The results from the mother fit are in black, the results from the Schilling method are in red. In the  $\cos \theta_{CM}^\omega = 0.95$  bin, the mother fit method does not provide measurements at all energies, while the Shilling method does.

There is a broad dip centered at 1900 MeV at angles backwards of  $\cos \theta_{CM}^\omega = 0$ . Above  $\cos \theta_{CM}^\omega =$

0, the center of the dip moves to lower energy until, by  $\cos \theta_{CM}^\omega = 0.65$ , it is practically at threshold. Starting at  $\cos \theta_{CM}^\omega = -0.15$ , a mild hump is visible centered at 2050 MeV. It is visible up to  $\cos \theta_{CM}^\omega = 0.65$ . Above  $\cos \theta_{CM}^\omega = 0.65$ , the data is flat and roughly 0.

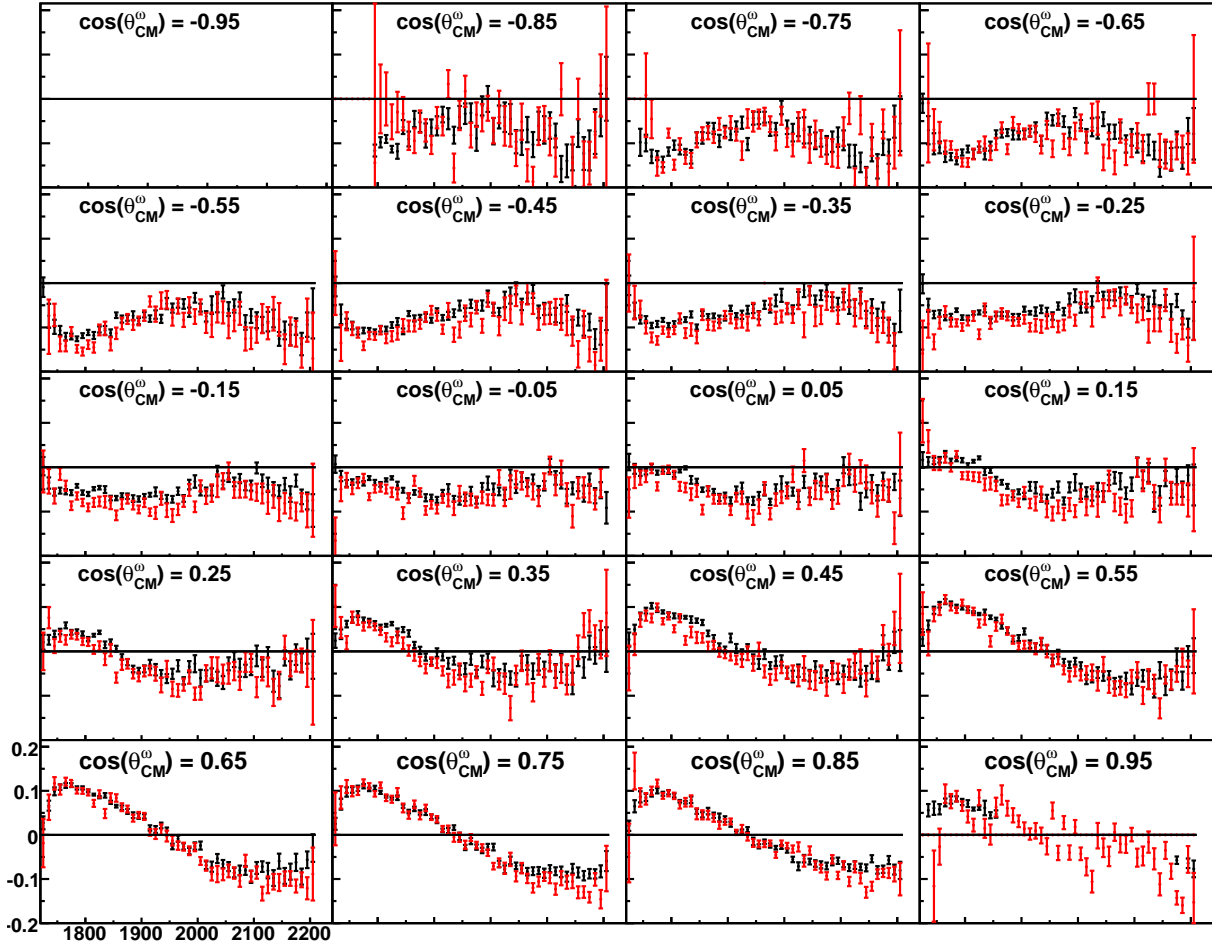


Figure 5.28:  $\text{Re}(\rho_{10}^1)$  element vs  $\sqrt{s}$  in bins of  $\cos \theta_{CM}^\omega$  for g8b. The results from the mother fit are in black, the results from the Schilling method are in red. In the  $\cos \theta_{CM}^\omega = 0.95$  bin, the mother fit method does not provide measurements at all energies, while the Shilling method does.

At angles backwards of  $\cos \theta_{CM}^\omega = -0.45$ , there is a very broad hump centered around 1950 MeV and a tighter dip can be seen around 1780 MeV as well. At central angles, the data is largely flat. At angles forward of  $\cos \theta_{CM}^\omega = 0.15$ , a very strong peak can be seen near 1780 MeV, similar to what is seen in the backward angles. There may be hints at a broad trough centered near 2050 MeV near  $\cos \theta_{CM}^\omega = 0.45$ .

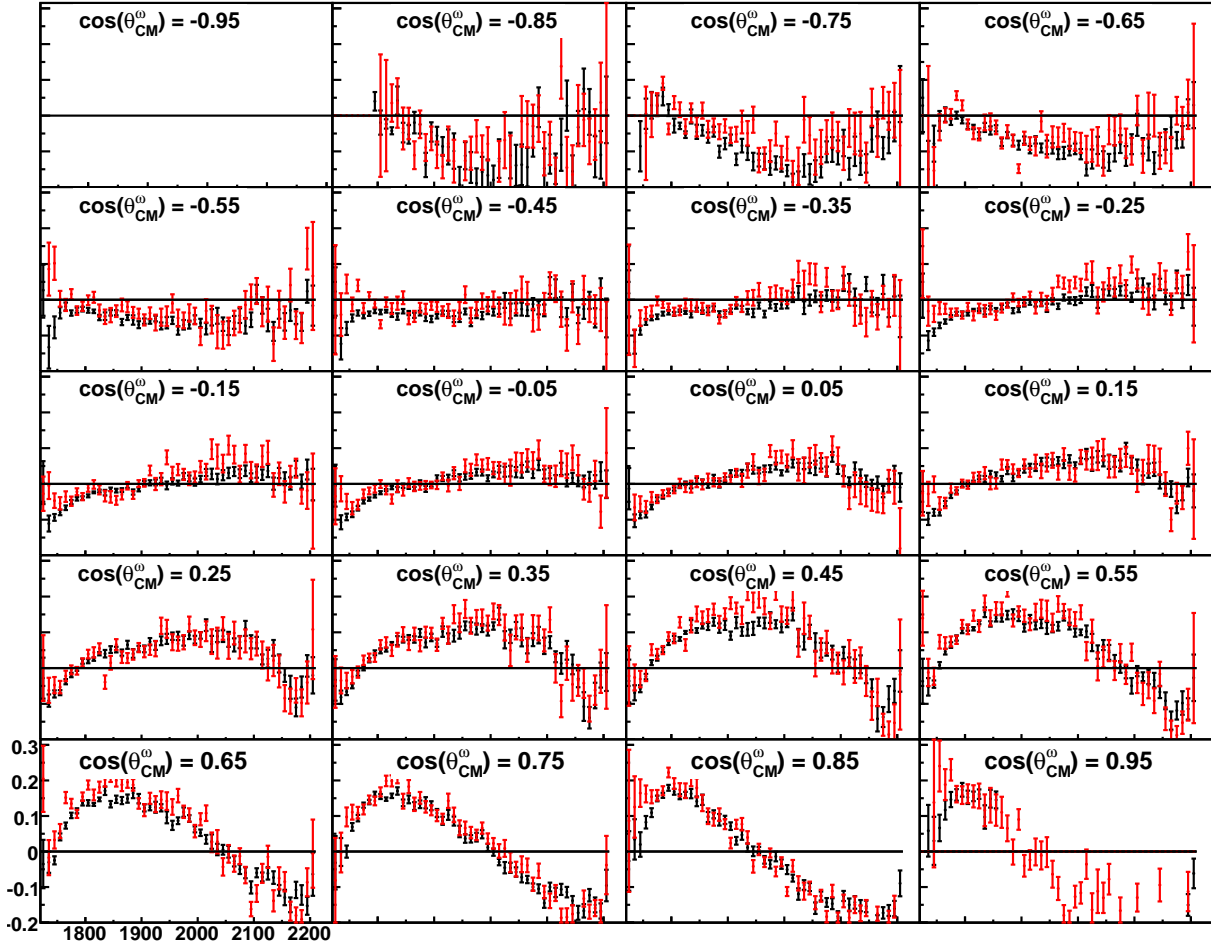


Figure 5.29:  $\rho_{1-1}^1$  element vs  $\sqrt{s}$  in bins of  $\cos \theta_{CM}^\omega$  for g8b. The results from the mother fit are in black, the results from the Schilling method are in red. In the  $\cos \theta_{CM}^\omega = 0.95$  bin, the mother fit method does not provide measurements at all energies, while the Shilling method does.

There is a broad trough around 2050 MeV at angles more backward than  $\cos \theta_{CM}^\omega = -0.55$ . The central angles are relatively flat, with only a gentle rise occurring as a function of energy. There is a broad peak that begins to appear at angles more forward than  $\cos \theta_{CM}^\omega = 0$ , but the position of the peak moves toward lower energies as the angle gets more forward.

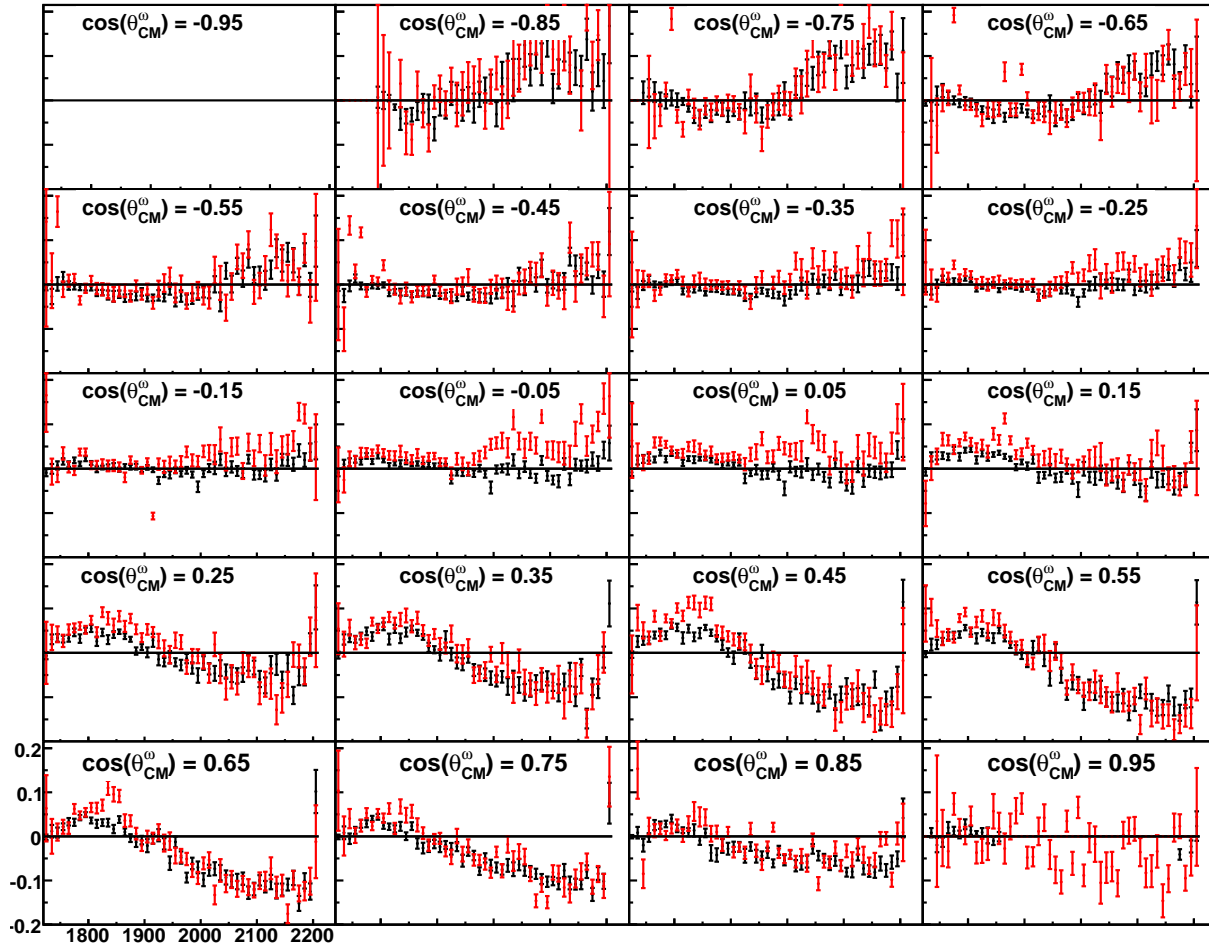


Figure 5.30:  $\rho_{11}^1$  element vs  $\sqrt{s}$  in bins of  $\cos \theta_{CM}^\omega$  for g8b. The results from the mother fit are in black, the results from the Schilling method are in red. In the  $\cos \theta_{CM}^\omega = 0.95$  bin, the mother fit method does not provide measurements at all energies, while the Shilling method does.

There are hints of structure at angles backwards of  $\cos \theta_{CM}^\omega = -0.55$  around 1900 MeV and 2100 MeV, but they are difficult to distinguish completely. From  $\cos \theta_{CM}^\omega = -0.55$  to  $\cos \theta_{CM}^\omega = 0.15$ , the data is almost completely flat. Above  $\cos \theta_{CM}^\omega = 0.15$ , a peak starts to develop near 1820 MeV followed by a gentle decline as  $\sqrt{s}$  gets higher.

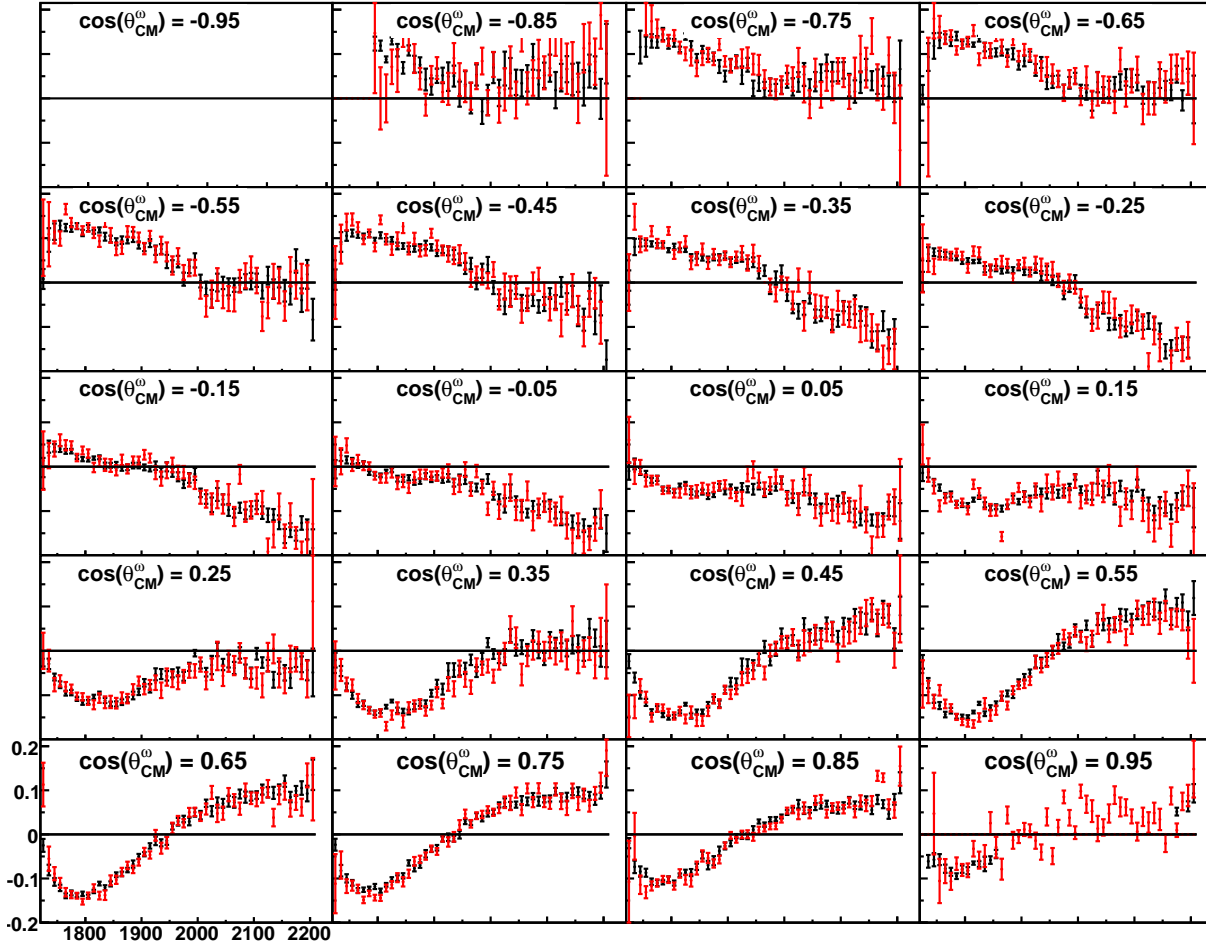


Figure 5.31:  $\text{Im}(\rho_{10}^2)$  element vs  $\sqrt{s}$  in bins of  $\cos \theta_{CM}^\omega$  for g8b. The results from the mother fit are in black, the results from the Schilling method are in red. In the  $\cos \theta_{CM}^\omega = 0.95$  bin, the mother fit method does not provide measurements at all energies, while the Shilling method does.

At angles backwards of  $\cos \theta_{CM}^\omega = 0$ , there is a fairly steady negative slope as a function of energy, with no changes of direction. Above  $\cos \theta_{CM}^\omega = 0$ , a trough begins to appear at low energies, generally centered around 1800 MeV, followed by a steady rise as a function of energy, which eventually flattens out at energies above 2050 MeV.

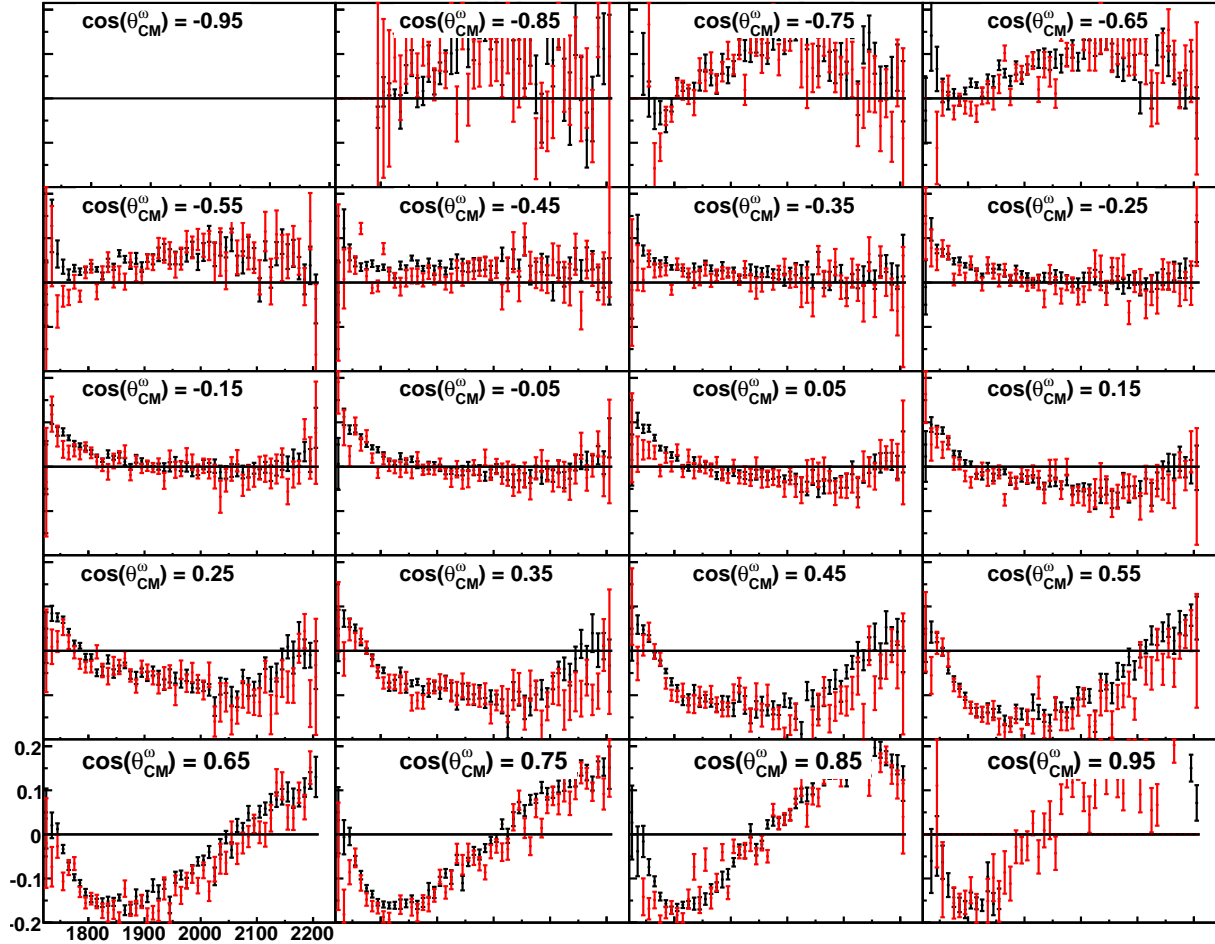


Figure 5.32:  $\text{Im}(\rho_{1-1}^2)$  element vs  $\sqrt{s}$  in bins of  $\cos \theta_{CM}^\omega$  for g8b. The results from the mother fit are in black, the results from the Schilling method are in red. In the  $\cos \theta_{CM}^\omega = 0.95$  bin, the mother fit method does not provide measurements at all energies, while the Shilling method does.

This element is the mirror of the  $\rho_{1-1}^1$  element and thus all the observations of that element apply here as well.

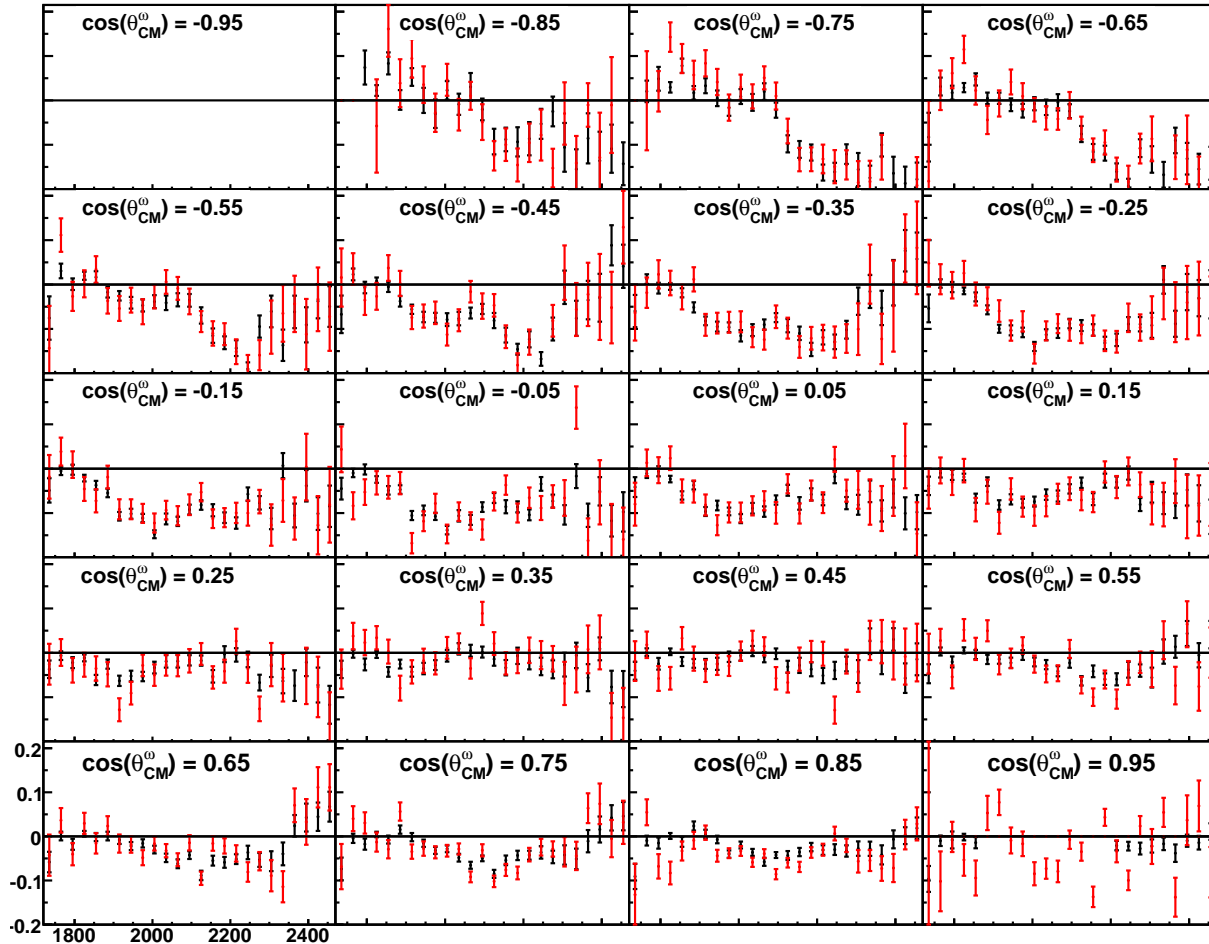


Figure 5.33:  $\text{Im}(\rho_{10}^3)$  element vs  $\sqrt{s}$  in bins of  $\cos \theta_{CM}^\omega$  for g1c. The results from the mother fit are in black, the results from the Schilling method are in red. In the  $\cos \theta_{CM}^\omega = 0.95$  bin, the mother fit method does not provide measurements at all energies, while the Shilling method does.

While there are some hints of structure in this element, particularly in the forwards direction, it is hard to tell where it is centered. The large error bars, wider bins, and lack of smoothness in the data make it difficult to determine the structure.

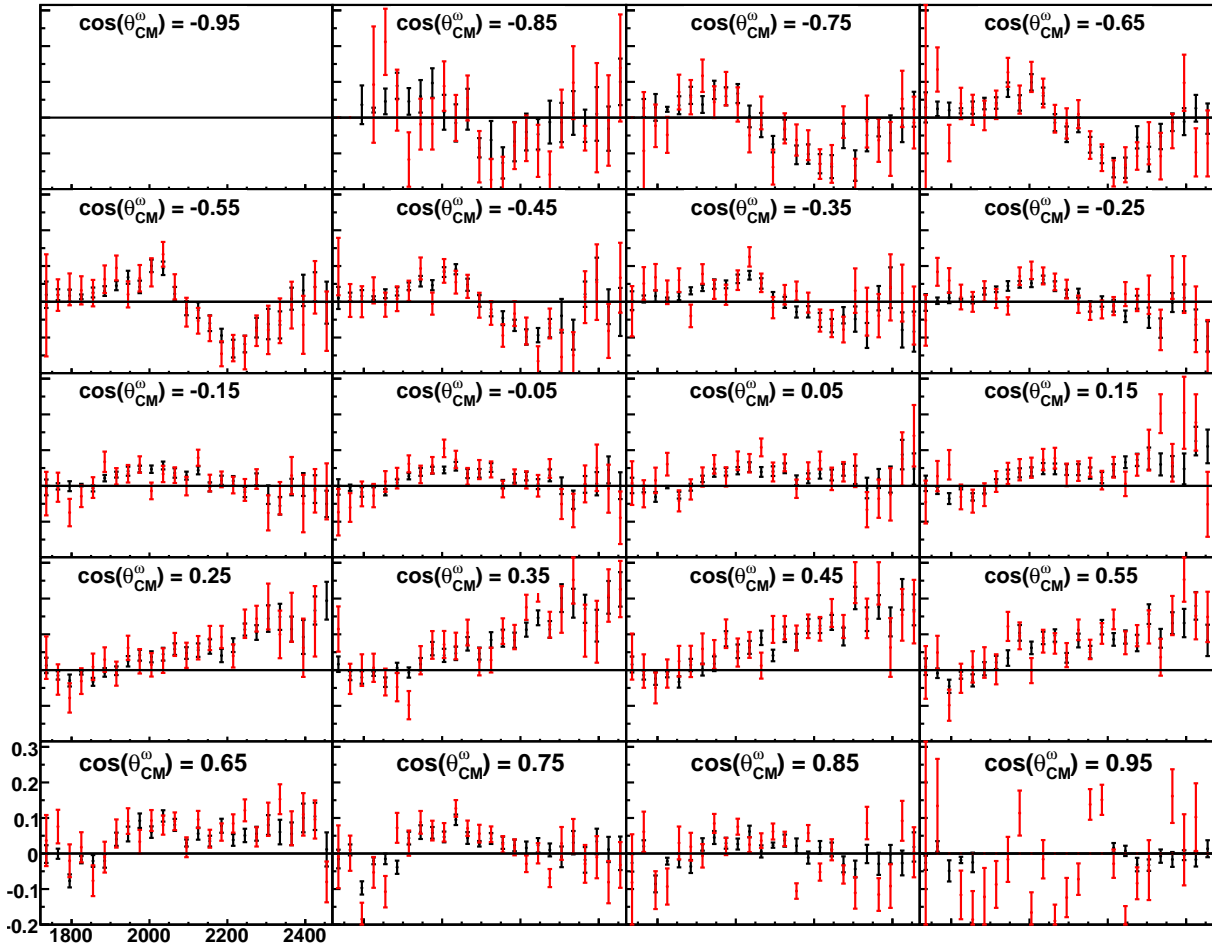


Figure 5.34:  $\text{Im}(\rho_{1-1}^3)$  element vs  $\sqrt{s}$  in bins of  $\cos \theta_{CM}^\omega$  for g1c. The results from the mother fit are in black, the results from the Schilling method are in red. In the  $\cos \theta_{CM}^\omega = 0.95$  bin, the mother fit method does not provide measurements at all energies, while the Shilling method does.

This element is also difficult to determine structure in, but it is possible. In the backwards direction, there are definite extrema near 2000 MeV and 2200 MeV, visible until  $\cos \theta_{CM}^\omega = -0.15$ . At the most forward angles, there seems to be some structure, but it is not consistent from bin to bin.

## 5.4 Summary

We have now presented our spin density matrix elements across a wide range of energies and angles. We have shown the direct comparisons, where possible, to the g11a dataset and have shown excellent agreement in almost every bin. In the few cases where there is a discrepancy with the g11a data, the g8b and g1c results agree well with each other. The g11a results have been compared to the rest of the world's data in [1] and our results are close enough to g11a that any comparisons to previous data are valid for all three datasets. We have then expanded our observables to include the spin density matrix elements that depend on the photon polarization. We have shown that there are

certain empirical symmetries present in these new elements, and that those symmetries generally break as we get to higher energies. This could be an indication that at lower energies there are relatively simple processes responsible for  $\omega$  production, but that at higher energies more resonances are involved. We have also shown that two separate methods of extracting the polarized SDMEs yield very similar results. These measurements have never been made before and hopefully will lead to better models for  $\omega$  photoproduction.

## Chapter 6

# Partial-Wave Analysis

The ultimate goal of this analysis is to be able to extract the resonance contributions important in  $\gamma p \rightarrow p\omega$ . The fits in the last chapter used all s-channel waves of both parities up to  $J = \frac{11}{2}$ . This allows our fits enough degrees of freedom to be able to fully describe the data. We will now assume that those fits *are* able to fully describe the data and proceed to use only a small number of  $J^P$  states, along with non-resonant contributions, to see which of these combinations are able to best describe the *mother* fit in each bin. We will determine the success of a fit based on the difference between the final value for the log likelihood and the log likelihood for the mother fit in the same bin, as well as its ability to reproduce the spin density matrix elements. The method we will be using is known as a mass-independent partial-wave analysis.

The resonances being sought are unstable particles, and the probability amplitudes for their propagation, or their *propagators*, are complex functions of their energy and momentum, and depend on how they interact with the vacuum. In principle, calculating these propagators would require summing over an infinite number of Feynman diagrams. However, if we are only interested in states that are unique in their quantum numbers, over a relatively large energy range, then it is possible to approximate the propagator with a constant-width Breit-Wigner. This function relies only on the Mandelstam s and parameters commonly taken to be the mass ( $m$ ) and width ( $\Gamma$ ) of the resonance. When there are multiple states with the same quantum numbers that are close together in mass, relative to their widths, then we cannot use this approximation, and we must use a different approximation. We have chosen to avoid this model dependency by binning our data very finely in  $\sqrt{s}$ , so that the propagator can be approximated by a complex constant in each narrow bin.

This method has been used in the past to study unpolarized  $\omega$  photoproduction for g11a [1] and the results of that run period will be presented alongside the results for g1c and g8b for comparison at each step of the process. We expect that we should see similar results to what was found in g11a, but that the polarization information will give new insight into the reaction. Unpolarized experiments have only three observables to compare, the  $\rho^0$  spin density matrix elements. The g1c run period adds in the two new  $\rho^3$  SDMEs, and the g8b run period adds in six new elements from the  $\rho^1$  and  $\rho^2$  matrices. g11a was able to reproduce the three SDMEs very well with as few as two s-channel waves coupled with the t-channel. The results were split into two regions: from threshold at 1720 MeV up to 2000 MeV the data were well-described by the t-channel and the  $J^P = \frac{3}{2}^-$  and  $\frac{5}{2}^+$  waves; from 2000 MeV to 2400 MeV the data were well described by the t-channel and the  $J^P = \frac{5}{2}^+$  and  $\frac{7}{2}^-$  waves.

## 6.1 Theoretical Models for Non-Resonant Photoproduction

In order to perform our searches it is necessary to have a model for the non-resonant contributions needed. In his thesis [1], Mike Williams determined that the Oh, Titov and Lee [14] model is the best available model for studying  $\omega$  photoproduction. Thus, we will continue to use this model to study g1c and g8b.

### 6.1.1 The Oh, Titov and Lee Model

This model, developed by Oh, Titov and Lee [14] (OTL), includes s-, t-, and u-channel terms. The model was fit to data from SAPHIR [9], SLAC [10], and Daresbury [12]. However, we are already using a model for the s-channel and Williams determined that the u-channel terms did a poor job describing the data at the backwards angles where u-channel processes are thought to dominate for  $\omega$  photoproduction. For energies below  $\sqrt{s} = 2000$  MeV there is no backwards peak in the cross section, thus omitting the u-channel was shown to have no adverse effects [1]. Above  $\sqrt{s} = 2000$  MeV, Williams determined that in the energy range under study, below 2400 MeV, the u-channel should have at most a 30% contribution to the backwards peak and could safely be ignored when searching for the dominant resonance contributions. Thus, he left it out and proceeded only with the s- and t-channel contributions.

#### t-channel

The t-channel model utilizes pseudo-scalar meson,  $\pi^0$  and  $\eta$ , and Pomeron exchange processes. As with the resonant amplitudes, the t-channel amplitudes are calculated according to the prescription set forth in [1], using the parameters listed in Table 6.1. The coupling constants were determined from experiments, except for the  $g_{\eta NN}$  constant which was set using  $g_{\pi NN}$  and an SU(3) relationship because there are not enough backwards angle measurements at high energies for the  $p\eta$  final state. The form factor cutoffs,  $\Lambda$ , come from fits to the data. The parameters for Pomeron exchange were determined by fitting all vector meson ( $\rho$ ,  $\omega$  and  $\phi$ ) total cross sections at high energies. There are no free parameters in this model.

Parameter	Value	Obtained From
$g_{\pi NN}$	13.26	$\pi N$ scattering
$g_{\eta NN}$	3.53	SU(3) relation and $g_{\pi NN}$
$g_{\gamma\pi\omega}$	1.823	$\omega \rightarrow \pi\gamma$ decay width
$g_{\gamma\eta\omega}$	0.416	$\omega \rightarrow \eta\gamma$ decay width
$\Lambda_{\pi NN}$	0.6	Fit to data
$\Lambda_{\gamma\pi\omega}$	0.7	Fit to data
$\Lambda_{\eta NN}$	1.0	Fit to data
$\Lambda_{\gamma\eta\omega}$	0.9	Fit to data
$g_{\omega NN}$	10.35	Fit to data
$\kappa_\omega$	0	Value used by previous models
$\Lambda_{\omega NN}$	0.5	Fit to data

Table 6.1: Oh, Titov and Lee model parameters [14].

## 6.2 The s-channel Scans

Now that we have determined that we will use the OTL t-channel contribution, with no free parameters, and no u-channel contributions, we begin to search for the resonance contributions. We will start by pairing a single s-channel wave with the t-channel and comparing the final log-likelihood values with those from the mother fits. Note that the fitting function and parameters for the s-channel waves are the same as for the mother fit (see Section 5.1.1). The energy range that we will study is from threshold up to  $\sqrt{s} = 2400$  MeV. The g8b dataset only goes up to 2210 MeV and thus we will stop there.

### 6.2.1 One s-channel Wave and OTL t-channel

With these single-wave scans, we are simply looking to see if any particular  $J^P$  state describes the data better than the other waves. Figure 6.1 shows the results of the comparisons to the mother fits for the waves of both parities up to  $J = \frac{7}{2}$  for all three datasets. Values that are closer to 0 indicate better fits than those further away, as it indicates it is closer to the value from the mother fit. We have chosen to divide the difference between the log likelihoods by the number of signal events in each bin. The reason for this is that the final value for the log likelihood per signal event is roughly constant across the entire energy range and it allows for direct comparison between the three datasets without having to account for the differences in statistics.

We can see that the g1c results very closely mirror what we see in g11a. Starting at threshold, the  $\frac{3}{2}^-$  fit is the best until we get to 1840 MeV, where the  $\frac{5}{2}^+$  wave becomes the best until about 2080 MeV. Above 2080 MeV, several waves are very close, and it is difficult to distinguish which is the best in g11a. However, in g1c, the  $\frac{3}{2}^-$  wave seems to be slightly better up to 2280 MeV when the  $\frac{5}{2}^-$  wave takes over. This can also be seen in g11a.

The g8b results are slightly different, mainly because the  $\frac{5}{2}^+$  starts out as the dominant wave from threshold up to 2000 MeV, with the  $\frac{3}{2}^-$  wave never being the best fit near threshold. From 2030-2130 MeV, the  $\frac{3}{2}^-$  wave takes over, as in g1c. Above 2130 MeV, the fits are not well-differentiated.

These results do not allow us to say that any particular resonance is actually present at any particular energy, however they will give us a guide as to which waves are important and which for waves we should look at the SDMEs in comparison to the values from their mother fits. For instance, all three datasets agree that, below 2000 MeV, the  $\frac{5}{2}^+$  wave is important, and that we should see how it interacts in combination with other s-waves.

### 6.2.2 Two s-channel Waves and OTL t-channel

We can now look at pairs of s-channel waves, again keeping the t-channel contribution fixed. The results of these fits for a selection of combinations can be seen in Figure 6.2. Note that all combinations of two waves were fit, those shown here are the best of those fits.

Again, we see excellent agreement between the g1c and g11a results. Both start at threshold with the pairing of  $\frac{3}{2}^-$  and  $\frac{5}{2}^-$  being the best fit for a few bins before the pairing of  $\frac{3}{2}^-$  and  $\frac{5}{2}^+$  becomes the best fit up to 2000 MeV. Several pairs alternate being the best from 2000 MeV up to 2100 MeV after which the  $\frac{5}{2}^+$  and  $\frac{7}{2}^-$  pair and the  $\frac{5}{2}^-$  and  $\frac{7}{2}^+$  pair become the best. At these energies it is not possible to distinguish between these two pairs as they are parity opposites and there is nothing to break the symmetry.

g8b agrees very well with what was seen in g11a and g1c except at threshold. There it shows that the  $\frac{3}{2}^-$ ,  $\frac{5}{2}^-$  pair is the best fit all the way out to 1780 MeV. g1c may also show this, but the 30 MeV wide bins do not allow us to determine precisely where the crossover between the two pairs occurs.

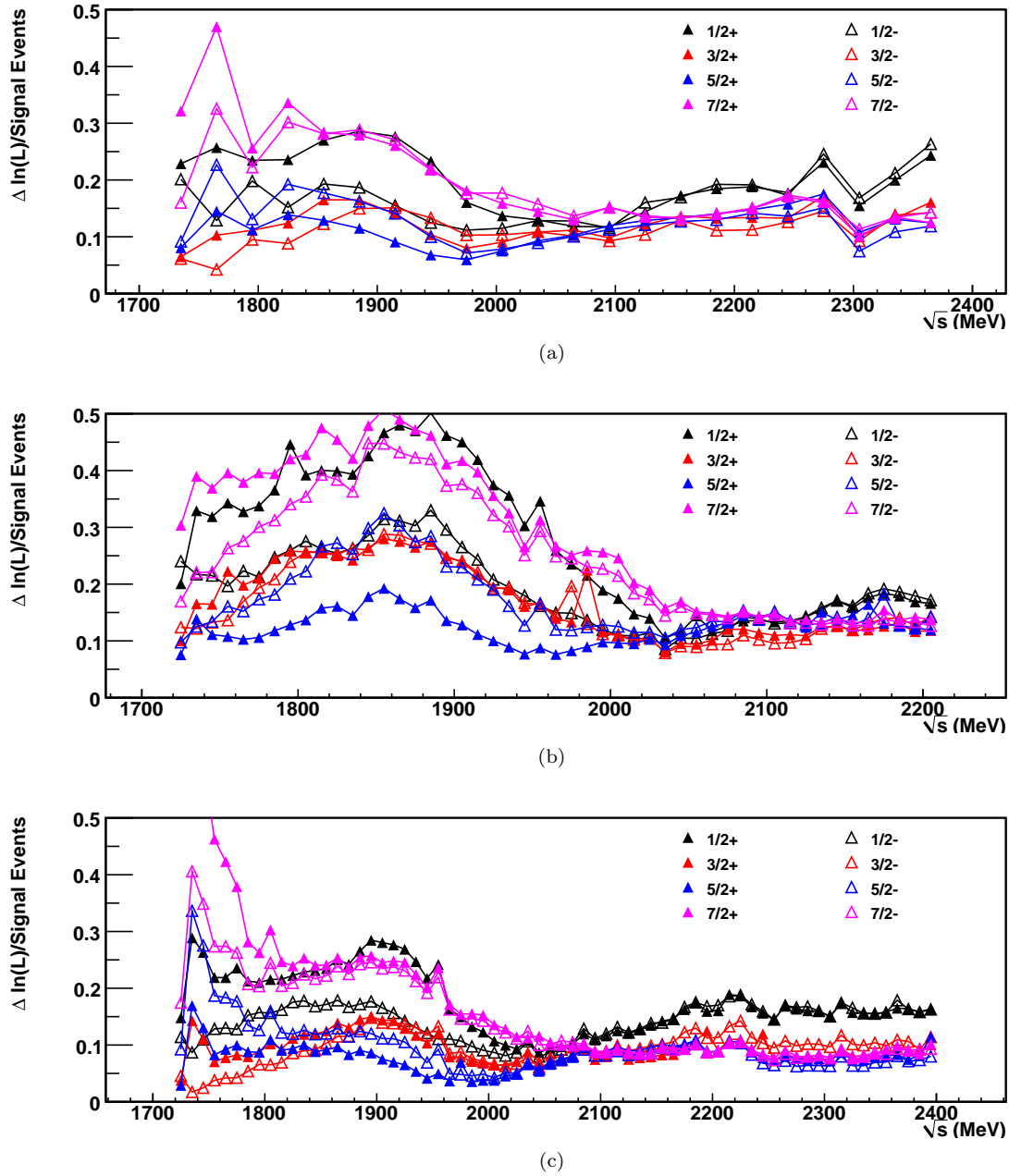


Figure 6.1: Goodness-of-fit plots showing  $\Delta \ln L/\text{signal events}$  vs  $\sqrt{s}$  for (a) g1c, (b) g8b and (c) g11a, for one s-channel wave plus t-channel. The g1c and g11a datasets agree very well, but the g8b dataset differs in the near-threshold bins.

We saw, in the previous section, that the  $\frac{5}{2}^+$  wave was important for all three datasets below 2000 MeV. Here we see that pairing it with the  $\frac{3}{2}^-$  wave gives the best fit for most of the range from threshold up to 2000 MeV in all three datasets.

At this point, we can start to notice something else about the datasets and the  $\Delta \ln(L)$ /signal events values as a function of  $\sqrt{s}$ . Recall that the closer a value is to 0 the better a fit it is and the closer it is to the mother fit. We can see that the best fits in g11a are significantly better than the best fits in g8b and somewhat better than the fits in g1c. This should be somewhat expected, as there is more information in the polarized fits than in the unpolarized fits and therefore it is more likely that there will be differences between the smaller fits compared to the mother fit. It is possible to come up with a  $\chi^2$  metric for the fits by comparing the values obtained from the fit for each of the spin density matrix elements, at each  $\cos \theta_{CM}^\omega$  value, to the mother fit values. This  $\chi^2$  value tracks with the difference in log likelihoods very well. This indicates that the value of  $\Delta \ln(L)$ /signal events is a measure of how well the fit can reproduce the SDMEs. Since there are only three SDMEs in the unpolarized g11a run period, the value should be expected to be less than in g1c where there are five SDMEs or in g8b where there are nine.

We can also see that in all three datasets the fits at threshold are better than those at higher energies. This could indicate that, at threshold, there is a fairly simple process involved in the production of  $\omega$  mesons, while at higher energies there is a more complicated process. This could be indicative of the number of resonances involved in production, or the presence of other processes. In g8b we notice something else as well: the fits between 1800 and 1900 MeV are much worse than those at threshold, while g11a and g1c do not see differences anywhere near that significant. This is a hint that there may be something in this energy range that we are not including in our model.

### 6.2.3 Three s-channel Waves and OTL t-channel

In order to further examine what is going in the 1800-1900 MeV energy range in g8b we have also looked at all combinations of three s-channel waves with the t-channel. With three waves, we start to have enough freedom available in the fits to be able to obtain good fits with multiple combinations of waves, even ones that don't make sense. For instance adding a  $\frac{7}{2}^+$  or  $\frac{7}{2}^-$  wave to the  $\frac{3}{2}^-$ ,  $\frac{5}{2}^-$  combination at threshold yields an excellent fit despite the fact that there is very little likelihood of a  $\frac{7}{2}$  wave being present at threshold. Thus, we do not use these fits as an indication of which combinations of waves to examine further, and have elected to not show a legend of the fits, but instead to better demonstrate what is happening between 1800 and 1900 MeV in g8b.

Figure 6.3 shows the results of the three wave fits for a selection of combinations. In g1c and g11a we can see a fairly steady rise, for the best fit, from threshold up to the higher energies, with a few individual bins showing spikes. In g8b, however, we see that, from 1730-1790 MeV, the value of the best fit is fairly constant, but then it quickly rises above 1800 MeV before coming back down at around 1950 MeV, and then rising very slowly up to the highest energies. Above 1950 MeV, it behaves much like g1c and g11a, but, from 1800-1950 MeV, the fits are much worse than we would otherwise expect them to be. This is an exaggerations of what was seen in the two wave fits.

This could be an indication that there is something significant that is not being accounted for in our models. The u-channel contribution, which has been ignored, does not seem likely as the solution because below 2000 MeV there is not a significant backwards peak, where the u-channel contributes most strongly. It is possible that multiple states with the same quantum numbers could be important in this range. Our model-independent fitting method should be able to take this into account, but it is possible that it is not accounting for it correctly. The shape of the hump looks like a resonance with a width of a few hundred MeV may be responsible, but all of the resonances have been included up to  $\frac{7}{2}$  and it is unlikely a  $\frac{9}{2}$  or  $\frac{11}{2}$  resonance could be found here. Perhaps the t-channel contribution needs to be tweaked. In any case, this is a strong indication that the present model is not completely accounting for everything and needs to be amended.

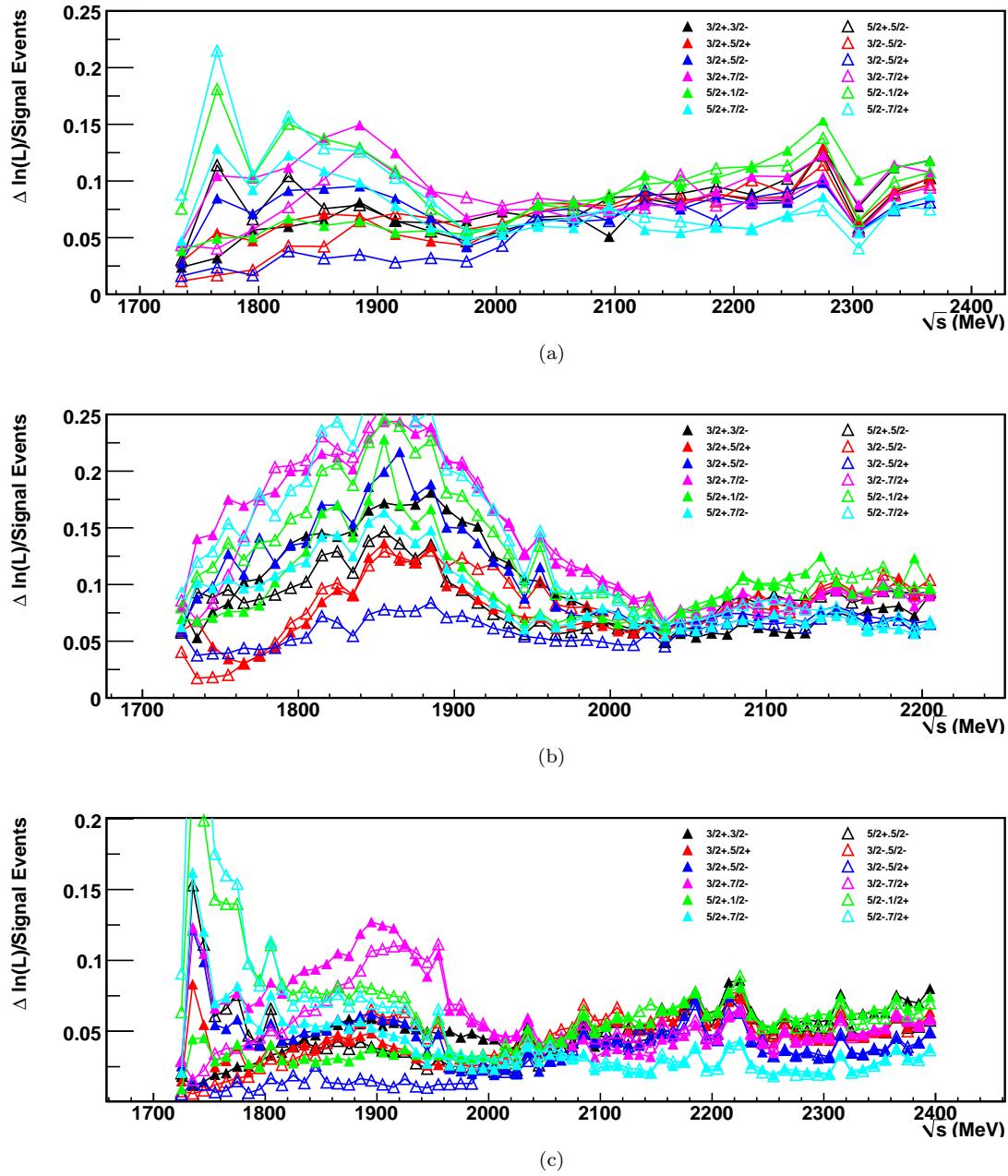


Figure 6.2: Goodness-of-fit plots showing  $\Delta \ln L/\text{signal events}$  vs  $\sqrt{s}$  for (a) g1c, (b) g8b and (c) g11a, for two s-channel waves plus t-channel. g8b and g1c agree with each other and g11a differs mainly near threshold.

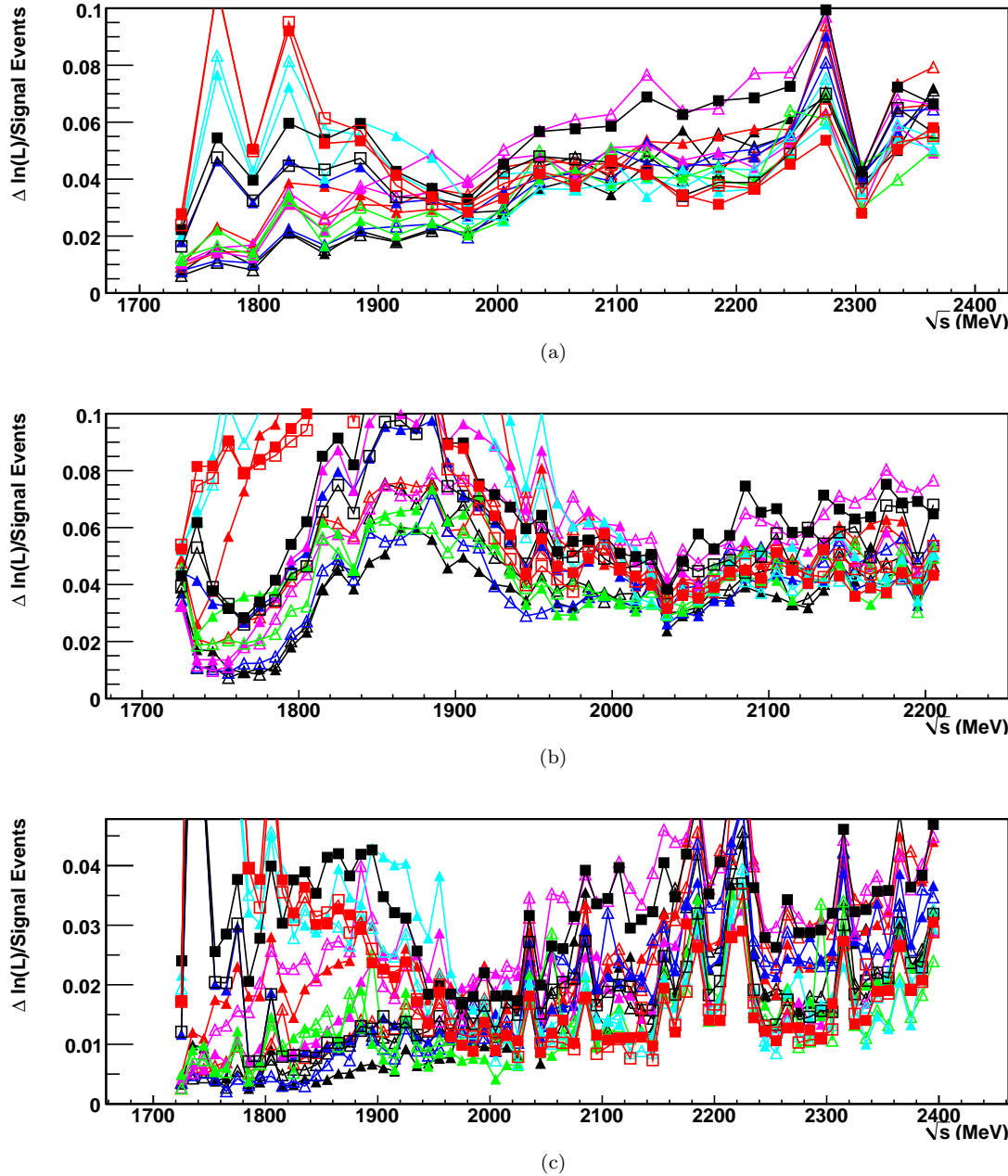


Figure 6.3: Goodness-of-fit plots showing  $\Delta \ln L/\text{signal events}$  vs  $\sqrt{s}$  for (a) g1c, (b) g8b and (c) g11a, for selected three s-channel waves plus t-channel. Notice the significant hump in the g8b results between 1800 and 1950 MeV. There is no legend because the identity of each fit is not important, but rather only the hump from 1800-1950 MeV in the g8b results.

## 6.3 Examining the Parameters

If we make the assumption that each  $J^P$  state included in the PWA fits is dominated by a single  $N^*$  state, then we can have some expectations about how the parameters will behave.

We have seen, in Figures 6.2(a) and 6.2(b), that, for both the g1c and g8b datasets, the  $\frac{3}{2}^-$ ,  $\frac{5}{2}^-$  plus t-channel combination works best below 1780 MeV, and the  $\frac{3}{2}^-$ ,  $\frac{5}{2}^+$  plus t-channel combination works best from 1780-2020 MeV. Also, in g1c we have seen that above 2100 MeV the  $\frac{5}{2}^+$ ,  $\frac{7}{2}^-$  combination fits the data the best. In this section and the next we will restrict our attention to only these fits.

Note that, for our purposes, seeing how the decays vary with respect to  $\sqrt{s}$ , we have opted to bin our data for g1c more finely than was used for extracting the SDMEs and doing the s-channel scans. Thus, we used 10-MeV-wide bins instead of the 30-MeV-wide bins used elsewhere. This is done to allow a better gauge of how quickly the parameters are varying.

### 6.3.1 Decay Parameters

The decay parameters, defined in (5.1), are so called because they account for the decay of the  $J^P$  state to the  $p\omega$  system, denoted by its orbital and spin angular momentum quantum numbers L and S. For  $J^P = \frac{1}{2}^\pm$  states, there are two possible combinations of L and S that the state can decay into; for all other  $J^P$  states, there are three possibilities.

Because we can think of the decay parameters as relating to the probability of the  $J^P$  state decaying into a particular L,S system, if there is only one  $N^*$  in a given  $J^P$ , then we can assume that the decay couplings will be either roughly constant or at least a smoothly varying function of  $\sqrt{s}$ . In short, the functional dependence on  $\sqrt{s}$  will be similar in all of the decay couplings. Thus, if we were to divide all of the decay parameters in a given  $J^P$  by one of the values, say of the lowest L,S state, then we would expect to see either constant values or a smoothly varying function of  $\sqrt{s}$  for all of the decay parameters (obviously the lowest L,S state would be constant at a value of 1). If the single  $N^*$  assumption is not true in this energy range, then we would expect to see non-smooth functions of  $\sqrt{s}$  and perhaps even discontinuities.

#### The $\frac{3}{2}^-$ , $\frac{5}{2}^-$ Plus t-channel Fits

In Figure 6.4, we can see the decay parameters in g8b for the  $\frac{3}{2}^-$ ,  $\frac{5}{2}^-$  combination, where each of the  $\frac{3}{2}^-$  parameters have been divided by the lowest L,S combination, here L=0, S= $\frac{3}{2}$ , and likewise the  $\frac{5}{2}^-$  parameters have been divided by the L=2, S= $\frac{1}{2}$  parameter. For the  $\frac{3}{2}^-$  decays, we can see that the L=2, S= $\frac{1}{2}$  state varies linearly until 1770 MeV, however the L=2, S= $\frac{3}{2}$  state is not as smooth. For the  $\frac{5}{2}^-$  decays, we can see that the L=2, S= $\frac{3}{2}$  state is constant, while the L=4, S= $\frac{3}{2}$  state is not smooth at all. It is difficult to draw reliable conclusions from this, since one parameter varies smoothly and the other does not in each  $J^P$  state. It could indicate that one parameter is necessary and the other is not, or that there is more than one  $N^*$  state present.

We can see the decay parameters in g1c for  $\frac{3}{2}^-$ ,  $\frac{5}{2}^-$  in Figure 6.5. We see very similar results to what was seen in g8b, where two of the parameters vary smoothly while the other two do not.

#### The $\frac{3}{2}^-$ , $\frac{5}{2}^+$ Plus t-channel Fits

In Figure 6.6, we can see the decay parameters in g8b for the  $\frac{3}{2}^-$ ,  $\frac{5}{2}^+$  combination, again dividing out the lowest L,S combination. Here, we see a slightly clearer story. For the  $\frac{3}{2}^-$  decays, the L=2, S= $\frac{1}{2}$  combination looks to be rising linearly with  $\sqrt{s}$ , until 1980 MeV, although there is a bit of scatter around that line; for the L=2, S= $\frac{3}{2}$  combination, we see a very smooth function, until 1950

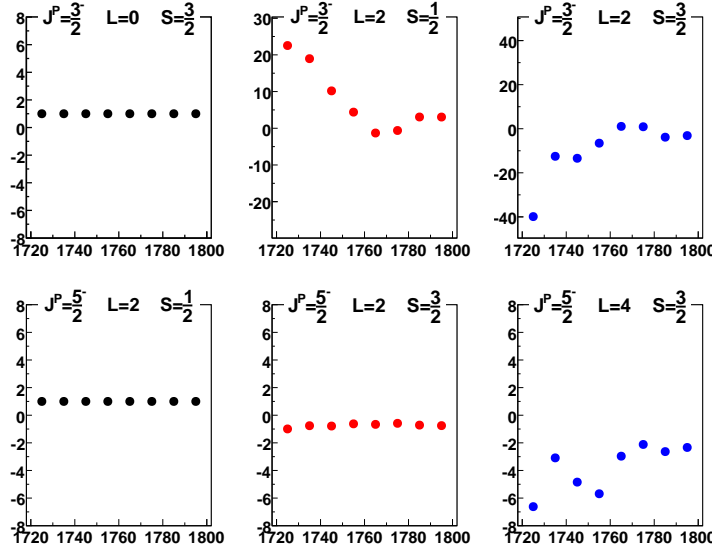


Figure 6.4: Decay Parameters for  $\frac{3}{2}^-$ ,  $\frac{5}{2}^-$  vs  $\sqrt{s}$  in g8b. The parameters have been normalized by the lowest (leftmost) L, S combination decay. This combination is found to be dominant over the range from 1720-1780 MeV. Since this is such a small range we should expect that if there were only a single  $N^*$  per  $J^P$  the decays should be constant, or vary smoothly. The parameters do not all vary smoothly over the entire range, indicating that the single  $N^*$  per  $J^P$  assumption may be invalid

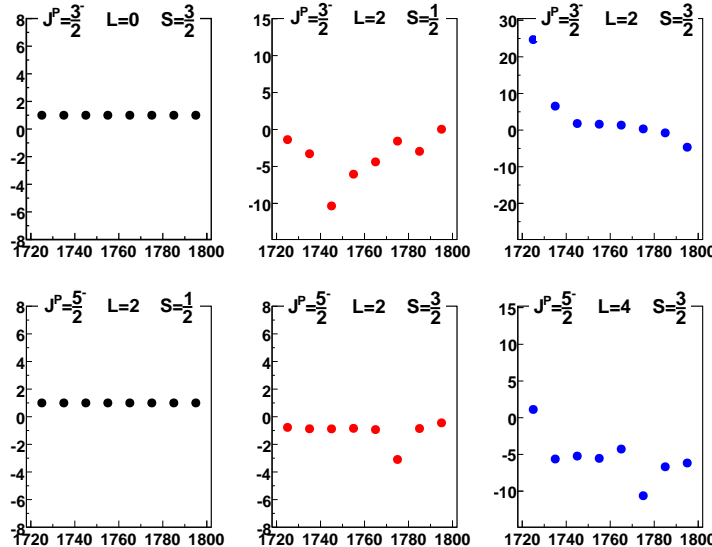


Figure 6.5: Decay Parameters for  $\frac{3}{2}^-$ ,  $\frac{5}{2}^-$  vs  $\sqrt{s}$  in g1c. The parameters have been normalized by the lowest (leftmost) L, S combination decay. The parameters do not all vary smoothly over the entire range, indicating that the single  $N^*$  per  $J^P$  assumption may be invalid

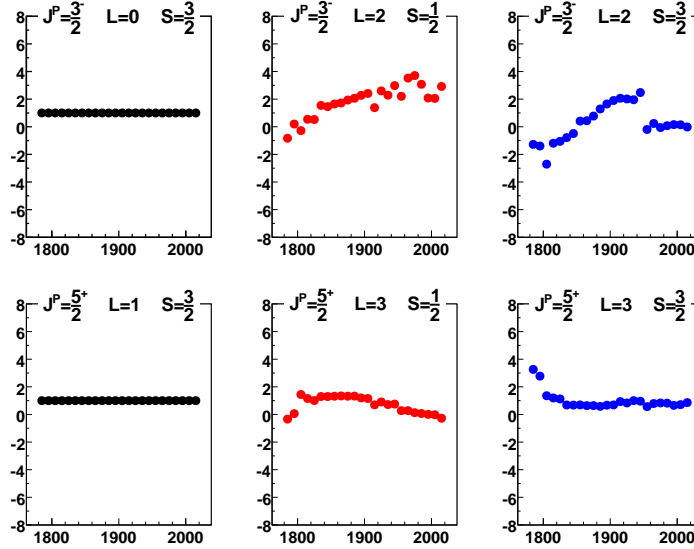


Figure 6.6: Decay Parameters for  $\frac{3}{2}^-$ ,  $\frac{5}{2}^+$  vs  $\sqrt{s}$  in g8b. The parameters have been normalized by the lowest (leftmost) L, S combination decay. The parameters vary smoothly except for a sharp discontinuity at 1950 MeV in the  $J^P = \frac{3}{2}^-$ ,  $L=2$ ,  $S=\frac{3}{2}$  parameter.

MeV where there is a sudden discontinuity after which the points go to 0. This discontinuity is a strong indication that an  $N^*$  state has either turned on or turned off near this energy. For the  $\frac{5}{2}^+$  decays, we see both are very smooth functions above 1800 MeV. This set of parameters is more indicative of a single  $\frac{3}{2}^- N^*$  and a single  $\frac{5}{2}^+ N^*$ , at least between 1800 and 1950 MeV.

The decay parameters for the  $\frac{3}{2}^-$ ,  $\frac{5}{2}^+$  combination in g1c can be seen in Figure 6.7. Both of the  $\frac{3}{2}^-$  decays show a significant discontinuity at 1840 MeV and then vary smoothly. This is in contrast to what was seen in g8b where the  $L=2$ ,  $S=\frac{3}{2}$  combination showed a discontinuity at 1950 MeV. Both of the  $\frac{5}{2}^+$  decay combinations vary smoothly over the entire range, similar to what was seen in g8b.

### The $\frac{5}{2}^+$ , $\frac{7}{2}^-$ Plus t-channel Fit

The decay parameters for the  $\frac{5}{2}^+$ ,  $\frac{7}{2}^-$  combination in g1c can be seen in Figure 6.8. The  $\frac{5}{2}^+$  decays do not seem smooth over any range. For the  $\frac{7}{2}^-$  decays, the  $L=4$ ,  $S=\frac{1}{2}$  combination is smooth and constant over the entire range, while the  $L=4$ ,  $S=\frac{3}{2}$  combination is smooth below 2250 MeV and then becomes very unstable.

We have seen similar results between the two datasets. The  $\frac{3}{2}^-$ ,  $\frac{5}{2}^+$  combination shows indications that our fit is not stable, which could either indicate multiple  $N^*$ 's per  $J^P$  state, or that we are missing another  $J^P$  state. The  $\frac{3}{2}^-$ ,  $\frac{5}{2}^+$  combination shows a distinct discontinuity in the  $\frac{3}{2}^-$  state in both datasets, although the two datasets disagree on where the discontinuity occurs. And, in the g1c dataset, we see indications that the fits are unstable, certainly above 2250 MeV.

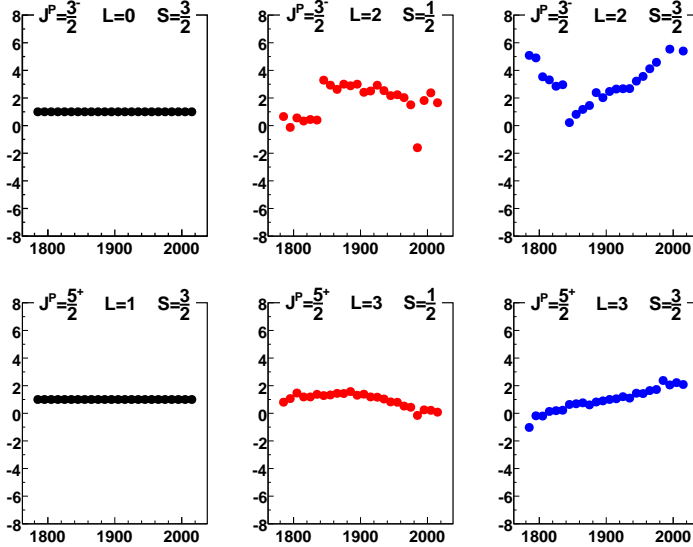


Figure 6.7: Decay Parameters for  $\frac{3}{2}^-$ ,  $\frac{5}{2}^+$  vs  $\sqrt{s}$  in g1c. The parameters have been normalized by the lowest (leftmost) L, S combination decay. For the most part, the parameters vary smoothly except for a sharp discontinuity at 1850 MeV in the  $J^P = \frac{3}{2}^-$  parameters.

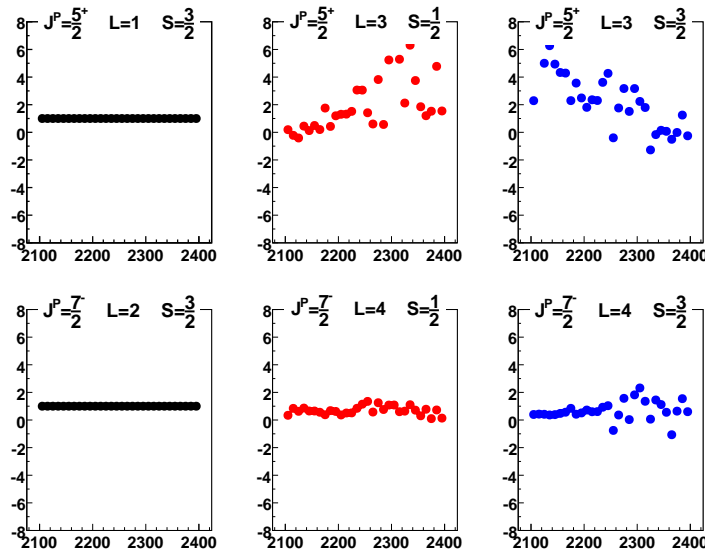


Figure 6.8: Decay Parameters for  $\frac{5}{2}^+$ ,  $\frac{7}{2}^-$  vs  $\sqrt{s}$  in g1c. The parameters have been normalized by the lowest (leftmost) L, S combination decay. The  $J^P = \frac{5}{2}^+$  parameters are not smooth over any range. The  $\frac{7}{2}^-$  parameters are mostly smooth below 2250 MeV.

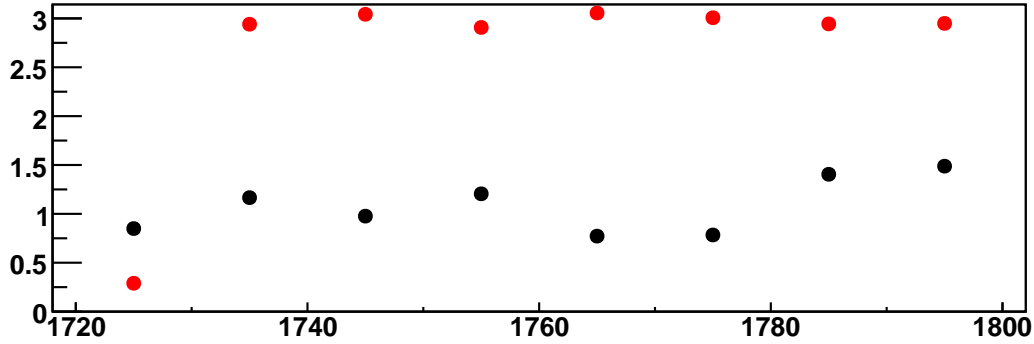


Figure 6.9: Multipole Parameters for  $\frac{3}{2}^-, \frac{5}{2}^-$  vs  $\sqrt{s}$  in g8b. The  $\frac{3}{2}^-$  parameter is in black; the  $\frac{5}{2}^-$  parameter is in red. Neither is a smooth function over the entire range.

### 6.3.2 Multipole Parameters

The amplitudes used in our fits are written using the multipole basis to account for the fact that two of the Lorentz invariant amplitudes at each  $\gamma p N^*$  vertex are not angularly independent. Recall, from (5.1), that one of our parameters is a multipole production angle,  $\theta_{JP}$ , which we take the cosine/sine of if our amplitude contains an electric/magnetic multipole. As a result of how it is defined, this angle will also be a smoothly varying function of  $\sqrt{s}$ , specifically an arctan function, if we assume that there is only one  $N^*$  contributing to each  $J^P$  state. So, we can now proceed to examine the multipole parameter for the same combinations used in examining the decays.

#### The $\frac{3}{2}^-, \frac{5}{2}^-$ Plus t-channel Fits

The multipole production angles for the  $\frac{3}{2}^-, \frac{5}{2}^-$  combination for g8b can be seen in Figure 6.9. We note similar results to what was seen for the decays for this combination, which is that neither can be taken to be a smooth function.

The multipole production angles for the  $\frac{3}{2}^-, \frac{5}{2}^-$  combination for g1c can be seen in Figure 6.10. Here, as in g8b and in the decay parameters for this combination in g1c, we see that there is no smooth function that will fit all of the points for either parameters.

#### The $\frac{3}{2}^-, \frac{5}{2}^+$ Plus t-channel Fits

The multipole production angles for the  $\frac{3}{2}^-, \frac{5}{2}^+$  combination for g8b can be seen in Figure 6.11. Again, we see very similar results to what was seen in the plots of the decay parameters. Both of the multipole parameters are smooth functions from 1780-1950 MeV and then there is a sharp discontinuity, after which both functions are smooth again. This bolsters our claim that there is something happening at 1950 MeV, either a resonance turning on or off, or another process that is not included in our fit. However, it could simply be a fit instability.

The multipole production angles for the  $\frac{3}{2}^-, \frac{5}{2}^+$  combination for g1c can be seen in Figure 6.12. Again, the parameters mirror what is seen in the decays for this combination, both are smooth functions with a sharp discontinuity at 1850 MeV.

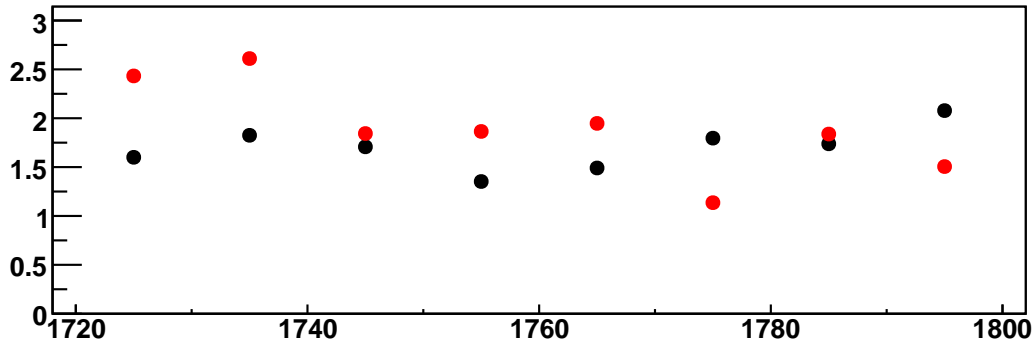


Figure 6.10: Multipole Parameters for  $\frac{3}{2}^-$ ,  $\frac{5}{2}^-$  vs  $\sqrt{s}$  in g1c. The  $\frac{3}{2}^-$  parameter is in black; the  $\frac{5}{2}^-$  parameter is in red. Neither is a smooth function over the entire range.

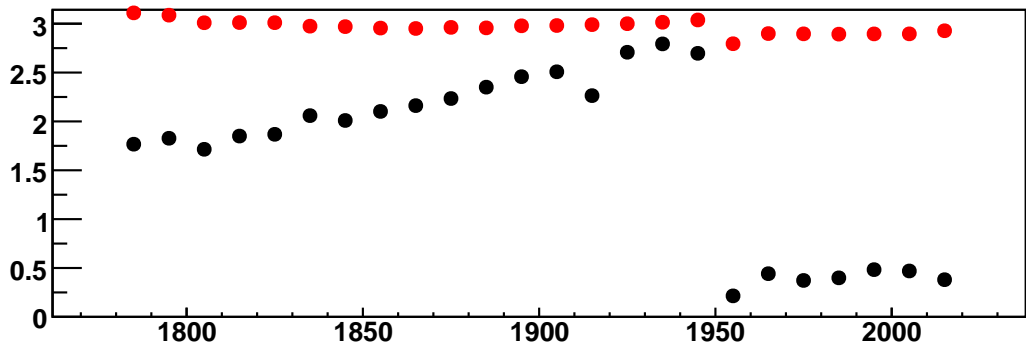


Figure 6.11: Multipole Parameters for  $\frac{3}{2}^-$ ,  $\frac{5}{2}^+$  vs  $\sqrt{s}$  in g8b. The  $\frac{3}{2}^-$  parameter is in black; the  $\frac{5}{2}^+$  parameter is in red. Both are smooth functions of energy except for a large discontinuity at 1950 MeV.

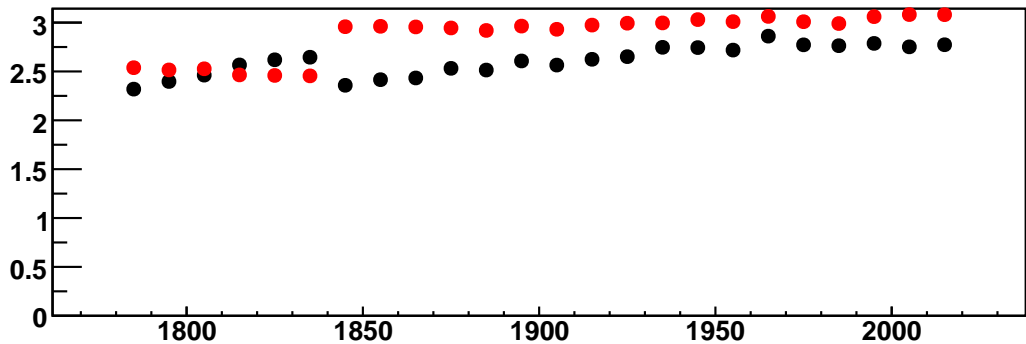


Figure 6.12: Multipole Parameters for  $\frac{3}{2}^-$ ,  $\frac{5}{2}^+$  vs  $\sqrt{s}$  in g1c. The  $\frac{3}{2}^-$  parameter is in black; the  $\frac{5}{2}^+$  parameter is in red. Both are smooth functions of energy except for a discontinuity at 1850 MeV.

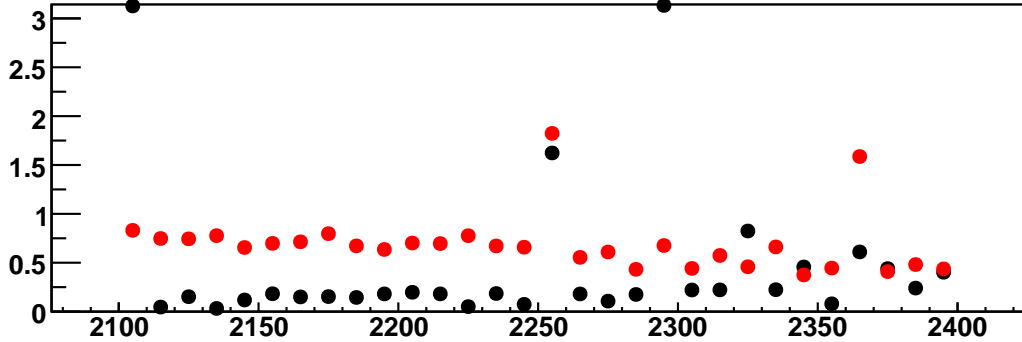


Figure 6.13: Multipole Parameters for  $\frac{5}{2}^+$ ,  $\frac{7}{2}^-$  vs  $\sqrt{s}$  in g1c. The  $\frac{5}{2}^+$  parameter is in black; the  $\frac{7}{2}^-$  parameter is in red. Both parameters are very smooth and almost constant functions of energy, with the exception of two points, at 2255 MeV and 2365 MeV, where for some reason the fits apparently were not able to converge.

#### The $\frac{5}{2}^+$ , $\frac{7}{2}^-$ Plus t-channel Fit

The multipole production angles for the  $\frac{5}{2}^+$ ,  $\frac{7}{2}^-$  combination for g1c can be seen in Figure 6.13. Here, we see very smooth and almost constant functions for each parameter, with the exception of three points, at 2100 MeV, 2255 MeV, and 2365 MeV. This is in sharp contrast to what was seen in the decays, where the  $\frac{7}{2}^-$  decay parameters were only reasonably well-behaved below 2250 MeV, but the  $\frac{5}{2}^+$  parameters were never smooth.

## 6.4 Comparison to SDMEs

We can now look at how well the best fits were able to reproduce the spin density matrix elements. These elements are a good gauge of how well the combination of waves chosen are fitting the data. All of the combinations are able to fit the cross section reliably, but the SDMEs are much more sensitive to the quality of the fit. Recall that the difference in the log likelihoods is similar to a  $\chi^2$  value computed using the differences between the SDMEs. For all of the figures in this section, the SDMEs measured from the mother fit will be presented as black points, with error bars, and the results from the two waves fits will be presented as red dashed lines, with no error bars. The errors have not been calculated for the two-wave fits because we are mainly just looking for trends and shapes, not a true measure of how different the two values are, that is already calculated in the difference of the log likelihoods. For each of the best fits we will show all of the SDMEs for a single bin, chosen to be in the middle of the energy range where that fit is the best, where the fits should be the most reliable. For one of the polarized SDMEs, from the  $\frac{3}{2}^-, \frac{5}{2}^+$  plus t-channel fit from g8b, we will show the entire range in  $\sqrt{s}$  to show that there is not much variation in the quality of the fits from bin to bin. However, showing all of the SDMEs for each fit, over the entire energy range would require too much space.

### 6.4.1 The $\frac{3}{2}^-, \frac{5}{2}^+$ Plus t-channel Fits

We can see the comparison of the SDMEs for g8b in the bin centered at 1755 MeV in Figure 6.14. The unpolarized SDMEs,  $\rho^0$ , do not match perfectly, but show qualitative agreement, especially with the shapes. The  $\text{Re}(\rho_{10}^0)$  element in particular shows very good agreement, although the agreement

is worse in the backwards angles,  $\cos \theta_{CM}^\omega \leq 0$ . The polarized SDMEs,  $\rho^1$  and  $\rho^2$ , also show good qualitative agreement, although here the major discrepancies are at the forward angles, beyond  $\cos \theta_{CM}^\omega = 0.5$ , especially in the  $\rho_{1-1}$  elements. The  $\text{Im}(\rho_{10}^2)$  element is shifted up slightly at all angles.

In Figure 6.15, we can see the comparison of the SDMEs for g1c in the bin centered at 1765 MeV. Here, we see excellent agreement at all angles for each of the SDMEs. The two polarized elements,  $\rho^3$ , are quite small and the two-wave fit remains flat across the entire angular range, while the results from the mother fit do have some shape to them; however, the agreement is still quite good.

Based on these comparisons, it is reasonable to say that the g1c data can be fit by the  $\frac{3}{2}^-$  and  $\frac{5}{2}^-$  wave quite well and that perhaps no other resonance is required. The g8b data, however, shows significant differences from the mother fit and indicates that another resonance or other process is required to fit the data fully.

### 6.4.2 The $\frac{3}{2}^-$ , $\frac{5}{2}^+$ Plus t-channel Fits

There was excellent agreement between the three unpolarized SDMEs extracted from the  $\frac{3}{2}^-$ ,  $\frac{5}{2}^+$  combination to those extracted from the mother fit in g11a [1]. Here, we will see how adding in the polarization information affects our results. In Figure 6.16, we can see the comparison of the SDMEs for g8b in the bin centered at 1885 MeV. The  $\rho_{00}^0$  element shows reasonable agreement in shape although it is shifted down at most angles from the mother fit. The  $\text{Re}(\rho_{10}^0)$  element is able to get the overall trend correct, but misses most of the nuance and shape of the mother fit. The  $\rho_{1-1}^0$  element shows a very different shape than the results from the mother fit, especially at forward angles. Based only on the unpolarized SDMEs, one could still qualify this fit as doing a reasonable job. The polarized SDMEs, however, reveal that this fit is much worse. Most of the polarized elements are not close on either shape or scale. The  $\text{Re}(\rho_{10}^1)$ , for instance, is almost a mirror image of what the mother fit result is doing, and the  $\text{Im}(\rho_{1-1})$  elements don't show any correlation at all to what the mother fit is doing, although they do still appear to be inverted copies of each other in the same way that the mother fit does.

Figure 6.17 shows a single polarized element, the  $\text{Re}(\rho_{10}^1)$  element, as it evolves in  $\sqrt{s}$  over the entire range in which this fit is the best combination of two s-channel waves plus t-channel in g8b. It is clear that this fit is unable to reliably reproduce the results of the mother fit for any bin in the range.

In Figure 6.18 we can see the comparison of the SDMEs for g1c in the bin centered at 1885 MeV. The unpolarized elements very closely match what was seen in g8b. Again, the  $\text{Re}(\rho_{10}^0)$  element is in poor agreement. The two polarized elements are in better agreement than what was seen in g8b, however, they don't follow the shape of the mother fit results, but rather cut across it, without shape of their own.

Both of these fits show that, even for the unpolarized SDMEs, some other process is needed to obtain a better match with the mother fit. The polarized elements further demonstrate that need. This is in contrast to what was seen in [1], where good agreement was seen for all three unpolarized SDMES. The difference between the two datasets shows the power of adding in the polarization information.

### 6.4.3 The $\frac{5}{2}^+$ , $\frac{7}{2}^-$ Plus t-channel Fits

In Figure 6.19 we can see the comparison of the SDMEs for g8b in the bin centered at 2185 MeV. Except for backwards of -0.5 in  $\rho_{00}^0$ , the unpolarized SDMEs are in very good agreement, although missing some of the nuances of the shape, for all three elements. Based only on this, we would be tempted to say that these two resonances are doing a very good job of fitting the data in this bin, but when we examine the polarized elements we can see that there is significantly less agreement.

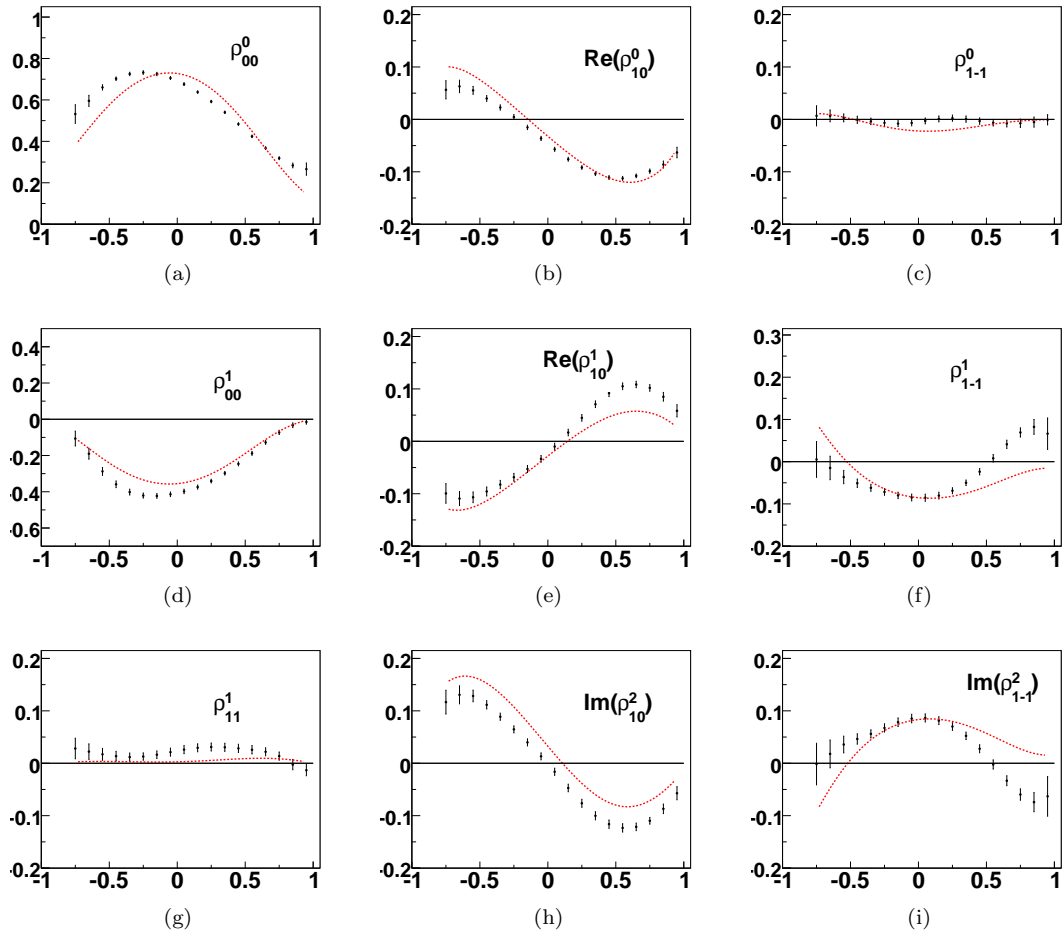


Figure 6.14: Spin Density Matrix elements vs  $\cos \theta_{CM}^\omega$  in the bin  $\sqrt{s} = 1755$  MeV, which is in the center of the energy range for which the  $\frac{3}{2}^-, \frac{5}{2}^-$  combination gives the best fit for the g8b dataset. The results from the mother fit are shown in black with error bars, the results from the  $\frac{3}{2}^-, \frac{5}{2}^-$  fit are shown as the red dashed lines. The unpolarized SDMEs,  $\rho^0$ , are in fairly good agreement. The polarized SDMEs,  $\rho^1$  and  $\rho^2$ , show reasonable agreement as well, although there is a noticeable discrepancy at angles beyond 0.5, especially in the  $\rho_{1-1}$  elements. The  $\text{Im}(\rho_{10}^2)$  element is shifted up slightly at all angles.

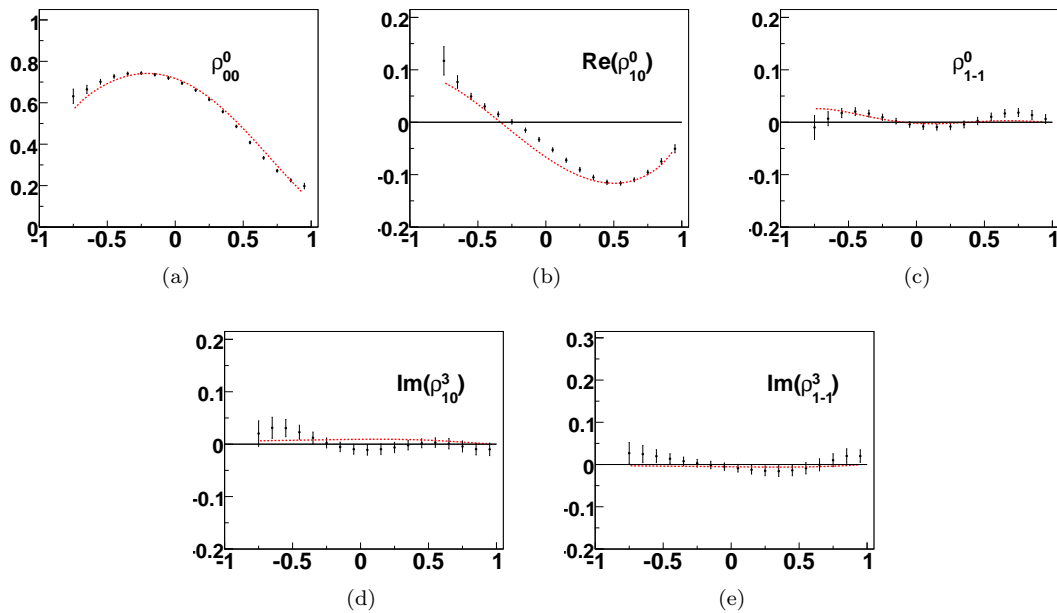


Figure 6.15: Spin Density Matrix elements vs  $\cos \theta_{CM}^\omega$  in the bin  $\sqrt{s} = 1765$  MeV, which is in the center of the energy range for which the  $\frac{3}{2}^-, \frac{5}{2}^-$  combination gives the best fit for the g1c dataset. The results from the mother fit are shown in black with error bars, the results from the  $\frac{3}{2}^-, \frac{5}{2}^-$  fit are shown as the red dashed lines. The results for the unpolarized,  $\rho^0$ , elements are excellent. The two polarized,  $\rho^3$  SDMEs are in good agreement as well.

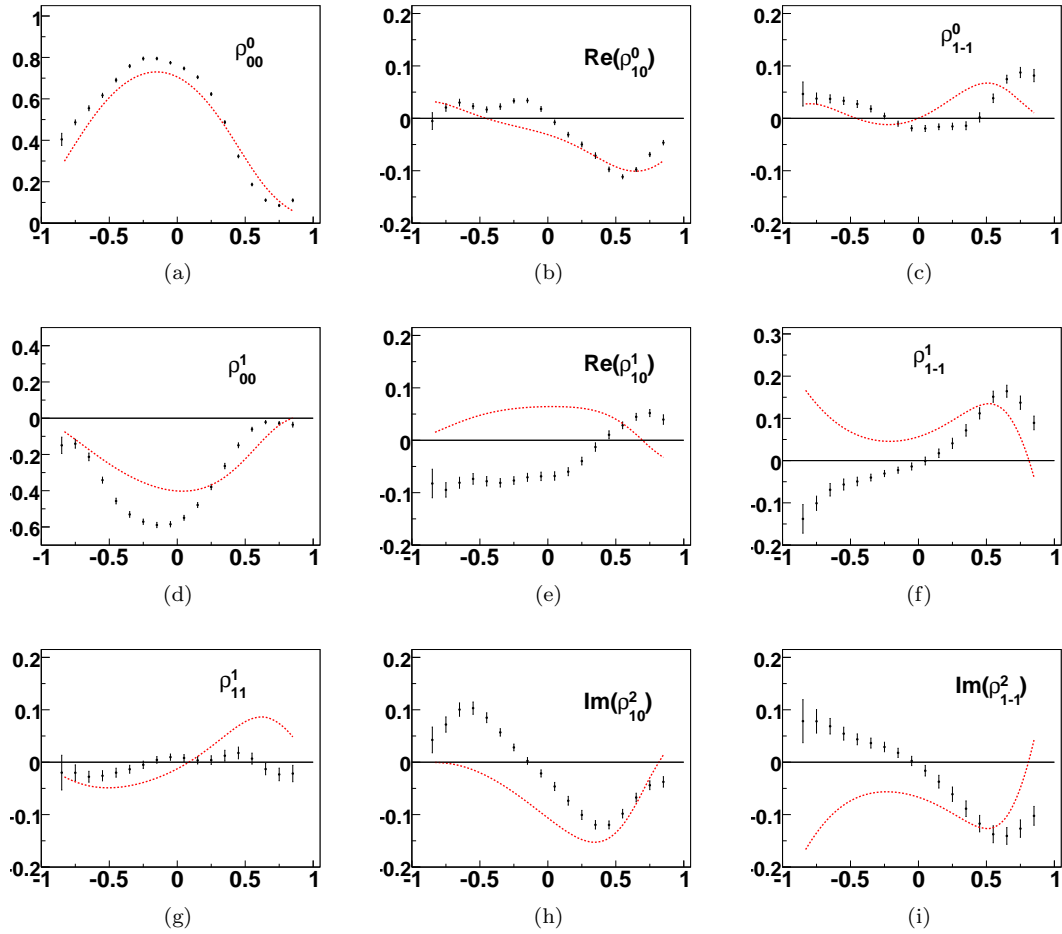


Figure 6.16: Spin Density Matrix elements vs  $\cos \theta_{CM}^\omega$  in the bin  $\sqrt{s} = 1885$  MeV, which is in the center of the energy range for which the  $\frac{3}{2}^-, \frac{5}{2}^+$  combination gives the best fit for the g8b dataset. The results from the mother fit are shown in black with error bars, the results from the  $\frac{3}{2}^-, \frac{5}{2}^+$  fit are shown as the red dashed lines. It is clear from these plots that, while the unpolarized SDMEs,  $\rho^0$ , are somewhat reasonably reproduced by the smaller fit, the polarized SDMEs,  $\rho^1$  and  $\rho^2$ , are in very poor agreement, indicating that the fit is missing some resonances.

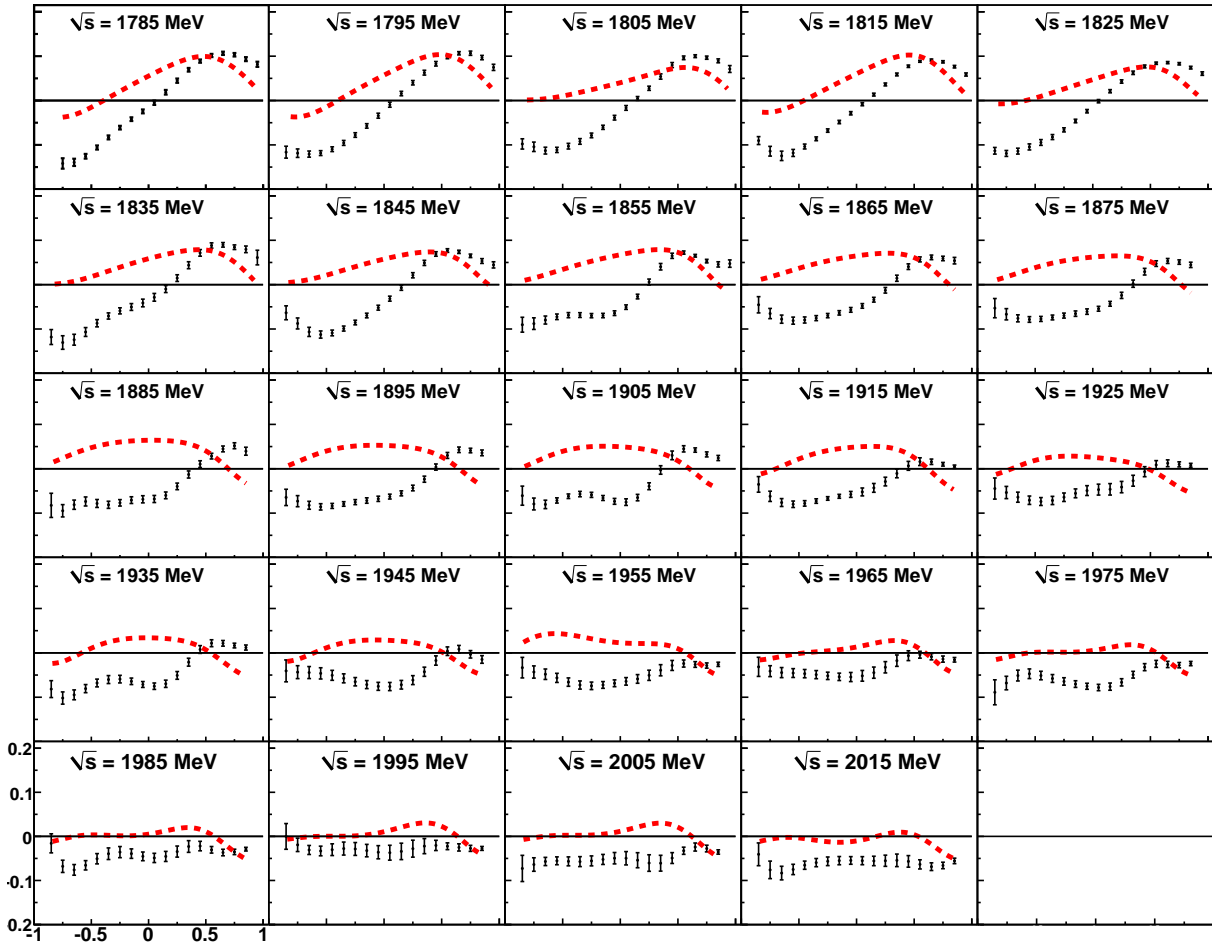


Figure 6.17:  $\text{Re}(\rho_{10}^1)$  element vs  $\cos(\theta_{CM}^\omega)$  in bins of  $\sqrt{s}$ . The results from the mother fit are shown in black with error bars, the results from the  $\frac{3}{2}^-$ ,  $\frac{5}{2}^+$  fit are shown as the red dashed lines. It is clear that these fits are not able to reproduce the results from the mother fit reliably.

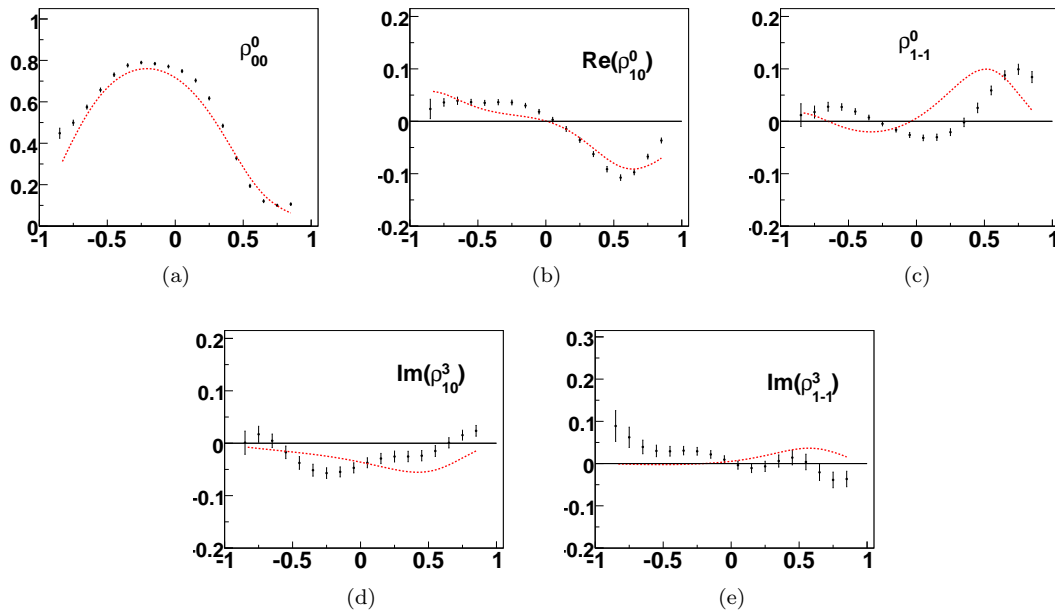


Figure 6.18: Spin Density Matrix elements vs  $\cos \theta_{CM}^\omega$  in the bin  $\sqrt{s} = 1885$  MeV, which is in the center of the energy range for which the  $\frac{3}{2}^-, \frac{5}{2}^+$  combination gives the best fit for the g1c dataset. The results from the mother fit are shown in black with error bars, the results from the  $\frac{3}{2}^-, \frac{5}{2}^+$  fit are shown as the red dashed lines. The results for the unpolarized,  $\rho^0$ , elements are very similar to what is seen in g8b. Here the two polarized,  $\rho^3$  SDMEs are in better agreement than what is seen in g8b.

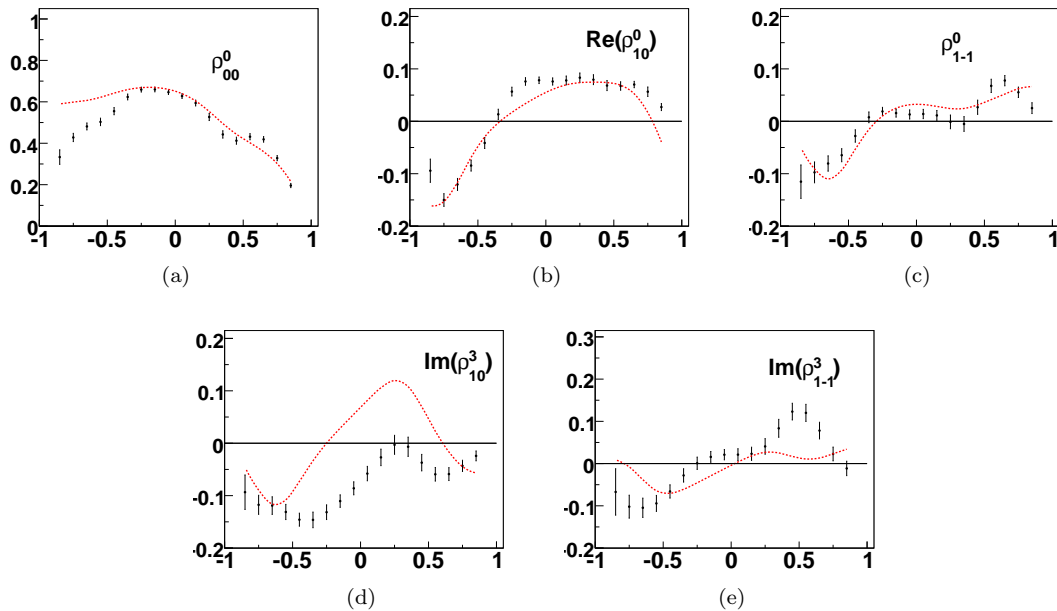


Figure 6.19: Spin Density Matrix elements vs  $\cos \theta_{CM}^\omega$  in the bin  $\sqrt{s} = 2185$  MeV, which is in the center of the energy range for which the  $\frac{5}{2}^+$ ,  $\frac{7}{2}^-$  combination gives the best fit for the g1c dataset. The results from the mother fit are shown in black with error bars, the results from the  $\frac{5}{2}^+$ ,  $\frac{7}{2}^-$  fit are shown as the red dashed lines. The results for the unpolarized,  $\rho^0$ , elements are in good agreement, except for the most backwards angles, backwards of  $\cos \theta_{CM}^\omega = -0.5$ , in the  $\rho_{00}^0$  element. However, the polarized SDMEs,  $\rho^3$ , show noticeably less agreement.

#### 6.4.4 Summary

We can determine how well a fit is able to represent the data by comparing the SDMEs to those obtained from the mother fit. By using polarized data, we are able to expand the number of observable SDMEs and thus better differentiate good and bad fits. A fit like the  $\frac{5}{2}^+$ ,  $\frac{7}{2}^-$  combination matches the unpolarized SDMEs very well, and it would be possible to think that only those two waves are present and necessary to fit the data, but the polarized SDMEs show that some other process is also important.

### 6.5 Combined Fits

In Section 4.6, we showed that it is possible to combine datasets together in a log likelihood fit by simply adding the likelihoods together. This was necessary for the g1c and g8b datasets, which each had two or more datasets in most energy bins. It is also possible to combine the g1c and g8b datasets, and also add in the g11a dataset. The combination of these three datasets will have significantly more statistics, and thus should be more stable. Also, because it will have both linear and circular polarization included, we should get a more robust fit. In order to combine the datasets together, we do require that they all have the same binning, and thus we will bin the g1c data in 10 MeV-wide-bins instead of the 30 MeV wide bins used previously. Recall that the g8b dataset only goes out to 2210 MeV, thus above 2210 MeV only the g11a and g1c datasets are involved in the fits.

In Figure 6.20, the SDMEs obtained from the combined g11a, g1c and g8b mother fit are presented for the 1885 MeV bin, in comparison to the values obtained from the other mother fits. The quality of the fits is apparent as there is almost no difference between the values from the two mother fits in the unpolarized SDMEs. For the polarized SDMEs there are a few small differences, but nothing significant. It should be noted that error bars were not calculated for the SDMEs for the combined fits due to the massive computational expense. Given how closely the values mirror each other they are not necessary. In all cases, they should be expected to be smaller than those from any of the datasets on their own.

#### 6.5.1 s-wave Scans

Since the mother fit is able to reproduce the SDMEs with good quality, we can proceed to look at the s-wave scans. In Figure 6.21, we can see the results of the one-, two- and three-wave scans. They are, of course, similar to what was seen in the single-dataset scans, but it is interesting to note where there were differences between the single-dataset scans. In the one-wave scan, g1c and g11a each showed the  $\frac{3}{2}^-$  wave dominant from threshold out to 1840 MeV, while g8b showed the  $\frac{5}{2}^+$  wave dominant over that same range. In the combined fit, the  $\frac{3}{2}^-$  wave is dominant from threshold out to only 1760 MeV. For the two wave fits, the g11a dataset had the  $\frac{3}{2}^-$ ,  $\frac{5}{2}^+$  combination takes dominance from the  $\frac{3}{2}^-$ ,  $\frac{5}{2}^-$  combination at 1750 MeV while in the g1c and g8b datasets that occurs at 1780 MeV. Here, the polarized datasets have won out and the crossing occurs at 1780 MeV. Also, note in both the two- and three-wave fits, that the pattern seen in g8b of significantly worse fits between 1800 and 1950 MeV recurs here as well.

#### 6.5.2 Examining the Parameters

Since the same combinations are dominant in the same places as in the single dataset scans we can look at the parameters in the same way as before.

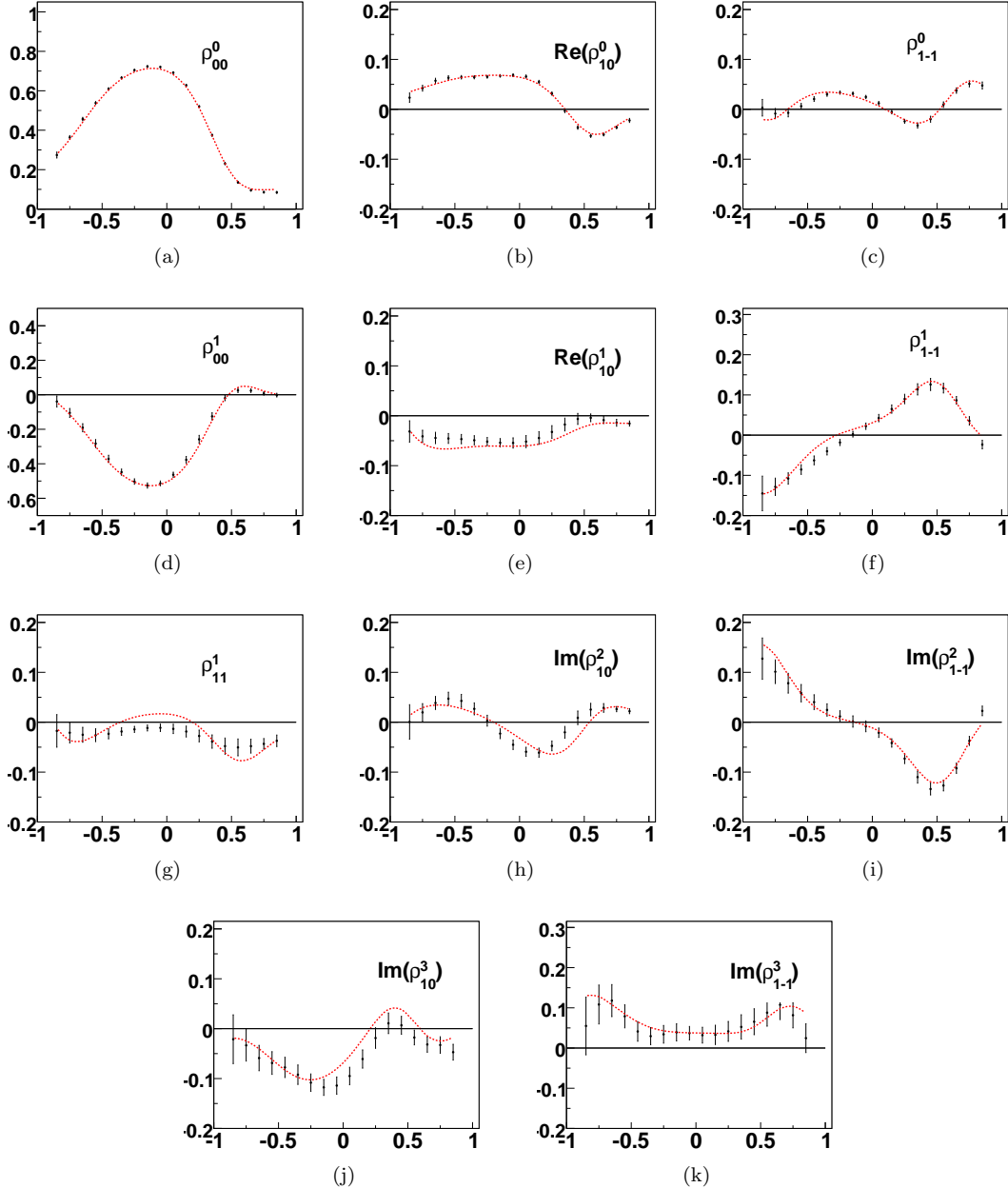


Figure 6.20: Spin Density Matrix elements vs  $\cos \theta_{CM}^\omega$  in the bin  $\sqrt{s} = 1965$  MeV, which is in the center of the energy range for the combined g1c, g8b and g11a datasets. For the unpolarized,  $\rho^0$ , elements, the black points are from the g11a mother fit; for the  $\rho^1$  and  $\rho^2$  elements, the black points are from the g8b mother fit; for the  $\rho^3$  elements, the black points are from the g1c mother fit (in 10-MeV-wide bins). The red dashed lines, shown without error bars, are from the combined g1c, g8b and g11a datasets mother fit. The  $\rho^0$  elements show near perfect agreement. The polarized elements are also in good agreement, although there are some small differences.

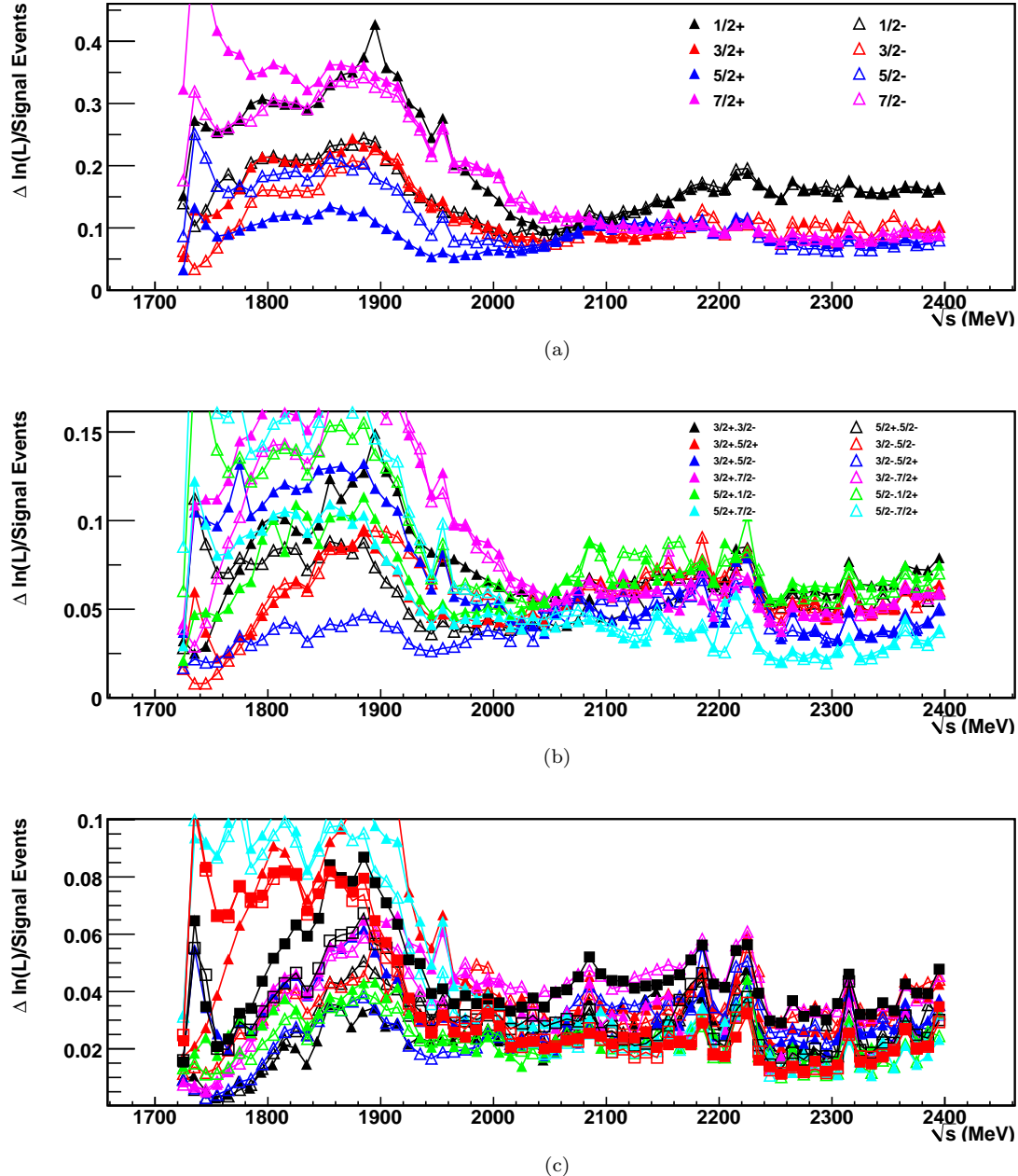


Figure 6.21: Goodness-of-fit plots showing  $\Delta \ln L/\text{signal events}$  vs  $\sqrt{s}$  for the combined g11a, g1c and g8b datasets. (a) The single-wave fits, (b) the two-wave fits, (c) the three wave fits.

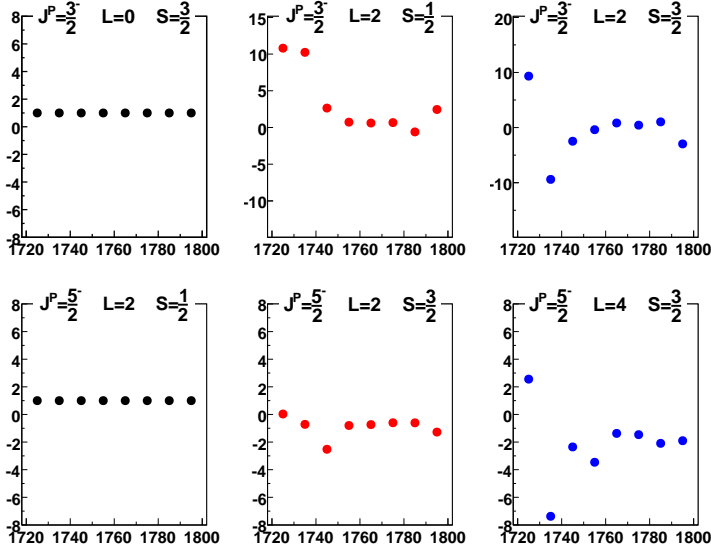


Figure 6.22: Decay Parameters for  $\frac{3}{2}^-$ ,  $\frac{5}{2}^-$  vs  $\sqrt{s}$  for the combined g11a, g1c and g8b datasets. The parameters have been normalized by the lowest (leftmost) L, S combination decay. None of the parameters vary smoothly with energy over the entire energy range.

### The $\frac{3}{2}^-$ , $\frac{5}{2}^-$ Plus t-channel Fits

Figure 6.22 shows the decay parameters and Figure 6.23 shows the multipole production angle parameters for the  $\frac{3}{2}^-$ ,  $\frac{5}{2}^-$  fit. The decay parameters are similar to what was seen in the single dataset fits, namely that the decay parameters are not smooth functions of energy. The multipole production angles however are very smooth and almost constant. Combining the datasets smoothed the variation of the production angles, but since the decays are still not smooth, it is difficult to conclude that there is a  $\frac{3}{2}^-$ ,  $\frac{5}{2}^-$  resonance combination present.

### The $\frac{3}{2}^-$ , $\frac{5}{2}^+$ Plus t-channel Fits

Figure 6.24 shows the decay parameters and Figure 6.25 shows the multipole production angle parameters for the  $\frac{3}{2}^-$ ,  $\frac{5}{2}^+$  fit. In the single dataset examination of this fit, the two datasets each showed smooth motion for both the decays and the production angles, with the exception of one discontinuity, but the discontinuity occurred at 1850 MeV in g1c and at 1950 MeV in g8b. In the combined fit, both discontinuities are present, although a bit shifted, to 1830 MeV and 1990 MeV, but there is a range between the two discontinuities where all of the variables are very smooth functions of energy or even constant. This could be further evidence that there are a  $\frac{3}{2}^-$  and  $\frac{5}{2}^+$  resonance present here, however it is clear that there are also other processes present that are not part of our fit, and without including them it is not possible to determine which particular  $N^*$ 's are present.

### The $\frac{5}{2}^+$ , $\frac{7}{2}^-$ Plus t-channel Fits

Figure 6.26 shows the decay parameters and Figure 6.27 shows the multipole production angle parameters for the  $\frac{5}{2}^+$ ,  $\frac{7}{2}^-$  fit. The decays show a much different picture than what was seen by looking at g1c alone. Here the decays are largely smooth, with a few points that are far away from

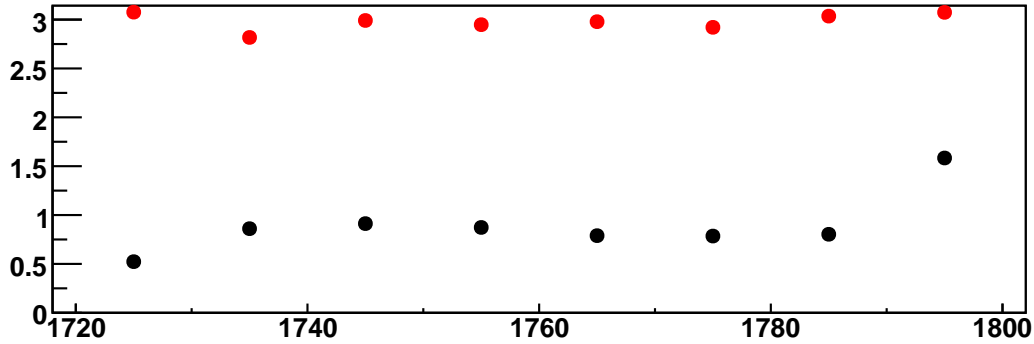


Figure 6.23: Multipole Parameters for  $\frac{3}{2}^-$ ,  $\frac{5}{2}^-$  vs  $\sqrt{s}$  for the combined g11a, g1c and g8b datasets. The  $\frac{3}{2}^-$  parameter is in black; the  $\frac{5}{2}^-$  parameter is in red. Both are smooth over the entire range.

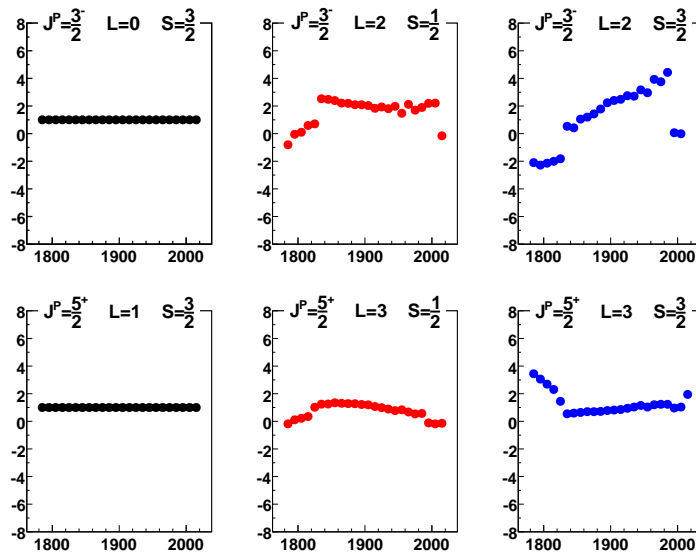


Figure 6.24: Decay Parameters for  $\frac{3}{2}^-$ ,  $\frac{5}{2}^+$  vs  $\sqrt{s}$  for the combined g11a, g1c and g8b datasets. The parameters have been normalized by the lowest (leftmost) L, S combination decay. There are discontinuities at 1830 MeV and 1990 MeV, but otherwise they are smooth functions of energy.

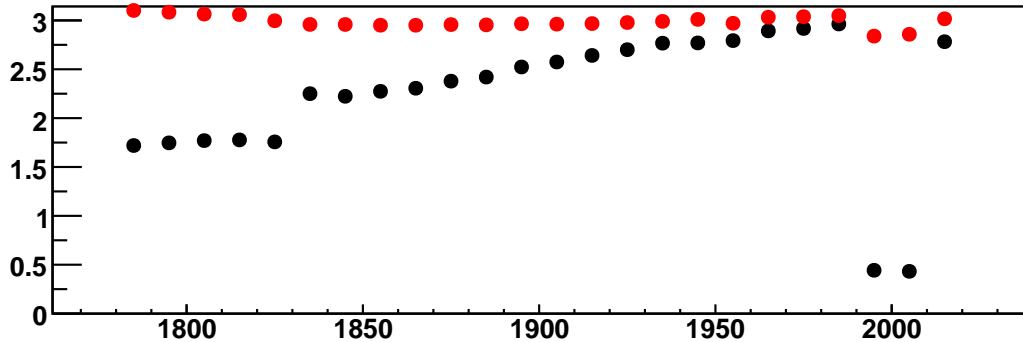


Figure 6.25: Multipole Parameters for  $\frac{3}{2}^-$ ,  $\frac{5}{2}^+$  vs  $\sqrt{s}$  for the combined g11a, g1c and g8b datasets. The  $\frac{3}{2}^-$  parameter is in black; the  $\frac{5}{2}^+$  parameter is in red. There are discontinuities at 1830 MeV and 1990 MeV, but otherwise they are smooth functions of energy.

the rest, except for a large discontinuity at 2270 MeV. The production parameters show the same result, a discontinuity at 2270 MeV and otherwise largely smooth, although there are two notably bad points in the 2205 and 2215 MeV bins.

### 6.5.3 Summary

In this section it was shown that it is possible to combine three different kinds of polarized data together into one fit that is able to produce all of the polarized SDMEs. We have also shown that combining the datasets can settle the parameters in the two wave fits allowing for easier discernment of the presence of resonances. However, given our current model the combined fits are still unable to determine which  $N^*$ 's are present.

## 6.6 Summary

We have presented the results of our partial-wave analysis. While they were not able to determine exactly which resonance are responsible for  $\omega$  photoproduction in our energy range, they have shown that adding in photon polarization increases the analyzing power of our fits. Both of our datasets did show agreement with g11a in terms of which combinations of  $J^P$  waves are important in  $\omega$  photoproduction. Adding in further polarization information, in the form of target polarization, should be able to even further increase the analyzing power. We also saw that the production processes near threshold are probably simpler, involving fewer resonances, than those at higher energies. The symmetries seen in the SDMEs in Chapter 5 suggested this as well, as their symmetries broke at higher energies. While it is unclear if there is any connection between these symmetries and the presence of resonances, it is an area that merits further study.

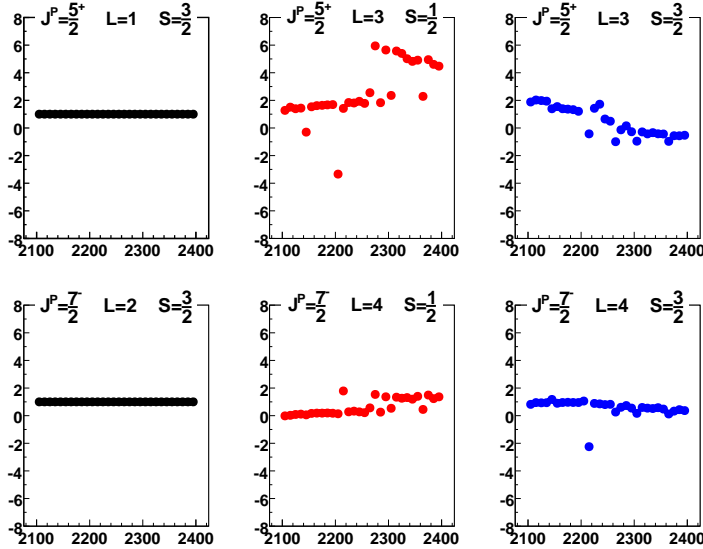


Figure 6.26: Decay Parameters for  $\frac{5}{2}^+$ ,  $\frac{7}{2}^-$  vs  $\sqrt{s}$  for the combined g11a, g1c and g8b datasets. The parameters have been normalized by the lowest (leftmost) L, S combination decay. Other than a few bad bins these parameters are largely smooth except for a significant discontinuity at 2270 MeV.

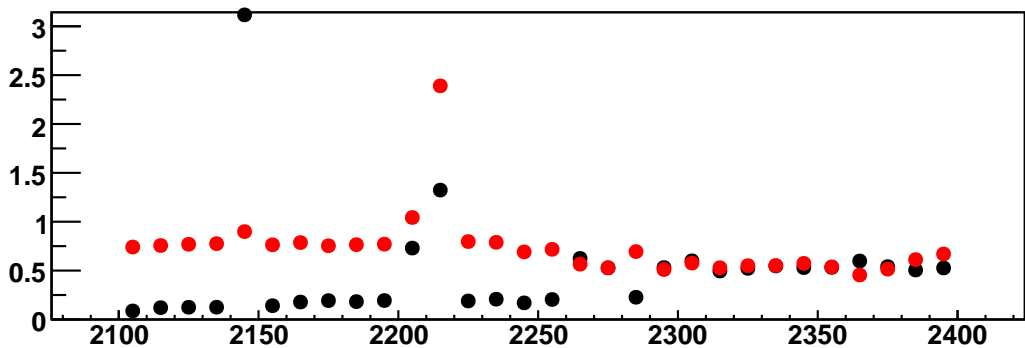


Figure 6.27: Multipole Parameters for  $\frac{5}{2}^+$ ,  $\frac{7}{2}^-$  vs  $\sqrt{s}$  for the combined g11a, g1c and g8b datasets. The  $\frac{3}{2}^-$  parameter is in black; the  $\frac{5}{2}^+$  parameter is in red. Other than a few bad bins these parameters are largely smooth except for a significant discontinuity at 2270 MeV.

# Chapter 7

## Summary

### 7.1 Recap of Analysis Procedure

It may be instructive to recap here our entire analysis procedure so that it can be easily followed step by step. Where possible, we will provide references to the section where the details of each step can be found.

The data were initially gathered using the devices and detectors described in Chapter 2, and then cooked before being our analysis process began. Starting from the cooked data, we first calculated the necessary tagger- and momentum-corrections using the methods laid out in Section 3.2. We then applied those corrections to the data and skimmed the dataset, looking for events with a final state of  $p, \pi^+, \pi^-$ , where the proton's magnitude of momentum is greater than 350 MeV, the total missing-mass is between 0 and 450 MeV, and the missing mass off the proton is within 150 MeV of the  $\omega$  mass. For events of that type, we performed a kinematic fit to the hypothesis of a missing  $\pi^0$ , discarding events if the confidence level is below 10%. Once we have selected our events we separate them into bins based only on their total, center-of-mass energy,  $\sqrt{s}$ .

After the data have been binned in  $\sqrt{s}$ , we perform a series of cuts. We perform a particle identification cut, as described in Section 3.4, and then fiducial cuts, and cuts on time-of-flight paddles, detailed in Section 3.5. Then we require  $\cos \theta_{CM}^{\pi^0} \leq 0.99$ , as was shown in Section 3.6.

Once all of those cuts have been performed, we separated the signal and background on an event-by-event basis by assigning a Q-value to each event that passes our cuts, using the methods detailed in Section 3.7. We took special precautions when dealing with the near-threshold bins. After the Q-values were calculated, the data were rebinned, this time using a tighter cut on the  $\omega$  mass and confidence level, looking only at events within 25 MeV of the  $\omega$  mass. The cuts and Q-values already calculated were used for each event which passed this  $\omega$  mass cut.

A set of Monte Carlo simulation data was generated, thrown according to phase space, both in the production and the decay of the  $\omega$ . That initial dataset is kept as the *raw* Monte Carlo. We then passed the raw Monte Carlo through the same software used to cook the data and other software that reproduced the acceptance of our detectors. The set of Monte Carlo that passed through that cooking process and was accepted in our detectors is referred to as the *accepted* Monte Carlo. The accepted Monte Carlo was then skimmed, looking for events detected as  $p, \pi^+, \pi^-$  in the same way as the data. Those events are then subject to the same initial cuts as the data and binned according to their  $\sqrt{s}$  value. The accepted Monte Carlo then underwent the same PID, fiducial, time-of-flight paddle, and  $\cos \theta_{CM}^{\pi^0}$  cuts as the data. However, they do not undergo signal-background separation, the events are either accepted or rejected. Every event in the raw Monte Carlo was also binned by its  $\sqrt{s}$  value, but there are no cuts placed on it.

Once the data have been binned and all of the cuts have been placed, amplitudes are generated for each event, up to  $J = \frac{11}{2}$ , of both parities, following the method set forth in [1]. All of those

amplitudes were then used in a *mother* fit, which allowed us to fully describe the data, and which was described in Section 5.1. From the parameters used in these fits, we were able to extract the spin density matrix elements, using the equations in (4.38). And, lastly, a partial-wave analysis was performed, as was detailed in Chapter 6.

## 7.2 Conclusions and Future Work

As we have said, the ultimate goal of this experiment is to be able to extract the resonance contributions important in  $\gamma p \rightarrow p\omega$ . While we have not been able to confirm the existence of any particular resonances in the data, we have seen that adding polarization information to the partial-wave analysis fits increases their analyzing power. Fits that seem to be very good when looking at only the unpolarized spin density matrix elements can be seen to be lacking once the polarized elements are analyzed. It may be that the unpolarized data masks the contributions of certain resonances, making it harder to detect their contributions, while bringing others to the fore. The polarized data is better able to separate out the contributions from one another, however if there are many resonances overlapping in a small energy range the method we have used may not be able to distinguish them.

We have seen that, for the most part, the g1c and g8b partial-wave analysis results match well what was seen in g11a [1] in terms of which combinations of  $J^P$  waves are important in different energy ranges. Between 1780 and 2000 MeV, all three datasets show the  $\frac{3}{2}^-, \frac{5}{2}^+$  combination to be the best. And between 2100 and 2400 MeV g1c and g11a agree that the  $\frac{5}{2}^+, \frac{7}{2}^-$  combination is best. However, the g8b and g1c datasets are not able to pin down which particular resonances are responsible, i.e. what the mass and width of those resonances are. We have seen, in Figures 6.2 and 6.3, that, at least between 1800 and 1950 MeV, there may be more going on than is accounted for in our model, and this may be hampering our ability to determine which resonances are present.

It seems clear, based on these results, that adding the polarization information adds to our ability to determine what resonances are responsible for  $\omega$  photoproduction in this energy range. Going forward, it is imperative to add even more polarization information, obtained by using a polarized target and combinations of a polarized target and polarized photon beam. Two such experiments have already been performed using CLAS and are under analysis by other groups. The g9 run period, known as the FROzen Spin Target (FROST) run period, used a butanol target that was polarized both longitudinally and transversely, along with a photon beam using both circular and linear polarization. The g14 run period, known as HD-ICE, used a longitudinally polarized deuterium target along with a photon beam using both circular and linear polarization. These run periods will be able to provide further measurements of the  $\rho^{1-3}$  SDMEs, as well as yield first measurements of the  $\rho^{4-15}$  SDMEs. These should allow an even greater ability to separate out the resonances from one another.

Other, simpler, experiments can also be run, with only polarized photons, at higher energies to see how the SDMEs evolve. The g8b dataset has excellent statistics and provided very stable results, but they only extend up to 2200 MeV, and we have seen that some of the symmetries present in the SDMEs starts to break only as we get to higher energies. Exploring the energy range above 2200 MeV could yield even more information than what we have seen. The g1c dataset has a larger energy range than g8b, but substantially less statistics. Another experiment with circularly polarized photons would be useful to increase our statistics as well as extend the energy range.

In addition to examining these datasets on their own, we have shown in this analysis that the data from multiple experiments can be combined together into a single fit, providing greater statistics and analyzing power than any of the experiments on their own can provide. Any new experiments can be added into the set of three experiments that we have used here. Additionally, it is possible to combine the results of different channels into a single fit. Data, from the same or different experiments, analyzed for the other vector mesons, the  $\phi$  and  $\rho$  mesons, could be added to the  $\omega$

data to further increase the analyzing power.

We also hope that this work will spark interest from theorists who can use the SDMEs presented to refine their theories. Perhaps they can find the reason for the symmetries present in the polarized SDMEs and why they break at higher energies. Since this work seems to indicate that more than two or three resonances may be present in small energy ranges, it may be necessary to change our method of partial-wave analysis to be able to pick them out, especially if there are multiple resonances of the same  $J^P$ , which may require a new model.

Many years have passed between when these dataset were collected and these results have been presented. We have worked diligently, and with many people and institutions, to study this data and ensure that everything has been properly calibrated and analyzed. In the end, we hope that we have been able to extend the knowledge of  $\omega$  photoproduction and spark interest in further research, which we hope will lead to a greater understanding of what is happening inside of a nucleon.



# Bibliography

- [1] Michael Williams. *Measurement of Differential Cross Sections and Spin Density Matrix Elements along with a Partial Wave Analysis for  $\gamma p \rightarrow p\omega$  using CLAS at Jefferson Lab.* Ph.D. thesis, Carnegie Mellon University, 2007.
- [2] K. Nakamura et al. *Particle Data Group.* J. Phys. G **37**, 075021 (2010) .
- [3] J. Beringer et al. *Review of Particle Physics.* Phys. Rev. D **86**, 010001 (2012).
- [4] V. Crede and W. Roberts *Progress towards understanding baryon resonances.* Rep. Prog. Phys. **76**, 076301 (2013).
- [5] S. Capstick and W. Roberts.  *$N\pi$  decays of baryons in a relativized model.* Phys. Rev. D **47**, 1994-2010 (1993).
- [6] M. Pichowsky, C. Savkli and F. Tabakin. *Polarization observables in vector meson photoproduction.* Phys. Rev. C **53**, 593-610 (1996).
- [7] F.J. Klein. Ph.D. Thesis, Bonn Universtiyy, 1996
- [8] M. Battaglieri et al. *Photoproduction of the  $\omega$  Meson on the Proton at Large Momentum Transfer.* Phys. Rev. Lett. **90**, 022002 (2003).
- [9] J. Barth et al. *Low-energy photoproduction of  $\omega$ -mesons.* Eur. Phys. J. A **18**, 117 (2003).
- [10] J. Ballam et al. *Vector-Meson Production by Polarized Photons at 2.8, 4.7, and 9.3 GeV.* Phys. Rev. D **7**, 3150 (1973).
- [11] D.P. Barber et al. *A Study Of The Reactions Gamma P to Omega P And Gamma P to Omega Delta+.* Z. Phys. C **26**, 343 (1984).
- [12] R.W. Clift et al. *Observation of a baryon exchange dip and parton effects in backward photoproduction of  $\omega$ .* Phys. Lett. B**72**, 144 (1977).
- [13] Q. Zhao. *Nucleonic resonance excitations with linearly polarized photons in  $\gamma p \rightarrow \omega p$ .* Phys. Rev. C **63**, 025203 (2001)
- [14] Y. Oh, A.I. Titov and T.S.H. Lee. *Nucleon resonances in  $\omega$  photoproduction.* Phys. Rev. C **63** (2001).
- [15] A.I. Titov and T.S.H. Lee. *Effective Lagrangian approach to the  $\omega$  photoproduction near threshold.* Phys. Rev. C **66**, 015204 (2002)
- [16] G. Penner and U. Mosel. *Vector meson production and nucleon resonance analysis in a coupled-channel approach for energies  $m_N < \sqrt{s} < 2 \text{ GeV}$ . II. Photon-induced results.* Phys. Rev. C **66**, 055212 (2002).

- [17] V. Shklyar, H. Lenske, U. Mosel, and G. Penner. *Coupled-channel analysis of  $\omega$ -meson production in  $\pi N$  and  $\gamma N$  reactions for c.m. energies up to 2 GeV.* Phys. Rev. C **71**, 055206 (2005).
- [18] Jefferson Lab. *The JLab Picture Exchange*, <http://www1.jlab.org/u1/jpix>
- [19] Jefferson Lab. <http://www.jlab.org/>
- [20] B.M. Dumham. *Jefferson Lab, a status report.* Thomas Jefferson National Accelerator Facility, 1997.
- [21] S. Gagnon. *Jefferson Lab Site Tour*,  
<http://education.jlab.org/sitetour/guidedtour05.1.alt.html>
- [22] D.I. Sober, et al. *The bremsstrahlung tagged photon beam in Hall B at JLab.* Nucl Inst Meth A **440**, 263 (2000).
- [23] Robert Bradford. *Measurement of Differential Cross Sections and  $C_x$  and  $C_z$  for  $\gamma p \rightarrow K^+ \Lambda$  and  $\gamma p \rightarrow K^+ \Sigma^0$  Using CLAS at Jefferson Lab.* Ph.D. thesis, Carnegie Mellon University, 2005.
- [24] Jefferson Lab. *Experimental Hall B*, <http://www.jlab.org/Hall-B/>
- [25] S. Christo. *The g11a Target Cell*, [http://www.jlab.org/~christo/g11a\\_target.html](http://www.jlab.org/~christo/g11a_target.html)
- [26] S. Taylor et al. *The CLAS Start Counter.* Nucl. Inst. Meth. A **462**, 484 (2001).
- [27] Y.G. Sharabian et al. *A new highly segmented start counter for the CLAS detector.* Nucl. Phys. A **556**, 246 (2006).
- [28] Alan J. Street et al. *Final site assembly and testing of the superconducting toroidal magnet for the CEBAF Large Acceptance Spectrometer (CLAS).* IEEE Trans. Mag. **32**, No. 4, 2074 (1996).
- [29] M.D. Mestayer et al. *The CLAS drift chamber system.* Nucl Inst Meth A **449**, 81 (2000).
- [30] E. Smith et al. *The time-of-flight system for CLAS.* Nucl Inst Meth A **432**, 265 (1999).
- [31] J. Ball and E. Pasyuk. *Photon Flux Determination Through Sampling of "out-of-time" Hits with the Hall B Photon Tagger.* CLAS Note 2005-002.
- [32] D.S. Carman and B.A. Raue. *Hyperson electroproduction at CLAS  $p(e,e',K^+)Y$  analysis.* CLAS Note 2002-107.
- [33] M. Williams and C.A. Meyer. *Kinematic Fitting in CLAS.* CLAS Note 2003-017.
- [34] E. Pasyuk. *The CLAS ELOSS Package.* Software available via the CLAS CVS repository under `clas/packages/utilities/eloss`.
- [35] S. Stepanyan. *Evidence for an Exotic Pentaquark Baryon State  $\Theta^+(1530)$ , in the  $\gamma d \rightarrow p K^+ K^- n$  reaction.* CLAS Analysis Note 2003-105.
- [36] M. Williams, D. Applegate and C.A. Meyer. *Determining Momentum and Energy Corrections for g1c Using Kinematic Fitting.* CLAS Note 2004-017.
- [37] D. Sober, H. Crannell and F.J. Klein. *The Tagger Energy Scale: Interpreting the CMU Kinematic Fit Results.* CLAS Note 2004-019.
- [38] G. Feldman and R. Cousins. *Unified approach to the classical statistical analysis of small signals.* Phys. Rev. D **57**, 3873 - 3889 (1998).

- [39] M. Williams, C.A. Meyer and M. Bellis. *Probabilistic Event Weighting to Separate Signal from Background*. CLAS Note 2007-013.
- [40] L.C. Maximon and H. Olsen *Photon and electron polarization in high-energy bremsstrahlung and pair-production with screening*. Phys. Rev. **114**, 887 (1959).
- [41] Ken Livingston. *Polarization from Coherent Bremsstrahlung Enhancement*. CLAS Note 2011-020.
- [42] M. Duggar, B.G. Ritchie. *Consistency corrections to the linear photon polarization for g8b data*. CLAS Note 2012-002.
- [43] M. Holtrop. *GSIM: CLAS GEANT Simulation*,  
[http://www.physics.unh.edu/maurik/Gsim/gsim\\_current\\_code\\_dev.shtml](http://www.physics.unh.edu/maurik/Gsim/gsim_current_code_dev.shtml)
- [44] S.U. Chung. *Formulas for Partial Wave Analysis: Version II*. BNL preprint BNL-QGS-93-05 (1999).
- [45] Donald H. Perkins. *Introduction to High Energy Physics*. 4th Edition, Cambridge University Press, 2000.
- [46] Greiner, Neise, Stöcker *Thermodynamics and Statistical Mechanics*. Springer, 2004.
- [47] K. Schilling, P. Seyboth and G. Wolf. *On The Analysis of Vector-Meson Production By Polarized Photons*. Nucl. Phys. B **15**, 397 (1970).
- [48] Biplob Dey. *Differential Cross Section and Polarization Extractions for  $\gamma p \rightarrow K^+ \Sigma^0$  and  $\gamma p \rightarrow \phi p$  using CLAS at Jefferson Lab, Towards a Partial Wave Analysis in Search of Missing Baryon Resonances*. Ph.D. thesis, Carnegie Mellon University, 2011.
- [49] Michael McCracken. *A Study of  $K^+ \Lambda$  Photoproduction in the CLAS g11a Dataset: Differential Cross Section, Recoil Polarization, and a Partial-Wave Analysis*. Ph.D. thesis, Carnegie Mellon University, 2008.
- [50] B. Efron *Bootstrap Methods: Another Look at the Jackknife*. The Annals of Statistics. Vol. 7, No. 1 (1979).



## Appendix A

# Issues with the Time-of-Flight Detectors in g8b

The g8b dataset was collected in the summer of 2005. It took several years before the data were cooked and ready to be analyzed. Even after the data were cooked, a full analysis could not be performed until final polarization values were measured for each event. Thus, it was February of 2012 before full analysis could begin on the dataset.

Once the full analysis began, all of the steps laid out in this work were performed, and the spin density matrix elements were extracted after running an initial mother fit. These SDMEs were compared to the g11a dataset, as can be seen for  $\rho_{00}^0$  in Figure A.1, for  $\text{Re}(\rho_{10}^0)$  in Figure A.2, and for  $\rho_{1-1}^0$  in Figure A.3, where only half of the bins have been shown. There was good agreement between the g8b and g11a results for the  $\text{Re}(\rho_{10}^0)$  and  $\rho_{1-1}^0$  elements, but not for the  $\rho_{00}^0$  element. The g8b results were consistently lower than the g11a results in the range  $-0.5 \leq \cos(\theta_{CM}^\omega) \leq 0.5$ . The error bars for both datasets are quite small, so it was clear that the agreement was poor.

Looking at the formulas to calculate the SDMEs using our amplitudes, (4.38), does not make it apparent where a problem could exist. However, if we recall the Schilling Method for measuring the SDMEs, explained in Section 4.3.5, we see that the formula used is

$$\begin{aligned} W(\cos\theta, \phi) = & \frac{3}{4\pi} \left( \frac{1}{2} (\rho_{11} + \rho_{-1-1}) \sin^2 \theta + \rho_{00} \cos^2 \theta \right. \\ & + \frac{1}{\sqrt{2}} (-\text{Re}\rho_{10} + \text{Re}\rho_{-10}) \sin 2\theta \cos \phi + \frac{1}{\sqrt{2}} (\text{Im}\rho_{10} - \text{Im}\rho_{-10}) \sin(2\theta) \sin(\phi) \\ & \left. - \text{Re}\rho_{1-1} \sin^2 \theta \cos 2\phi + \text{Im}\rho_{1-1} \sin^2 \theta \sin 2\phi \right), \end{aligned} \quad (\text{A.1})$$

which depends only on  $\cos\theta$  and  $\phi$ , calculated in the Adair frame. If there are any issues with these two angles, it would affect the resulting SDMEs. At this point, the SDMEs were extracted from the data using the Schilling method and those results agreed very well with the results of the mother fit. In other words, they still showed a significant discrepancy with g11a.

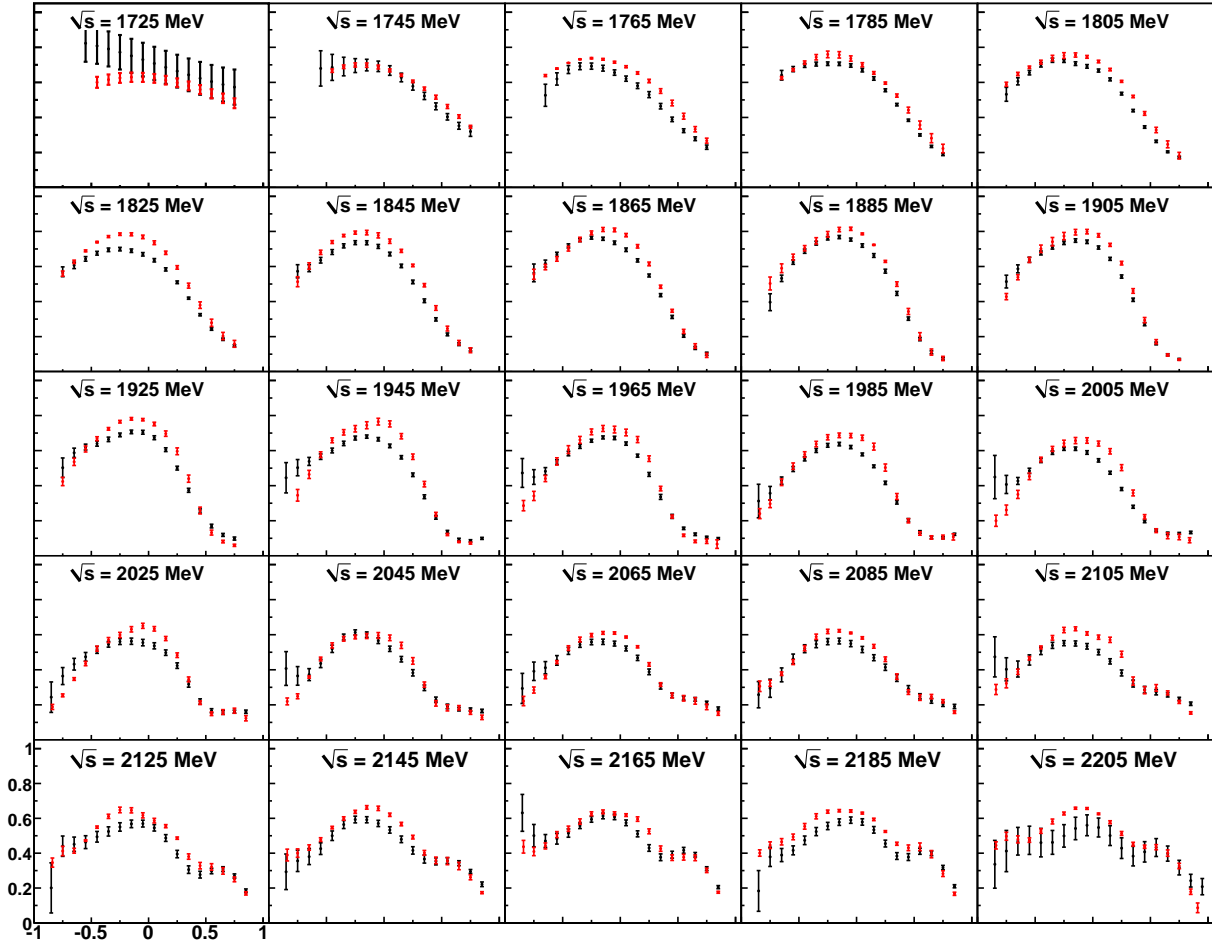


Figure A.1:  $\rho_{00}^0$  element vs  $\cos(\theta_{CM})$  in bins of  $\sqrt{s}$ . The results from g8b (black) are shown in comparison to the g11a (red) values. The errors are as calculated in Section 5.2.1. Note that only half of the bins have been shown here.

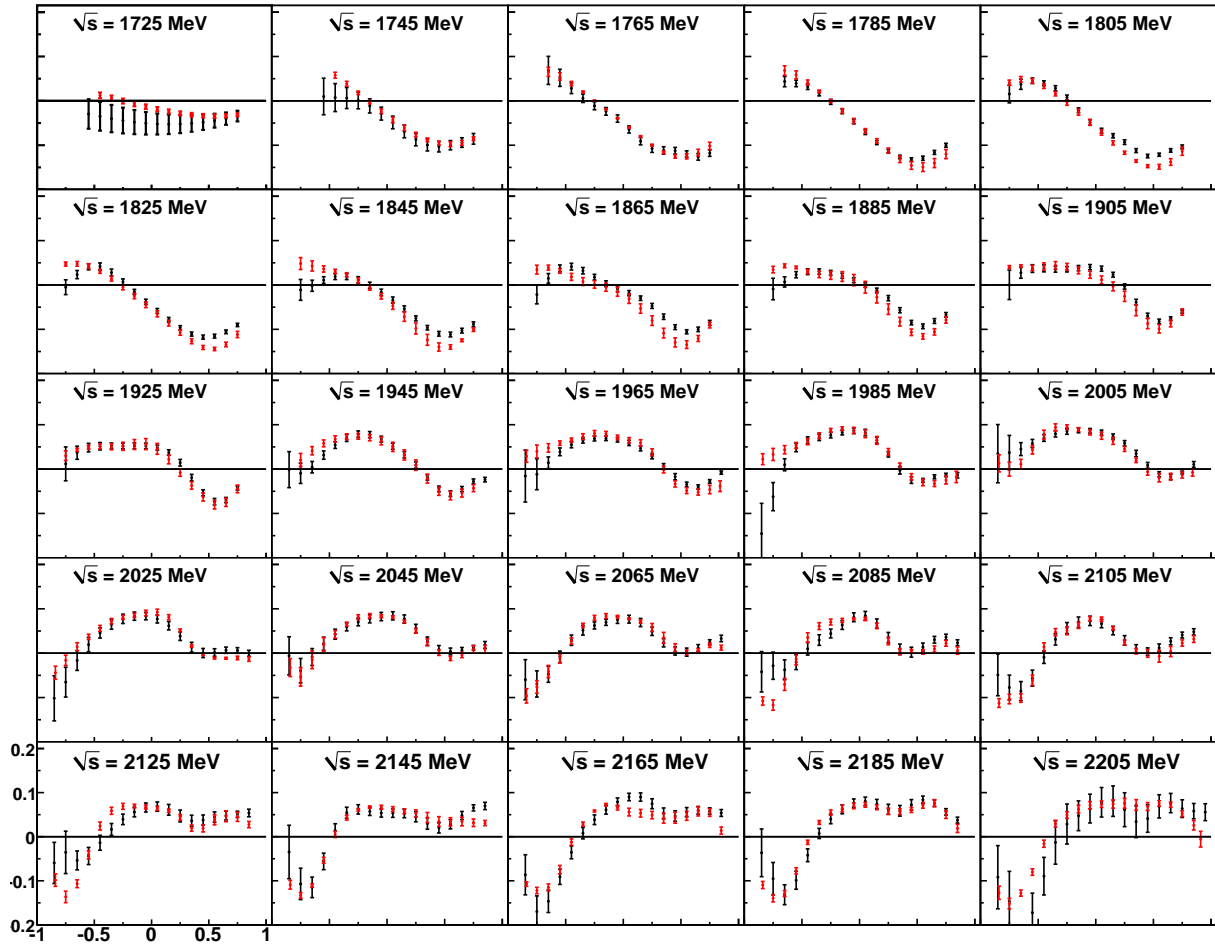


Figure A.2:  $\text{Re}(\rho_{10}^0)$  element vs  $\cos(\theta_{CM}^\omega)$  in bins of  $\sqrt{s}$ . The results from g8b (black) are shown in comparison to the g11a (red) values. The errors are as calculated in Section 5.2.1. Note that only half of the bins have been shown here.

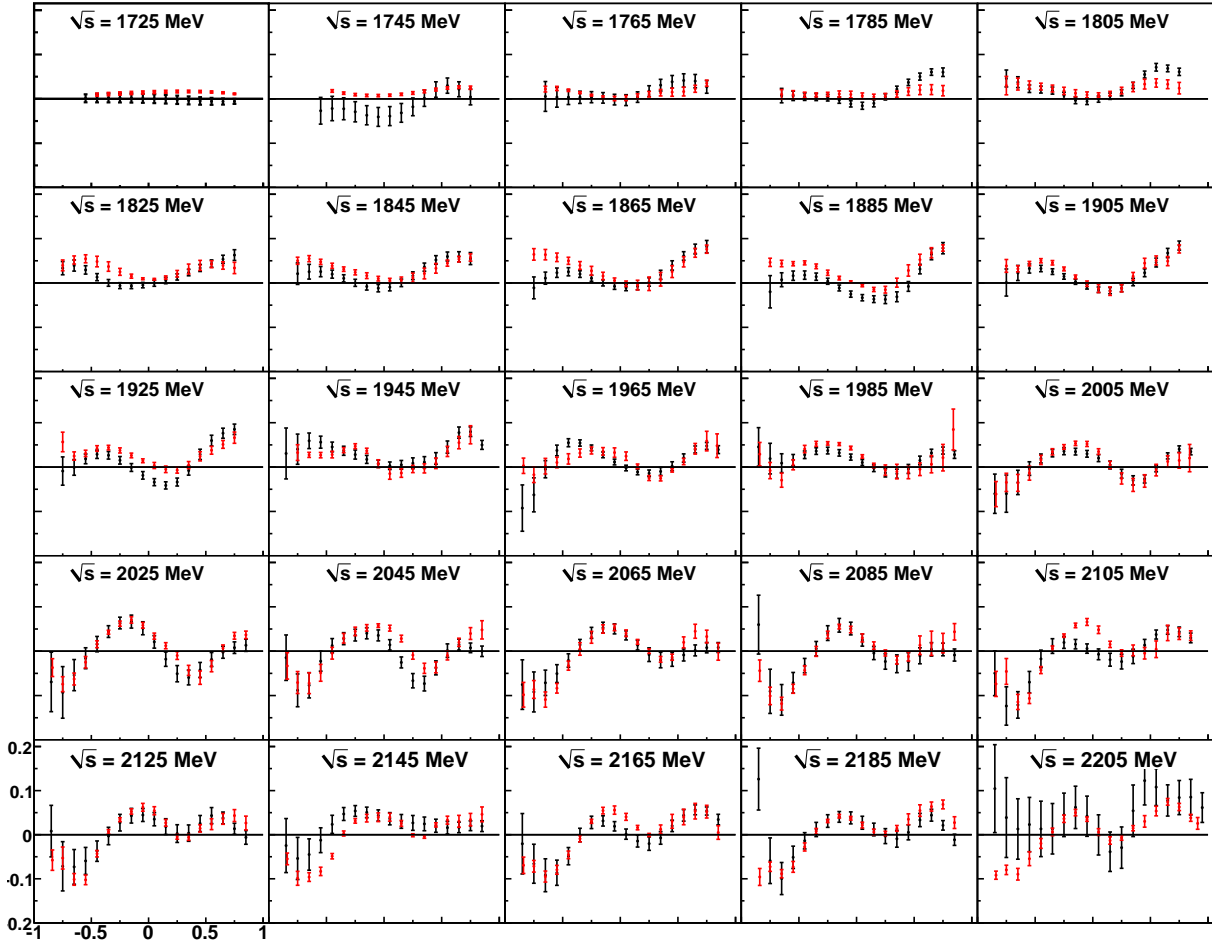


Figure A.3:  $\rho_{1-1}^0$  element vs  $\cos(\theta_{CM})$  in bins of  $\sqrt{s}$ . The results from g8b (black) are shown in comparison to the g11a (red) values. The errors are as calculated in Section 5.2.1. Note that only half of the bins have been shown here.

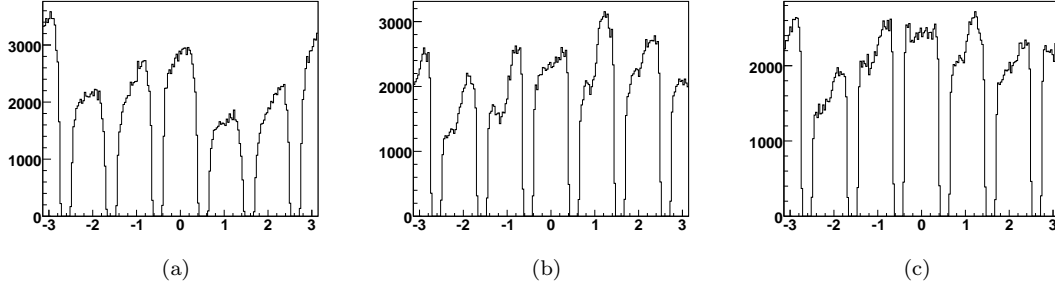


Figure A.4:  $\phi_{lab}$  (radians) from all events in the horiz 1.5 dataset from g8b for (a) protons, (b)  $\pi^+$ , and (c)  $\pi^-$ . Each figure shows six bands in  $\phi_{lab}$ , which are a result of the six sectors in CLAS. Each sector should be roughly flat, but these show significant structure as a function of  $\phi_{lab}$ , which is an indication that there is something wrong.

## A.1 The Adair Angles

Simply looking at the Adair angles would not resolve the issue because there was no known *correct* distribution for these angles. The g11a dataset used the same target and most of the same detectors, but the target was in a different location, and so the distributions would not be the same. Instead, it was necessary to look into the variables used to calculate the Adair angles. Recall, from (4.1), that our axes are defined as

$$\hat{x} = \frac{(\vec{k} \times \vec{q}) \times \vec{k}}{|\vec{k} \times \vec{q}| \times |\vec{k}|} \quad (\text{A.2a})$$

$$\hat{y} = \frac{\vec{k} \times \vec{q}}{|\vec{k} \times \vec{q}|} \quad (\text{A.2b})$$

$$\hat{z} = \frac{\vec{k}}{|\vec{k}|}. \quad (\text{A.2c})$$

The decay angles are then defined as

$$\cos \theta = \hat{\pi} \cdot \hat{z} \quad (\text{A.3a})$$

$$\cos \phi = \frac{\hat{y} \cdot (\hat{z} \times \hat{\pi})}{|\hat{z} \times \hat{\pi}|} \quad (\text{A.3b})$$

$$\sin \phi = -\frac{\hat{x} \cdot (\hat{z} \times \hat{\pi})}{|\hat{z} \times \hat{\pi}|}, \quad (\text{A.3c})$$

where  $\hat{\pi}$  is defined to be the normal to the  $\omega$  decay plane in the  $\omega$  rest frame. These equations lead us to look at the angular distribution, in the lab frame, of our three detected particles.

Figure A.4 shows the  $\phi_{lab}$  distributions for our three detected particles, and it is clear that they do not look uniform. Recall that CLAS is divided into six  $60^\circ$  sectors, which can plainly be seen in each figure. Aside from minor acceptance issues near the torus, which have been removed from our dataset by the fiducial cuts, there should be roughly equal acceptance, as a function of  $\phi_{lab}$ , in any given sector. Each sector will have its own acceptance, and so differences between the number of events in each sector are to be expected, but in any given sector there should be no  $\phi_{lab}$  dependence. Here we see not only smooth  $\phi_{lab}$  dependence, as we see for the proton, but also sharp discontinuities, as for pions. After ruling out the start counter, which was one of two detectors that could induce some  $\phi_{lab}$  dependence, it was determined that the time-of-flight paddles were associated with the problem.

## A.2 The Time-of-Flight Detectors

g8b was the first run period to use a new set of TDCs and ADCs for the TOF counters. As a result, when the data were first cooked, the cutoff value for the TDCs was improperly set. Recall that there are 57 TOF paddles in each sector (though some are combined together to give a total of 48 usable paddles). Each paddle has two PMTs, each of which is read out by a TDCs and an ADCs, for a total of 684 TDCs and ADCs. The old detectors used 12-bit electronics, thus they could only record values up to  $2^{12}$ . The new ones have 16-bit electronics, able to record values up to  $2^{16}$ . When the data are cooked, a cutoff is placed on the TDC and ADC values to ensure that only acceptable values have been recorded. The low cutoff is 0 and the high cutoff is the maximum possible value for the detector, either  $2^{12}$  or  $2^{16}$ . However, when g8b was initially cooked, this high cutoff was left at  $2^{12}$ .

The values measured by each TDC roughly resemble a Gaussian, with a width of a couple hundred channels, see Figure A.5. Unfortunately, during this run period, the center of this Gaussian was usually just a little bit less than  $2^{12}$ , which meant that part of the Gaussian was cut off in nearly every TDC. If a particle registers a value above the cutoff in one of the TDCs for a paddle, it is sometimes salvageable, as long as the value it registers in the other TDC is below the cutoff. However, in most cases, being above the cutoff means that the particle is not recorded in the cooked data, in which case there is no end time for that particle, and particle identification is not possible, meaning that particle gets ignored. If a particle is ignored then that event will be passed by when we skim and it is not able to be used. In some cases, more than 30% of the events were above the cutoff in both TDCs for a detector. In that case, the paddle could not be calibrated and so we just ignore that paddle. This means that any event that has any particle hitting that paddle would be ignored. This problem caused 29 paddles to be removed from the g8b analysis, nearly 10% of the total number of measurable paddles. Given that our analysis contains three particles, there was a significant chunk of our data that was being ignored.

Fortunately, the problem was entirely software-based, not hardware-based. All of the data were correctly recorded, it was only in the cooking process that these events were being cut. Thus, we were able to fix the error, recalibrate all of the paddles and recook the data. After recocking the data, we were able to use all of the paddles without cutting any. This led to a huge increase in our statistics, which went up threefold in every energy bin, and even more near threshold at 1720 MeV, as can be seen in Figure A.6.

## A.3 The Effects on Monte Carlo

While the main impetus for recocking the data was as a result of the issue with the time-of-flight paddles, it also allowed for several other detectors to be recalibrated. After recocking the data, it was also necessary to recock the Monte Carlo. This was done to ensure that all of the changes made while recalibrating the detectors for the data were also applied to the Monte Carlo. Before recocking the dataset it was impossible to have correctly modeled the acceptance of the time-of-flight paddles. The Monte Carlo data does not simulate TDC and ADC values that could have been affected by the same cuts as the data. For paddles that were entirely ignored in the data, we could ignore them in the Monte Carlo. But, for most paddles, a certain subset of the particles that passed through it and were detected were simply ignored, and this behavior could not be included in the simulation. Thus, the Monte Carlo data were not accurately modeling the experimental data.

The recock also allowed us to be sure that the software suite that was used to cook the data was the same one used to cook the Monte Carlo. Several years had gone by between the cooking of the data initially and the cooking of the Monte Carlo the first time, and in that time it is possible that changes were made to some of the software. Any changes between the software used to cook the data and the Monte Carlo could cause acceptance issues, which could have manifested themselves in the discrepancy between the  $\rho_{00}^0$  values.

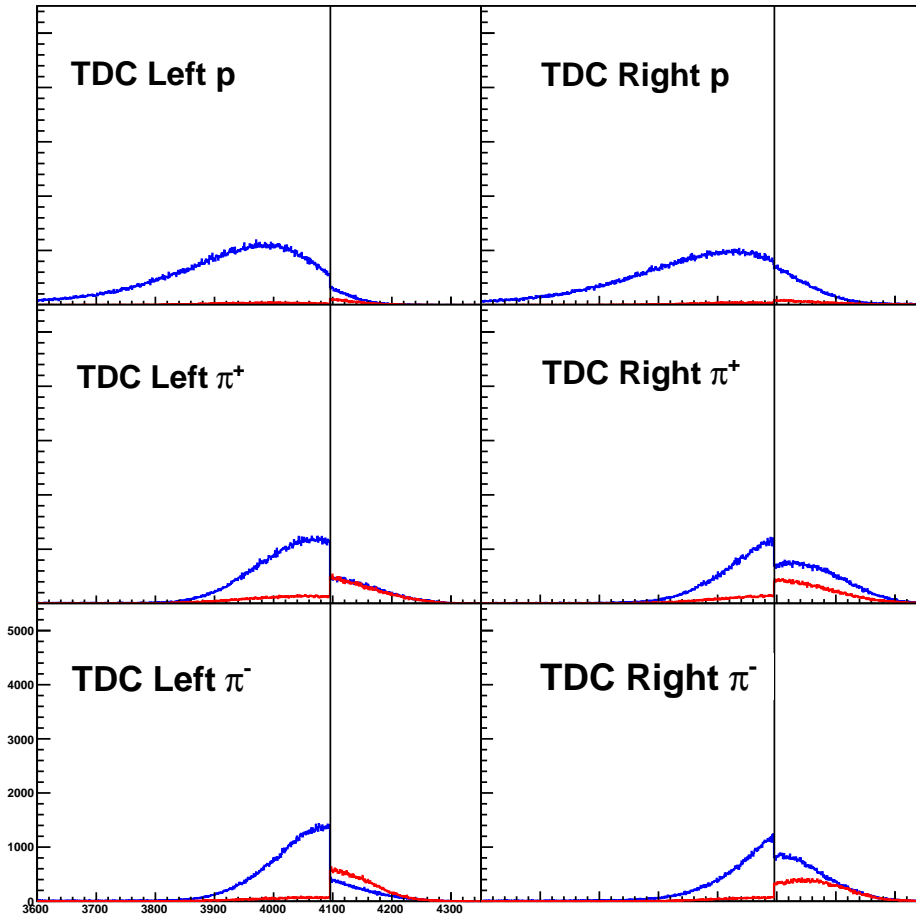


Figure A.5: The values for both TDCs in paddle 23 of sector 3, separated out by the kind of particle detected. The blue line represents particles that were kept in the first cooking while the red lines represent particles that were rejected. The black vertical line is at  $2^{12}$ . Above that value most particles were rejected. The pions are clearly very strongly affected.

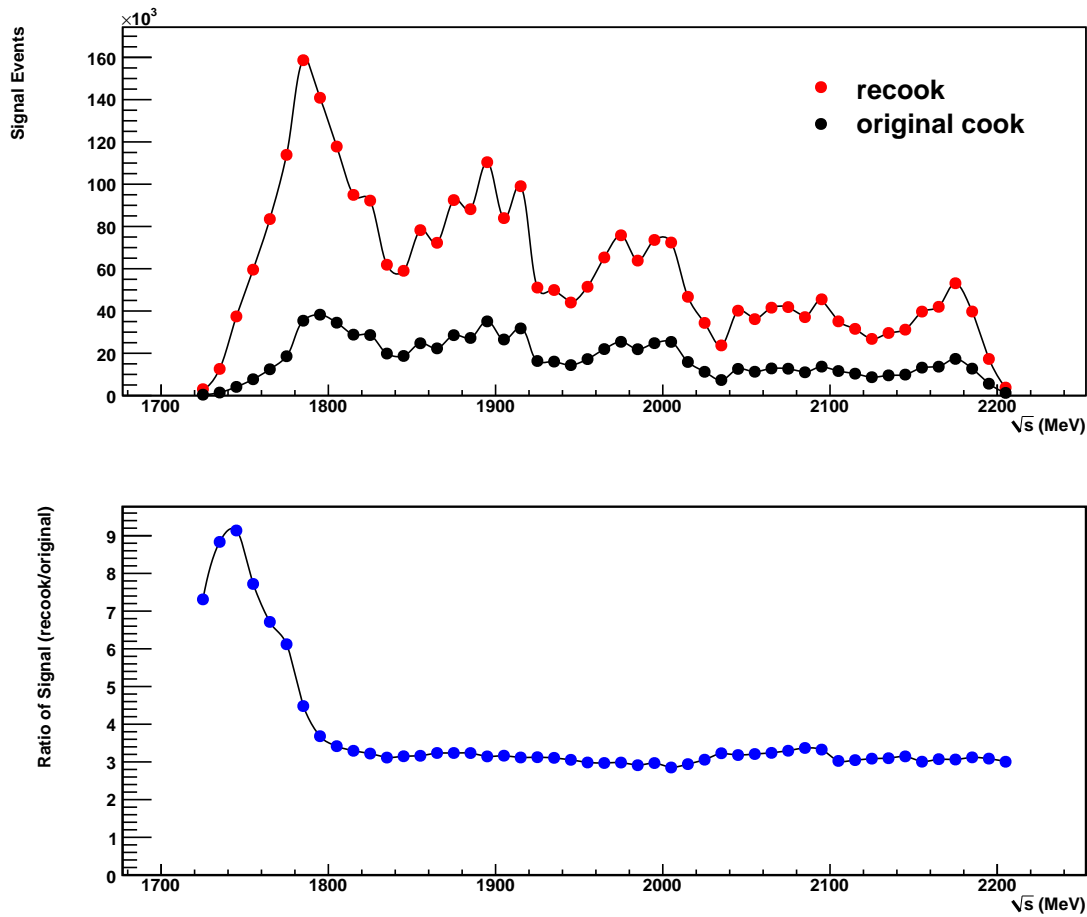


Figure A.6: Total signal events vs  $\sqrt{s}$  for the original cook and the recooked data in g8b, along with a ratio of the recooked signal to the original cook signal. In all bins there is at least three times the signal in the recooked dataset; in the bins below 1800 MeV that ratio is even higher.

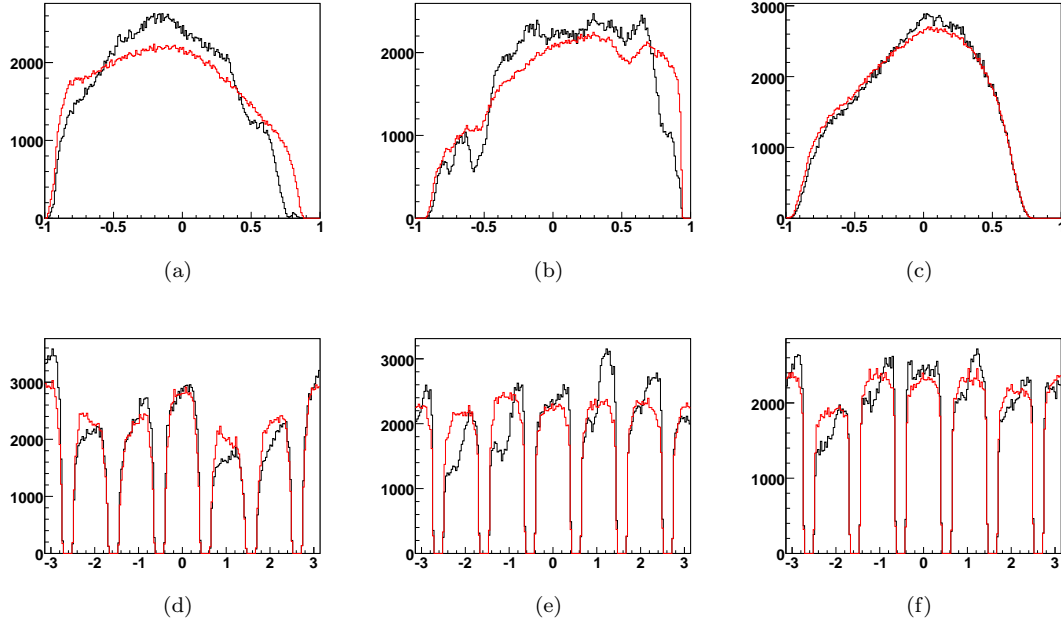


Figure A.7:  $\cos \theta_{CM}$  from all events in the PARA 1.5 dataset from g8b before the recook (black) and after the recook (red) for (a) protons, (b)  $\pi^+$ , and (c)  $\pi^-$ , and  $\phi_{lab}$  (radians), from the same events, for (d) protons, (e)  $\pi^+$ , and (f)  $\pi^-$ . Note that, due to the increase in statistics from the recook, we have scaled the results from the recook by a factor of 0.27, which is the ratio between the number of events before and after the recook. Notice that, in the results from after the recook, the distribution is flatter in each sector as a function of  $\phi_{lab}$ .

## A.4 After Recooking

After the data were recooked, there was a significant change in the angular distribution for each of the three particles, which can be seen in Figure A.7. Note that the data from after the recook have been scaled by the ratio of the number of events before and after the recook to allow for direct comparison. Clearly, the  $\cos \theta_{CM}$  for protons and  $\pi^+$  particles were very strongly affected, while the  $\pi^-$  particles were not affected as strongly. The  $\phi_{lab}$  distribution for all particles, though, has been radically changed. The sharp discontinuities seen in certain sectors for the pions has been removed and we see flat distributions in each sector for them. The  $\phi_{lab}$  distribution for the protons does show a slight slope in several of the sectors, however, it is not as pronounced as was seen before. In Figure A.8 we can see the two Adair angles before and after the recook. The  $\phi_{Ad}$  distribution did not change with the recook, even though the  $\phi_{lab}$  distributions changed significantly. But the  $\cos \theta_{Ad}$  distribution did change slightly, getting a little bit higher near  $\cos \theta_{Ad} = 0$  and a little bit lower at the most forward and backwards angles. This change may not seem significant, but does affect the SDMEs.

The  $\rho_{00}^0$  SDMEs extracted from fits performed after the recook may be seen in Figures 5.7 and 5.8, but here we will look at the change in a single bin. Figure A.9 shows the  $\rho_{00}^0$  element in the bin at  $\sqrt{s} = 1845$  MeV before and after the recook. It is readily apparent that the results have gotten much closer to what was seen in g11a. The other  $\rho^0$  elements did not change significantly. Interestingly, the polarized SDMEs also showed no change as a result of the recook. It is unclear why the  $\rho_{00}^0$  element was so strongly tied to this issue.

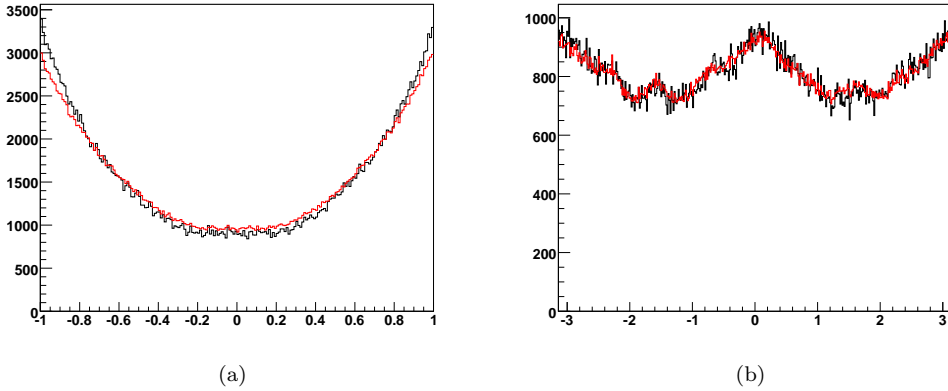


Figure A.8: (a)  $\cos \theta_{Ad}$  from all events in the PARA 1.5 dataset from g8b before the relook (black) and after the relook (red) and  $\phi_{Ad}$  (radians), from the same events. Note that due to the increase in statistics from the relook we have scaled the results from the relook by a factor of 0.27, which is the ratio between the number of events before and after the relook.

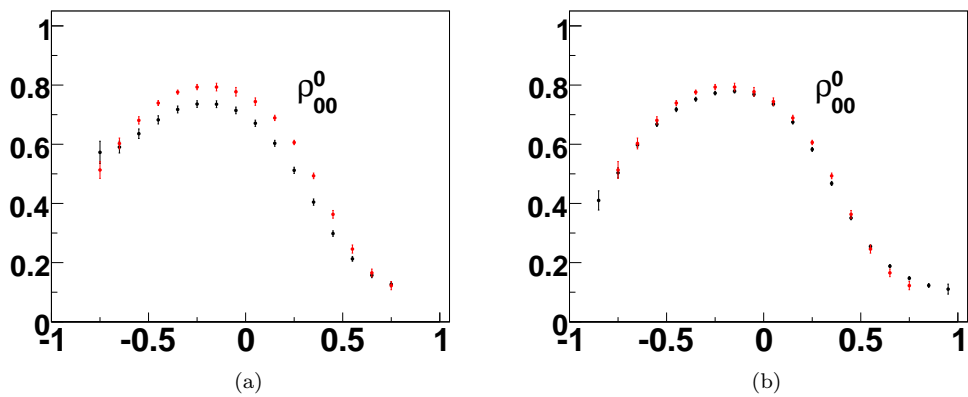


Figure A.9:  $\rho_{00}^0$  element vs  $\cos \theta_{CM}^\omega$  in the bin  $\sqrt{s} = 1845$  MeV (a) before the recoil, and (b) after the recoil. The results from g8b (black) are shown in comparison to the g11a (red) values. The errors are as calculated in Section 5.2.1.

## A.5 Summary

There are many issues that arise in the course of analyzing a dataset, and the cause of the issues are not always easy to track down. In this case it was a single number in a single file among a suite of software that encompasses thousands of files. We may never be able to tell whether the issue was resolved simply by fixing that one number, or by recalibrating some of the other detectors, or by ensuring that the Monte Carlo was cooked with exactly the same software as the data. But, it is instructive to see how important it is to know and be able to model the acceptance in an experiment.



## Appendix B

# Special Comparisons of the SDMEs

In this appendix, we present comparisons between the various spin density matrix elements. The purpose is to illustrate the symmetries present among the SDMEs. We also show the comparisons between the g11a, g1c, and g8b datasets for two of the  $\rho^0$  matrix elements to demonstrate the agreement between g1c and g8b in areas where they differ from g11a. When comparing g11a, g1c, and g8b, we have used the 30-MeV-wide binning used for g1c. This means that for a bin labeled  $\sqrt{s} = 1855$  MeV, we are using the bin with range  $1850 \leq \sqrt{s} \leq 1860$  for g11a and g8b, and the bin with range  $1840 \leq \sqrt{s} \leq 1870$  for g1c.

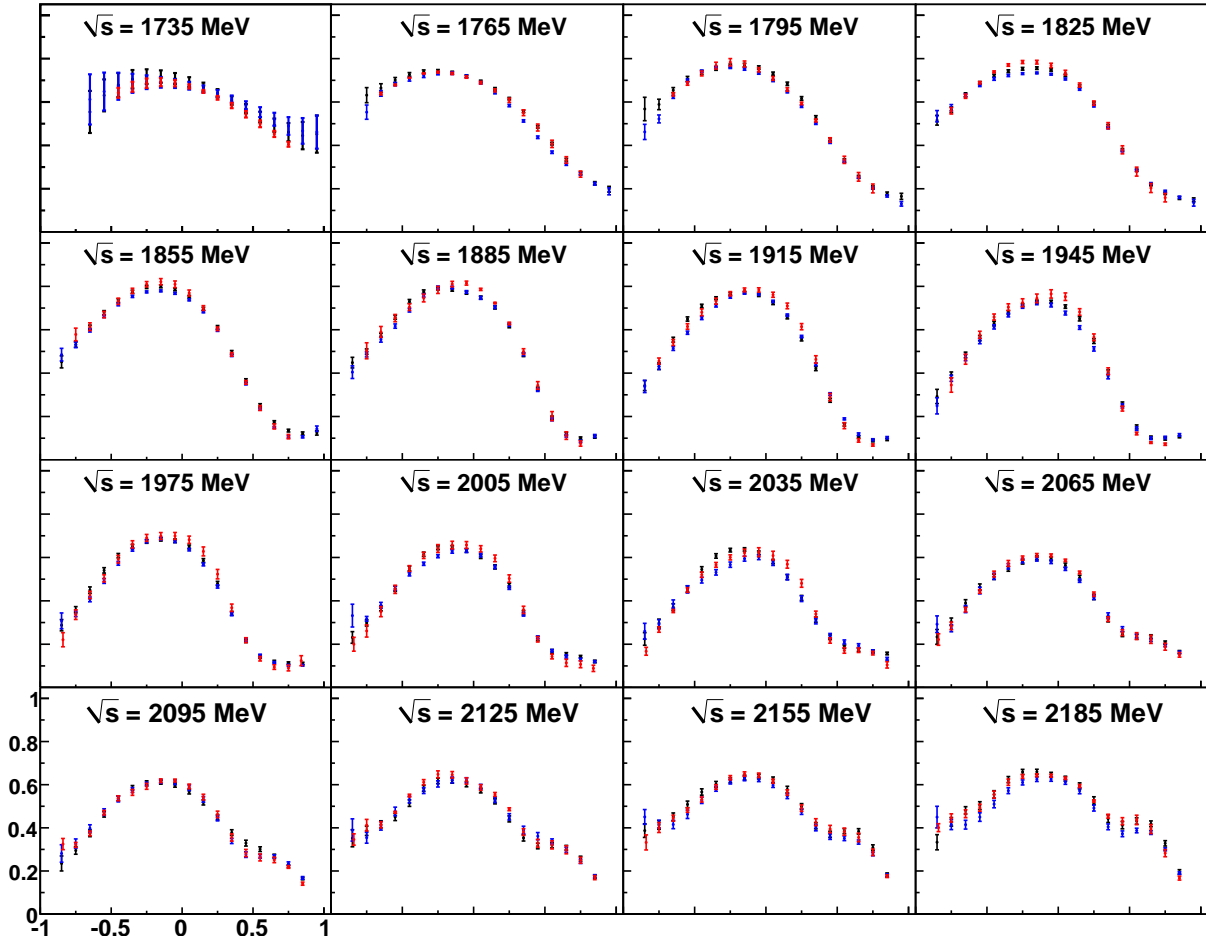


Figure B.1:  $\rho_{00}^0$  element vs  $\cos \theta_{CM}$  in bins of  $\sqrt{s}$ . The results from g1c (black) are shown in comparison to the g8b (blue) values and the g11a (red) values. The errors for g1c and g8b are as calculated in Section 5.2.1. Notice that in the 1825 MeV bin and the 1915-2035 MeV bins, where there are noticeable differences from the g11a dataset, the g1c and g8b datasets agree well with each other.

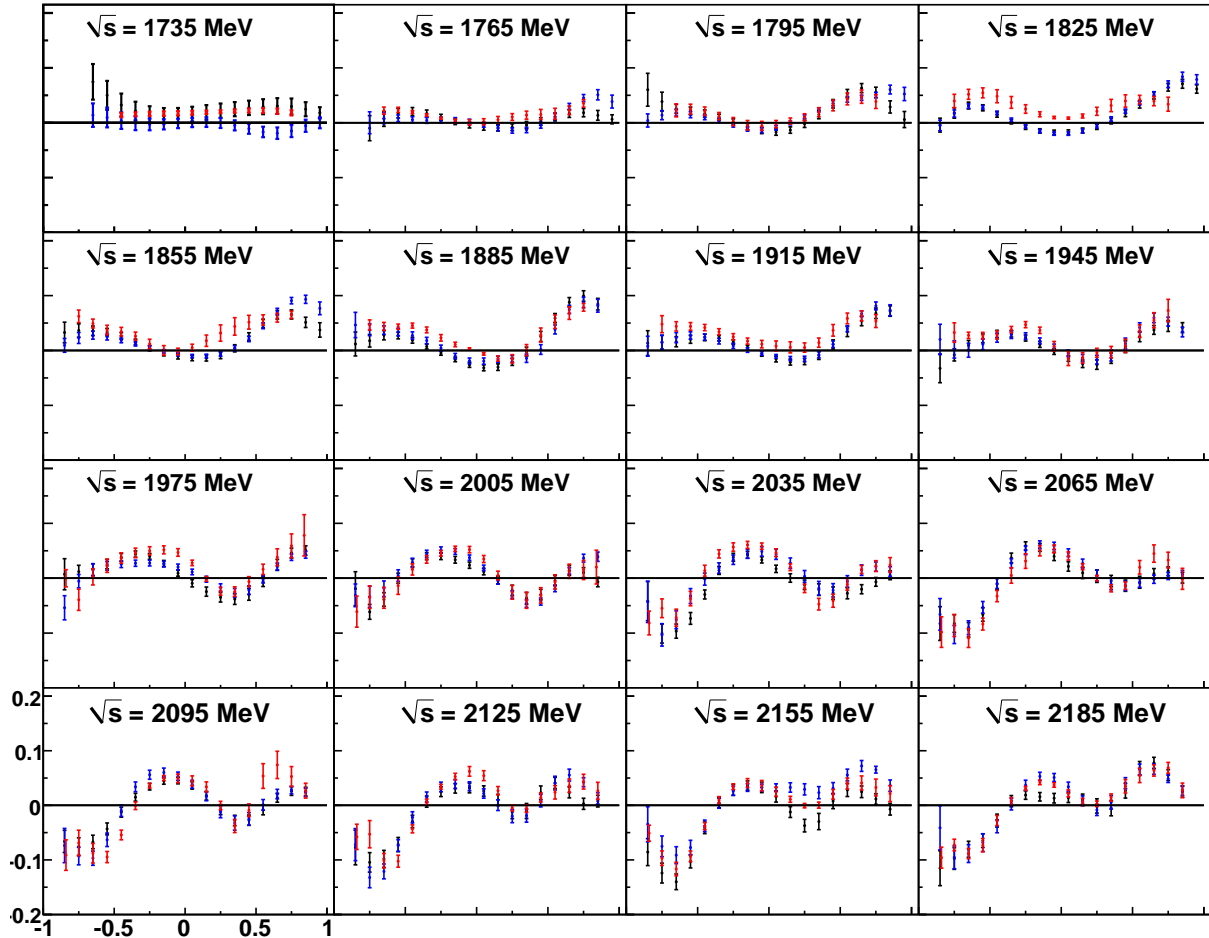


Figure B.2:  $\text{Re}(\rho_{1-1}^0)$  element vs  $\cos \theta_{CM}^\omega$  in bins of  $\sqrt{s}$ . The results from g1c (black) are shown in comparison to the g8b (blue) values and the g11a (red) values. The errors for g1c and g8b are as calculated in Section 5.2.1. Notice that in the 1795-1975 MeV bins, where there are noticeable differences from the g11a dataset, the g1c and g8b datasets agree well with each other.

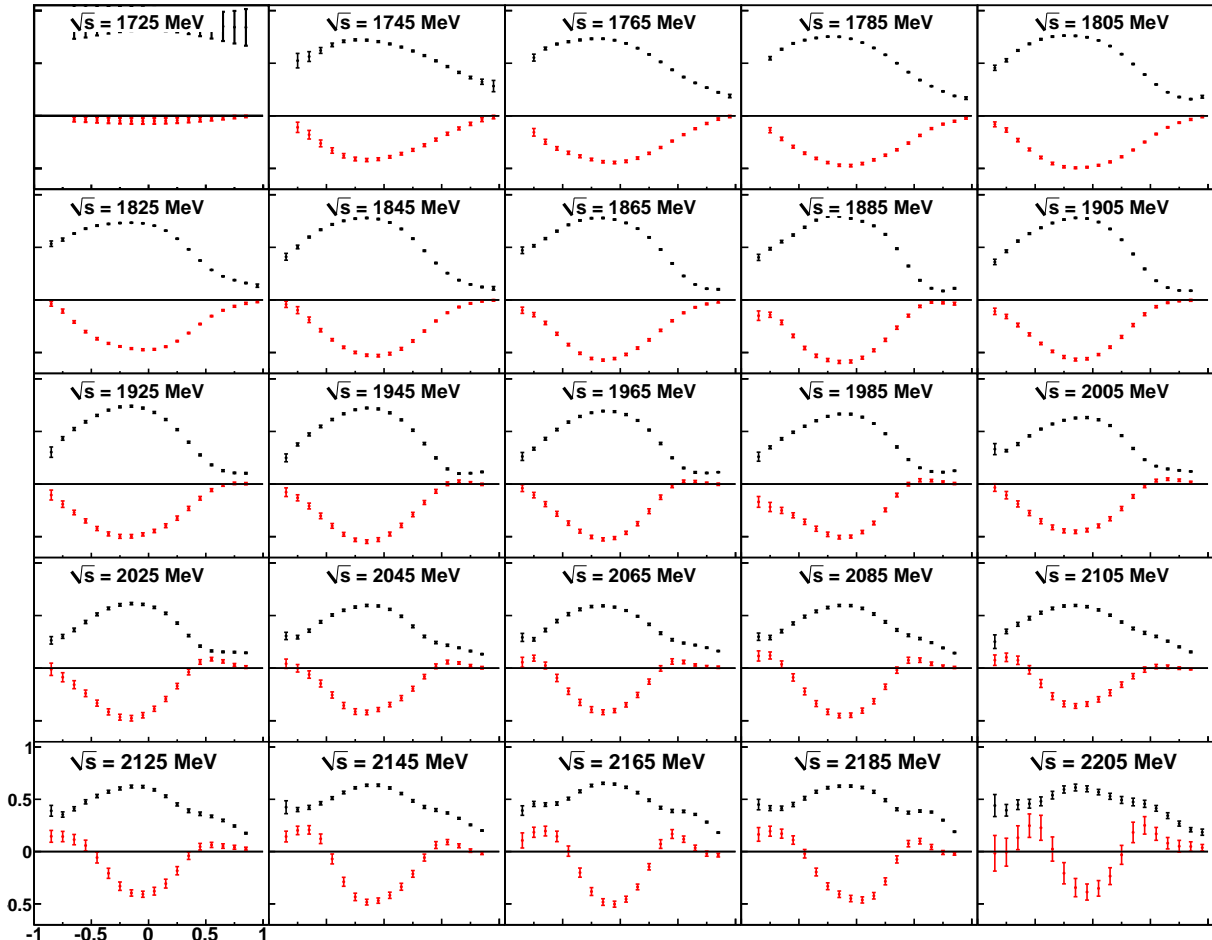


Figure B.3:  $\rho_{00}^0$  (black) and  $\rho_{00}^1$  (red) elements vs  $\cos \theta_{CM}^\omega$  in bins of  $\sqrt{s}$  for g8b. The errors for g1c and g8b are as calculated in Section 5.2.1. Only half of the bins have been shown to save space. Over almost the entire energy range, the  $\rho_{00}^1$  values evolve in  $\cos \theta_{CM}^\omega$  in the reverse of the  $\rho_{00}^0$  values; where the  $\rho_{00}^0$  values rise the  $\rho_{00}^1$  values fall, and vice versa. Above 2025 MeV, this symmetry starts to break in the forward angles, above  $\cos \theta_{CM}^\omega = 0.5$ . Above 2125 MeV, the  $\rho_{00}^1$  values are varying more than the  $\rho_{00}^0$  values at all angles, though they do still share the same turning points.

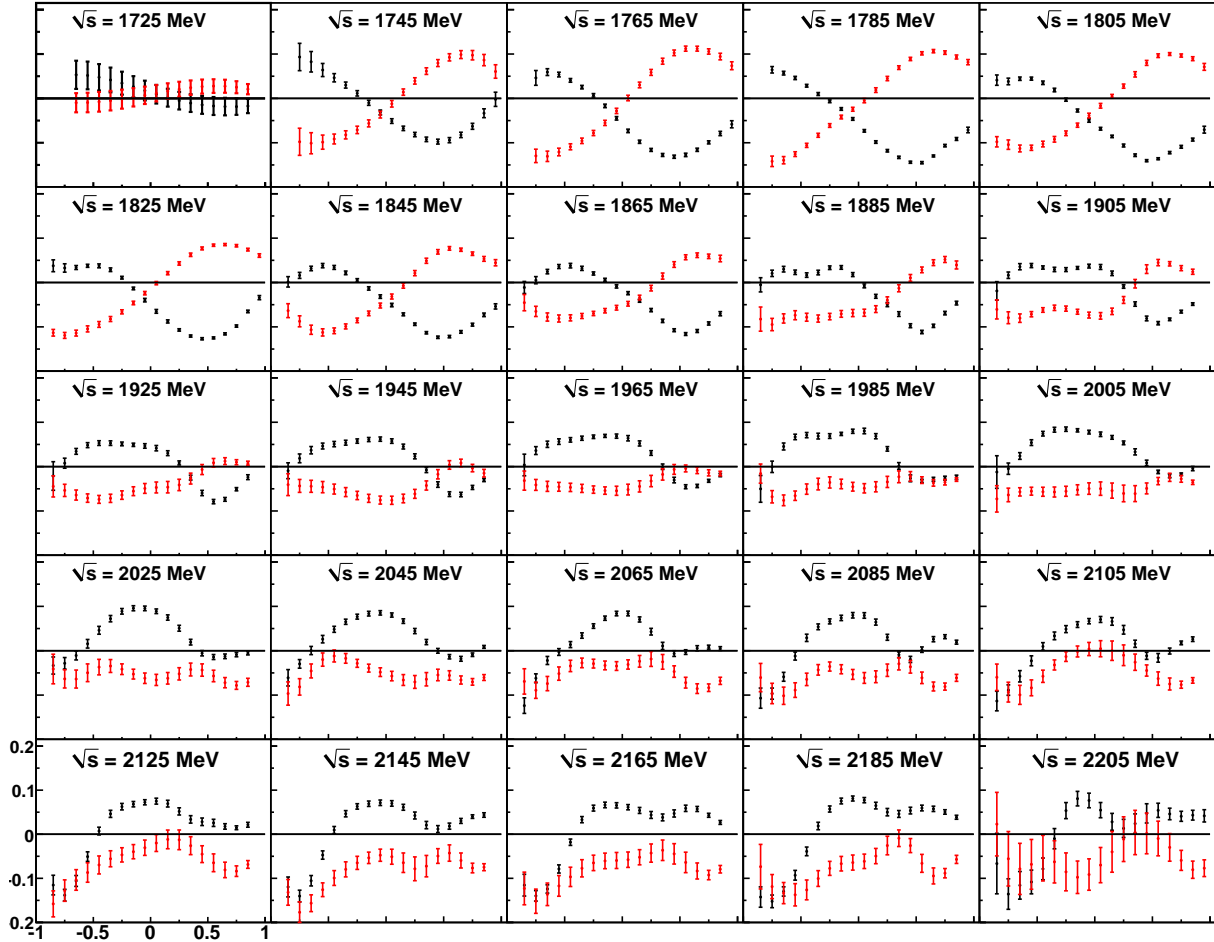


Figure B.4:  $\text{Re}(\rho_{10}^0)$  (black) and  $\text{Re}(\rho_{10}^1)$  (red) elements vs  $\cos \theta_{CM}^\omega$  in bins of  $\sqrt{s}$  for g8b. The errors for g1c and g8b are as calculated in Section 5.2.1. Only half of the bins have been shown to save space. Below 1970 MeV, the  $\text{Re}(\rho_{10}^1)$  element is very strongly related to the  $\text{Re}(\rho_{10}^0)$ , one rising when the other falls, and vice versa. Above 1970 MeV, the symmetry breaks the two elements evolve independently.

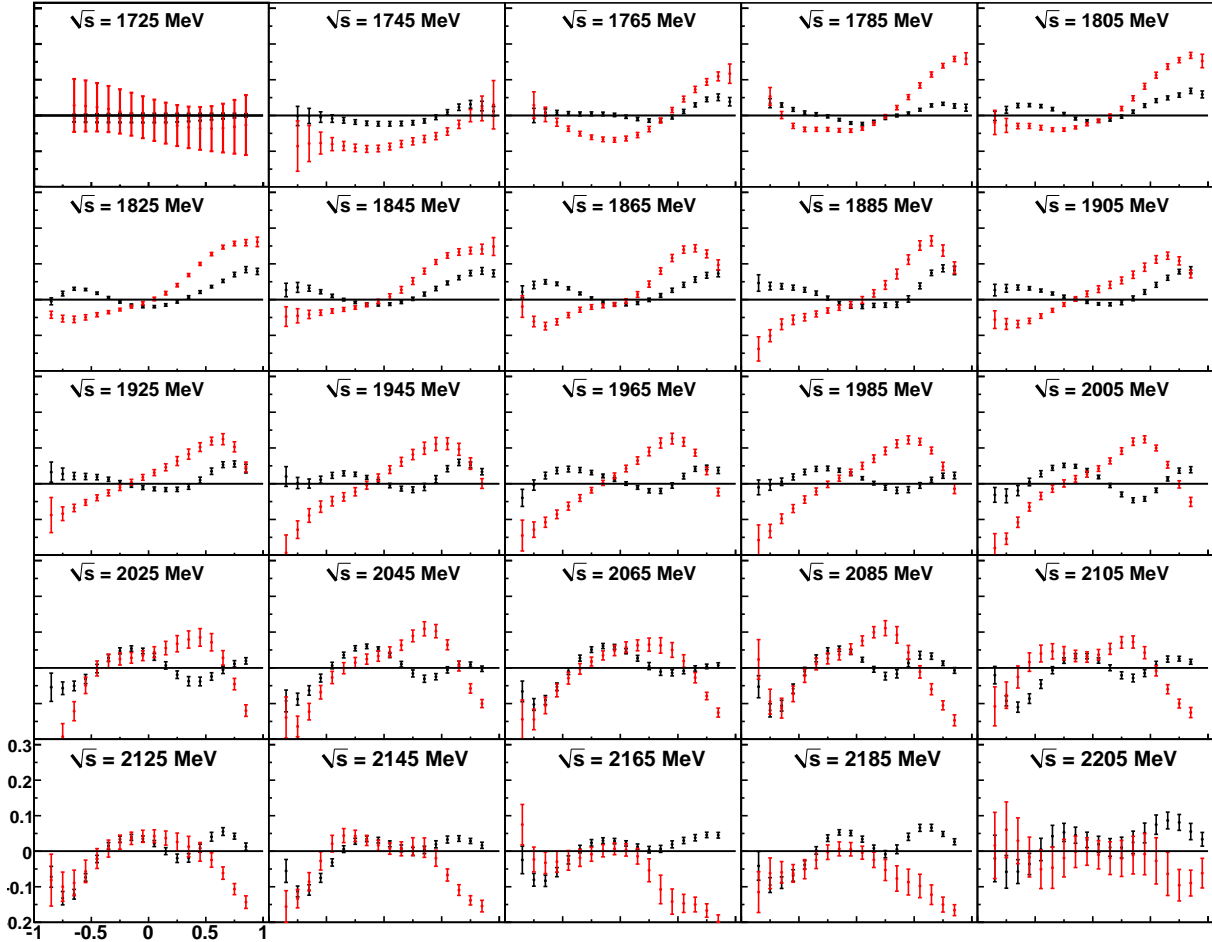


Figure B.5:  $\rho_{1-1}^0$  (black) and  $\rho_{1-1}^1$  (red) elements vs  $\cos \theta_{CM}^\omega$  in bins of  $\sqrt{s}$  for g8b. The errors for g1c and g8b are as calculated in Section 5.2.1. Only half of the bins have been shown to save space. At low energies, there is not much correlation between the two elements. Above 2030 MeV, the backwards angles, below  $\cos \theta_{CM}^\omega = 0$ , are roughly equal in most bins.

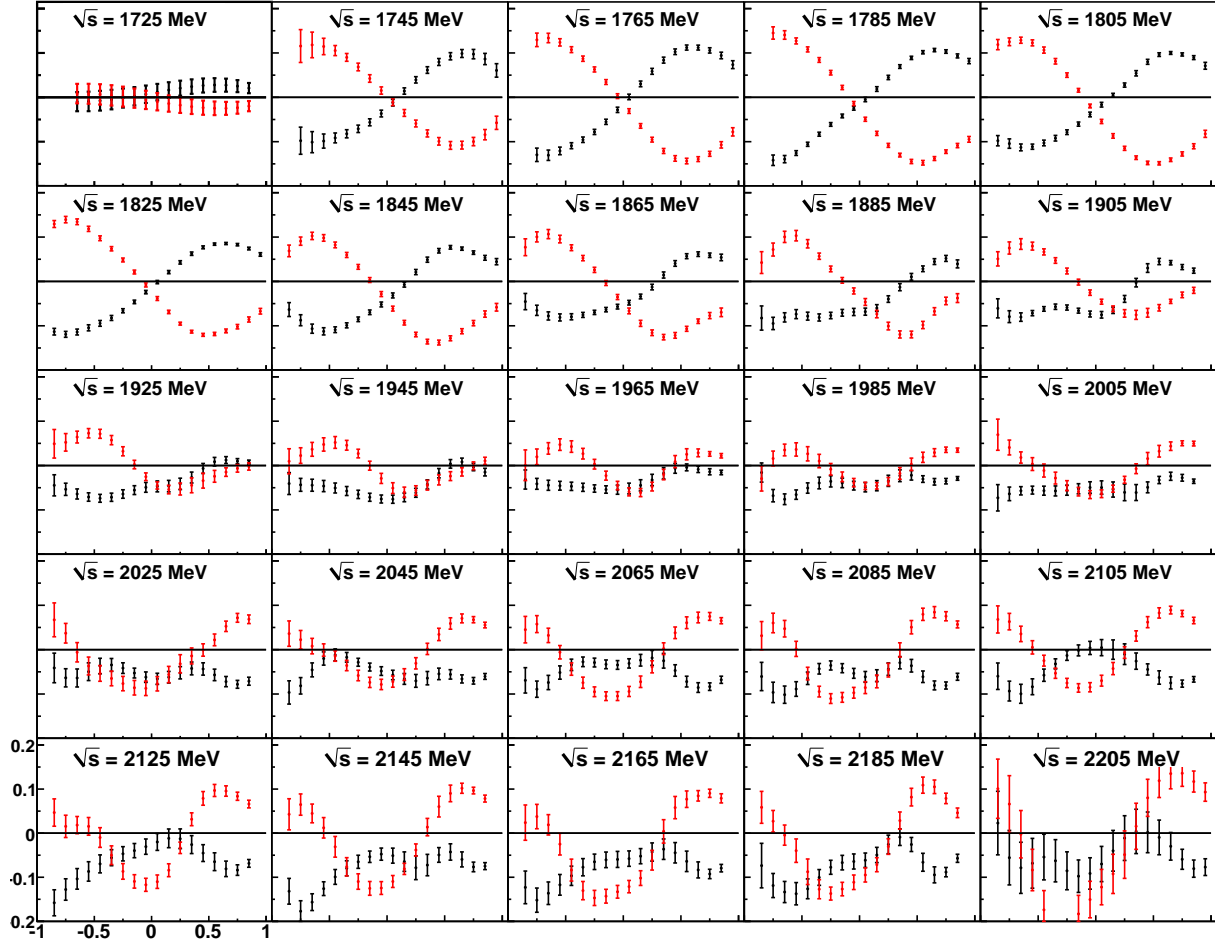


Figure B.6:  $\text{Re}(\rho_{10}^1)$  (black) and  $\text{Im}(\rho_{10}^2)$  (red) elements vs  $\cos \theta_{CM}^\omega$  in bins of  $\sqrt{s}$  for g8b. The errors for g1c and g8b are as calculated in Section 5.2.1. Only half of the bins have been shown to save space. For energies below 1840 MeV, the two elements mirror each other at all angles. Above 1845 MeV, the symmetry breaks and the two evolve independently, except for angles forward of  $\cos \theta_{CM}^\omega = 0.45$ , where they remain mirrors for almost the entire range.

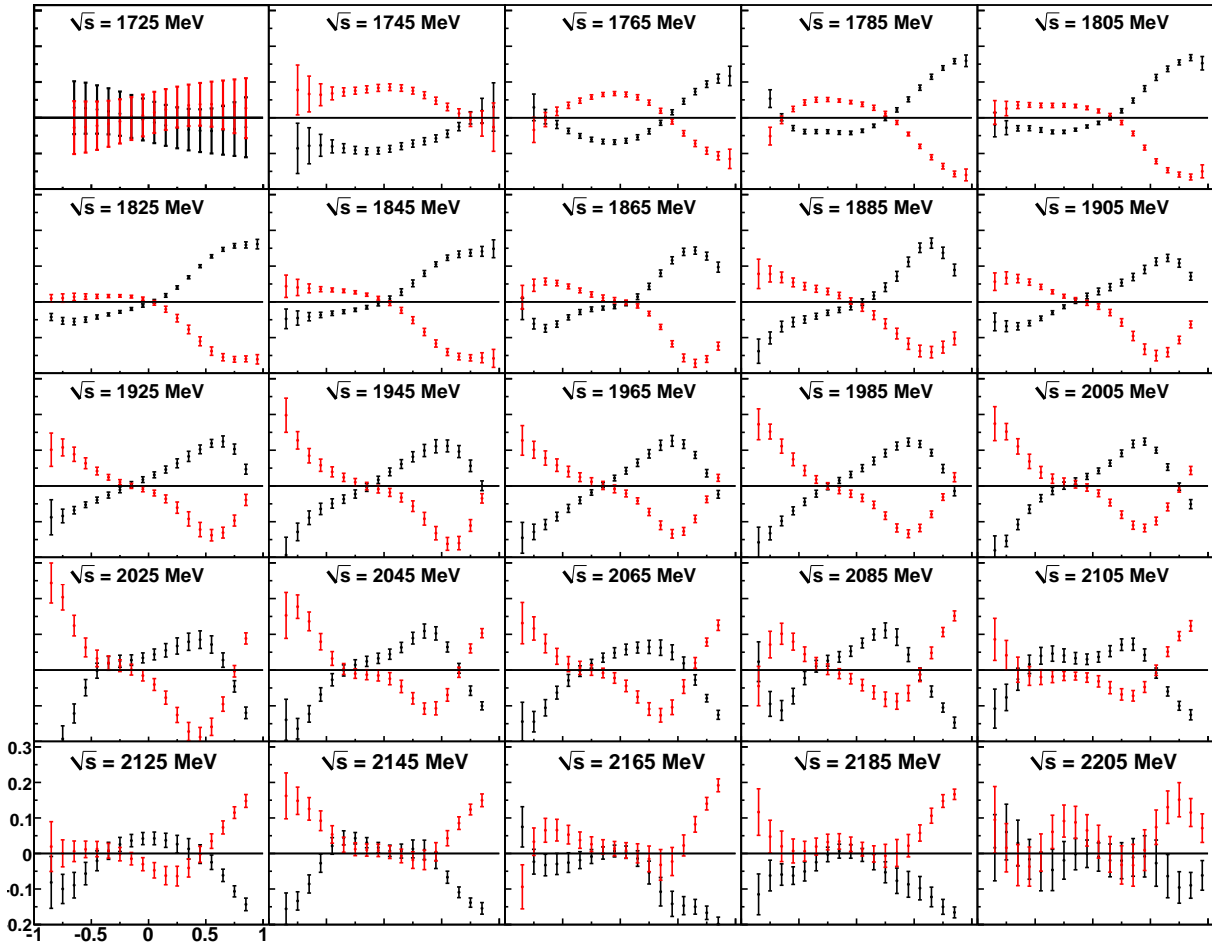


Figure B.7:  $\rho_{1-1}^1$  (black) and  $\text{Im}(\rho_{1-1}^2)$  (red) elements vs  $\cos \theta_{CM}^\omega$  in bins of  $\sqrt{s}$  for g8b. The errors for g1c and g8b are as calculated in Section 5.2.1. Only half of the bins have been shown to save space. For energies up to 2010 MeV, these two elements are a near exact mirror image of each other, not only in shape and but also in value. Above 2010 MeV, they are still mostly mirror images of each other, however there are some slight differences. Notice, for instance, values near  $\cos \theta_{CM}^\omega = 0.5$  in the 2125 MeV bin, or the 2165 MeV bin. It is unclear if these discrepancies are due to the errors, which are larger at higher energies, or the symmetry is starting to break.

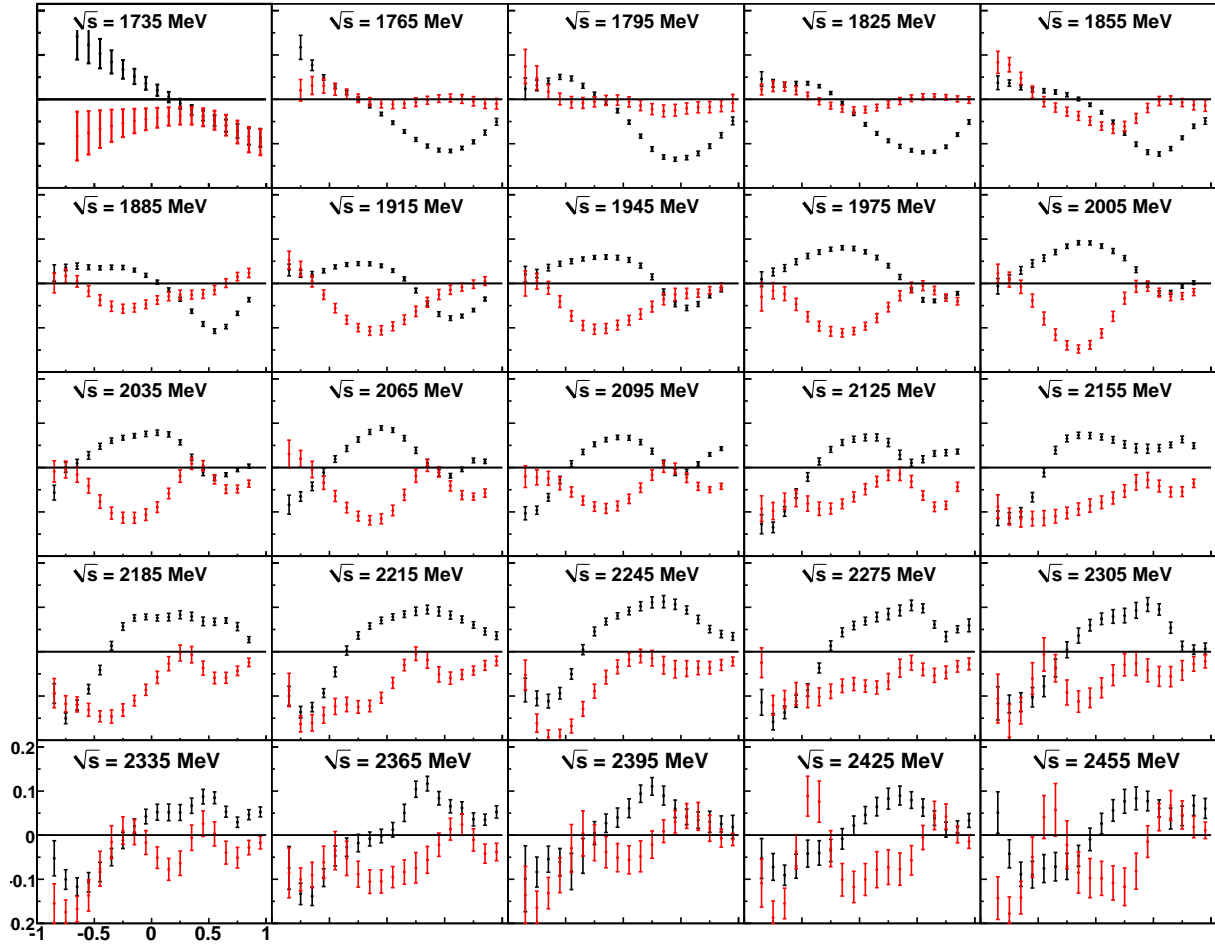


Figure B.8:  $\text{Re}(\rho_{10}^0)$  (black) and  $\text{Im}(\rho_{10}^3)$  (red) elements vs  $\cos \theta_{CM}$  in bins of  $\sqrt{s}$  for g8b. The errors for g1c and g8b are as calculated in Section 5.2.1. At certain energies, particularly from 1915-2095 MeV, there is some evidence of symmetry between the two elements, however, it is not as strong as was seen in other elements and there is little correlation between the two at other energies.

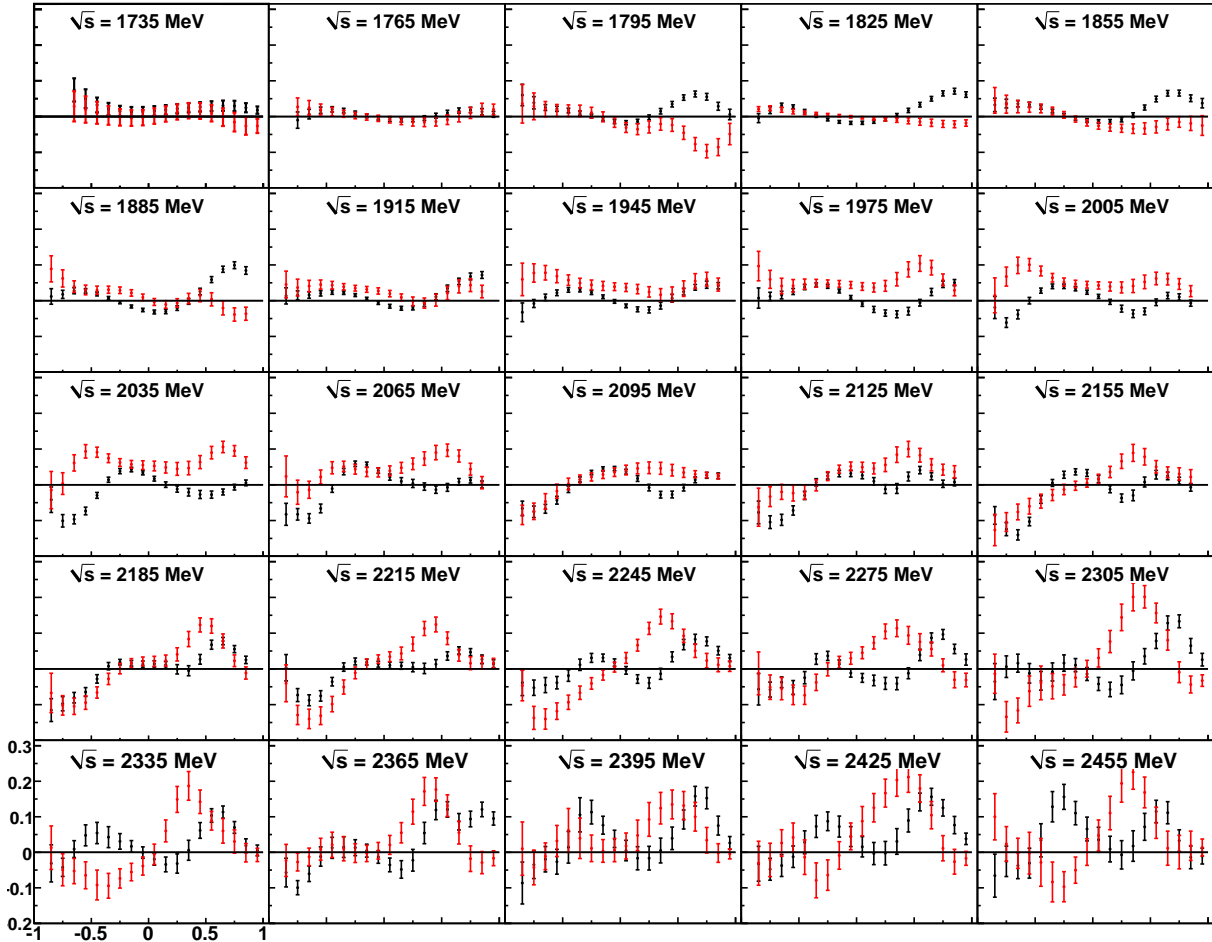


Figure B.9:  $\rho_{1-1}^0$  (black) and  $\text{Im}(\rho_{1-1}^3)$  (red) elements vs  $\cos \theta_{CM}^\omega$  in bins of  $\sqrt{s}$  for g8b. The errors for g1c and g8b are as calculated in Section 5.2.1. For energies below 1860 MeV, the backwards angles of the two elements are roughly equal, however, they are both quite small, so this may be incidental. At all other energies, there is little consistent correlation between the two elements.